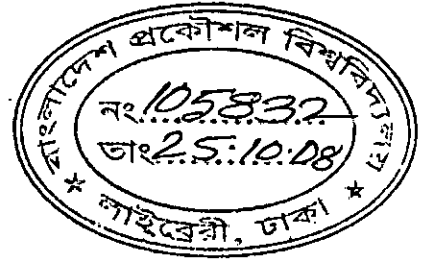


# Analytical Model of a VCSEL Considering External Optical Feedback

A Thesis submitted

by



**Ashim Kumar Saha**  
(Roll 040506246F)

under the supervision of

**Prof. Dr. Saiful Islam**



**Electrical & Electronic Engineering Department**  
**Bangladesh University of Engineering & Technology, Dhaka**

October Semester 2007

February 2008

# **Analytical Model of a VCSEL Considering External Optical Feedback**

A Thesis submitted to the Electrical and Electronic Engineering Department of Bangladesh University of Engineering & Technology (BUET) Dhaka Bangladesh in partial fulfillment of the requirements for the degree of Master of Science in Electrical and Electronic Engineering.

**Ashim Kumar Saha**  
(Roll 040506246F)

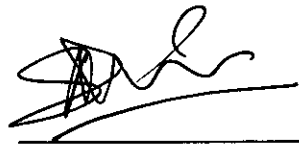
**Electrical and Electronic Engineering Department**  
**Bangladesh University of Engineering & Technology, Dhaka**

October Semester 2007

February 2008

## Declaration

This is to certify that this thesis is the outcome of the original work of the undersigned student. No part of this work has been submitted elsewhere partially or fully for the award of any other degree or diploma. Any material reproduced in this thesis has been properly acknowledged.

A handwritten signature in black ink, appearing to read 'Ashim Kumar Saha', is written over a horizontal line.


**Ashim Kumar Saha**  
Roll 040506246F

## Approval

The Thesis titled “**Analytical Model of a VCSEL Considering External Optical Feedback**” has been submitted by **Ashim Kumar Saha** Roll 040506246F of the Electrical and Electronic Engineering Department of Bangladesh University of Engineering & Technology, Dhaka in partial fulfillment of the requirements for the degree of Master of Science in Electrical and Electronic Engineering on 13 February 2008 and has been accepted as satisfactory.

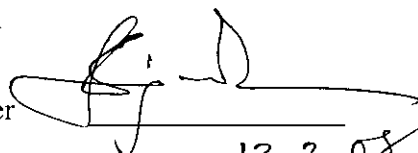
1. Prof. Dr. Saiful Islam (Supervisor)  
Professor  
Electrical & Electronic Engineering Department  
Bangladesh University of Engineering  
& Technology,  
Dhaka

Chairman

  
\_\_\_\_\_

2. Prof. Dr. Satya Prasad Majumder  
Professor and Head  
Electrical & Electronic Engineering Department  
Bangladesh University of Engineering  
& Technology,  
Dhaka

Ex-Officio Member

  
\_\_\_\_\_

13.2.08

3. Prof. Dr. Quazi Deen Mohd Khosru  
Professor  
Electrical & Electronic Engineering Department  
Bangladesh University of Engineering  
& Technology,  
Dhaka

Member

  
\_\_\_\_\_

4. Prof. Dr. Jalalur Rahman  
Professor  
Applied Physics, Electronics and  
Communication Engineering Department  
Dhaka University  
Dhaka

External Member

  
\_\_\_\_\_

## Acknowledgements

I express my whole hearted gratitude to my supervisor Prof. Dr. Saiful Islam for his sincerest help and guidance throughout the period of this research work. Throughout this working period he gave time beyond office hours and worked over sufficiently long time even up to very late evening to give me guidance in this work. He has always been involved with the high quality research. This has definitely inspired me at least to try to do some quality work. Without his tireless efforts it would have been impossible to achieve this quality of work. I sincerely thank him for the bottom of my heart for his wonderful supervision.

I would like to acknowledge Mr. Md. Noor Islam, Assistant Professor of Electrical & Electronic Engineering Department, Khulna University of Engineering & Technology (KUET) (now studying at South Korea) and Mr. Pallab Kumar Choudhury, Assistant Professor of Electronics and Telecommunications Engineering Department, Khulna University of Engineering & Technology (KUET) for supplying me photocopy of a number journal research paper during my literacy survey at the beginning of this work. I will thankful to them.

Thanks are given to my fellow teachers Mr. Rinku Basak and Mr. Hasan Imam from the Engineering Faculty of American International University-Bangladesh (AIUB) for their support encouragement and many valuable discussions.

In the end, I would like to give special thanks and express my sincerest gratitude to the Management of American International University-Bangladesh (AIUB) for giving me the whole hearted support, encouragement and also provide me printing, photocopy, internet and computer facilities for this work.

## Abstract

In this work, a new technique of obtaining the transfer matrix of a multilayer DBR stack is presented. By extending this technique the transfer matrix of a complete VCSEL with an active layer sandwiched between a bottom DBR stack and a top DBR stack is developed. The new technique of forming the transfer matrix is termed as Sampled Transfer Matrix Method (STMM). Using the STMM it is possible to compute the transfer matrix of a DBR stack or a complete VCSEL accurately even if the layers are constructed using smoothly varying refractive index layers.

It is difficult to compute the transfer matrix as well as Reflectivity and Transmittivity of a DBR stack containing smoothly varying refractive index layers by using the previously used Transfer Matrix Method (TMM). In the STMM the layers of smoothly varying refractive index layers are divided into many thin layers having a thickness of  $d$  which is many times less than the actual thickness of the layers. Each of such a sampled layer may be considered as a constant index layer. The transfer matrix of the complete DBR stack is computed by multiplying all of the transfer matrices of each of the sampled layers. Reflectivity and Transmittivity of a DBR stack and a complete VCSEL containing graded index layers as well as step index layers can be computed accurately by using this STMM. If the number of sampled layers are increased calculation for smooth variation of refractive indices of the layers provides more accurate results.

Using the transfer matrix formed by using STMM it is possible to compute the electric field distribution inside a VCSEL. The electric field intensity at any point between the center of the cavity and the end of the top or bottom DBR stack can be computed by imagining a plane at that point. Then compute the transfer matrix of the remaining portion of the VCSEL (from imagining plane to the top or bottom facet) and applying the relation presented in the section (5.3), the electric field intensity at the imagined plane can be computed. In this way the electric field distribution inside the VCSEL can be computed.

The optical feedback effect on the performance parameters of a VCSEL from the external reflectors has been studied utilizing the transfer matrix formed using the above mentioned STMM. The transfer matrix of a VCSEL having external reflectors has been formed using STMM. Using this model next, the position of the external reflector is varied to determine the variations of threshold current, external differential quantum efficiency and output power of a VCSEL.

Rate equations based model of a VCSEL with optical feedback is presented in a new way. Parts of the rate equation related to optical feedback is modified and computed from the STMM based model. Then the modified Rate equations are solved numerically by using the Finite Difference (FD) method. Carrier density, Photon density, Photon fluctuation due to optical feedback and Relative Intensity Noise (RIN) has been computed.

It is worthwhile mentioning here that the computation of the performance parameters of a complete VCSEL in presence of optical feedback has been done by computing the electric field inside the VCSEL. In addition to this, output optical power versus time and output optical power versus injection current have been computed using the rate equation based model.

Finally, the obtained result has been analyzed and it has been found that the STMM based model of computing the performance parameters of a complete VCSEL in presence of optical feedback is capable of providing better results compared to the results that were obtained previously by using other models.

# Contents

	Page No.
Declaration	(i)
Approval Sheet	(ii)
Acknowledgement	(iii)
Abstract	(vi)
<b>Chapter 1. Introduction</b>	<b>1</b>
1.1 Historical Background	1
1.2 Distributed Bragg Reflector (DBR) as Mirror in a VCSEL	1
1.3 TMM for Calculating Reflectivity of DBR Mirror in a VCSEL	2
1.4 CMT for Calculating Reflectivity of DBR Mirror in a VCSEL	2
1.5 <i>Tanh</i> Substitution Technique to Find the Reflectivity of DBR Mirror in a VCSEL	2
1.6 FBT for Calculating Reflectivity of DBR Mirror in a VCSEL	2
1.7 Objectives of This work	3
1.8 Introduction to This Thesis	3
<b>Chapter 2. Theory of Semiconductor Laser</b>	<b>5</b>
2.1 Introduction	5
2.2 Construction and Operation of a Semiconductor Laser	6
2.3 Double Heterostructure Laser	7
2.4 Spontaneous Emission, Stimulated Emission and Absorption	10
2.5 Relationship between Spontaneous and Stimulated Emission	12
2.6 Stimulated Gain Spectra of Semiconductors	16
2.7 Condition of Oscillation in a Fabry-Perot laser	21
2.8 Materials Used for Fabricating a Semiconductor Laser	25
2.9 Types of Semiconductor Lasers	26
2.10 Edge Emitting Lasers	27
2.11 Surface Emitting Lasers	28
2.12 Structure of a Semiconductor Laser in the Lateral Direction Perpendicular to the Plane of the Junction	32
2.13 Structure of a Semiconductor Laser in the Direction Parallel to the Plane of the Junction	34
2.14 Summary	36
<b>Chapter 3. Vertical-Cavity Surface-Emitting Laser VCSEL</b>	<b>37</b>
3.1 Introduction	37
3.2 Construction of a VCSEL	37
3.3 Different Structures of VCSELS	38
3.4 Operating Parameters of a VCSEL Compared with an Edge Emitting Laser	42
3.5 Distributed Bragg Reflector	43
3.6 Variation of Refractive Index of some of the Direct Bandgap Semiconductor Materials with the Emission Wavelength	44
3.7 Reflectivity Spectrum of DBR Stacks	49
3.8 Reflectivity Spectrum of a VCSEL Resonator	53
3.9 Electric Field Distribution inside the VCSEL	54
3.10 Relative Confinement Factor of a VCSEL	58

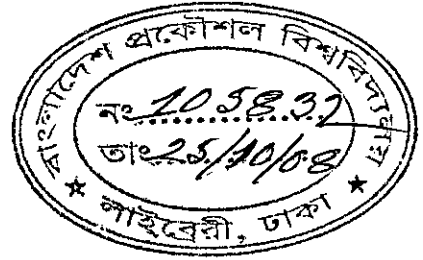
3.11 Threshold Current and Photon Lifetime	60
3.12 Radiation Efficiency and Conversion Efficiency	60
3.13 Summary	64
<b>Chapter 4. Rate Equations Based Model of a VCSEL</b>	<b>65</b>
4.1 Introduction	65
4.2 Rate Equations of a Semiconductor Laser	65
4.3 Rate Equation for Carrier Density	66
4.4 Rate Equation for Photon Density	66
4.5 Rate Equation for the Optical Phase	66
4.6 Threshold Current Density and Threshold Carrier Density of a Semiconductor Laser	68
4.7 Current versus Light Output of a Semiconductor Laser	70
4.8 Rate Equations of a VCSEL	73
4.9 Calculation of Turn on Delay	76
4.10 Output Power of a VCSEL	81
4.11 Summary	84
<b>Chapter 5. Transfer Matrix Method (TMM) Based Analysis of a VCSEL</b>	<b>85</b>
5.1 Introduction	85
5.2 Calculation of Reflectivity and Transmittivity of DBR Stacks by using TMM	85
5.3 Calculation of Reflectivity and Transmittivity of a Complete VCSEL by using TMM	88
5.4 Summary	90
<b>Chapter 6. A Novel Method of Calculating DBR Reflectivity Spectrum and the Electric Field Distribution inside a VCSEL</b>	<b>91</b>
6.1 Introduction	91
6.2 Basic idea of Sampled Transfer Matrix Method (STMM)	91
6.3 Computation of Reflectivity and Transmittivity of a Generalized DBR Stack using STMM	94
6.4 Computation of Reflectivity of Graded Index Layered DBR Stacks using STMM	96
6.5 Computation of Reflectivity of DBR Stacks having Sinusoidal Variation in the Refractive Index	100
6.6 Reflectivity and Transmittivity Spectra of a Complete VCSEL	102
6.7 Electric Field distribution inside the VCSEL	106
6.8 Field Intensity inside the Different Types of VCSEL Resonator	111
6.9 Summary	114
<b>Chapter 7. Operation of a VCSEL in the Presence of Optical Feedback</b>	<b>115</b>
7.1 Introduction	115
7.2 Analytical Model of VCSEL with Optical Feedback	115
7.3 Electric Field Distribution inside a VCSEL due to Different Positions of the External Reflector	119
7.4 Electric Field Distribution inside a VCSEL having Different DBR Structures Considering the External Optical Feedback	119
7.5 Effects of Optical Feedback on the Operation of a VCSEL	122
7.6 Variation of Threshold Current due to External Optical Feedback	123



7.7 Variation of External Differential Quantum Efficiency	124
7.8 Analysis of Output Power Variation of a VCSEL	125
7.9 Summary	126
<b>Chapter 8. Dynamic Behaviour of a VCSEL with and without External Optical Feedback</b>	<b>127</b>
8.1 Introduction	127
8.2 Different Types of Noise in Semiconductor Laser	127
8.3 Rate Equations of a VCSEL with Various Noise Sources	129
8.4 Rate Equations of a VCSEL with External Optical Feedback	130
8.5 Small Signal Modulation Response	135
8.6 Determination of Relative Intensity Noise (RIN)	137
8.9 Summary	140
<b>Chapter 9. Discussions and Conclusions</b>	<b>141</b>
9.1 Discussions	141
9.2 Suggestions for Future Work	143
9.3 Conclusions	143
<b>References</b>	<b>145</b>

## Chapter 1

### Introduction



## **1.1 Historical Background**

Vertical Cavity Surfacing Emitting Lasers (VCSELs) has recently become one of the most promising semiconductor light source for optical communications, information read-write and fast parallel optical interconnects. In a typical VCSEL, an optical cavity is formed with an active layer placed between one bottom set and one top set of Distributed Bragg Reflectors (DBR) acting as mirrors. The cavity and the reflectors are placed in a line which is in the direction of growth of the device.

Vertical-cavity surface-emitting lasers (VCSELs) have a number of advantages over the edge emitting laser. These are (i) low threshold current, (ii) single-longitudinal-mode operation, (iii) circular and low divergence output beams and (iv) wafer scale integrability [1, 2].

In the application of VCSELs, special attention needs to be given to external optical feedback phenomenon because of the undesirable disturbances in its operation due to such feedback. Optical feedback in VCSELs has been investigated in the past, both from the non-linear dynamics point of view and also from the view point of potential applications [3-5]. It is well known that optical feedback in lasers leads to increased noise, mode hopping, linewidth narrowing or broadening, and coherence collapse [6-8]. Further study of the operation of VCSEL in presence of optical feedback is still very much needed.

In the previous works [3-5] transfer matrix method (TMM) has been used to compute the effects of optical feedback. Using this method (TMM) it is possible to compute the transfer matrix of a VCSEL if step index DBR layers are used. However, while using this method difficulties arise in the computation of transfer matrix if graded index DBR layers are used. Due to these difficulties it is necessary to search for an alternative method of forming the transfer matrix of a VCSEL having graded index DBR layers. Using this alternative method of forming a transfer matrix it is necessary to develop an analytical method in order to calculate the threshold current, external differential quantum efficiency and output power variation of a VCSEL with optical feedback for graded index as well as step index DBR layers. In this work, a new technique (Sampled Transfer Matrix Method (STMM)) of forming the transfer matrix for step index as well as graded index DBR layers of a VCSEL will be developed. Using this new technique an analytical method will be developed to compute the effects of optical feedback in a VCSEL.

## **1.2 Distributed Bragg Reflector (DBR) as Mirror in a VCSEL**

The VCSELs have the very short optical gain region as compared to edge-emitting lasers, hence requiring very high (>99%) reflectivity mirrors to achieve lasing action. This can be achieved only by Distributed Bragg reflectors (DBRs), whose design criteria are related to maximum optical reflectivity, thermal and electrical conductivity, material index contrast and optical absorption. DBR analysis is critical in VCSEL design, because their reflectivity strongly affects all laser fundamental properties such as threshold gain, external differential quantum efficiency hence output power. Long wavelength VCSELs require ternary or quaternary semiconductor alloys, having substantially lower thermal conductivities than binary counterpart due to alloy scattering [13].

Heat conduction is one of the most recurrent problem arising for DBRs in long-wavelength VCSEL. Thermal heating and consequent deterioration of laser performance is related with the high series resistance of DBR stacks, due to the large band gap difference at the hetero-interfaces, resulting in carrier flow impediment. Therefore, it is evident that an accurate investigation of optimized distributed Bragg reflectors is still a fundamental task in VCSEL design [14].

### **1.3 TMM for Calculating Reflectivity of DBR Mirror in a VCSEL**

Numerical calculations of multilayered mirrors are generally carried out by the transfer matrix method (TMM) [15-17] or the coupled mode theory (CMT) [18]. Floquet-Bloch Theory (FBT) has been applied to the simulation of distributed Bragg reflectors in vertical cavity surface emitting lasers (VCSELs) [19].

### **1.4 CMT for Calculating Reflectivity of DBR Mirror in a VCSEL**

TMM is commonly used to analyse the multilayered mirrors with abrupt interfaces. By this method it is possible to analytically formulate the reflectivity, provided the thickness of each quarter wavelength dielectric layer. However, the losses due to scattering at layer interfaces are not taken into account and the numerical implementation is often computationally onerous. CMT provides simple analytical expressions, also for mirrors having graded interfaces. This is simply done by modifying the coupling constant with the introduction of some approximations, so the applicability of the method is limited to DBR structures with small index contrast, where the perturbation induced by the index periodicity (grating) can be considered weak.

### **1.5 *Tanh* Substitution Technique to Find the Reflectivity of DBR Mirror in a VCSEL**

Corzine et al. [20] developed a *Tanh* substitution technique to find the reflectivity of abrupt and graded multilayered mirrors, that does not introduce any advantage in terms of accuracy, but only in terms of simplicity.

### **1.6 FBT for Calculating Reflectivity of DBR Mirror in a VCSEL**

Leonardis et al. [19] introduced Floquet-Bloch Theory (FBT) based technique to find the reflectivity of abrupt and graded multilayered mirrors but did not give any mathematical equation or analysis in their work.

It is also important to know the electric field distribution inside a VCSEL to design a high performance VCSEL. FBR or *Tanh* substitution technique does not present the way to determine the electric field distribution. Electric field distribution can be calculated by using TMM only in case of abrupt index multilayer [17].

The effect of external optical feedback on the operation of a surface emitting semiconductor laser has been extensively investigated by various scientists in the recent past [21-25], because this feedback affect the operation of a semiconductor laser significantly[22-23]. The effect of external optical feedback has strong influence in the operation of a VCSEL as well [24-25]. As a result it is necessary to study the effect of external optical feedback in a VCSEL.

## 1.7 Objectives of This Work

The first objective of this research is to develop a Sampled Transfer Matrix Method (STMM) based analytical model for the analysis of the effect of optical feedback on the operation of a VCSEL. The target is to develop the STMM based model to compute the reflectivity and transmittivity of a DBR stacks having step index layers.

The second objective is to compute the reflectivity and transmittivity of a DBR stack having graded index layers using the developed STMM based model. Reflectivity and transmittivity spectra of a complete VCSEL having graded index layered DBR stacks will also be computed.

The third objective is to calculate the internal electric field distribution in the VCSEL using the developed model. The standing wave pattern inside the VCSEL without optical feedback and with optical feedback will be determined by the developed model. The standing wave pattern for different position of the external reflector will also be determined

The fourth objective is to calculate (i) the threshold current, (ii) external differential quantum efficiency and (iii) output power after determining the effective power transmittivity and reflectivity of a VCSEL.

The fifth objective is to compute the fluctuation of photon density, fluctuation of output power, small signal modulation response and Relative Intensity Noise (RIN) of a VCSEL by solving the rate equations of a VCSEL numerically with and without optical feedback.

The final objective is to compare the results obtained by this model with the theoretical results of some of the previous works obtained by other different models.

## 1.8 Introduction to This Thesis

In Chapter 2, an introduction to the theory of semiconductor laser has been presented. This chapter basically deals with the common and basic theory of edge emitting semiconductor lasers.

The structure of a VCSEL along with the basic principles of operation of a VCSEL has been presented in Chapter 3. The theory of a VCSEL is also be presented in this chapter.

In Chapter 4, the rate equations necessary to compute the photon density and carrier density in a semiconductor laser are introduced at the beginning of this chapter. The rate equations of a VCSEL have been deduced in this chapter.

In Chapter 5, the Transfer Matrix Method (TMM) of calculation the reflectivity of a DBR stack as well as a complete VCSEL has been presented. Some other methods like, CMT, FBT and tanh substitution techniques are also introduced in this chapter.

A new technique named Sampled Transfer Matrix Method (STMM) of calculating the reflectivity of a DBR stack as well as a complete VCSEL has been presented in the Chapter 6. Electric field distribution in a VCSEL has been computed by using the new technique.

In Chapter 7, the analytical model of a VCSEL with external optical feedback has been developed. Calculation of the electric field distribution, threshold current, external differential quantum efficiency and output power of a VCSEL has been presented in this chapter.

Rate equations of a VCSEL with external optical feedback are presented in the Chapter 8. Computation of Output power fluctuation, fluctuation of carrier density, small signal modulation response and Relative Intensity Noise (RIN) has been presented in this chapter.

Finally, Chapter 9 summarises the results of the research work and provides suggestions for future research.

## Chapter 2

### Theory of Semiconductor Laser

#### 2.1 Introduction

In this chapter, the basic theory and characteristics of stimulated emission and optical amplification gain in semiconductors will be discussed. In a semiconductor laser stimulated emission is a vital process to obtain coherent light output. On the other hand, optical amplification gain is a parameter which is essential in the analysis of a semiconductor laser. First, the process of stimulated emission in semiconductor laser has been explained, and then the optical amplification gain has been derived as a function of emission wavelength and applied junction voltage. The structure of a basic Fabry-Perot (FP) type semiconductor laser has been described. The theory of oscillation of a FP semiconductor laser is also presented. Finally, an introduction to different types of semiconductor lasers and their structures have been presented.

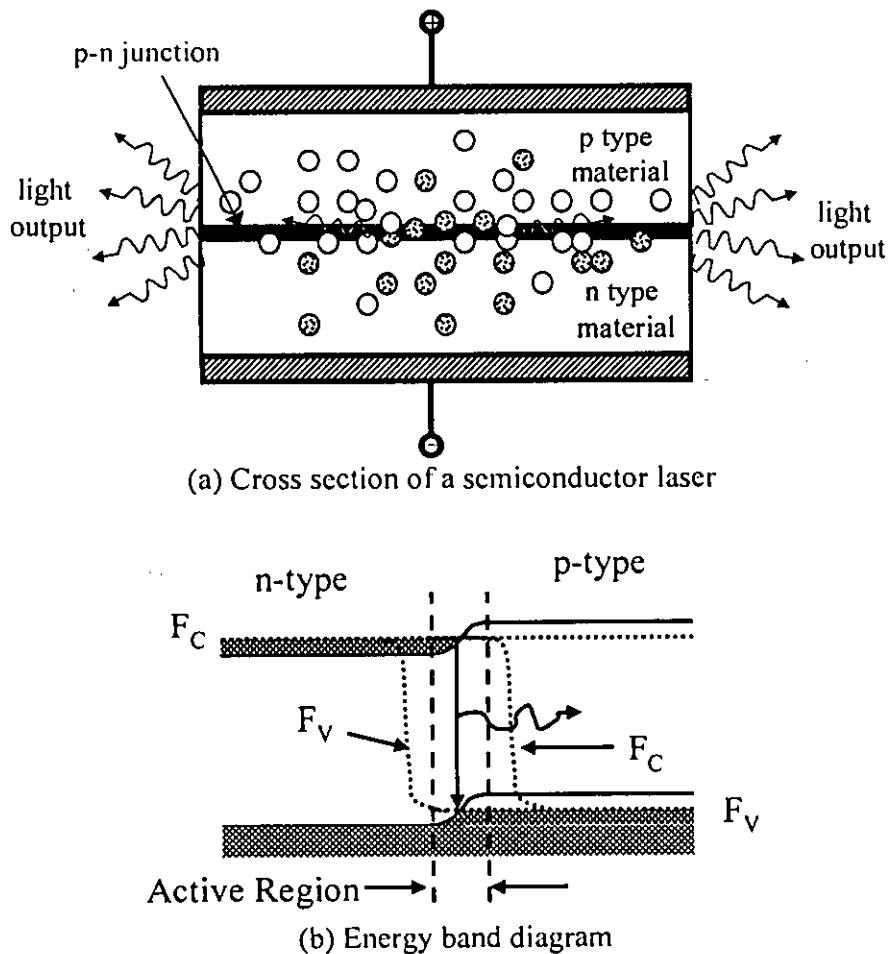


**Figure 2.1** Representation of a simple p-n junction (homojunction) semiconductor laser diode. (a) Shows the cross section of the junction (b) shows the energy band diagram of the junction under forward bias.

## 2.2 Construction and Operation of a Semiconductor Laser

Semiconductor lasers are quite different compared to other types of lasers in terms of appearance, construction and operation. They are very small, operate with relatively low power input, and are very efficient. They also operate in a different way. A basic semiconductor laser consists of a p-n junction using a p-type and an n-type III-V semiconductor material as shown in the Figure 2.1.

The laser action occurs in the interface between those two materials. One of the materials has an excess of electrons (n-type) and the other material (p-type) has a deficit of electrons or an excess of holes (missing electrons). When a forward bias voltage is placed across this junction as indicated in Figure 2.2, electrons are forced into the region from the n-type material and holes are forced into junction from the p-type material. These electrons with a negative charge and the holes with a positive charge are attracted to each other, and when they "collide" they neutralize each other and in the process emit recombination radiation. The electrons in the n-type material exist (at normal operating temperatures) at a higher energy (conduction band) than the holes (valence band). This energy difference is designated as the band gap energy of the material, the amount of energy that is released when the radiative recombination process occurs. Different material combinations have different band gaps and thus emit different wavelengths of light.

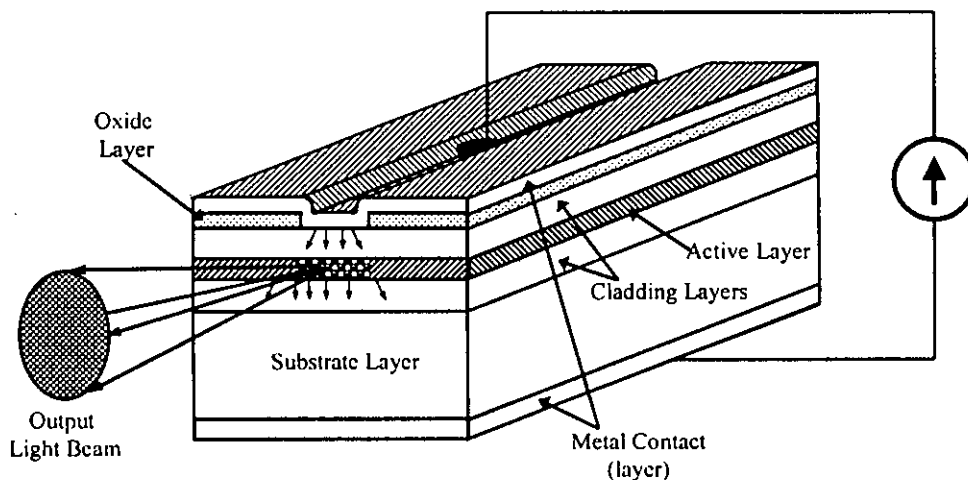


**Figure 2.2** Schematic diagram of a double heterostructure semiconductor laser diode. Current is injected through a narrow strip from the top side and confined in to the active layer by oxide layers.

The p-n junction semiconductor diodes are referred to as homojunction diodes, since they involve one p-type material and one n-type material. The threshold electrical current density required for these homojunction diodes to produce significant recombination radiation is extremely high. This threshold current density is generally expressed in units of  $A/cm^2$  flowing across the junction. The junction region is the only region of high resistance (low conductivity) because this is where the electrons and holes have neutralized each other. In contrast, both the n-doped region and p-doped region away from the junction are heavily doped and thus exhibit high conductivity. Therefore, if the junction region has a large surface cross-sectional area then the large volume of the junction region leads to a high ohmic dissipation of heat, which can rapidly lead to damage of the material. It would thus be desirable to minimize the surface area of the junction region and thereby produce high excitation in a region of small volume; this would preserve the effective excitation within the region and yet minimize the heat produced. The volume can be reduced in the direction of current flow by

making heterojunction and quantum-well laser materials. A schematic diagram of a double heterostructure edge emitting semiconductor laser diode is presented in Figure 2.2.

### 2.3 Double Heterostructure Laser

Laser structure discussed in previous section is not used in practice. Practical semiconductor lasers are usually Double Heterojunction (DH) type. A heterojunction is a junction formed between two dissimilar semiconductors where as a DH consists of two heterojunctions. Heterojunctions have been extensively studied, and many important applications have been made, among them the room-temperature injection laser, light-emitting diode (LED), photodetector, solar cell etc. In many of these applications, by forming periodic heterojunctions with layer thickness of the order of 10 nm, quantum wells and superlattices are produced.

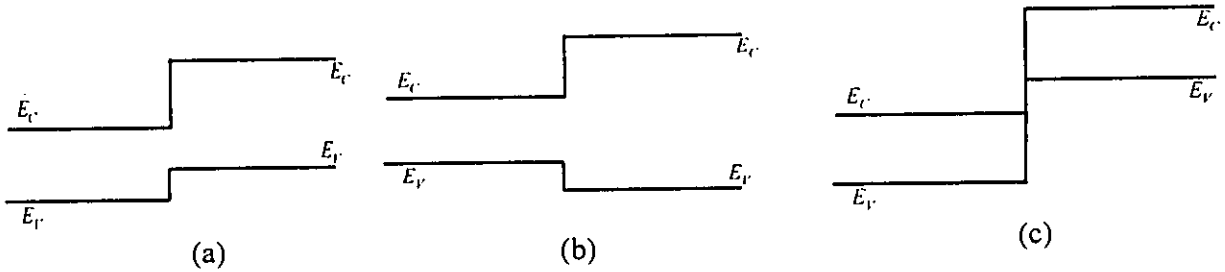


**Figure 2.3** Classification of heterojunctions. (a) Type-I or straddling heterojunction. (b) Type II or staggered heterojunction. (c) Type III or broken-gap heterojunction.

Due to having different energy gaps, the electron affinities of these semiconductors are also different and need to be considered in device applications. This leads to different combinations of  $E_C$  and  $E_V$  alignment at the interface. According to their band alignment, heterojunctions can be classified into three groups as shown in Figure. 2.3, (a) Type I or straddling heterojunction, (b) Type II or staggered heterojunction, and (c) Type III or broken-gap heterojunction.

In a Type-I (straddling) heterojunction, one material has both lower  $E_C$  and higher  $E_V$  and naturally it must have a smaller energy gap. In a Type II (staggered) heterojunction, the locations of lower  $E_C$  and higher  $E_V$  are displaced, so electrons being collected at lower  $E_C$  and holes being collected at higher  $E_V$  are confined in different spaces. A Type III (broken-gap) heterojunction is a special case of Type II, but the  $E_C$  of one side is lower than the  $E_V$  of the other. The conduction band thus overlaps the valence band at the interface, hence the name broken gap.

When the two semiconductors have the same type of conductivity, the junction is called an isotype heterojunction. When the conductivity types differ, the junction is called an anisotype heterojunction which is a much more useful and common structure than its counterpart.

Figures 2.4. (a) and (c) show the energy-band diagrams of two isolated semiconductors of opposite types. The two semiconductors are assumed to have different bandgaps  $E_{g1}$  and  $E_{g2}$ . The difference in energy of the conduction-band edges in the two semiconductors is represented by  $\Delta E_C$ , and that in the valence-band edges by  $\Delta E_V$ .



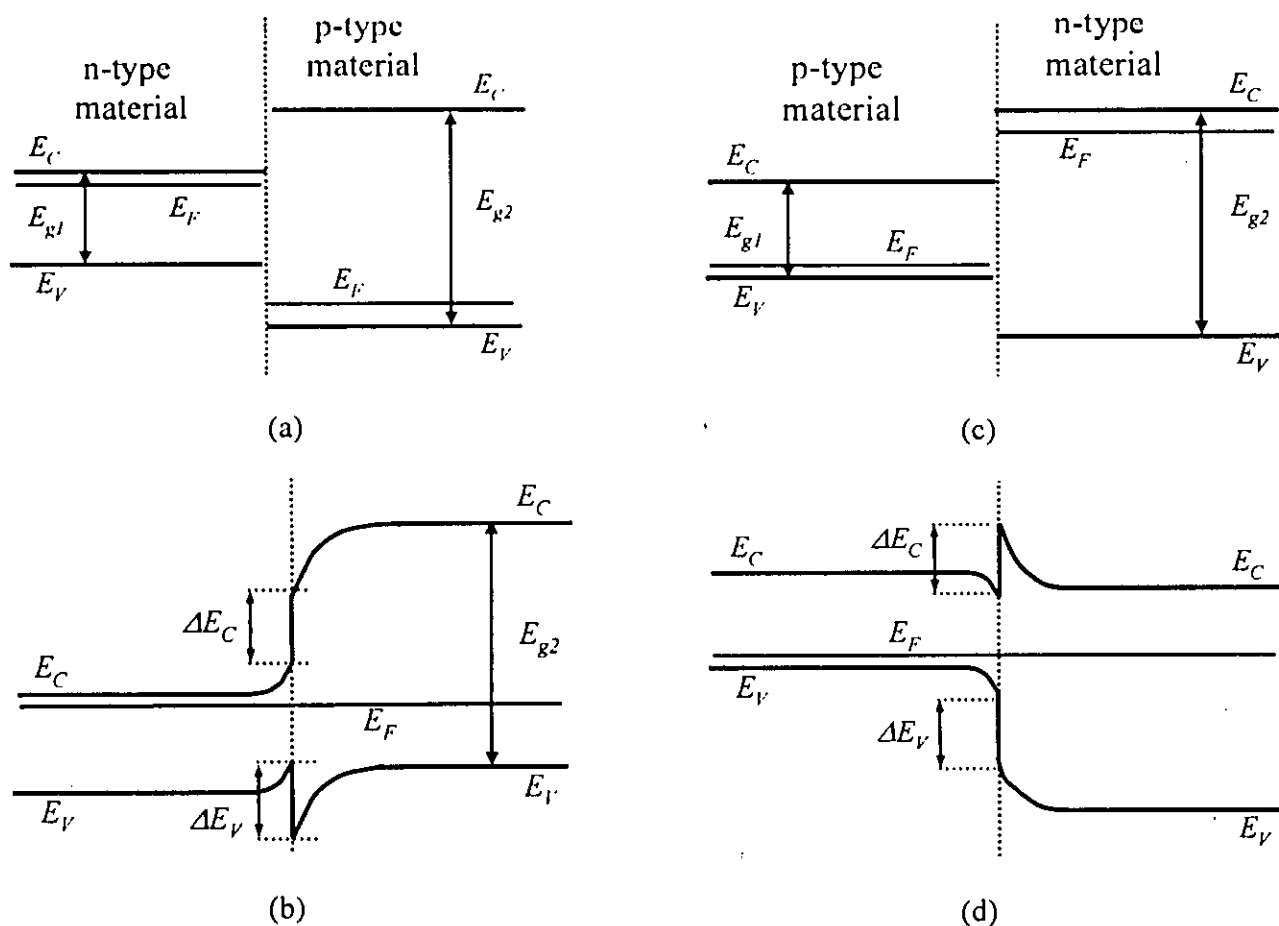


**Figure 2.4** Energy-band diagrams for (a) two isolated semiconductors of opposite types and different  $E_g$  (of which the smaller bandgap is n-type) and (b) their idealized anisotype heterojunction at thermal equilibrium. In (c) and (d), the smaller bandgap is p-type.

When a junction is formed between these semiconductors, the energy-band profile at equilibrium is as shown in Figures 2.4 (b) and (d) for an n-p and p-n anisotype heterojunctions respectively. Since the Fermi level must coincide on both sides in equilibrium, the discontinuity in the conduction-band edges ( $\Delta E_C$ ) and valence-band edges ( $\Delta E_V$ ) is invariant with doping in those cases where  $E_g$  is not function of doping (i.e., nondegenerate semiconductors).

The case of an isotype heterojunction is somewhat different. In an n-n heterojunction, the energy bands will be bent oppositely as shown in figure 2.5 (a) to those for the n-p case as shown in figure 2.4 (b).

One of the important objectives is to make a laser operate at a lower injection current. In order to achieve high carrier densities at low currents it is necessary to confine the recombining carriers to as small volume as possible. This can be done by using a double-heterostructure (DH). In DH the carriers recombine in an active layer embedded between the barrier layers having larger bandgap energies than the active layer. A schematic energy band diagram of a double heterostructure laser diode under forward bias has been shown in Figure. 2.6.

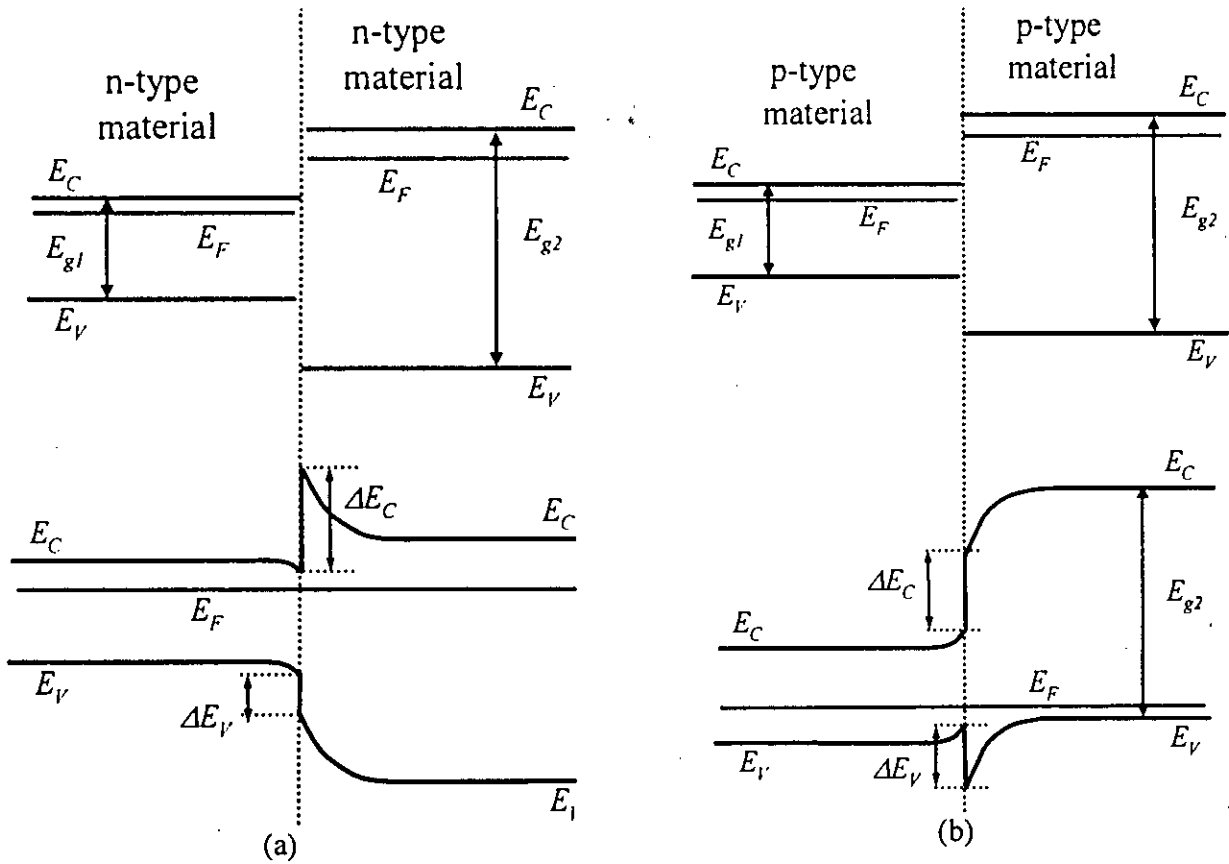
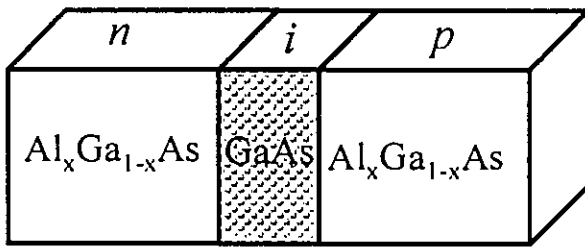
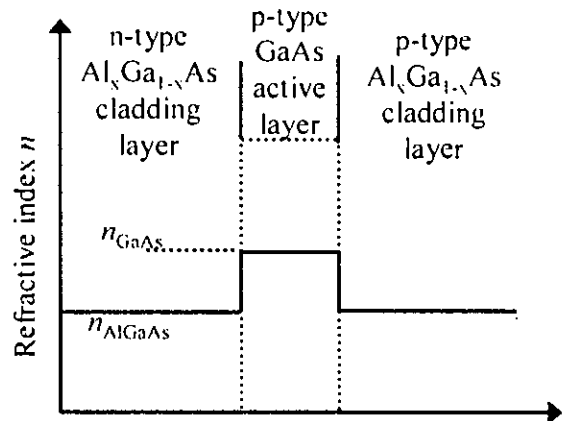


**Figure 2.5** Energy-band diagrams for ideal (a) *n-n* and (b) *p-p* isotype heterojunctions.

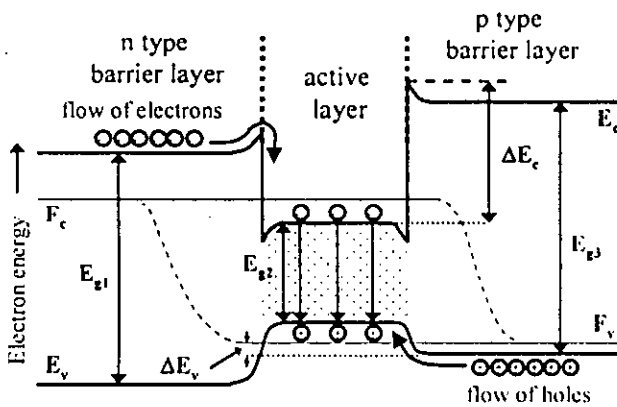
The Fermi levels of the conduction and valence bands are denoted as  $F_c$  and  $F_v$ , respectively, and the energy gaps of the *n*-type barrier layer, active layer, and *p*-type barrier layer are  $E_{g1}$ ,  $E_{g2}$ , and  $E_{g3}$ , respectively. When the diode is under forward bias, the current flows yields an injection of electrons from the *n*-doped confinement layer and holes from the *p*-type barrier layer into the active region. At the interface between the active layer and the *p*-type barrier, the energy step  $\Delta E_c$  prevents electrons from leaving the potential well and the energy step  $\Delta E_v$  prevents holes from passing into the *n*-doped confinement layer. Finally, the injected carriers recombine predominantly in the active layer, since there the electrons in the conduction band with energy  $E_c$  and an almost identical number of holes in the valence band with energy  $E_v$ .



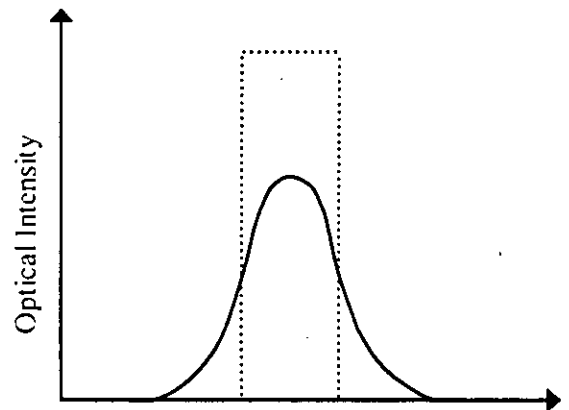
(a)



(c)



(b)



(d)

**Figure 2.6** Representation of a double heterojunction laser diode. (a) shows the schematic diagram of a DH formed by sandwiching a GaAs layer between two  $\text{Al}_x\text{Ga}_{1-x}\text{As}$  layers. (b) shows the Energy band diagram of the double heterojunction laser under forward bias. (c) shows the refractive index profile of the double heterojunction laser and (d) shows the optical intensity profile inside the double heterojunction laser.

## 2.4 Spontaneous Emission, Stimulated Emission and Absorption

The interaction of light with matter takes place in discrete packet of energy or quanta called photon. Quantum theory suggests that atoms exist only in certain discrete energy states such that absorption and emission of light cause them to make a transition from one discrete energy state to another. If  $E_1$  and  $E_2$  are the energy of lower and higher states respectively.  $E$  is the energy differences between the states. Then the transition of atoms between these two states is related by the following relation.

$$E = E_2 - E_1 = hf \quad (2.1)$$

Here,  $h$  is the planks constant ( $6.626 \times 10^{-34}$  J) and  $f$  is the frequency of absorption or emission.

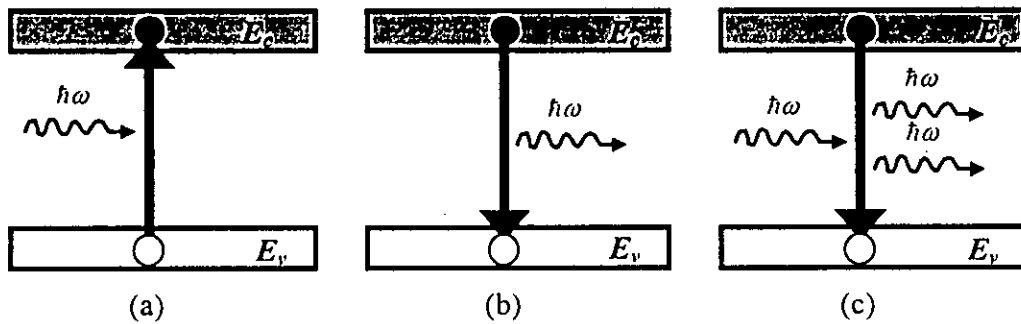


**Figure 2.7** Transition between conduction band and valence band. (a) absorption, (b) spontaneous emission and (c) stimulated emission.

Absorption and radiations have been shown schematically in Figure 2.7. In Figure. 2.7 (a) a process is shown in which the electron transits from a lower energy state to a higher one by absorbing energy from the incident light. Absorption occurs when the energy of the incident light ( $\hbar\omega$ ) is equal to the band gap energy ( $E_g = E_c - E_v$ ) of the material. Since this transition is induced by the incident light, it is sometimes called induced absorption.

There are two types of radiation or emission e.g. (i) spontaneous emission and (ii) stimulated emission. As shown in Figure. 2.7 (b), spontaneous emission is a radiative process in which an excited electron decays (from the higher state to lower state) in a certain lifetime and a photon is emitted having energy according to equation (2.1). The spontaneous emission takes place irrespective of incident lights. In contrast, in the stimulated emission illustrated in Figure. 2.7 (c), an incident light induces a radiative transition of an excited electron. The emitted light due to the stimulated emission has the same wavelength, phase, and direction as the incident light. Therefore, the light generated by the stimulated emission is highly monochromatic, coherent, and directional. In the stimulated emission, one incident photon generates two photons, one is the incident photon itself, and the other is an emitted photon due to the stimulated emission. As a result, the incident light is amplified by the stimulated emission

When a light is incident on a material, the stimulated emission and the absorption simultaneously take place. In thermal equilibrium, there are more electrons in a lower energy state than in a higher one, because the lower energy state is more stable than the higher one. Therefore, in thermal equilibrium, only the absorption is observed when a light is incident on a material. In order to obtain a net optical gain, it is necessary to make the number of electrons in a higher energy state larger than in the lower one. This condition is referred to as inverted population, or population inversion, because the electron population is inverted compared with that in thermal equilibrium. In semiconductors, the population inversion is obtained only in the vicinity of the band edges by excitation of the electrons through optical pumping or electric current injection. The population inversion generates many electrons at the bottom of the conduction band and many holes at the top of the valence bands.

The laser oscillators use fractions of the spontaneous emission as the optical input and amplify the fractions by the stimulated emission under population inversion. Once the optical gains exceed the optical losses in the laser oscillators, laser oscillations take place.

## 2.5 Relationship between Spontaneous and Stimulated Emission

Figure 2.8 represents an idealized unit volume of material with  $N_1$  states at energy  $E_1$  of which  $n_1$  occupied by electrons, and  $N_2$  states at energy  $E_2$  of which  $n_2$  are occupied. Since it is a unit volume, the number of electrons at the upper level is also the electron density  $n_1$  and similarly the hole density  $P = N_2 - n_2$ . Also within the volume there are  $S$  photons, which can absorb or stimulate further photons.

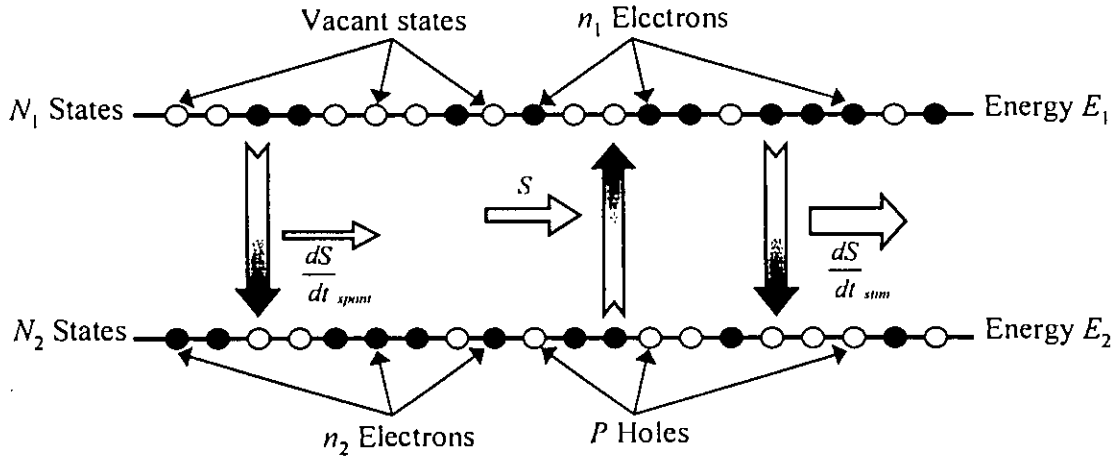


**Figure 2.8** Photon electron interactions in an idealized two energy level system.

The first process to consider is spontaneous emission where electrons at a higher energy spontaneously fall to a lower energy giving out photons at the energy difference. The spontaneous power-output per unit volume is proportional to the number of high-energy electrons  $n_1$  and the number of vacant states (holes, density  $P$ ) available for spontaneous recombination [26], hence

$$\left. \frac{dS}{dt} \right|_{spont} = K_{sp} n_1 P \cong \frac{N_{ref}}{\tau_{sp}} \quad (2.2)$$

Here,  $K_{sp}$  is a constant of proportionality and the recombination time  $\tau_{sp}$  is a parameter often measured experimentally. In a typical laser with  $N_{ref} \cong n_1 \cong P \cong 10^{18} \text{ cm}^{-3}$  then  $\tau_{sp} = 10^{-9} \text{ s}$ .

The second process is stimulated emission where again electrons at a higher energy fall into the vacant states at a lower energy but in this case are stimulated to make the transition by the photons already present. The rate of stimulated power within the unit volume is therefore again proportional to the same numbers of holes and electrons as above, but also now proportional to the photon number  $S$ , and with a different constant of proportionality  $K_{stim}$  and hence one obtains

$$\left. \frac{dS}{dt} \right|_{stim} = K_{stim} S n_1 P \quad (2.3)$$

However, this stimulated photon rate is offset by absorption, which is proportional to the number of holes at the upper energy ( $N_1 - n_1$ ) and the number of electrons at the lower energy  $n_2 = (N_2 - P)$  and also proportional to the photon density  $S$ , so that

$$\left. \frac{dS}{dt} \right|_{\text{absorption}} = -K_{stim} S (N_1 - n_1) (N_2 - P) \quad (2.4)$$

The net rate of emission is the sum of these three processes above:

$$\begin{aligned} \left. \frac{dS}{dt} \right|_{\text{net}} &= \left. \frac{dS}{dt} \right|_{\text{spont}} + \left. \frac{dS}{dt} \right|_{\text{stim}} + \left. \frac{dS}{dt} \right|_{\text{absorption}} \\ &= K_{sp} n_1 P + K_{stim} S n_1 P - K_{stim} S (N_1 - n_1) (N_2 - P) \end{aligned} \quad (2.5)$$

$$\begin{aligned} &= K_{stim} S \{ n_1 P - (N_1 N_2 - n_1 N_2 - N_1 P + n_1 P) \} + K_{sp} n_1 P \\ &= K_{stim} S (n_1 N_2 + P N_1 - N_1 N_2) + K_{sp} n_1 P \end{aligned} \quad (2.6)$$

To obtain the net rate of generation of photons being coupled into a lasing mode, all of the stimulated photons  $S$  at the lasing frequency above contribute, but spontaneous photons are emitted almost isotropically and also over a much wider band of frequencies than the lasing linewidth. Consequently only a very small proportion of spontaneously emitted photon  $\beta_{sp}$  (typically  $10^{-6}$  to  $10^{-2}$ ) couple to the lasing mode and equation (2.6) must be modified as

$$\frac{dS}{dt} = K_{stim} S (n_1 N_2 + P N_1 - N_1 N_2) + \beta_{sp} K_{sp} n_1 P \quad (2.7)$$

Under lasing conditions when injected charge  $n_1$  dominates over doping,  $n_1 \cong P$  and  $P$  may be replaced by  $n_1$ .

$$\begin{aligned} \frac{dS}{dt} &= K_{stim} S (n_1 N_2 + n_1 N_1 - N_1 N_2) + \beta_{sp} K_{sp} n_1^2 \\ &= K_{stim} S (N_1 + N_2) \left( n_1 - \frac{N_1 N_2}{N_1 + N_2} \right) + \beta_{sp} K_{sp} n_1^2 \\ &= G'_m (n_1 + N_{tr}) S + \beta_{sp} K_{sp} n_1^2 \end{aligned} \quad (2.8)$$

where,  $G'_m = K_{stim} (N_1 + N_2)$  is the differential power gain per unit time, and  $N_{tr} = N_1 N_2 / (N_1 + N_2)$  is the transparency value of electron density at which the stimulated optical gain is cancelled by the stimulated optical absorption, i.e. the material is transparent for the light at that frequency.

To produce laser oscillation gain must exceed the losses. In order to obtain a value of gain higher than the absorption the necessary condition can be deduce from equation (2.3) and (2.4). This condition is a shown bellow.

$$n_1 P - (N_1 - n_1) (N_2 - P) > 0 \quad (2.9)$$

$$n_1 P \left\{ 1 - \frac{(N_1 - n_1)(N_2 - P)}{n_1 P} \right\} > 0$$

$$n_1 P \left\{ 1 - \left( 1 - \frac{N_1}{n_1} \right) \left( 1 - \frac{N_2}{P} \right) \right\} > 0$$

$$\left( 1 - \frac{N_1}{n_1} \right) \left( 1 - \frac{N_2}{P} \right) < 1 \quad (2.10)$$

But electron density  $n_1$  and photon density  $P$  are related to the number of states  $N_1$  and  $N_2$  via the Fermi relationships shown below

$$F_n(E_1) = \frac{1}{1 + \exp\left(\frac{E_1 - E_{fn}}{kT}\right)} = \frac{n_1}{N_1} \quad (2.11)$$

$$F_p(E_2) = \frac{1}{1 + \exp\left(\frac{E_{fp} - E_2}{kT}\right)} = \frac{P}{N_2} \quad (2.12)$$

where,  $E_{fn}$  is the quasi-Fermi level for determining the density of electrons and  $E_{fp}$  is the quasi-Fermi level for determining the occupation probability of holes. Putting the values of  $N_1/n_1$  and  $N_2/P$  from equation (2.11) and (2.12) in to equation (2.10), the following equation can be found.

$$\left\{ 1 - \left( 1 + \exp\left(\frac{E_1 - E_{fn}}{kT}\right) \right) \right\} \left\{ 1 - \left( 1 + \exp\left(\frac{E_{fp} - E_2}{kT}\right) \right) \right\} < 1$$

$$\exp\left(\frac{E_1 - E_{fn} + E_{fp} - E_2}{kT}\right) < 1$$

$$E_1 - E_{fn} + E_{fp} - E_2 < 0$$

$$E_1 - E_2 < E_{fn} - E_{fp}$$

$$E_{fn} - E_{fp} = qV, > E_1 - E_2 \quad (2.13)$$

Equation (2.13) confirms that the voltage  $V$ , applied to the laser junction which is equal to the separation of quasi-Fermi levels, must be greater than the equivalent bandgap voltage of the material to obtain lasing action. A further implication is that, if the contact resistances in the laser structure could be made very low, the carrier density in the active region would be determined solely by the applied voltage and the optical gain could then be regarded as a direct function of applied voltage, rather than the electron density.

Now in thermal equilibrium, net photon-emission rate  $dS/dt$  is zero with no voltage applied across the junction (i.e.  $E_{fn} = E_{fp}$ ). Also, select the situation where spontaneous and stimulated emission cover the same frequency ranges and angles so that the coupling factor  $\beta_{sp} = 1$ . These conditions force the system to be in equilibrium at a temperature  $T$  with black-body thermal radiation described by Planck's formula for the photon density over a range of frequencies, say  $\Delta_{sp}f$ , around an optical frequency  $f$ :

$$S = \frac{8\pi f^2 n^2 n_g \Delta_{sp} f}{c^3 \exp\left(\frac{hf}{kT} - 1\right)} \quad (2.14)$$

Here,  $n$  is the refractive index of the medium and  $n_g$  is the group refractive index, i.e.  $c/n_g = v_g$  is the group velocity or the velocity at which the energy propagates while  $c/n = v_p$  is the phase velocity. In case of thermal equilibrium,  $dS/dt=0$ , and equation (2.6) becomes

$$\begin{aligned} \left. \frac{dS}{dt} \right|_{net} &= \left. \frac{dS}{dt} \right|_{spont} + \left. \frac{dS}{dt} \right|_{stim} + \left. \frac{dS}{dt} \right|_{absorption} = 0 \\ K_{sp} n_1 P + K_{stim} S n_1 P - K_{stim} S (N_1 - n_1) (N_2 - P) &= 0 \\ K_{stim} S n_1 P - K_{stim} S n_1 P \left( \frac{N_1}{n_1} - 1 \right) \left( \frac{N_2}{P} - 1 \right) + K_{sp} n_1 P &= 0 \\ K_{stim} S \left\{ 1 - \left( \frac{N_1}{n_1} - 1 \right) \left( \frac{N_2}{P} - 1 \right) \right\} + K_{sp} &= 0 \\ K_{stim} S \left\{ 1 - \left( \frac{N_1}{n_1} - 1 \right) \left( \frac{N_2}{P} - 1 \right) \right\} + K_{sp} &= 0 \\ K_{stim} S \left\{ 1 - \exp\left(\frac{E_1 - E_{fn}}{kT}\right) \exp\left(\frac{E_{fp} - E_2}{kT}\right) \right\} + K_{sp} &= 0 \\ K_{stim} S \left\{ \exp\left(\frac{E_1 - E_{fn}}{kT}\right) \exp\left(\frac{E_{fp} - E_2}{kT}\right) - 1 \right\} &= K_{sp} \end{aligned} \quad (2.15)$$

Since at thermal equilibrium  $E_{fn} = E_{fp}$  the above equation can be written as

$$S = \frac{K_{sp}}{K_{stim}} \frac{1}{\exp\left(\frac{E_1 - E_{f2}}{kT} - 1\right)} \quad (2.16)$$

In the simple two-level system,  $hf = E_1 - E_2$  so comparing equations (2.14) and (2.16) one can write



$$\frac{K_{sp}}{K_{stim}} = \frac{8\pi f^2 n^2 n_x \Delta_{sp} f}{c^3} \quad (2.17)$$

This is the relationship between spontaneous and stimulated emission coefficients. Now the spontaneous and stimulated emission coefficient can be related to the differential gain with electron density given from  $G'_m = K_{stim} (N_1 + N_2)$ . Consider  $(N_1 + N_2) = N_{ref}$  then using this as a reference density where  $n_1 = P = N_{ref}$  in equation 2.2 so that  $K_{sp} = 1/N_{ref} \tau_{sp}$ , one can write

$$\begin{aligned} G'_m &= K_{stim} N_{ref} = \frac{K_{stim}}{K_{sp}} \\ &= \frac{c^3}{8\pi f^2 n^2 \tau_{sp} n_x \Delta_{sp} f} \end{aligned} \quad (2.18)$$

Using the group velocity  $v_g$  to link the spatial distance  $z$  traveled by the light with the time  $t$  gives  $z = tv_g = ct/n_g$  and the material's optical power gain/absorption per unit distance may be written as:

$$\frac{1}{S} \frac{dS}{dz} = \frac{c^2 (n_1 - N_{tr})}{8\pi f^2 n^2 \tau_{sp} \Delta_{sp} f} \quad (2.19)$$

The power gain per unit time  $G_m(n_1)$  and the field gain per unit distance  $g_m(n_1)$  are related because the photon density is proportional to the square of the optical field amplitude.

$$\frac{1}{S} \frac{dS}{dz} = 2g_m(n_1) = \frac{G_m(n_1)}{v_x} \quad (2.20)$$

## 2.6 Stimulated Gain Spectra of Semiconductors

The band diagram of direct bandgap semiconductor materials is shown in Figure 2.9. The band structure has parabolic  $E/k$  relationship. The energies of the lower end of the conduction band and the upper end of the valence band are denoted by  $E_c$  and  $E_v$  respectively. The band gap energy,  $E_g = E_c - E_v$ . The effective mass of electrons in the conduction band is  $m_c$  and the effective mass of holes in the valence band is  $m_v$ .

Using effective mass approximation [27] the energy of electrons near the conduction and valence band edges can be written as

$$E_c(k) = E_c + \delta E_c(k) = E_c + \frac{\hbar^2}{2m_c} k^2 \quad (2.21)$$

$$E_v(k) = E_v + \delta E_v(k) = E_v + \frac{\hbar^2}{2m_v} k^2 \quad (2.22)$$

Comparing the energy of electrons near the conduction and valance band edges with the energy of higher state and lower state considered in section 2.1, the following relationship can be written

$$\begin{aligned}
 hf &= E_c - E_v = \{E_c + \delta E_c(k)\} - \{E_v - \delta E_v(k)\} \\
 &= E_g + \frac{\hbar^2 k^2}{2m_c} + \frac{\hbar^2 k^2}{2m_v} = E_g + \frac{\hbar^2 k^2}{2} \left( \frac{1}{m_c} + \frac{1}{m_v} \right) \\
 &= E_g + \frac{\hbar^2 k^2}{2m_r}
 \end{aligned} \tag{2.23}$$

where,  $m_r$  gives a combined effective mass ('reduced mass') from the effective masses in the conduction and valance bands. Now for a spread of photon energies  $d(hf)$  there is a spread  $dk$  in the magnitude of the electron momenta and a consequential spread of their energies in the conduction band  $dE$  and in the valance band  $d(\delta E_v)$ .

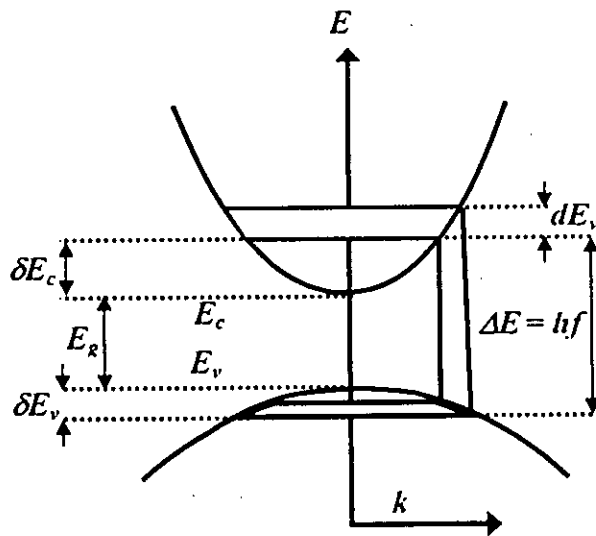


**Figure 2.9** Transition between energy level in the conduction and valance bands of a direct bandgap semiconductor materials.

Equations (2.24), (2.25) and (2.26) can be deduced by differentiating the equations (2.23), (2.21) and (2.22) with respect to  $k$ .

$$\frac{d(hf)}{dk} = \frac{\hbar^2 k}{m_r} \tag{2.24}$$

$$\frac{dE}{dk} = \frac{\hbar^2 k}{m_c} \tag{2.25}$$

$$\frac{d(\delta E_v)}{dk} = \frac{\hbar^2 k}{m_v} \quad (2.26)$$

Using the equations (2.24), (2.25) and (2.25) one can write

$$dE = \frac{m_r}{m_c} d(hf) \text{ and } d(\delta E_v) = \frac{m_r}{m_v} dE \quad (2.27)$$

Now consider a density of photon  $S'$   $d(hf)$  spread over a range of frequencies  $df$  around a frequency  $f$  interacting with a density of available electrons in the energy states equivalent to  $N_1$  at an energy  $E_1$  as discussed in the section 2.5. In this section  $E_1 = E = E_c + \delta E_c$  and takes a spread  $dE$ . Density of available electrons  $n_1$  can be found by finding the density of states  $N_1$  in the energy range  $dE$ .

$$N_1 = 4\pi \left( \frac{2m_c}{h^2} \right)^{3/2} (E - E_c)^{1/2} dE \quad (2.28)$$

Replace  $E_1$  and  $E_{fn}$  of equation (2.11) by  $E$  and  $E_c$  respectively. Now by using the equations (2.11) and (2.28), the effective density of electron  $n_1$  for stimulated emission can be written as

$$n_1 = N_1 F_n(E) = 4\pi \left( \frac{2m_c}{h^2} \right)^{3/2} (E - E_c)^{1/2} F_n(E) dE \quad (2.29)$$

Since the spread of energies  $(m_c/m_v)dE$  in the valance band corresponds to the spread of  $dE$  in the conduction band for the same  $k$  values. Similarly by replacing  $E_2$  and  $E_{fp}$  of equation (2.12) with  $E-hf$  and  $E_v$  respectively, the effective density of vacant states or holes  $P$  for stimulated recombination can be written as

$$P = N_2 F_p(E - hf) = 4\pi \left( \frac{2m_v}{h^2} \right)^{3/2} (E_v - E + hf)^{1/2} F_p(E - hf) \left( \frac{m_c}{m_v} \right) dE \quad (2.30)$$

Now  $hf$  along with the spread  $d(hf)$  will be held constant but the whole range of  $E$  can be permitted, consistent with  $E \geq E_c$  and  $E-hf \leq E_v$ , i.e.,

$$0 \leq E - E_c \leq (hf - E_v) \quad (2.31)$$

Then on summing or integrating over whole energy range of permitted  $E$ , the equivalent stimulated emission rate given in equation (2.3) now becomes

$$\begin{aligned} \left. \frac{dS}{dt} \right|_{sim} d(hf) &= K_{sim} S n_1 P d(hf) \quad (2.32) \\ &= K_{sim} 16\pi^2 \left( \frac{4m_c m_v}{h^4} \right)^{3/2} \left( \frac{m_c}{m_v} \right) S \left\{ \int (E - E_c)^{1/2} (E_v - E + hf)^{1/2} F_n(E) F_p(E - hf) dE \right\} d(hf) \end{aligned}$$

$$= A_{stim} S \left\{ \int (E - E_c)^{1/2} (E_v - E + hf)^{1/2} F_n(E) F_p(E - hf) dE \right\} d(hf) \quad (2.33)$$

where, the  $A_{stim} = K_{stim} 16 \pi^2 (4 m_c m_v / h^4)^{3/2} (m_c / m_v)$  with  $K_{stim}$  as in equation (2.3) and the range of integration is limited by equation (2.31).

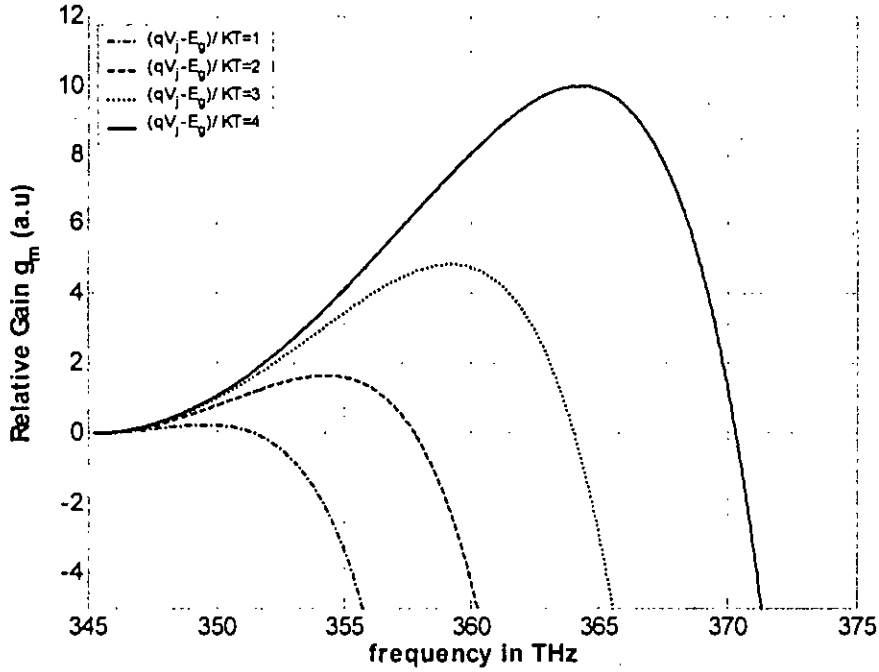


**Figure 2.10** Optical gain against frequency due to different junction voltage  $V_j$ . For different junction voltages the variation of relative gain with respect to frequency is shown in the plot. Peak gain occurred at the frequency of 355 THz for  $(qV_j - E_g)/kT = 2$  (dashed line) whereas the peak gain for  $(qV_j - E_g)/kT = 4$  occurred at the frequency around 364 THz (solid line).

It may be seen that the equivalent expression for stimulated absorption is the same as the stimulated emission except that the occupation probabilities  $F_n$  and  $F_p$  of electrons and holes respectively have to be replaced by  $(1 - F_n(E))$  and  $(1 - F_p(E - hf))$ .

$$(1 - F_n(E)) = F_n \exp\left(\frac{E - E_m}{kT}\right) \quad (2.34)$$

$$(1 - F_p(E - hf)) = F_p \exp\left(\frac{E_m - E + hf}{kT}\right) \quad (2.35)$$

Multiplying equation (2.34) by equation (2.35)

$$(1 - F_n(E))(1 - F_p(E - hf)) = F_n F_p \exp\left(\frac{E - E_m}{kT}\right) \exp\left(\frac{E_m - E + hf}{kT}\right)$$

$$= F_n F_p \exp\left(\frac{hf - qV_j}{kT}\right) \quad (2.36)$$

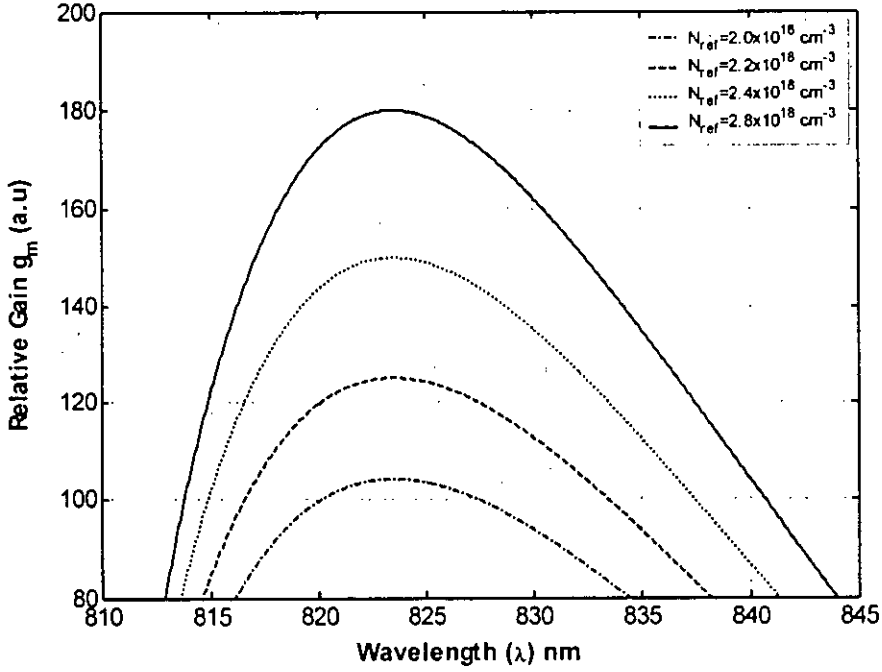


**Figure 2.11** Optical gain against wavelength (inverse of frequency) due to different carrier density  $N_{ref}$ . The spectral width increases with the increase of  $N_{ref}$ .

Hence according to the equation (2.4), the stimulated absorption can be written as

$$\left. \frac{dS}{dt} \right|_{\text{absorption}} d(hf) = A_{stim} S \exp\left(\frac{hf - qV_j}{kT}\right) \left[ \int \sqrt{(E - E_c)} \{ (hf - E_c) - (E - E_c) \} F_p(E - hf) F_n(E) dE \right] \times d(hf) \quad (2.37)$$

The range of integration is given in equation (2.31). Now the gain spectrum is given from the net stimulated (emission - absorption) so that approximating the Fermi-Dirac distribution to unity over the limited range of energies, the following equation can be written

$$\frac{1}{S} \frac{dS}{dz} = 2g_m = \left(\frac{n_k}{c}\right) A_{stim} \left\{ 1 - \exp\left(\frac{hf - qV_j}{kT}\right) \left[ \int (E - E_c)^{1/2} \{ E_c - E + (hf - E_c) \}^{1/2} dE \right] \right\} \quad (2.38)$$

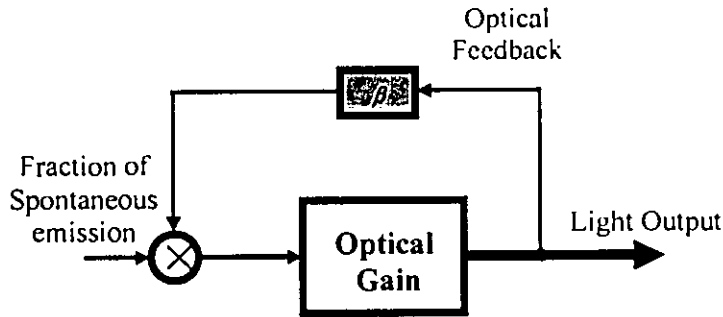
$$g_m(hf, V_j) = \frac{\pi n_k A_{stim}}{8c} (hf - E_c)^2 \left\{ 1 - \exp\left(\frac{hf - qV_j}{kT}\right) \right\} \quad (2.39)$$

Figure (2.10) shows the dependence of gain on the optical frequency and the junction voltage  $V_j$ . Here, GaAs semiconductor has been selected as gain medium. Band gap energy  $E_g$  of GaAs is 1.424 eV. As the junction voltage increases, the peak optical gain occurred at increased frequency. The spectral bandwidth  $\Delta f$  also increased with the increase of junction voltage. Dependence of

material gain for optical field due to the variation of carrier densities is shown in figure 2.11. The gain amplitude increased with the increase of the carrier density.

## 2.7 Condition of Oscillation in a Fabry-Perot laser

Simplified representation of laser operation is shown in the Figure 2.12. The lasers use a fraction of spontaneously emitted lights as the input and amplify that fraction by the stimulated emission. To feed back the light, the optical resonators, or the optical cavities, which consist of reflectors, are used. The resonance conditions of the optical resonators determine lasing conditions such as a threshold and an oscillation wavelength.



**Figure 2.12** Key elements of laser operation.

The schematic diagram of a Fabry-Perot resonator is shown in Figure 2.13. The resonator is simply constructed by two mirrors separated by the distance  $L$ . This distance is called the resonator length. Spontaneous emission takes place in the cavity region and propagates towards the mirrors. While the light wave generated by spontaneous emission, is propagating through the cavity materials it is stimulated by the gain of the materials. The mirrors provide the necessary feedback required to produce oscillation in the cavity. The mirror-1 and mirror-2 have the amplitude reflection and transmission coefficients  $r_1, t_1$  and  $r_2, t_2$  respectively. Consider an incident wave  $E_i$  at  $z < 0$ , with a complex amplitude  $E_0$ .

The equation of the incident wave can be written as:

$$E_i = E_0 \exp(-i\gamma z) \quad (2.40)$$

where,  $\gamma = \beta - i\alpha/2$  is the propagation constant.  $\beta = 2\pi n/\lambda$  is the wave number,  $n$  is the refractive index of the medium,  $\alpha = \alpha_{int} - g_m$  is the intensity absorption coefficient,  $\alpha_{int}$  is the internal loss coefficient of the cavity and  $g_m$  is the material gain per unit length.

Transmitted wave from the mirror-2 as shown in Figure 2.13 can be written as

$$E_t = E_l + E_{3L} + E_{5L} + \dots \quad (2.41)$$

$$\text{or } E_t = t_1 t_2 E_0 \exp(-i\gamma L) \sum_{j=0}^{\infty} [(r_1 r_2)^j \exp(-2j\gamma L)] \quad (2.42)$$

$$\begin{aligned}
&= t_1 t_2 E_0 \exp(-i\gamma L) \sum_{j=0}^{\infty} \left[ \{(r_1 r_2) \exp(-2i\gamma L)\}^j \right] \\
&= t_1 t_2 E_0 \exp(-i\gamma L) \{1 - r_1 r_2 \exp(-2i\gamma L)\}^{-1} \\
&= \frac{t_1 t_2 E_0 \exp(-i\gamma L)}{1 - r_1 r_2 \exp(-2i\gamma L)} \tag{2.43}
\end{aligned}$$

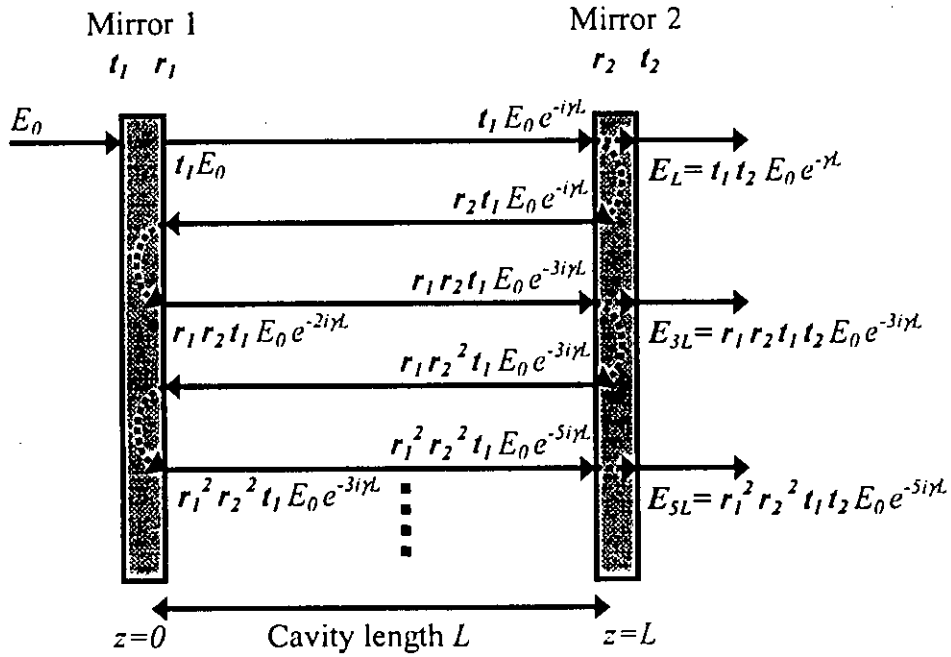


**Figure 2.13** Schematic arrangement of a Fabry-Perot resonator.

According to the equation (2.43), it is possible to get infinite output from the resonator by applying a small amount of input (produced due to spontaneous emission) if the denominator of the equation (2.43) become zero. This phenomenon actually occurred in the laser. So one of the conditions for the oscillation of a laser is

$$1 - r_1 r_2 \exp(-2i\gamma L) = 0$$

or  $r_1 r_2 \exp(-2i\gamma L) = 1$

or  $r_1 r_2 \exp\left[-2i\left\{\beta - \frac{i}{2}(\alpha_{im} - g_m)\right\}L\right] = 1$

or  $r_1 r_2 \exp[(g_m - \alpha_{im})L] \exp[-2i\beta L] = 1$

or  $r_1 r_2 \exp[(g_m - \alpha_{im})L] = 1 \tag{2.44}$

When the material gain become equal to the internal loss of the cavity then that gain is termed as threshold gain. From equation (2.44) the threshold condition can be written as:

$$g_{th} = \alpha_{im} + \frac{1}{L} \ln\left(\frac{1}{r_1 r_2}\right) \quad (2.45)$$

The equation (2.45) is known as the gain condition of oscillation of a laser. For stable resonance, the phase of the wave after single round trip must be in phase with the when it started. The phase condition can be written as

$$\text{or } \exp[-2i\beta L] = 1$$

$$\text{or } 2\beta L = 2m\pi$$

$$\text{or } \frac{4\pi m}{\lambda_m} L = 2m\pi \quad (2.46)$$

Here,  $m$  is an integer representing the number of modes. The equation (2.46) is known as the phase condition of oscillation of a laser. Wavelength separation between two adjacent modes  $\Delta\lambda$  can be written as

$$\Delta\lambda = \lambda_{m+1} - \lambda_m$$

$$\Delta\lambda = \frac{\lambda^2}{2Ln\left(1 - \left(\frac{\lambda}{n}\right)\left(\frac{dn}{d\lambda}\right)\right)} \quad (2.47)$$

Now, some properties of the Fabry-Perot resonators need to be discussed to design a proper resonator. To compute the transmittivity and the number of oscillating modes of a Fabry-Perot resonator one has to determine the input and output light intensity of the resonator. The input and output light intensity  $I_0$  and  $I_t$  of the resonator are directly proportional to the square of the electrical field  $E_0$  and  $E_t$  as shown in the figure 2.13.

$$I_0 \propto E_0^* E_0 \text{ and } I_t \propto E_t^* E_t$$

Transmittivity can be defined as the ratio of output light to the input light. If the mirror 2 is considered as the output mirror then the transmittivity of the resonator can be written as

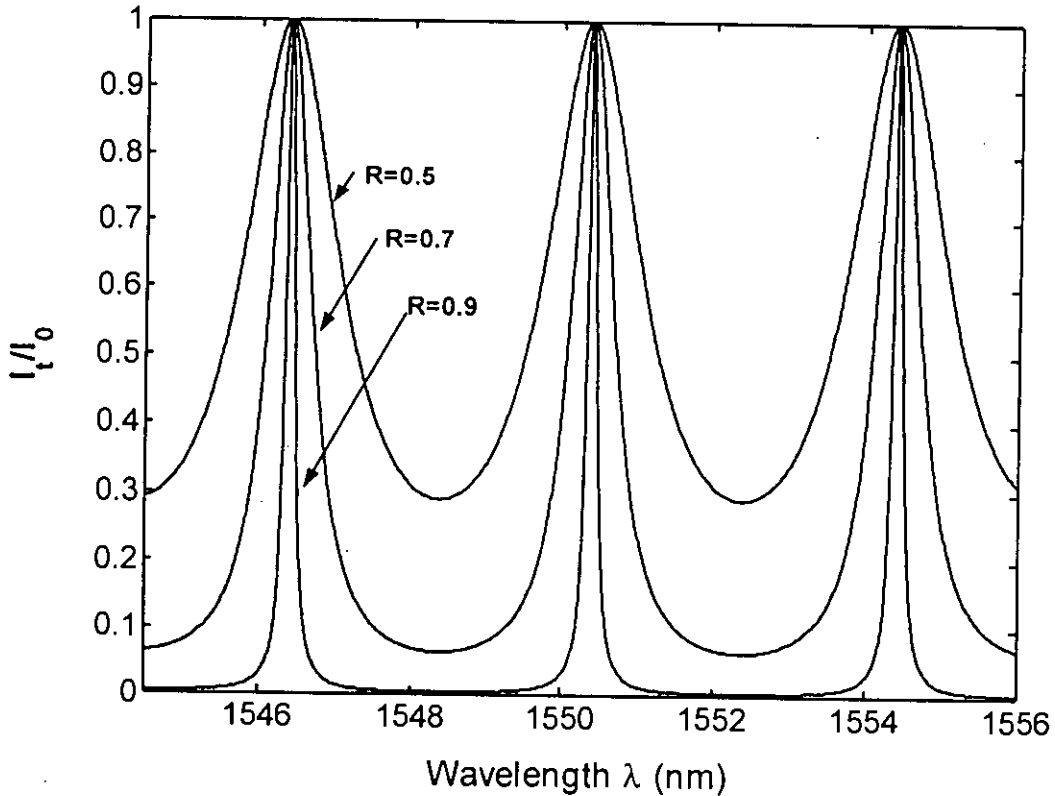
$$\begin{aligned} \frac{I_t}{I_0} &= \frac{\left\{t_1 t_2 E_0 \exp\left(\frac{\alpha}{2} L\right) \exp(-i\beta L)\right\} \left\{t_1 t_2 E_0 \exp\left(\frac{\alpha}{2} L\right) \exp(i\beta L)\right\}}{\left\{1 - r_1 r_2 \exp(\alpha L) \exp(-i2\beta L)\right\} \left\{1 - r_1 r_2 \exp(\alpha L) \exp(i2\beta L)\right\}} \\ &= \frac{(t_1 t_2)^2 G_s}{1 + (r_1 r_2)^2 G_s^2 - 2r_1 r_2 G_s \cos(\delta)} \end{aligned} \quad (2.48)$$

where  $G_s = \exp(\alpha L)$  and  $\delta = 2\beta L$



Power reflection coefficient of the mirrors are  $R_1 = r_1^2$  and  $R_2 = r_2^2$  and power transmission coefficient of the mirrors are  $T_1 = t_1^2$  and  $T_2 = t_2^2$ . Now the equation (2.48) can be written as

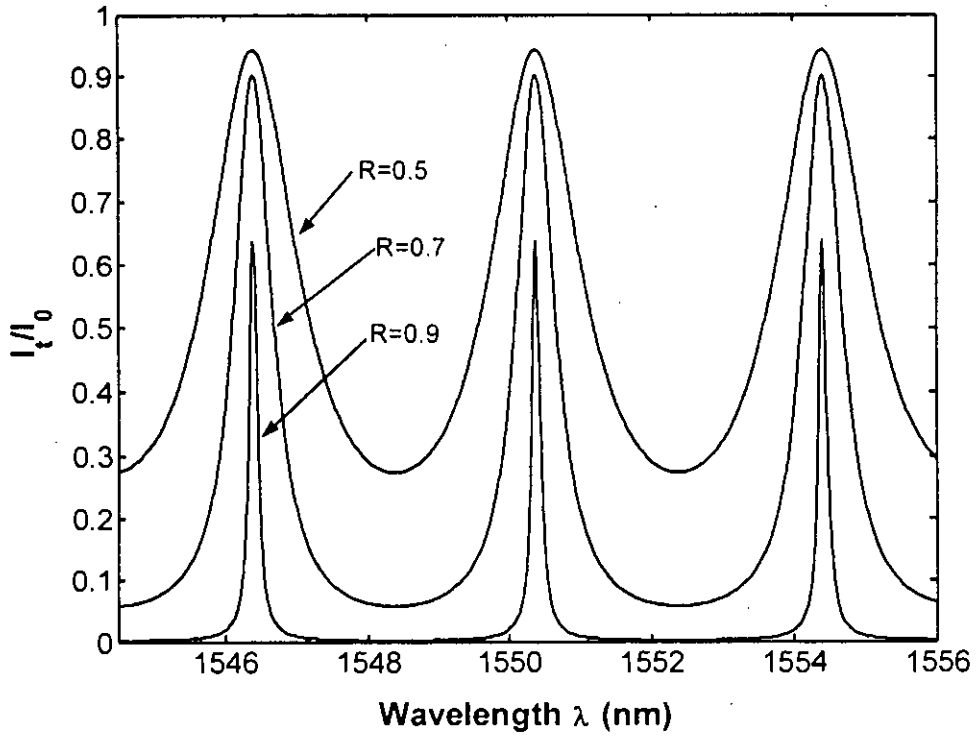
$$\frac{I_t}{I_0} = \frac{T_1 T_2 G_s}{1 + R_1 R_2 G_s^2 - 2\sqrt{R_1 R_2} G_s \cos(\delta)} \quad (2.49)$$



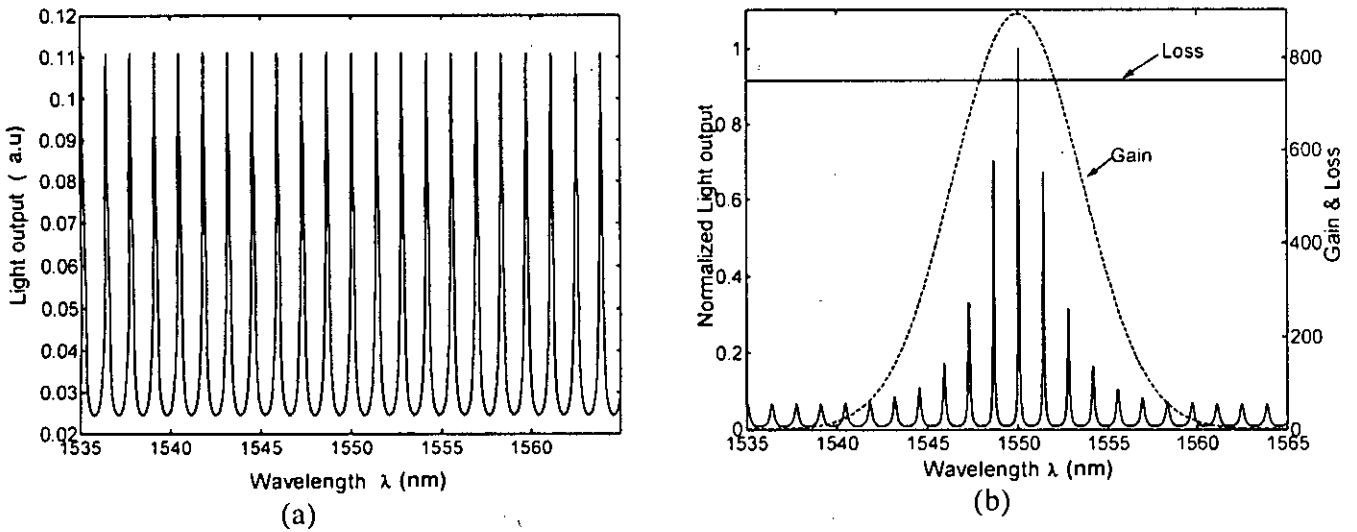
**Figure 2.14** Transmittivity spectra of 100  $\mu\text{m}$  FP laser without mirror loss.

Figure 2.14 and 2.15 shows the plot of transmittivity of a Fabry-Perot resonator with net gain  $G_s=1$ , i.e.  $\alpha=0$ . Without mirror loss, ( $T=1-R$ ) all the oscillating modes have the maximum value for the different values of mirror reflectivities as shown in figure 2.14. With 20% of mirror loss, ( $T=0.8-R$ ) all the oscillating modes do not have equal maximum value for the different values of mirror reflectivities as shown in figure 2.15. The magnitude of the oscillating mode decrease with the increase of mirror reflectivity.

The output mode spectrum of a Fabry-Perot laser is shown in figure 2.16 (b). Some of the oscillating modes in the resonator without gain or losses are shown in figure 2.16 (a). The material gain has been selected as a line-shape function,  $G_s = g_{th} \exp((\lambda - \lambda_c)/15e-9)$  and  $\alpha_{int} = 750 \text{ m}^{-1}$ . Figure 2.16 (b) shows the modes for which gain exceed the loss become amplified and other modes are decayed.



**Figure 2.15** Transmittivity spectra of 100µm FP laser with 20% mirror loss.



**Figure 2.16** Power spectrum of a 250µm Fabry-Perot laser operating at 1550nm central wave length  $\lambda_c$ . The mode separation is  $\Delta\lambda=1.32$  nm. (a) Shows the oscillating modes without gain or losses. (b) Shows the oscillating modes due to gain and losses.

## 2.8 Materials Used for Fabricating a Semiconductor Laser

Semiconductor lasers are based upon one of four different types of materials, depending upon the wavelength region of interest. Three of them are from the group III-V semiconductors, consisting of materials in columns III and V of the periodic table. Column-III atoms are lacking one electron

when in a crystalline matrix, and column-V atoms have one extra electron. Hence they form a charge balance when combined into a binary compound. Column-III atoms include Al, Ga, In, and Tl, and column V atoms are N, P, As, and Sb. The semiconductor lasers in this category are based on GaAs for a wide range of lasers in the near infrared and extending into the visible using GaAs/AlGaAs layered materials, since its bandgap occurs at 1.43 eV. Indium phosphide (InP), with a bandgap of 1.35 eV, is used to produce lasers in the 1.5-um wavelength region with InP/InGaAsP layered materials. Gallium nitride (GaN) has a bandgap of 3.49 eV and thus allows the development of blue and ultraviolet lasers.

The other materials are the II-VI compounds, with the column-II atoms lacking two electrons and the column-VI atoms having two extra electrons available for a binary compound. The column-II materials are Zn and Cd, which are combined with S, Se, and Te from column VI to form binary compounds. ZnSe has a bandgap of 2.71 eV and forms the basis for blue-green semiconductor lasers. A listing of a number of possible semiconductor laser compounds (along with their band gap energies) is given in Table 2.2.

**Table: 2.1**

Bandgap energies of Several Semiconductor Laser Compounds

Materials	Abbreviation	Bandgap Energy (in eV at 300 <sup>0</sup> K)
<i>Group III-V compounds</i>		
Aluminum arsenide	AlAs	2.16
Aluminum phosphide	AlP	2.45
Aluminum antimonide	AlSb	1.58
Boron nitride	BN	7.5
Boron phosphide	BP	2.0
Gallium arsenide	GaAs	1.42
Gallium nitride	GaN	3.36
Gallium phosphide	GaP	2.26
Gallium antimonide	GaSb	0.72
Indium arsenide	InAs	0.36
Indium phosphide	InP	1.35
Indium antimonide	InSb	0.17
<i>II-VI Compounds</i>		
Cadmium sulfide	CdS	2.42
Cadmium selenide	CdSe	1.70
Cadmium telluride	CdTe	1.56
Zinc sulfide	ZnS	3.68
Zinc selenide	ZnSe	2.71
Zinc telluride	ZnTe	2.393

## 2.9 Types of Semiconductor Lasers

Depending on the direction of light output semiconductor laser devices are two types: i) edge emitting lasers and ii) surface emitting lasers. Edge emitting lasers have the laser beam parallel to the surface of the junction region. Typically the mirrors for edge emitting lasers are produced by using

the cleaved surfaces at the ends of the laser crystal or by distributed feedback (DFB) within the crystal or Distributed Bragg Reflecting (DBR) structures at the ends of the crystal. The surface emitting lasers have the laser beam emitting in a direction perpendicular to the junction region with multilayer Bragg reflecting mirrors incorporated into the crystal.

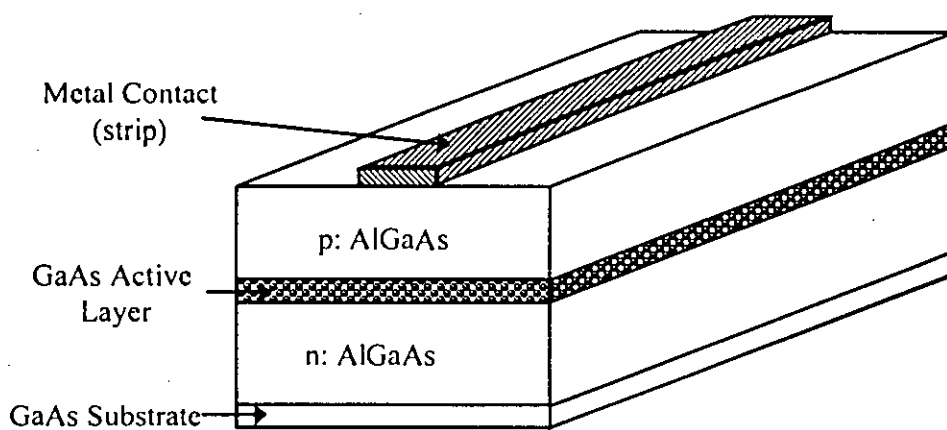
## 2.10 Edge Emitting Lasers

The length in the axial or laser direction of the semiconductor laser is typically about 0.2-1 mm, and the material providing the gain is uniform over that length. In one of the two transverse directions of a double heterostructure laser, the additional semiconductor materials are grown in layers of various thicknesses ranging from 5 to 1,000 nm to form the heterojunction. The additional layers are used to confine the electron-hole recombination region (so as to minimize the generation of excess heat) and also to confine the optical beam. In the other lateral direction, material boundaries are fabricated with lithographic techniques to widths of the order of a few hundred microns to provide confinement and guiding of the electrical current and/or the optical beam, as shown in Figure 2.17.

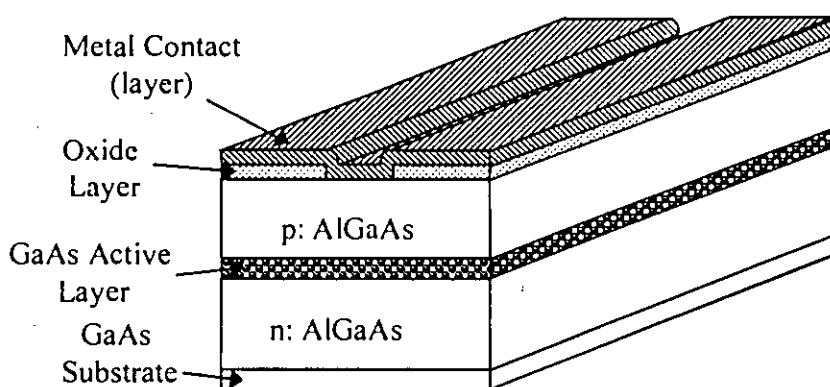
The heterojunction is typically grown upon a substrate material such as GaAs or InP, with a metalization layer under the substrate to provide for electrical contact. Above the heterojunction is another metalization layer for electrical contact. The current density flowing perpendicular to the plane of the junction is of the order of  $800 \text{ A/cm}^2$ , whereas the maximum current that can be used before extensive thermal damage occurs is of the order of 50 mA. Thus the current must be confined in the lateral direction in the plane of the junction by devising a narrow electrical contact that minimizes the region where current flows. This electrical contact takes the form of either a narrow strip of metal above the heterojunction or a broad uniform layer under which an insulator is applied, leaving a narrow stripe region without insulation through which current can flow shown in Figure 2.17.

The laser cavity can be produced in one of two ways. The first is the typical Fabry-Perot cavity, but in this case the mirrors are produced at the ends of the laser gain medium by cleaving the ends of the semiconductor crystal perpendicular to the optical axis of the crystal (a natural cleavage plane). Because of the high index of refraction of the material (typically  $n \sim 3.5$ ), the reflectivity at those cleaved interfaces is of the order of 30%. The reflectivities can be altered by adding dielectric coatings to the surfaces. In commercial semiconductor lasers, the laser cavity length  $L$  typically ranges from 0.2 to 1.0 mm. This cleaved type of cavity produces a relatively broad spectrum laser output that can consist of many longitudinal modes, although typically a single mode at the wavelength of the highest gain will dominate because of homogeneous broadening. The second type of cavity is one that produces a very narrow-spectrum, single-frequency output.

There are several general types of structures for edge emitting lasers. These include both gain and index guided structures, using either the traditional heterojunctions or quantum-well active regions, and semiconductor arrays.



(a) Metal strip electrode



(b) oxide insulating layer

**Figure 2.17** Lateral confinement of the injection current in a semiconductor laser: (a) shows the structure where current is injected through a metal stripe electrode just above the active layer (b) shows the laser structure where oxide layers under the metal contact layer have been used to confine the injected current into the active layer.

## 2.11 Surface Emitting Lasers

Semiconducting lasers emitting in a direction normal to the axis of the laser gain medium are referred to as surface emitting lasers (SELs). They can be fabricated in large two-dimensional arrays, which prove useful from two standpoints.

First, if such lasers can be individually turned on and off and so act as individual amplifiers, they can be used in applications associated with optical memory, optical computing, and optical data storage.

Second, when a large number of diode lasers within an array are lasing simultaneously, the extremely high-power output makes such lasers suitable for optically pumping other solid-state lasers, such as the Nd: YAG laser.

Surface emitting lasers are fabricated in two different types of structures. One is a semiconductor laser with a distributed grating coupler, where the grating redirects a portion of the laser beam out of the cavity in a direction normal to the gain axis of the laser. This is known as a grating coupler surface emitting laser, or GSEL. The other structure is a vertical cavity surface emitting laser, or VCSEL. It is fabricated with the laser gain axis mounted perpendicular to the semiconductor substrate, with the mirrors attached at the ends of the gain medium as part of the fabrication process.

### Grating Surface Emitting Diode Laser (GSEL)

An example of the structure of a GSEL is shown in Figure 2.18. If a second-order grating is fabricated within the laser then the first-order diffraction occurs in a direction perpendicular to the grating surface, thereby providing the laser output as indicated in the figure. Such gratings are presently fabricated by creating holographic interference patterns on the laser surface using Ar ion and He-Cd lasers. Electron-beam writing can also be used to generate such patterns.

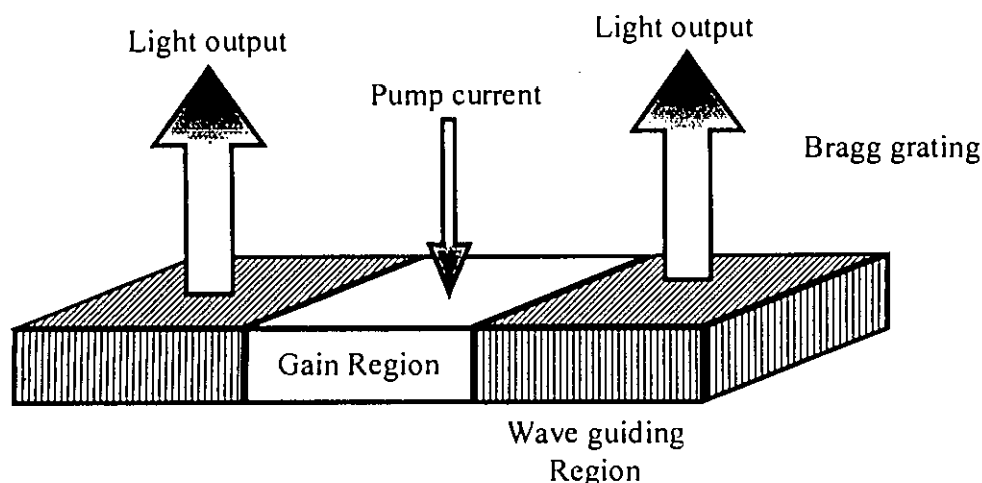


**Figure 2.18** Grating Surface Emitting Diode Laser (GSEL). Two Bragg gratings are used at the two sides of the active region. Pump current is injected directly into the active layer and light comes out at the direction perpendicular to the Bragg gratings.

### Vertical Cavity Surface Emitting Laser (VCSEL)

The VCSEL is shown in Figure 2.19. In this laser, the gain length is limited to very short dimensions. High-reflectivity (Bragg Reflector) mirrors are therefore necessary to allow the gain to exceed the losses within the cavity. Thin metal films as well as alternating high- and low-index dielectric layers have been used to create such mirrors. One technique for making such lasers is to deposit the various layers of material uniformly over the surface of the entire structure and then etch away the material from around the individual lasers to produce structures similar to that shown in Figure 2.19. Figure 2.20 shows a diagram of a VCSEL that has a three-quantum-well stack sandwiched between two sets of Distributed Bragg Reflector (DBR) mirrors. Gain is produced in the quantum wells via current flowing in the vertical direction. The spacing of the quantum wells and also the Bragg reflecting mirrors are designed such that a standing-wave pattern of laser intensity is produced so as to have a maximum value at the center of each quantum well as shown in the figure 2.20 (a) and thus efficiently extract the gain from those active regions.

The overall quantum-well gain region is tapered as shown in figure 2.20 (b), using oxide materials to narrow the cross-sectional area of current flow and thereby reduce total current requirements. This also allows the current density to be increased in the central region, increasing the effective gain while reducing the overall current. VCSELs can be made in two-dimensional arrays using microfabrication techniques on large wafers to provide high yield and low cost per laser. The packaging cost can also be quite low. The lasers have a low threshold current and, in contrast with edge emitters, provide a circular beam output. For applications in which a single longitudinal mode is desirable, the VCSEL is particularly useful. The extremely short cavity length, of the order of a few microns, yields a very large longitudinal mode spacing, thereby allowing only a single longitudinal mode to fall within the gain bandwidth of the laser.

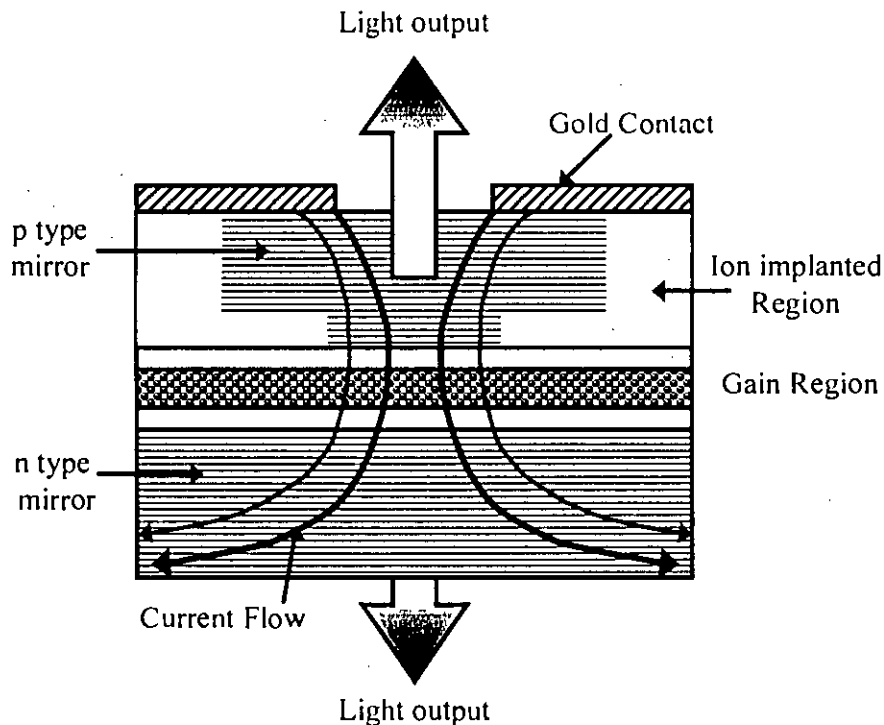


**Figure 2.19** Vertical Cavity Surface Emitting Laser (VCSEL). P-type mirror is placed at the top of the active layer and n-type mirror is placed at the bottom side of the active layer. Contact layers are placed at the top and bottom side for the current injection. Some of the region inside the p-type mirror is made ion implanted to confine the injected current into the active layer.

VCSELs have been produced commercially at wavelengths of 780 nm, 850 nm, and 1.3  $\mu\text{m}$ . The lasers at 780 nm are used in CD systems; those at 850 nm are used for diode pumping of solid-state lasers and also for local connections in optical communications networks. The 1.3  $\mu\text{m}$  lasers are used in high-speed long-distance optical communications. The lasers are made from GaAs, AlGaAs, and InGaAsN materials. VCSELs are cheaper to manufacture than edge emitting lasers because they can be fabricated in quantity on a 3-inch-diameter wafer. They also are easier to test and are more efficient, requiring less electrical current to operate. Efforts are now underway to make VCSELs operating at 1.55  $\mu\text{m}$  for optical communications at the wavelength where fibers have the lowest loss. A chart comparing the properties of VCSELs and edge emitting lasers is shown as Table 2.2.

**Table: 2.2** Comparison between VCSEL and Edge Emitting Laser

Property	VCSEL	Edge Emitter
Beam shape	circular	elliptical
Beam divergence (FW-y M)	13°	20° x 60°
Power consumption	20 mW	100 mW
Power emitted	2mW	100 mW
Spectral width	10-3A	10~3A
Spectral temperature dependence	0.6A/°C	3A/°C
Mode hopping	no	yes
Processing	standard GaAs	cleaved facets
Testing	on wafer	component only
Arrays	1D and 2D	1D only
Speed	2.5-10 Gigabits/s	500 Megabits/s
Cost	<\$1	\$500

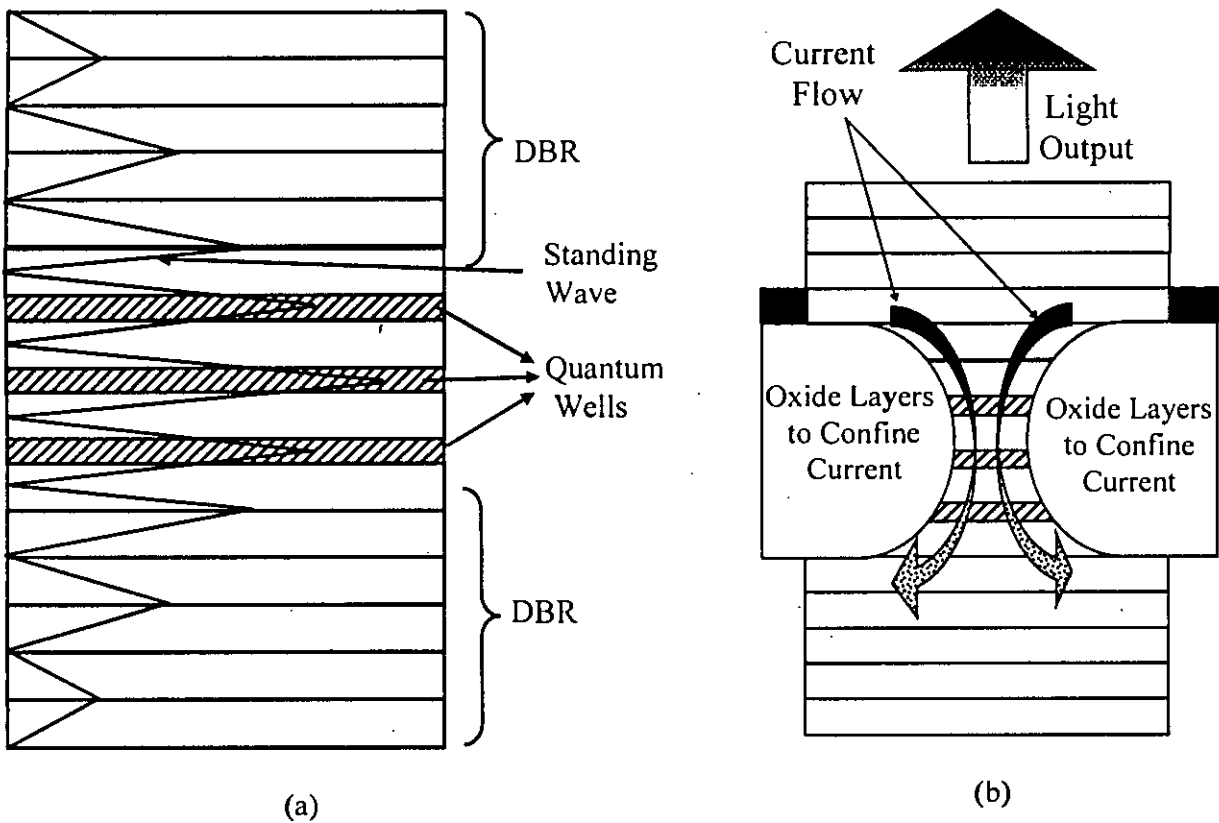


**Figure 2.20** Schematic diagram of a VCSEL. (a) showing three quantum wells (MQWs) sandwiched between two Bragg reflecting mirrors; also shown is the standing-wave pattern within the laser, peaked at the quantum wells for high efficiency. (b) Showing the current flow and light output.



## 2.12 Structure of a Semiconductor Laser in the Direction Perpendicular to the Plane of the Junction

In the direction perpendicular to the plane of the junction, a semiconductor laser consists of several thin layers of various types of semiconducting material of varying thicknesses. These thin layers are epitaxial layers, which are grown on top of a substrate by one of the three techniques: i) liquid phase epitaxy (LPE); ii) molecular beam epitaxy (MBE); or iii) metal-organic chemical vapor deposition (MOCVD). LPE is used for growing typical heterojunction structures, but the thinner quantum-well layers are grown by the more precise methods of either MBE or MOCVD.

### Homojunction

Homojunctions consist of a single junction of the n- and p- doped materials. Because of the large amount of heat dissipation and the gradual tapering off of the gain in directions away from the junction, this type of device can be effectively operated only at very low temperatures (well below room temperature). The first semiconductor lasers were operated with this junction arrangement, but they are not practical devices.

### Heterojunction

Heterojunctions consist of several layers of various materials: semiconductor materials both doped and undoped; insulating layers, usually in the form of oxides; and metallic layers for conduction of current. A single layer in the center of these layers, the active layer where gain is produced is a direct bandgap material that is an efficient radiator, while the adjacent layers (cladding layers) can be indirect bandgap material.

Heterojunction or heterostructure devices are fabricated from a range of lattice-matched semiconductor materials. Two of the materials most often used are GaAs/Al<sub>x</sub>Ga<sub>1-x</sub>As and In<sub>1-x</sub>Ga<sub>x</sub>As<sub>y</sub>P<sub>1-y</sub>/InP, which are all group III-V semiconductor alloys (obtained from the third and fifth columns of the periodic table of the elements). The x and y indicate the fraction or concentration of impurity material in the layer. The GaAs/Al<sub>x</sub>Ga<sub>1-x</sub>As based systems are closely lattice matched to and therefore grown upon a GaAs substrate. They typically have either a pure GaAs active region or an Al<sub>x</sub>Ga<sub>1-x</sub>As active region with  $x < 0.15$ . These junction materials provide laser wavelengths ranging from 0.78 to 0.87  $\mu\text{m}$ .

The In<sub>1-x</sub>Ga<sub>x</sub>As<sub>y</sub>P<sub>1-y</sub>/InP based systems can be lattice matched to InP substrates. In these lasers, the active region is In<sub>1-x</sub>Ga<sub>x</sub>As<sub>y</sub>P<sub>1-y</sub>, with InP forming the cladding layers and substrate. The choice of the fractions x and y must be selected to achieve the appropriate lattice matching and laser wavelength. The typical wavelength range for these lasers is from 1.1 to 1.65  $\mu\text{m}$ . This range includes the optimum wavelengths for transmission of laser pulses through optical fibers of 1.3  $\mu\text{m}$ , where the minimum material dispersion occurs in a quartz-based fiber and 1.55  $\mu\text{m}$ , where the lowest loss occurs.

### Quantum-Well Lasers

When the active layer thickness is reduced (in the direction perpendicular to the plane of the junction) to dimensions of the order of 10 nm or less, changes the conduction and valence bands from being normal, parabolic, continuous bands to step function bands with discrete energies. The net effects of this in a semiconductor laser device are i) to decrease the threshold current by increasing

the density of states associated with the upper laser level population, and ii) to minimize the volume within which heat is generated, since most of the heating occurs within the active region.

The laser wavelength can also be changed by varying the quantum-well thickness. Varying the composition of the quantum well can also produce different laser wavelengths by changing the energy bandgap. This is accomplished by using materials of different lattice dimension than that of the substrate, thereby disrupting the regular alignment of the atoms.

Although making lasers with ultra thin quantum-well layers requires more precise control of the fabrication process, the advantages of these lasers are so great that most new laser designs incorporate such quantum-well gain regions. It is possible to stack several quantum wells in parallel to achieve more gain in the device while still retaining the important confining features of the quantum well. Such devices are known as multiple quantum wells (MQW).

The advantage of a quantum-well laser is in providing a much narrower active region where recombination radiation and thus laser gain can occur, so as to reduce the total resistance and thus the heat loading within the junction region. A quantum well also lowers the threshold current by increasing the electron concentration per unit volume at a given energy and thus the laser gain.

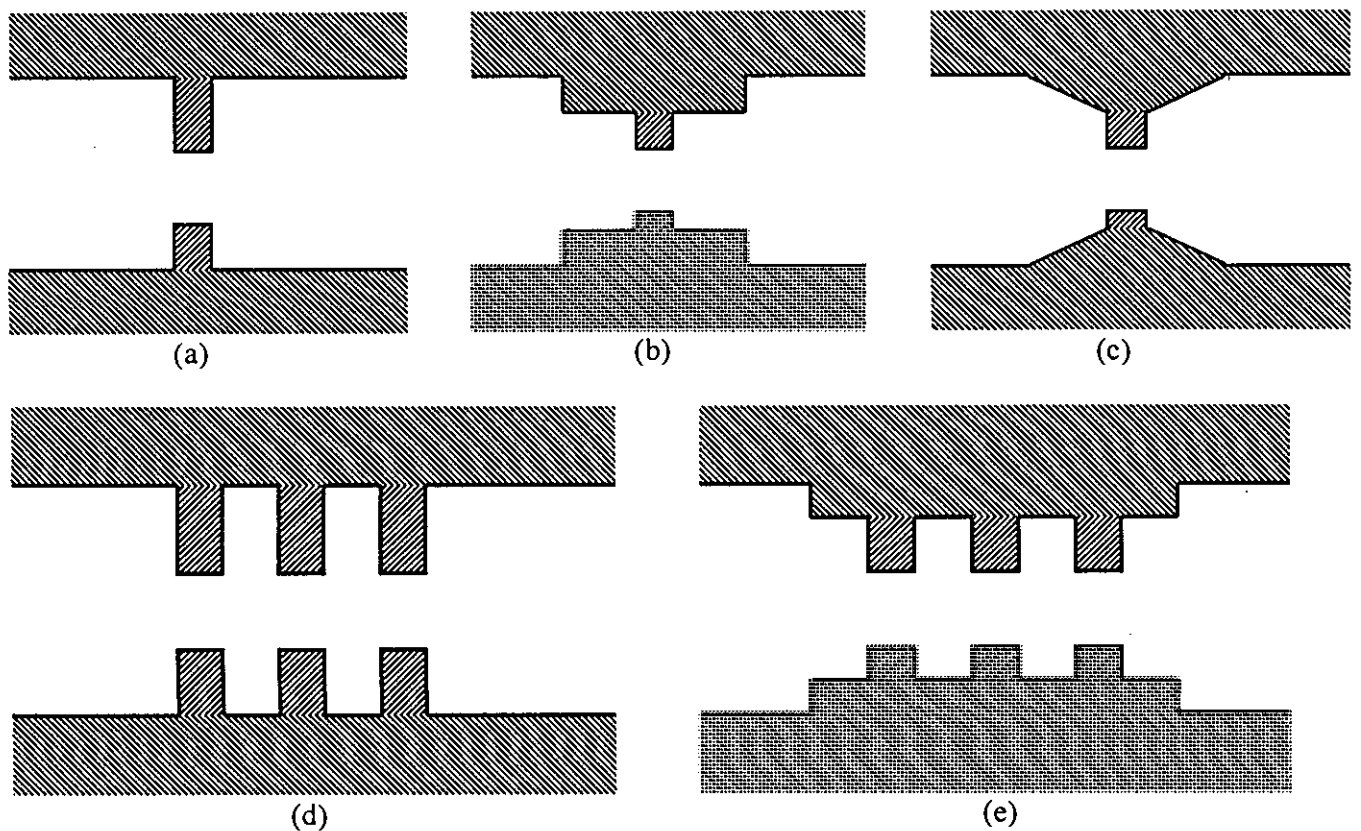


**Figure 2.21** Various quantum heterostructures for quantum well lasers: (a) Single Quantum Well (SQW), (b) Modified SQW, (c) Graded Index Separate Confined Heterostructure Single Quantum Well (GRIN-SCH-SQW), (d) Multiple Quantum Well (MQW) and (e) Modified MQW. The ordinate represents electron energy, and the abscissa is along the direction perpendicular to the junction plane. The upper and lower shaded areas indicate the conduction band and the valence band, respectively.

Use of quantum well(s) as an active layer allows implementation of quantum well lasers offering performances better than those of ordinary DH lasers. Reduction in the active layer thickness of a DH laser to form a SQW or MQW structure does not lead to realization of high performances, since the resultant quantum well (QW) is too thin in comparison with the optical wavelength to ensure strong optical confinement, and therefore a high effective gain for the guided wave cannot be attained. Another problem is that it is not easy to attain a high efficiency of carrier injection in MQW structures having many heterojunctions, and the carriers injected in the thin QW may leak, thereby reducing the effective carrier injection efficiency. The disadvantage is that the total volume of the active region is reduced and thus the total power output is lower, since the total number of electrons participating in the laser output is reduced.

To overcome these problems and to implement high-performance quantum well lasers, various improved structures as shown in Figure 2.21. has been developed. They are separate-confinement heterostructures (SCHs), consisting of the QW active layer for carrier confinement and a refractive index structure for optical confinement outside it, and their modifications.

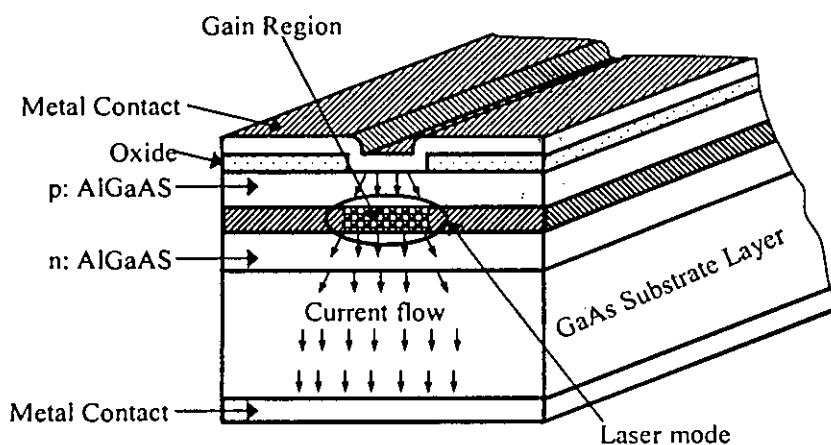


**Figure 2.22** Gain-guided laser structure

### 2.13 Structure of a Semiconductor Laser in the Lateral Direction Parallel to the Plane of the Junction

There are two types of structures used to determine the transverse or lateral dimension of the useful gain region of an edge emitting semiconductor laser. In one case, the region over which gain is produced is limited and thus serves to define the laser width; this is referred to as gain guiding. Alternatively, an index-of-refraction change is fabricated into the laser so that the beam is confined by reflection at that interface; this is referred to as index guiding.

#### Gain-Guided Structures

In heterostructure lasers, confinement of the current to a narrow strip (Figure 2.17) will limit the amount of current flowing in the laser and thus prevent thermal damage to the semiconductor. Such a localized current region also limits the laser gain region and thus the laser mode dimension in the lateral direction. Hence when the current flows through the semiconductor layers and into the active region, it produces gain only in a narrow Gaussian-shaped stripe, as shown in Figure 2.22.

When excitation is applied, the laser mode develops where the gain exists. This minimizes the amount of current required to provide a specific gain by restricting the lateral extent of the current flow.

A disadvantage of this type of device is that the effective width of the gain region broadens as the current applied to the structure is increased. In many applications it is desirable to control the width independently of the current, as described in what follows.

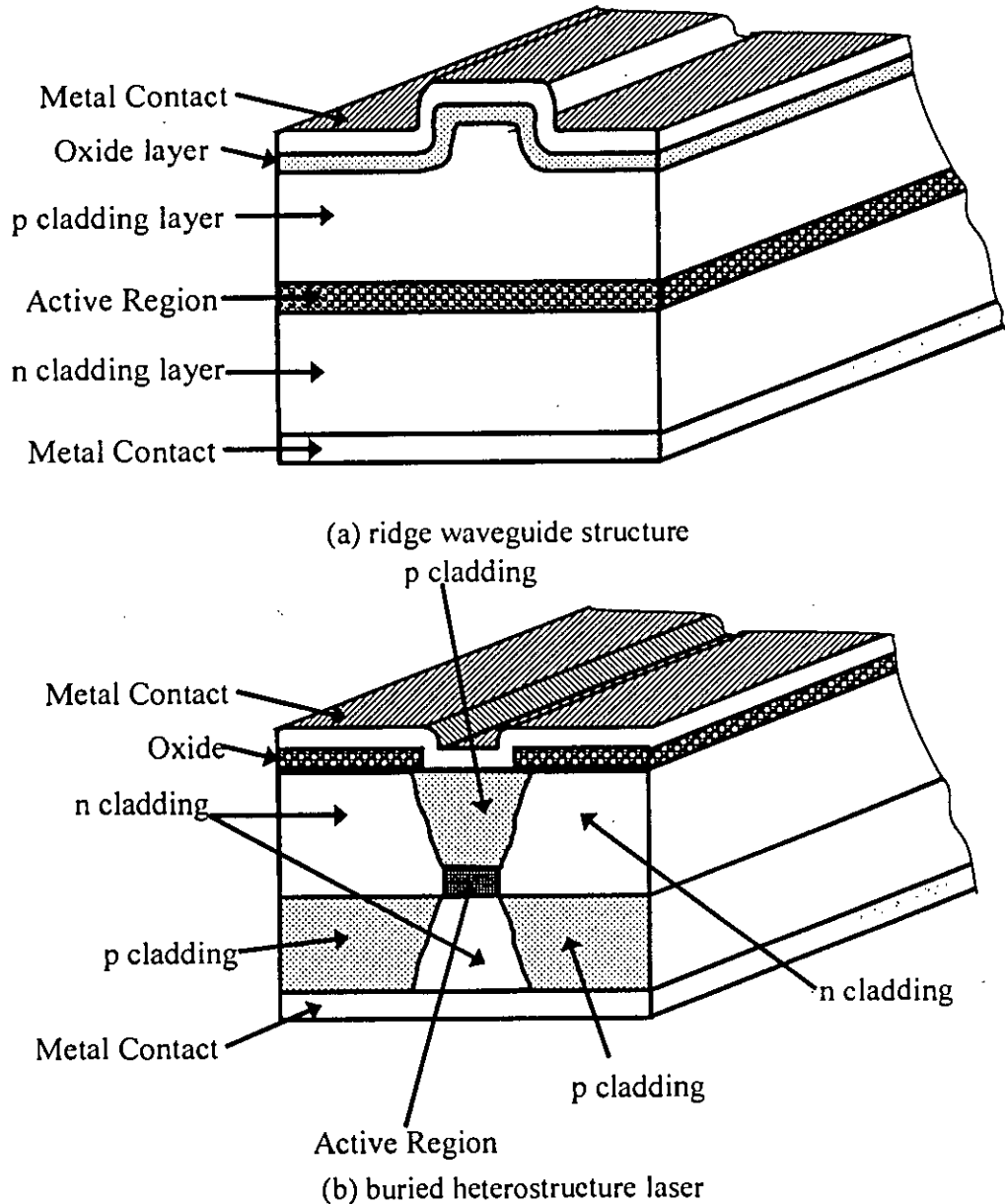


**Figure 2.23** Two examples of index-guided laser structures

**Index-Guided Structures**

Confinement of the laser mode in the lateral direction can also be achieved by fabricating stripes of material of lower index of refraction adjacent to the gain region, as shown in the ridge

waveguide structure of Figure 2.23 (a). A ridge of p-type material such as p:AlGaAs is formed above the active region (GaAs, for example), with the oxide coating adjacent to the ridge as shown. This provides a low-index-of-refraction material adjacent to the higher-index p-type material; the laser mode extending above the active region is confined by this index barrier. Thus the laser operates in a waveguide mode that is determined by the width of the index barrier. This type of laser has many patented configurations relating to the details of the index barrier. The buried heterostructure laser is shown in Figure 2.23 (b).

## 2.14 Summary

An introduction to the construction, energy band diagram and operation of a simple p-n homojunction laser diode and a double heterostructure semiconductor laser diode have been presented at the beginning of this chapter. The relationship between the spontaneous and stimulated emission inside a semiconductor laser is presented. The equation of stimulated gain spectra of semiconductor, which are needed to understand the operation of semiconductor laser, are presented in this chapter. Next the condition of oscillation in a Fabry-Perot laser be introduced in the form of equation and the plot showing the oscillating modes (below/above threshold). A list of materials which need to be used to fabricate a semiconductor laser is presented. At the end, different types of semiconductor lasers are introduced.

## Chapter 3

### Vertical-Cavity Surface-Emitting Laser VCSEL

#### 3.1 Introduction

In this chapter, complete model of VCSEL will be presented. Different structures of VCSELs required to confine the optical field and carrier density in the active region will be presented. Operating parameters of a VCSEL will be determined by comparing with the Edge Emitting Lasers. Construction of Distributed Bragg Reflector (DBR) and different types of DBR will be discussed. Finally the Electric Field distribution inside a VCSEL will be calculated.

#### 3.2 Construction of a VCSEL

In Figure 3.1 a schematic cross section of a VCSEL has been shown. The amplifying layers or active layers are surrounded by electrically conductive layer stacks. These stacks form the laser mirrors which provide optical feedback to the amplifying layers to produce laser oscillation. In GaAs/AlGaAs VCSELs require about  $8\ \mu\text{m}$  of epitaxially grown material, whereas the active region is composed of just a few quantum wells (QWs) of a few nanometer thickness each. The p-i-n type doping configuration is similar to conventional edgeemitting lasers (EELs). In the most simple device layouts, electric current is injected from ohmic contacts on the top epitaxial side and on the backside of the substrate.

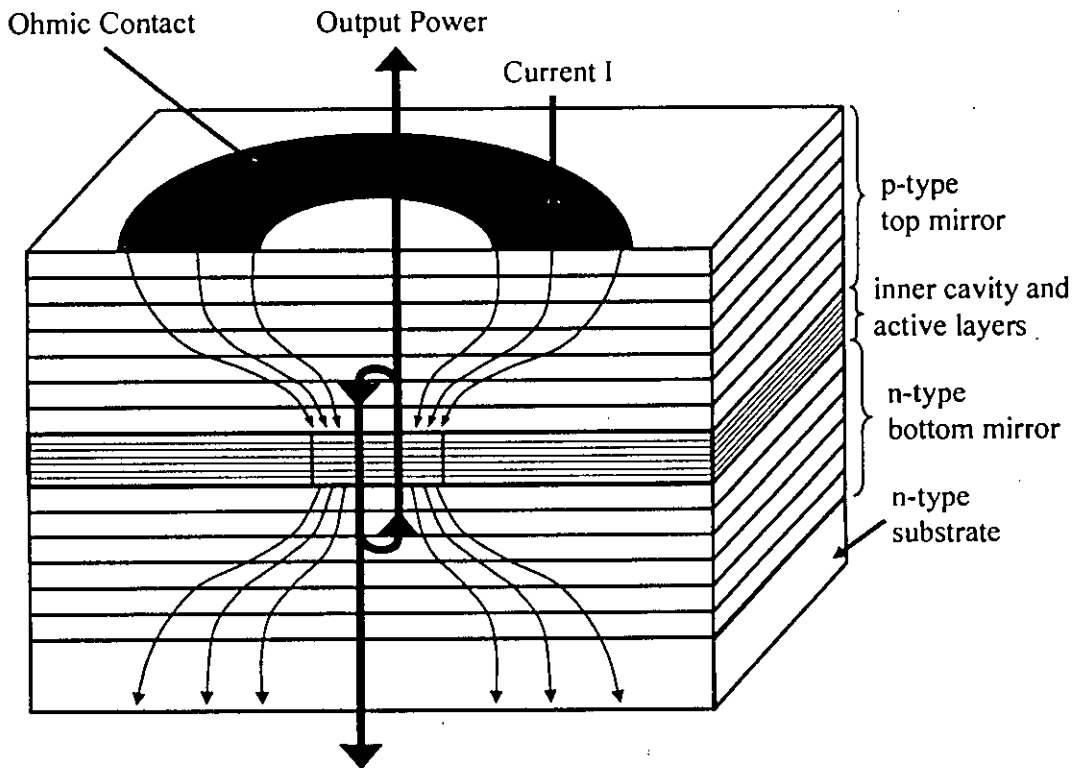


**Figure 3.1** Schematic view of cross section of a Vertical Cavity Surface Emitting Laser (VCSEL).

### 3.3 Different Structures of VCSELs

To improve the device efficiency it is necessary to confine the injected carrier as well as optical field in to the active region. In order to effectively confine carriers in the active region and efficiently extract light from the device, different confinement schemes should be considered in the VCSELs' design.

The most important technological approaches to achieve electrical and optical confinement will be presented in this paragraph.

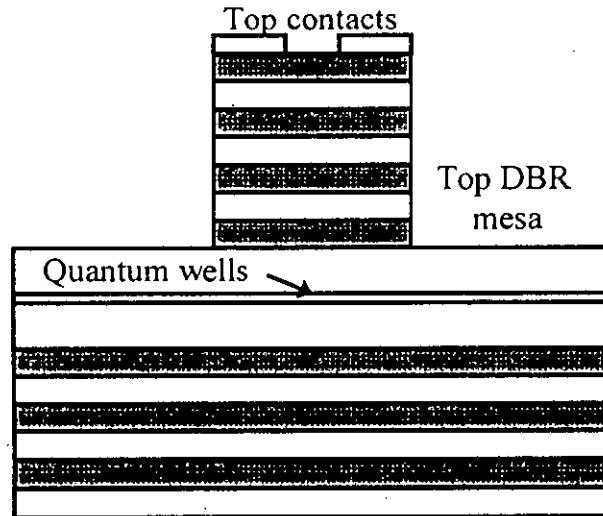


**Figure 3.2 (a)** Schematic view of a simple mesa etched VCSEL

A confinement solution that takes advantage of the index guiding is that of air-post VCSELs as shown in Figure 3.2 a. To introduce lateral optical confinement plasma etch processing can readily make small area, deeply etched pillars with large index confinement due to the high contrast between the semiconductor and the air, but at the expense of increasing lateral losses due to optical scattering or surface recombination.

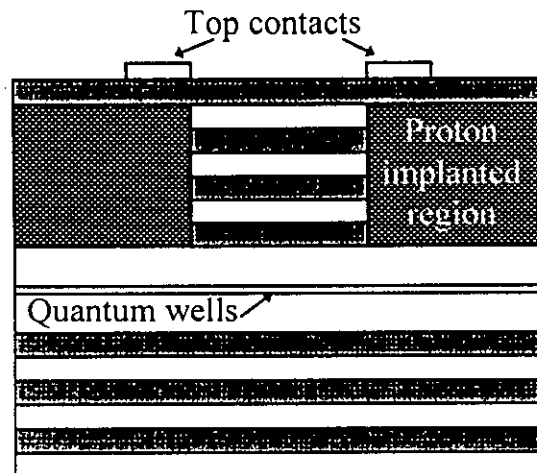


**Figure 3.2 (b)** Schematic view of a proton implanted VCSEL

Gain guiding is used in devices that employ proton implant (Figure 3.2 b) for confinement. The principle is the electrical isolation of the device by ion implantation. The optical confinement is achieved exploiting the gain-guiding mechanism, i.e. the increase in refractive index in the presence of a high density of free carriers but this is a drawback for small device sizes. Therefore the proton implantation solution is reserved only for large devices, which require high threshold currents and have inherent multi-transverse mode operation. Also a special concern is to prevent damaging the active layer. The certain advantage of this structure is the planar configuration that allows a quite easy growth and processing. Actually, the most commercially available VCSELs are proton-implanted devices with multi-transverse mode behavior. Proton implantation has already been brought to perfection to fabricate commercial VCSELs of outstanding producibility and reliability [29], [30].

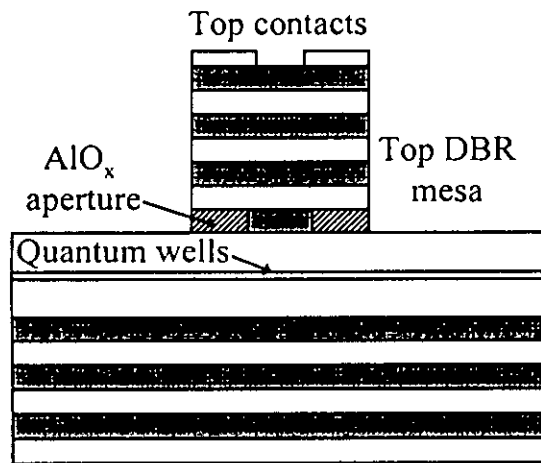


**Figure 3.2 (c)** Schematic view of an oxide confined VCSEL

In contrast to strong index confinement along the entire cavity length, a somewhat surprising result is achieved by introducing the index-confinement into the cavity in only a strategically placed thin layer, thus forming an intracavity dielectric aperture. The dielectric aperture within the low loss planar microcavity introduces a small area, low loss optical mode. And by using the aperture to also confine the injected carriers a very low threshold current VCSEL can be achieved. An attractive means of introducing the dielectric aperture exists in the selective oxidation of AIAs. The introduction of oxide-confinement (Figure 3.2 c) marked a real revolution in VCSELs technology. This procedure is based on the extremely high oxidation selectivity, i.e. the rapidly increasing oxidation speed with Al content in the AlGaAs layer. The selective conversion of high Al composition epitaxial AlGaAs into a stable native oxide ring is performed using the “wet oxidation” process. Typically  $\text{Al}_{0.98}\text{Ga}_{0.02}\text{As}$  composition is used in oxide aperture technology because of the problems associated with the high reactivity of the pure AIAs and device lifetime limitations. The oxide impact on VCSEL design can be two-fold. Its use as a dielectric aperture overcomes the limitations due to optical surface scattering and allows device scaling down to a few microns. Efforts at reducing electrical parasitics, optimizing output coupling, and optimizing the index confinement and thus mode overlap with the injected carriers has resulted in remarkable low threshold, high efficiency VCSEL performance for devices that use all semiconductor DBRs and the oxide-aperture confinement [4]. It might seem that in many respects the oxide-confined VCSEL has rapidly developed into a near optimum device, especially for AlGaAs, GaAs, InGaAs based devices, except for some interesting and outstanding problems in achieving high single mode power. However, the present oxide-confined VCSELs emitting around  $0.98 \mu\text{m}$  wavelength have the most impressive all-



around performance for mode diameters in the 3–5  $\mu\text{m}$  range (unless one desires high output power and multimode behavior, which is achieved at larger diameters). As the lateral size is decreased further, optical losses begin to dominate and increase the threshold current density and decrease the efficiency. Although quite low thresholds have been achieved, it has been at the expense of high threshold current densities and low output efficiencies. The second possible impact of the oxide resides in the possibility to form high-contrast  $\text{AlO}_x/\text{GaAs}$  DBRs that can be monolithically integrated under the VCSEL cavity. The shortening of the effective cavity length allows lateral size reduction smaller than what can be achieved with  $\text{AlGaAs}/\text{GaAs}$  DBRs. A concern about designing a VCSEL based on the  $\text{AlO}_x/\text{GaAs}$  DBRs is the strain associated with the selectively oxidized material because of the volume contraction of  $\sim 10\%$  associated with the oxidation of AlAs. The volume contraction is reduced with the addition of a few percent of Ga, but this is at the expense of slowing the oxidation rate. The volume contraction and the different thermal expansion coefficients between the native oxide and semiconductor can result in severe device damage for heat treatments beyond that used in the oxide formation.

The buried oxide layer has profound implications, leading to new optical phenomena in the cavity. One novel optical effect is the strong modification of the longitudinal cavity resonance under the oxide layer relative to the as-grown cavity resonance. This is because the refractive index is reduced from 3 for the original  $\text{AlGaAs}$  layer to  $\sim 1.6$  for the oxidised layer. The introduction of the oxide aperture determines a blue shift of the cavity resonance relative to the unoxidised cavity resonance and which has to be taken into account in the design of the layers' thicknesses. In addition, the reflectivity across the mirror stop band is increased for the DBR containing the oxide layer as compared to the as-grown DBR. Both of these attributes arise from the significantly smaller refractive index of the oxide layer, and lead to unique lasing characteristics.

Another important issue in oxidised VCSELs concerns the placement of the oxide aperture and its effects on device characteristics. It is true that the introduction of low index apertures in the cavity confines the optical mode size and the current. But the aperture can also introduce losses. Different methods to reduce optical losses have been proposed such as reducing the thickness of the apertures or making tapered apertures. By placing apertures at a node in the electric field standing wave, diffraction losses in the DBR can be reduced and high single-mode output powers can be obtained.

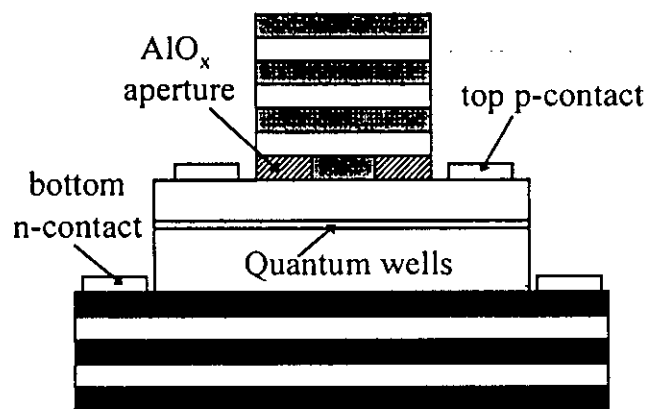


**Figure 3.2 (d)** Schematic view of an intracavity contacted oxide-apertured VCSEL.

Actually when  $\text{AlO}_x$  apertures are placed at a node there is no aperture dependent loss. It has also been shown that displacing apertures into the DBR where the optical field is reduced can also

reduce these diffraction losses enabling fabrication of VCSELs with submicron apertures. However, when the apertures are placed at an antinode the internal loss is clearly a function of aperture size. For large multimode devices, the aperture placement does not play a role in the internal loss. As a rule of thumb, planar, selectively oxidized VCSELs without extended cavity emit in a single transverse mode, up to active diameters of about 4  $\mu\text{m}$ . Larger devices start lasing on several higher radial and azimuthal order modes right above or even at threshold. The light-current curve has a constant slope above threshold, as common for laser diodes, but shows a characteristic rollover for higher currents due to internal heating.

Furthermore, the design of oxide-apertured VCSELs allows the fabrication of intracavity contacted VCSELs (Figure 3.2 d) where the current is bypassing the DBRs [32]. Thus the high series electrical resistance introduced by the reflectors is avoided.

Generally, index-guided VCSELs are expected to have better performance than gain guided devices owing to the strong overlap of the electromagnetic field with the gain region in the device and current independent modal control.

One of the main advantages of a VCSEL is that due to its short cavity length – typically of the order of magnitude of the resonant wavelength – the longitudinal cavity mode spacing is very large. Actually it is possible to have the mode spacing larger than the gain bandwidth of the active material. This is clearly shown in Figure 1.3 where for the EEL there are a few modes favored by the gain curve while in the VCSEL there is only a single mode within the gain region due to higher free spectral range. Therefore a VCSEL is inherently single longitudinal mode. Also, since the cavity is vertical, the device needs to be not much larger than the desired spot size. Thus, the chip area required is small.

The different geometry of VCSELs as compared to that of EELs has advantages both for applications and for fabrication. The first difference lies in the cavity length, which for VCSELs is at least two orders of magnitude smaller than for EELs. Typically, this length is 300  $\mu\text{m}$  for EELs, whereas for VCSELs in many cases it comprises only one optical wavelength plus the effective thickness of the distributed laser mirrors. Fabrication of EELs necessarily includes cleavage of the semiconductor wafer while this is not required for VCSELs. Concerning the output beams, EELs emit highly elliptical and strongly divergent beams as a result of the highly asymmetric transverse guiding. In contrast, VCSELs emit a low divergence circular beam, which is advantageous for efficient coupling into optical fibers. On the other hand, the transverse asymmetry in EELs puts strong constraints on the polarization of the output light. Nevertheless, practical VCSELs with a perfect cylindrical symmetry are generally reported to emit linearly polarized light which, however, has a poor orientational stability [33]. The most obvious advantage of VCSELs over conventional EELs is the possibility to fabricate large two-dimensional arrays. Although from EELs one-dimensional arrays may be produced by employing a number of parallel stripes, the production of two-dimensional arrays is practically impossible. For VCSELs the number of devices that can be processed on one wafer is only limited by the size of the wafer and the minimum distance between the individual devices. The lateral dimensions of a single device can be smaller than 5  $\mu\text{m}$ , which allows very high packing density.

### 3.4 Operating Parameters of VCSELs Compared With Edge Emitting Lasers

To determine the operating parameters of a VCSEL, it is necessary to start by comparing a conventional Edge Emitting Laser (EEL) with a VCSEL. Conventional EEL has a cavity length  $L_{edge} \sim 240\mu\text{m}$  and facet power reflectivity  $R_{edge} \sim 30\%$ , where as a VCSEL has a cavity length  $L_{vcsel} \sim 1\mu\text{m}$  and the facet power reflectivity  $R_{vcsel}$  to be determined as shown in figure 3.3.

Assume that the net material field gains per unit length are  $g_{edge}$  and  $g_{vcsel}$  of the conventional EEL and VCSEL respectively with confinement factors of  $\Gamma_{edge} \sim 0.5$  and  $\Gamma_{vcsel} \sim 1$ . Putting  $r_1 = r_2 = \sqrt{R}$  into the equation 2.45 and neglecting the internal loss of the cavity and considering the confinement factors, one can write the following equations

$$\text{For EEL, } \Gamma_{edge} g_{edge} = \frac{1}{L_{edge}} \ln\left(\frac{1}{R_{edge}}\right) \quad (3.1)$$

$$g_{edge} \sim 100\text{cm}^{-1}$$

$$\text{For VCSEL, } \Gamma_{vcsel} g_{vcsel} = \frac{1}{L_{vcsel}} \ln\left(\frac{1}{R_{vcsel}}\right) \quad (3.2)$$

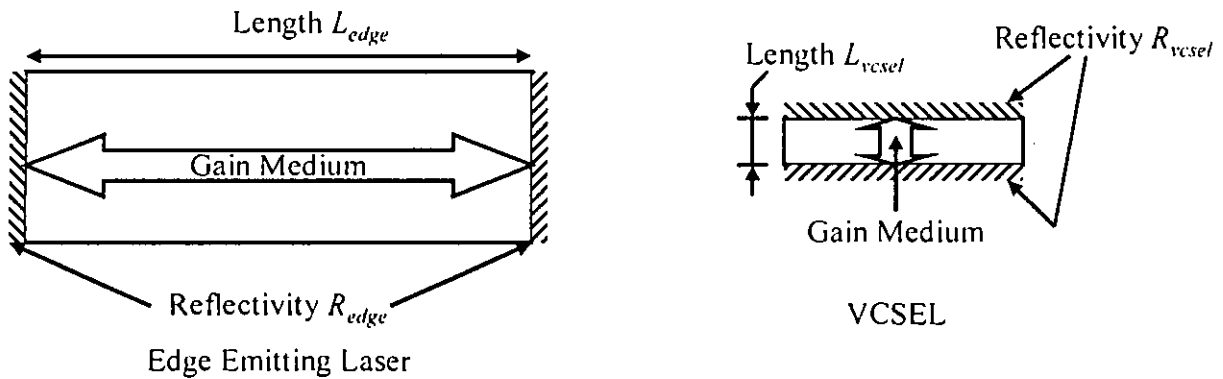


**Figure 3.3** Schematic edge emitting laser and VCSEL.

From equation 3.1 it is found that the power gain of conventional edge emitting lasers is  $\sim 100\text{cm}^{-1}$ . If VCSELs are to operate at high temperature or need the long operating lives of conventional lasers, the gain for lasing and the resulting carrier density in the active region must not significantly higher than in conventional edge emitting lasers. For comparable power gains around  $100\text{cm}^{-1}$ , it can be seen from equation 3.2 that the VCSEL requires both top and bottom power reflectivities to be greater than 99%. However, these values cannot readily be achieved by metal reflectors or single dielectric interfaces. Such a high reflectivity mirrors can be produced by using Distributed Bragg Reflector (DBR) at the top and bottom sides of a VCSEL. The construction and characteristics of DBR will be discussed in the next section

### 3.5 Distributed Bragg Reflector

Consider a layer of index  $n_h$  between layers  $0$  and  $s$  of lower indices  $n_0$  and  $n_s$  as shown in figure 3.4. The reflection from the front interface has a phase of  $\pi$  radians relative to the incident wave because of the positive index step ( $n_h > n_0$ ). At the rear interface the forward traveling wave is reflected with a relative phase of  $0$ , as there is a negative index step ( $n_h > n_s$ ). If the thickness of the layer is a quarter wavelength the two reflections add in phase at the front interface due to the  $\pi$  round trip phase delay for the second reflection. For a stack with many alternate quarter wave layers of low and high index, all interfacial reflection will add in phase.

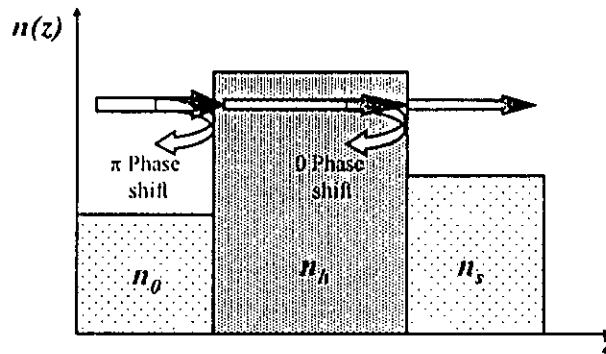


**Figure 3.4** Representation of the Relative phase of a reflected wave at the interface between two dielectric layers having different refractive indices.

Distributed Bragg Reflectors (DBRs) are made from alternate quarter wavelength layers of indices  $n_l$  and  $n_h$  as shown in figure 3.5. The reflectivity  $R$  at the resonant wavelength of the DBR stack with  $m$  dielectric pairs is given by [34]

$$R = \left[ \frac{1 - \frac{n_s}{n_0} \left( \frac{n_l}{n_h} \right)^{2m}}{1 + \frac{n_s}{n_0} \left( \frac{n_l}{n_h} \right)^{2m}} \right]^2 \quad (3.3)$$

Equation (3.3) is valid only at the resonant wavelength. At other wavelengths the reflectivity will be less as the layers will no longer be of quarter wave thickness and reflections will not add in phase.

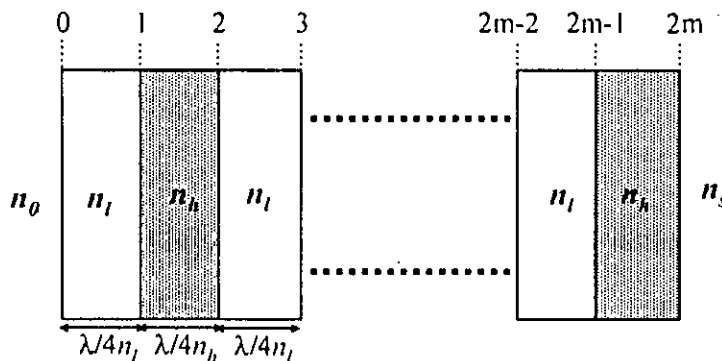


**Figure 3.5** Schematic arrangement of a Bragg Reflector consisting of  $m$  pairs of quarter wavelength thick dielectric layers having the indices  $n_l$  and  $n_h$  alternately. The indices of the two sides of the Bragg Reflector are  $n_0$  and  $n_s$ .

As discussed in the section 3.2, VCSEL requires DBR mirror having power reflectivity greater than 99%. Figure 3.6 gives rough estimate of the minimum number of quarter wavelength layer pairs that will be required to achieve this reflectivity. When the adjacent layers have a normalized step in the refractive index ( $\delta n/\Sigma n = (n_h - n_l)/(n_h + n_l)$ ) falling below, say 0.05, then more than 30 layer pairs are required to obtain adequate reflectivity.

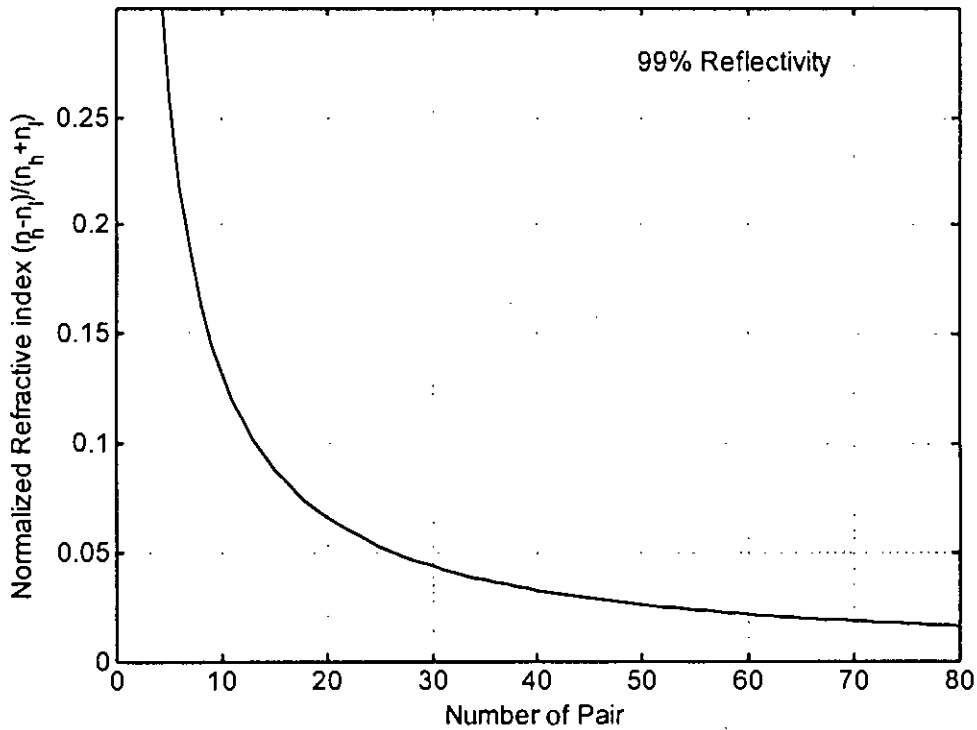


**Figure 3.6** Approximate number of pairs required to achieve 99% as a function of  $\delta n/\Sigma n = (n_h - n_l)/(n_h + n_l)$  considering  $n_0 = n_s$ .

### 3.6 Variation of Refractive Index of some of the Direct Bandgap Semiconductor Materials with the Emission Wavelength.

The refractive index a semiconductor material is not constant with different wavelength. In the energy range below or near the fundamental absorption edge the dispersion of the refractive index  $n(\lambda)$  of GaAs can be calculated by the first-order Sellmeier equation [35]

$$n(\lambda) = \sqrt{A + \frac{B}{1 - \frac{C^2}{\lambda^2}}} \tag{3.4}$$

In this equation the symbols and constants have the following meaning in the case of GaAs at room temperature

- $\lambda$  is the light wavelength in the vacuum in  $\mu\text{m}$
- $A = 8.950$  is an empirical coefficient

$B = 2.054$  is an empirical coefficient  
 $C^2 = 0.390$  is an empirical coefficient

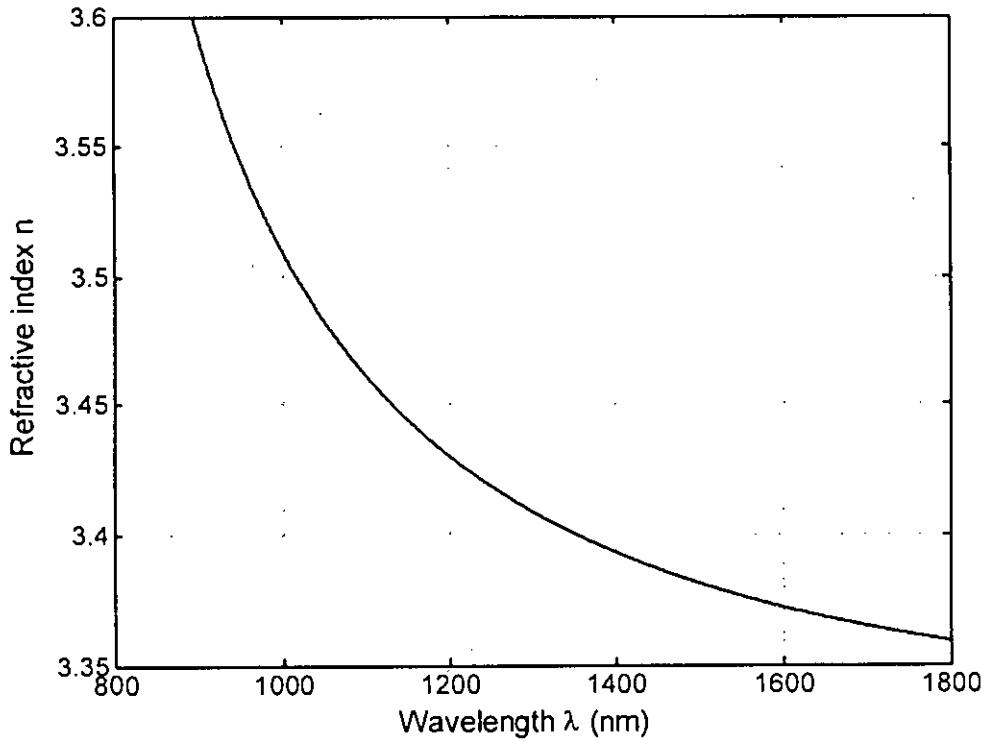


**Figure 3.7** The variation of refractive index  $n(\lambda)$  of GaAs with wavelength. The refractive index is decreased with the increase in wavelength.

According to Sadao Adachi [36] the real part of the refractive index  $n(\lambda)$  of AIAs below the band gap edge can be expressed by:

$$n(\lambda) = \sqrt{A_0 \left[ f(\chi) + \frac{f(\chi_{s0})}{2} \left( \frac{E_0}{E_0 + \Delta_0} \right)^{\frac{3}{2}} \right]} + B_0 \quad (3.5)$$

With  $\chi = \frac{hc}{\lambda E_0}$ ,  $f(\chi) = \frac{2 - \sqrt{1 + \chi} - \sqrt{1 - \chi}}{\chi^2}$  and  $\chi_{s0} = \frac{hc}{\lambda(E_0 + \Delta_0)}$

In this equation the symbols and constants have the following meaning in the case of AIAs at room temperature:

$n$  is the (real part) of the refractive index

$\lambda$  is the wavelength in the vacuum

$h = 6.626 \cdot 10^{-34}$  Js, is the Planck's constant

$c = 2.998 \cdot 10^8$  m/s, is the speed of light in the vacuum

$hc/\lambda$  is the photon energy

$A_0 = 25.3$ , is a constant, determined by fitting with experimental data

$B_0 = -0.8$ , is a constant, determined by fitting with experimental data

$E_0 = 2.95$  eV, is the fundamental band gap at  $\Gamma$ -point  
 $E_0 + \Delta_0 = 3.25$  eV, with  $\Delta_0$  spin-orbit splitting energy

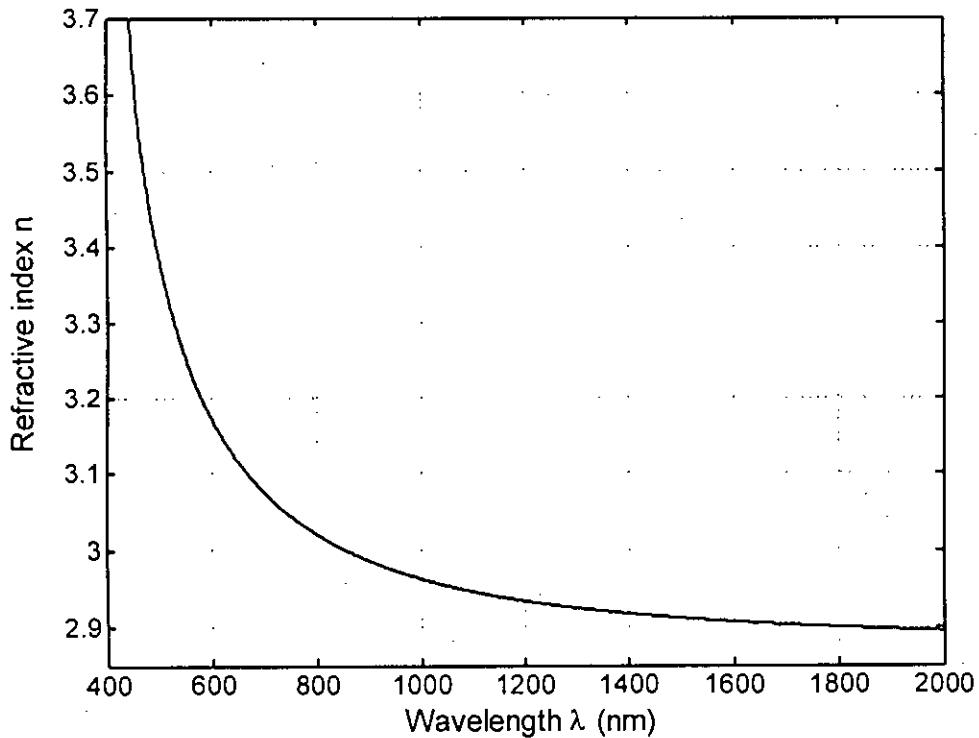


**Figure 3.8** The variation of refractive index  $n(\lambda)$  of AlAs with wavelength. The refractive index is decreased with the increase in wavelength.

According to Sadao Adachi [36] the real part of the refractive index  $n(\lambda)$  of a zincblende material below the direct band gap edge can be expressed due to a simplified interband-transition model as:

$$n(\lambda) = \sqrt{A_0 \left[ f(\chi) + \frac{f(\chi_{s0})}{2} \left( \frac{E_0}{E_0 + \Delta_0} \right)^{\frac{3}{2}} \right] + B_0} \quad (3.6)$$

With  $\chi = \frac{hc}{\lambda E_0}$ ,  $f(\chi) = \frac{2 - \sqrt{1 + \chi} - \sqrt{1 - \chi}}{\chi^2}$  and  $\chi_{s0} = \frac{hc}{\lambda(E_0 + \Delta_0)}$

In this equation the symbols and constants have the following meaning in the case of  $\text{Al}_x\text{Ga}_{1-x}\text{As}$  at room temperature:

- $n$  is the (real part) of the refractive index
- $\lambda$  is the wavelength in the vacuum
- $h = 6.626 \cdot 10^{-34}$  Js, is the Planck's constant
- $c = 2.998 \cdot 10^8$  m/s, is the speed of light in the vacuum
- $hc/\lambda$  is the photon energy
- $A_0(x) = 6.3 + 19.0x$ , is a constant, determined by fitting with experimental data

$B_0(x) = 9.4 - 10.2x$ , is a constant, determined by fitting with experimental data  
 $x$  is the Al fraction in the  $\text{Al}_x\text{Ga}_{1-x}\text{As}$  alloy  
 $E_0(x) = (1.425 + 1.155x + 0.37x^2)$  eV, is the fundamental band gap at  $\Gamma$ -point  
 $E_0(x) + \Delta_0(x) = (1.765 + 1.115x + 0.37x^2)$  eV, with  $\Delta_0$  spin-orbit splitting energy

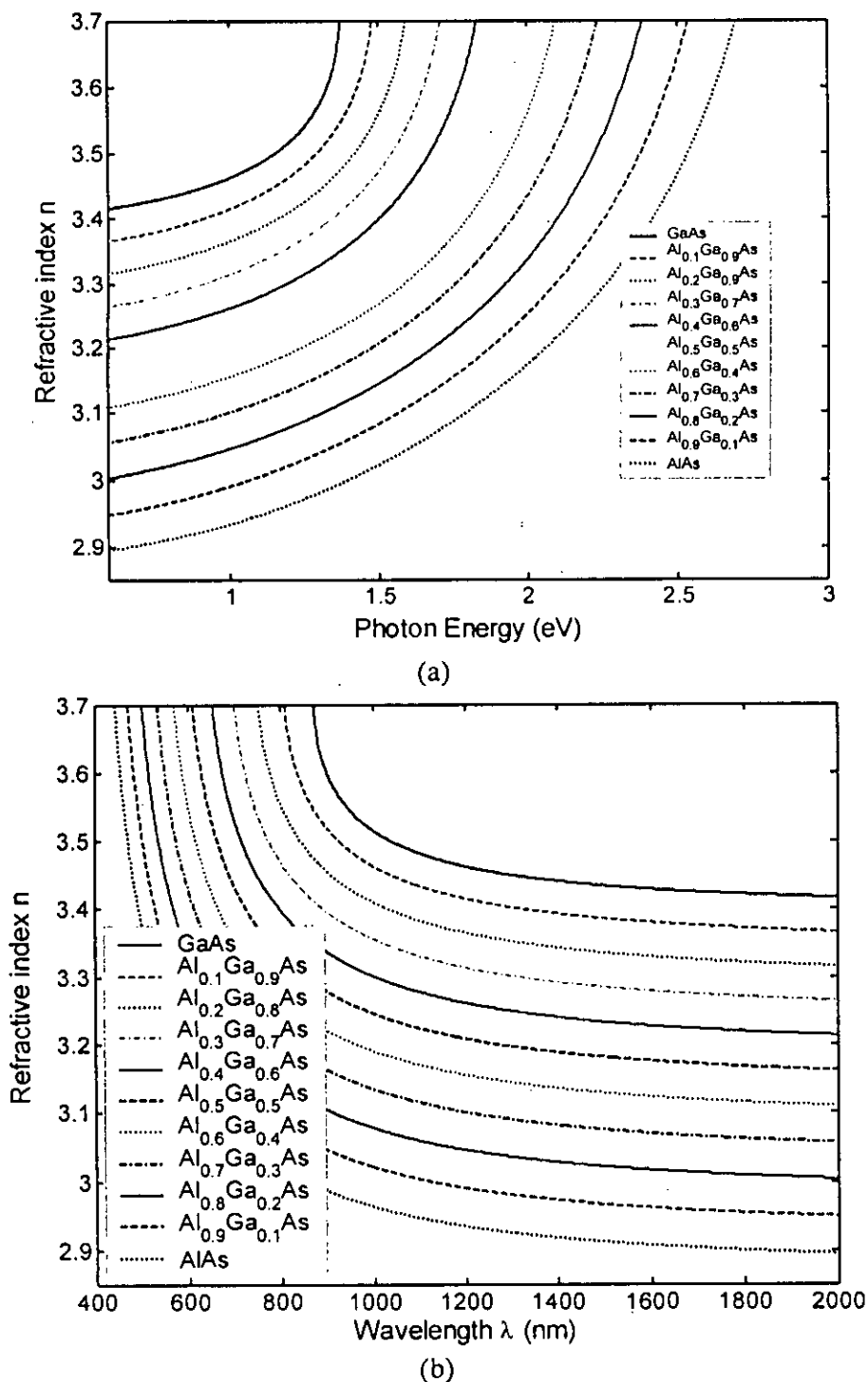


**Figure 3.9** The variation of refractive index of  $\text{Al}_x\text{Ga}_{1-x}\text{As}$  (a) with photon energy (b) with wavelength. The refractive index is increased with the increase in photon energy where as refractive index is decreased with the increase in wavelength.



Graphs with calculated refractive indices of  $\text{In}_x\text{Ga}_{1-x}\text{As}$  alloys as a function of the photon energy  $E=hf$  (in a) or wavelength  $\lambda=hc/E$  (in b) with  $x$ -compositions from 0 to 1 calculated with equation (3.6) is shown in figure 3.9.

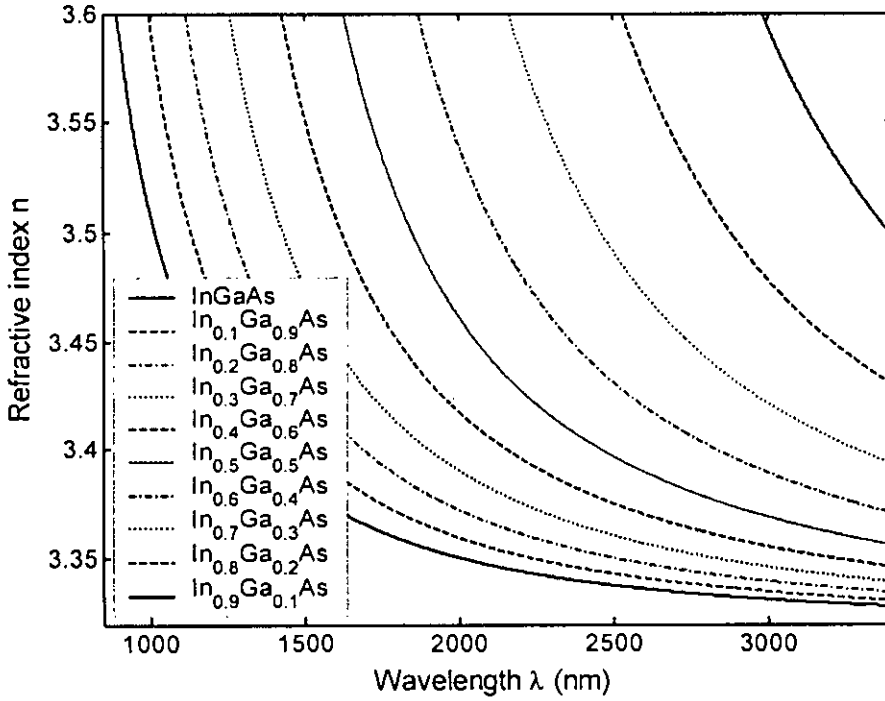


**Figure 3.10** The variation of refractive index of  $\text{In}_x\text{Ga}_{1-x}\text{As}$  with the wavelength. The refractive index is decreased with the increase in wavelength as well as the refractive index is increased with the increase in composition of In content.

Using the Sellmeier equation (3.4) for GaAs a simple model based on the shift of the band gap energy  $E_g(x)$  of the  $\text{In}_x\text{Ga}_{1-x}\text{As}$  alloy leads to the expression:

$$n(\lambda) = \sqrt{A + \frac{B}{1 - \left[ C \frac{E_{g_{\text{GaAs}}}}{\lambda \cdot E_g(x)} \right]^2}} \quad (3.7)$$

with  $E_g(x) = E_{g_{\text{GaAs}}} - x \cdot 1.50 \text{ eV} + x^2 \cdot 0.436 \text{ eV}$

In this equation the symbols and constants have the following meaning in the case of  $\text{In}_x\text{Ga}_{1-x}\text{As}$  alloys at room temperature ( $T = 300 \text{ K}$ ):

- $n(\lambda)$  is the (real part) of the refractive index
- $A = 8.950$  is an empirical coefficient
- $B = 2.054$  is an empirical coefficient
- $C = 0.6245$  is an empirical coefficient
- $x$  is the In fraction in the  $\text{In}_x\text{Ga}_{1-x}\text{As}$  alloy
- $E_{g_{\text{GaAs}}} = 1.424 \text{ eV}$  is the fundamental band gap of GaAs at room temperature (300 K)
- $\lambda$  is the light wavelength in the vacuum in  $\mu\text{m}$

Graphs with calculated refractive indices of  $\text{In}_x\text{Ga}_{1-x}\text{As}$  alloys as a function of the wavelength  $\lambda$  for x-compositions from 0 (smallest) to 0.9 (longest) with step differences of  $\Delta x = 0.1$ .

### 3.7 Reflectivity Spectrum of DBR Stacks

As discussed before that the refractive index of the materials varies with the wavelength, the reflectivity of the DBR will also vary with the wavelength. This variation can be determined by using the transfer matrix method as discussed below. Consider the DBR shown in the figure 3.11 has  $m$  pairs of alternate low and high refractive index layers. The forward and backward traveling plane wave's amplitude at the input plane and output plane are  $F_0, R_0$  and  $F_L, R_L$  respectively. Relation between the waves at input and output plane can be written as [26].

$$\begin{bmatrix} F_0 \\ R_0 \end{bmatrix} = M \begin{bmatrix} F_L \\ R_L \end{bmatrix} = \begin{bmatrix} M_{11} & M_{12} \\ M_{21} & M_{22} \end{bmatrix} \begin{bmatrix} F_L \\ R_L \end{bmatrix} \quad (3.8)$$

$$M = M_{01} \prod_{i=1}^{2m} [M_{i\varphi} M_{i1}] \quad (3.9)$$

where  $M_{i1}$  is the interface matrix of the  $i_{th}$  interface between the layer of index  $n_i$  and  $n_{i+1}$ . The matrix  $M_{i\varphi}$  is the phase matrix of the layer of index  $n_i$  and thickness  $d_i$ . The interface matrix and the phase matrix can be determined as

$$M_{i1} = \frac{1}{2n_i} \begin{bmatrix} n_i + n_{i+1} & n_i - n_{i+1} \\ n_i - n_{i+1} & n_i + n_{i+1} \end{bmatrix} \quad (3.10)$$

$$M_{i\varphi} = \begin{bmatrix} \exp^{j\varphi_i} & 0 \\ 0 & \exp^{-j\varphi_i} \end{bmatrix} \quad (3.11)$$

Where  $\varphi_i = 2\pi n_i d_i / \lambda$  is the phase change of the plane wave into the layer of index  $n_i$ .

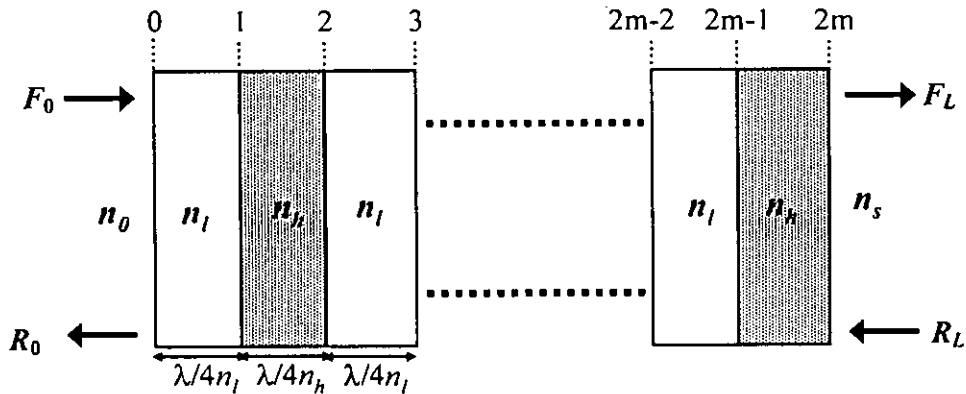


**Figure 3.11** Schematic representation of a GaAs/AlAs Bragg Reflector consisting of  $m$  pairs of low and high indices layers. The indices of the two sides of the Bragg Reflector are  $n_0$  and  $n_s$ .  $F_0$  and  $R_0$  are the incident and reflected wave at the input interface.  $F_L$  and  $R_L$  are the reflected and incident wave at the output interface. The thickness of each layer is quarter wavelength ( $\lambda_B/4n_{l,h}$ ).

The amplitude reflection coefficient of the DBR can be defined as the ratio of the reflected wave to the incident wave at the input plane with no incident wave at the output plane.

$$r = \frac{R_0}{F_0} = \frac{M_{11}}{M_{21}} \quad (3.12)$$

The power reflectivity  $R$  is related with the amplitude reflection coefficient by the following relation

$$r = \sqrt{R} \exp(j\varphi_r) \quad (3.13)$$

Where  $\varphi_r$  is the phase of the reflection.

For  $m$  mirror pairs with the layer thickness  $d_l = \lambda_B / (4n_l)$  and  $d_h = \lambda_B / (4n_h)$  total thickness of the Bragg Reflector is

$$L_B = m(d_l + d_h) = m \frac{\lambda_B}{4} \left( \frac{1}{n_l} + \frac{1}{n_h} \right) \quad (3.14)$$

The coupling coefficient is defined as  $k = 2\Delta n / \lambda_B$ , where  $\Delta n = n_h - n_l$  is the refractive index difference of the composing layers.

Figure 3.12 displays the numerically determined spectral reflectivity  $R(\lambda)$  and phase  $\varphi_r(\lambda)$  for a Bragg mirror shown in the Figure 3.11. The phase of the complex amplitude reflection coefficient ( $\varphi_r$ ) is zero at the Bragg wavelength  $\lambda_B$  but varies almost linearly with phase coefficient  $\beta$  or inverse wavelength deviation, i.e.

$$\varphi_r = 2l_{eff}(\beta_B - \beta) = 4\pi \left( \frac{n(\lambda_B)}{\lambda_B} - \frac{n(\lambda)}{\lambda} \right) \quad (3.15)$$

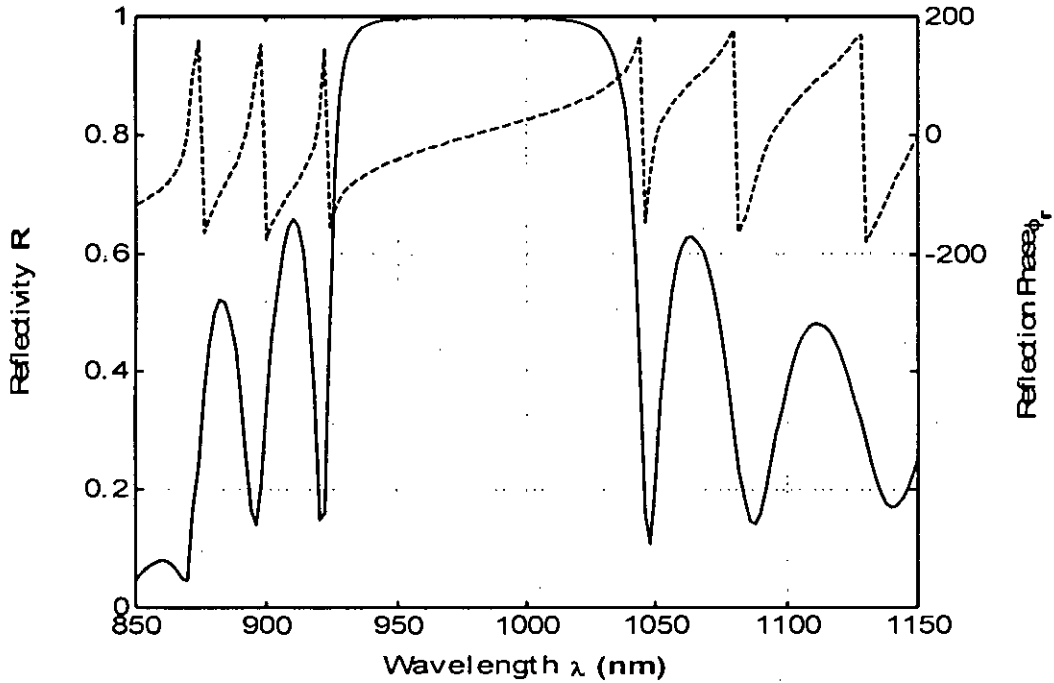
The effective mirror length  $l_{eff}$  can be defined by considering the phase penetration depth of the incident wave into the Bragg reflector. From the phase change, the penetration depth is obtained as [40]

$$\begin{aligned} l_{eff} &= -\frac{1}{2} \frac{d\varphi_r}{d\beta} = \frac{\lambda^2}{4\pi \langle n_{gr} \rangle} \frac{d\varphi_r}{d\lambda} \\ &= \frac{\sqrt{R}}{2k} = \frac{\sqrt{R} \lambda_B}{4\Delta n} \approx \frac{\lambda_B}{4\Delta n} \end{aligned} \quad (3.16)$$

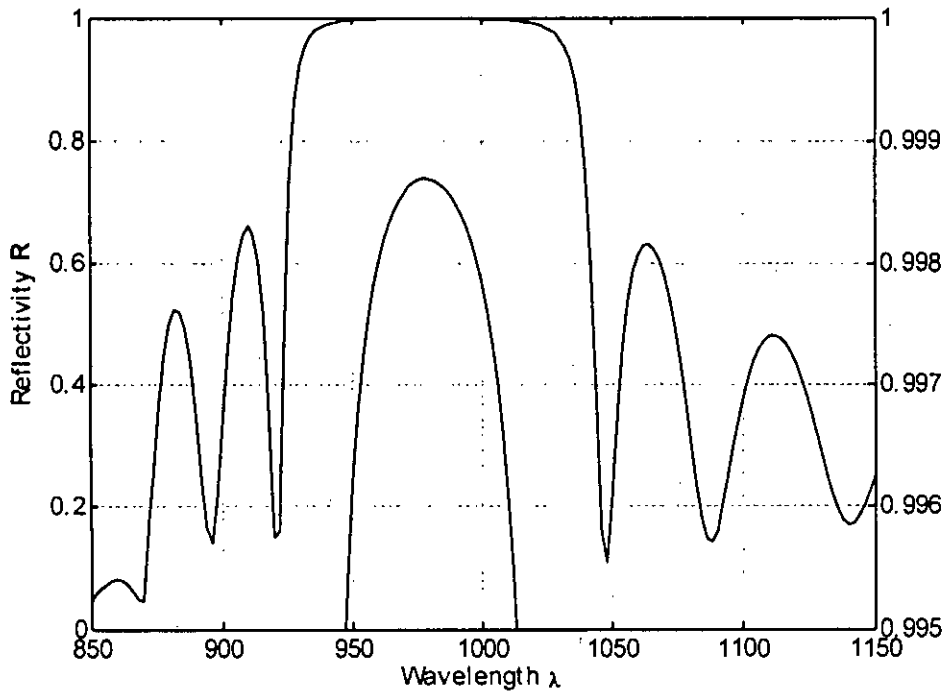
Where  $\langle n_{gr} \rangle$  is the spatially averaged group refractive index and can be represented as

$$n_{gr} = n - \lambda \frac{dn}{d\lambda} \quad (3.17)$$

For a AlAs/GaAs bragg mirror of  $\lambda_B=980\text{nm}$ , the value of  $n_l$  and  $n_h$  are found to be 2.98 and 3.58 by using the equation (3.5) and (3.6) respectively. Hence  $\Delta n=0.557$  gives the effective length of the DBR mirror is  $l_{eff}=440\text{ nm}$ .



(a)



(b)

**Figure 3.12** Spectral dependence of the power reflectivity  $R$  and the phase  $\phi_r$  of the amplitude reflectivity for a Bragg mirror consisting of 20 pairs of AlAs/GaAs layers. Surroundings are  $\text{Al}_{0.3}\text{Ga}_{0.7}\text{As}$  layers at the bottom and air at the top.

A broad spectral width of high reflectivity as shown in the figure 3.12, often denoted as stop-band, appears around the Bragg wavelength  $\lambda_B$ , the width of which can be roughly estimated from as

$$\Delta\lambda_{stop} = \frac{2\lambda_B \Delta n}{\pi \langle n_{gr} \rangle} \quad (3.18)$$

The group refractive index  $n_{gr} = 3.69$  is calculated by using equation (3.17). The stop band of the AlAs/GaAs Bragg mirror shown in the figure 3.11 is computed by using the equation 3.18. Value of the stop band is  $\Delta\lambda_{stop} \approx 94\text{nm}$ .

Finally the effective length of the cavity of a VCSEL is the sum of the length of the active layer plus the effective length of the top and bottom DBR.

$$L_{eff} = L + l_{eff,t} + l_{eff,b} \quad (3.19)$$

This effective cavity length can be used to estimate the longitudinal mode spacing from

$$\Delta\lambda_m = \frac{\lambda^2}{2L_{eff} \langle n_{gr} \rangle} \quad (3.20)$$

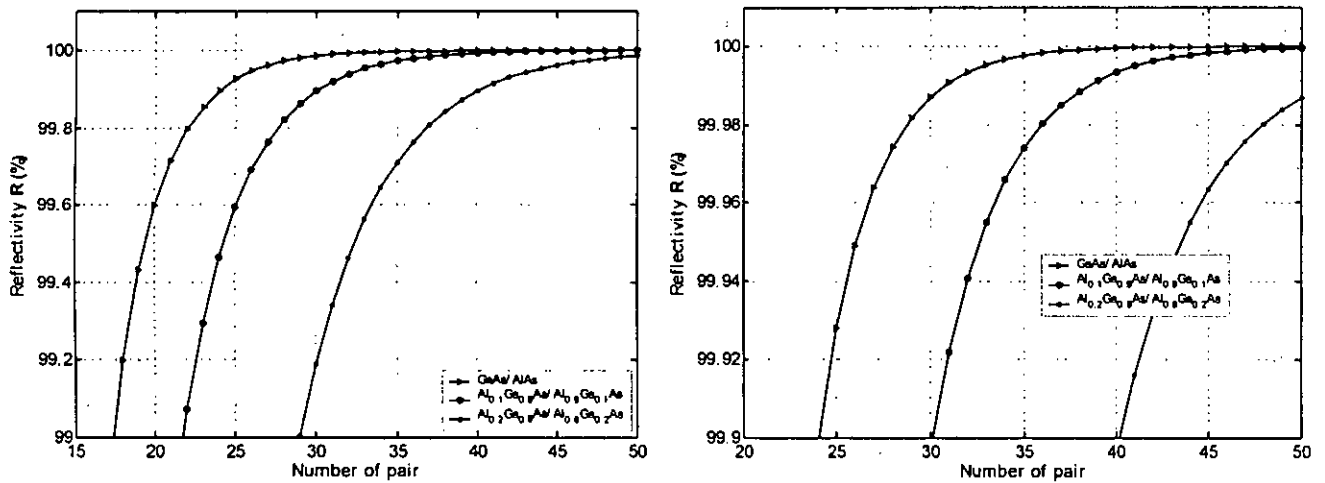


**Figure 3.13** Representation of the power reflectivity R of a 20 pairs Al<sub>x</sub>Ga<sub>1-x</sub>As / Al<sub>1-x</sub>Ga<sub>x</sub>As Bragg mirror. As the composition of x is increased, the number of pair required to achieve the reflectivity over 99% is also increased. (a) Represent that 17.5 pairs of GaAs/AlAs or 22 pairs of Al<sub>0.1</sub>Ga<sub>0.9</sub>As/Al<sub>0.9</sub>Ga<sub>0.1</sub>As or 29 pairs of Al<sub>0.2</sub>Ga<sub>0.8</sub>As /Al<sub>0.8</sub>Ga<sub>0.2</sub>As is required to achieve 99% reflectivity. (b) Represent that 24 pairs of GaAs/AlAs or 30 pairs of Al<sub>0.1</sub>Ga<sub>0.9</sub>As/ Al<sub>0.9</sub>Ga<sub>0.1</sub>As or 40 pairs of Al<sub>0.2</sub>Ga<sub>0.8</sub>As /Al<sub>0.8</sub>Ga<sub>0.2</sub>As is required to achieve 99% reflectivity.

Total elective cavity length of VCSEL having  $\lambda_B/n$  active layer thickness is  $L_{eff} \approx 1.2 \mu\text{m}$ . The mode spacing  $\Delta\lambda_m \approx 110 \text{ nm}$ , extending far beyond the mirror stop-band and even being larger than the spectral gain bandwidth of the QW material. Therefore just a single longitudinal mode can oscillate in a VCSEL with a thin inner cavity. The spectral position of this mode can readily be

theoretically or experimentally determined by localizing the sharp dip appearing in the reflectivity spectrum of the complete layer stack

As mention before that number of pairs of dielectric layers in a DBR to achieve a power reflectivity over 99% is depends on the refractive index contrast between two adjacent layers. The figure 3.13 shows the power reflectivity of a GaAs/AlAs DBR of different numbers of layers.

### 3.8 Reflectivity Spectrum of a VCSEL Resonator

Technique of calculating the reflectivity and transmittivity of a DBR has been discussed in the section 3.7. Following the same technique the reflectivity and transmittivity spectra of VCSEL resonator will be determined in the following section.

Figure 3.14 shows the layered arrangement of a VCSEL. One important point to take note is that the order of arrangement of the layers must be symmetrical at both sides. In other words, if a refractive index,  $n_i$  on the left side of the cavity, a refractive index,  $n_i$ , must be placed at the right side of the cavity region. Low index and high index materials must be arranged alternatively.

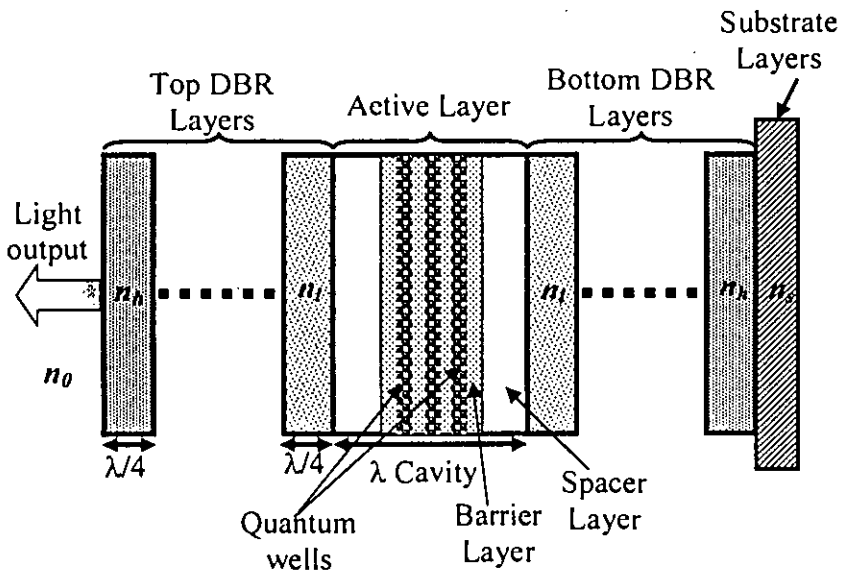


**Figure 3.14** Arrangement of different layers of semiconductor materials of a VCSEL.

The transfer matrix  $M_t$  of the Top DBR and  $M_b$  of the bottom DBR can be calculated by using the technique described in the chapter 2. Then the transfer matrix  $M_{act}$  of the active layer will be calculated. Now, the transfer matrix  $M_{VCSEL}$  of the whole VCSEL will be formed by multiplying all of the transfer matrices for each sections.

$$M_{VCSEL} = M_b \times M_{act} \times M_t \tag{3.21}$$

Figure 3.15 shows the reflectivity spectrum of a VCSEL. The top and bottom DBR have 20 pairs of GaAs/AlGaAs layers and the active layer is constructed by  $Al_{0.8}Ga_{0.2}As$  layer. Reflectivity spectrum indicates that there is a stop band for which the reflectivity is greater than 99%.

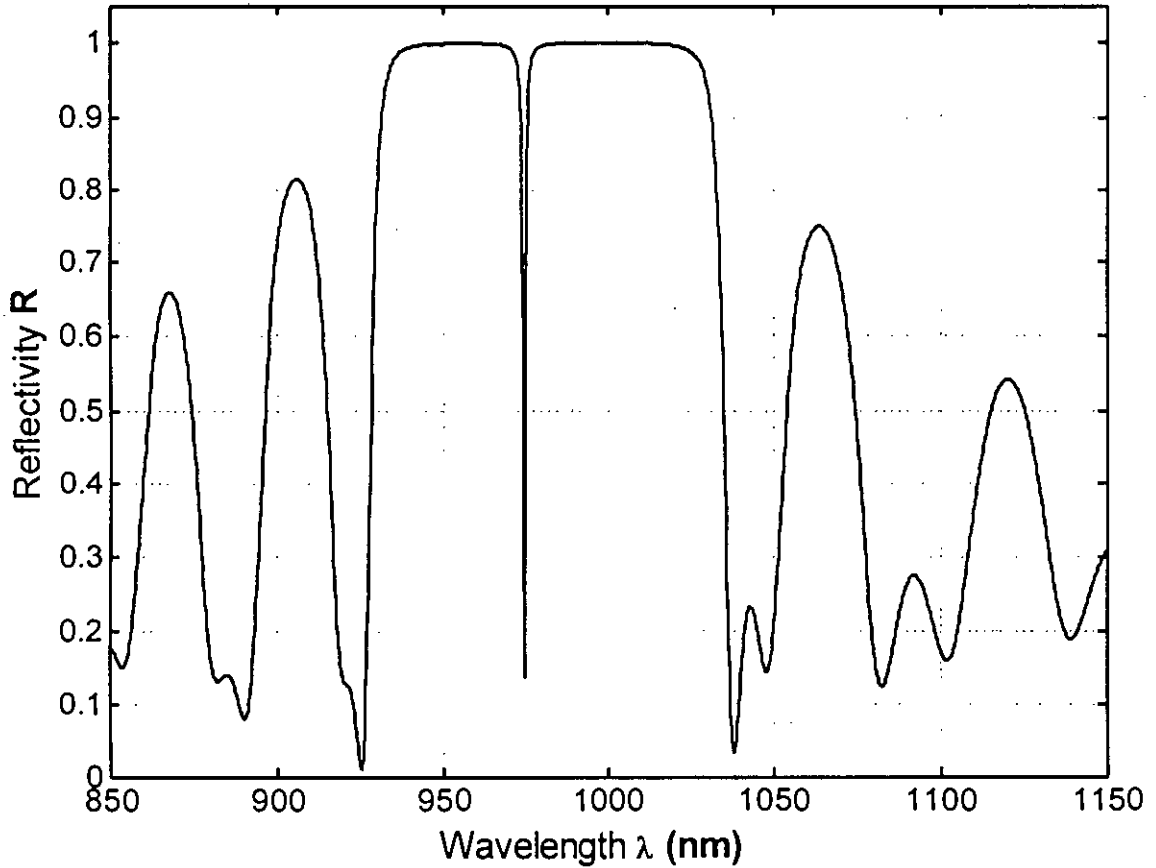


**Figure 3.15** Reflectivity spectrum of a  $\lambda$  cavity VCSEL. Top DBR has 18 pairs and bottom DBR has 20 pairs of  $\text{Al}_{0.2}\text{Ga}_{0.8}\text{As}/\text{Al}_{0.9}\text{Ga}_{0.1}\text{As}$  dielectric layers. Bragg wavelength is considered to 980 nm. The cavity region consists of 3 GaAs quantum wells each of 8 nm thick are separated by 11 nm thick  $\text{Al}_{0.27}\text{Ga}_{0.73}\text{As}$  barrier layer and two  $\text{Al}_{0.57}\text{Ga}_{0.43}\text{As}$  spacer layers are place at the two sides of the inner cavity.

### 3.9 Electric Field Distribution inside the VCSEL.

It is important to know the electric field distribution in the resonator for designing the high performance VCSELs. The layer structure of the device can be represented by the multilayer system depicted in Figure. 3.16. For a linearly polarized wave in a one-dimensional approach, the Helmholtz equation describing the wave propagation in z-direction has the form

$$\frac{d^2 E(z)}{dz^2} + \gamma^2 E(z) = 0 \quad (3.22)$$

The complex propagation coefficient  $\gamma$  in each homogeneous layer of index  $m$  can be defined as:

$$\gamma_m = \beta_m - i \frac{\alpha_m}{2} \quad (3.23)$$

where  $\alpha_m$  is the intensity absorption coefficient of the  $m$ -th layer. The value of  $\alpha_m$  is positive ( $\alpha_m > 0$ ) every-where in the VCSEL except in the quantum wells. In the quantum well gain leads the internal losses of the cavity, hence  $\alpha_m$  is negative. The real part of the propagation constant  $\beta_m$  is related to the real part of the refractive index  $n_m$  of the  $m$ -th layer by

$$\beta_m = \frac{2\pi n_m}{\lambda} \quad (3.24)$$

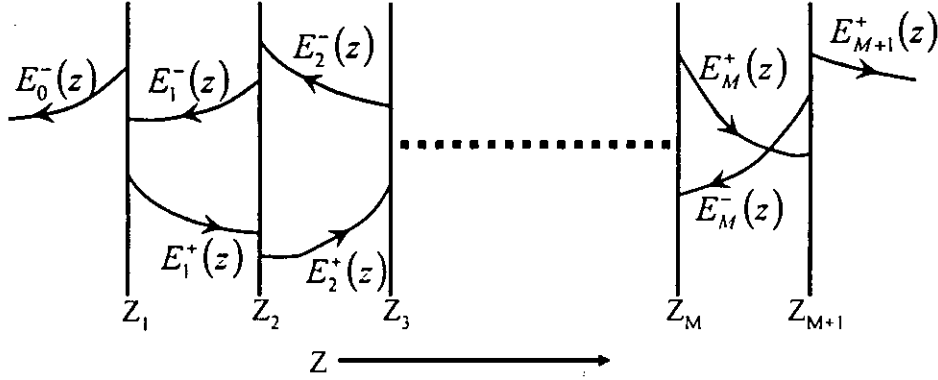


**Figure 3.16** Multilayer structure and traveling wave components for the one dimensional transfer matrix method

In each layer, the electric field  $E(z)$  is the superposition of two monochromatic plane waves of  $\exp(i\omega t)$  harmonic time dependence, counter propagating in  $z$ -direction can be written as

$$E(z) = E_m^+ \exp[-i\gamma_m(z - z_m)] + E_m^- \exp[+i\gamma_m(z - z_m)] \quad (3.25)$$

According to Figure.3.15,  $E_m^+$  and  $E_m^-$  denote the complex field amplitudes of the forward and backward travelling waves at the interface  $z = z_m$  in  $m$ -th section with  $z_m \leq z \leq z_{m+1}$ , where  $m = 1, 2, \dots, M$  with  $M$  as the total number of layers.

The continuity conditions for the transverse components of electric and magnetic fields between amplitudes in the subsequent layers, lead to relations [40]

$$E_m^+ = (\gamma_m^+ E_{m+1}^+ + \gamma_m^- E_{m+1}^-) \exp\{+i\gamma_m(z_{m+1} - z_m)\} \quad (3.26)$$

$$E_m^- = (\gamma_m^- E_{m+1}^+ + \gamma_m^+ E_{m+1}^-) \exp\{-i\gamma_m(z_{m+1} - z_m)\} \quad (3.27)$$

with

$$\gamma_m^+ = \frac{\gamma_m + \gamma_{m+1}}{2\gamma_m} \quad (3.28)$$

$$\gamma_m^- = \frac{\gamma_m - \gamma_{m+1}}{2\gamma_m} \quad (3.29)$$



The equation (3.26) and (3.27) can be rearranged as

$$\begin{bmatrix} E_m^+ \\ E_m^- \end{bmatrix} = \begin{bmatrix} A & B \\ C & D \end{bmatrix} \begin{bmatrix} E_{m+1}^+ \\ E_{m+1}^- \end{bmatrix} = [T_m] \begin{bmatrix} E_{m+1}^+ \\ E_{m+1}^- \end{bmatrix} \quad (3.30)$$

$[T_m]$  is called the transfer matrix with elements  $A$ ,  $B$ ,  $C$  and  $D$  as shown bellow:

$$A = \gamma_m^+ \exp\{+i\gamma_m(z_{m+1} - z_m)\} \quad (3.31)$$

$$B = \gamma_m^- \exp\{+i\gamma_m(z_{m+1} - z_m)\} \quad (3.32)$$

$$C = \gamma_m^- \exp\{-i\gamma_m(z_{m+1} - z_m)\} \quad (3.33)$$

$$D = \gamma_m^+ \exp\{-i\gamma_m(z_{m+1} - z_m)\} \quad (3.34)$$

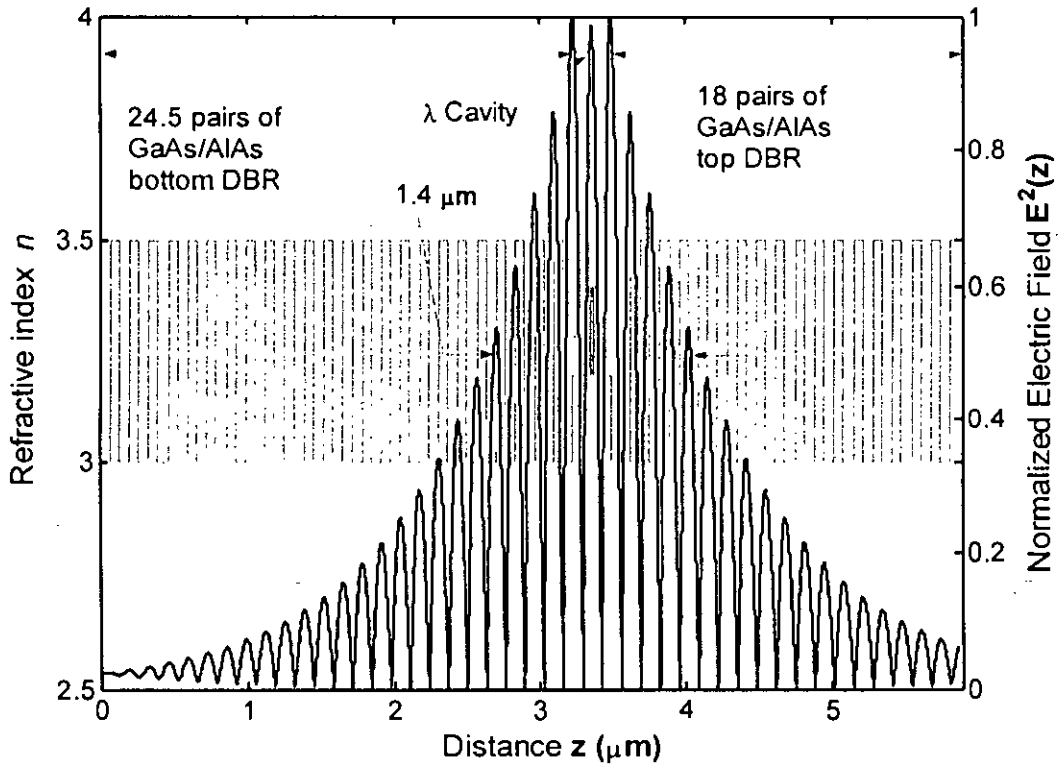


**Figure. 3.17** Standing-wave pattern of the electric field in a VCSEL. The length of the cavity region is 1 wavelength and the top and bottom DBR has 18 and 24.5 pairs of dielectric layers.

The amplitude reflection coefficient  $r_m$  is defined as the ratio between the backward and the forward travelling wave in region  $m$  as

$$r_m = \left. \frac{E_m^-}{E_m^+} \right|_{E_{m+1}^- = 0} \quad (3.35)$$

The amplitude transmission coefficient  $t_m$  is given by dividing the forward travelling wave amplitude in region  $m+1$  by the forward travelling wave amplitude in region  $m$  such that the backward travelling wave in medium  $m + 1$  vanishes, i.e.

$$t_m = \frac{E_{m+1}^+}{E_m^+} \Big|_{E_{m+1}^- = 0} \quad (3.36)$$

The power reflectivity  $R_m$  and transmittivity  $T_m$  are the square of the amplitude reflection coefficient  $r_m$  and transmission coefficient  $t_m$  respectively.

$$R_m = |r_m|^2 \text{ and } T_m = |t_m|^2 \quad (3.37)$$

For lossless media  $R_m + T_m = 1$ . The calculation of the field in the multilayer stack using the matrix notation (equation 3.30) is known as Transfer Matrix Method (TMM). In addition to continuity at the interfaces, lasing requires just outgoing waves in the terminating sections  $m = 0$  and  $m = M + 1$ , i.e.

$$E_0^+ = 0 \text{ and } E_{M+1}^- = 0 \quad (3.38)$$

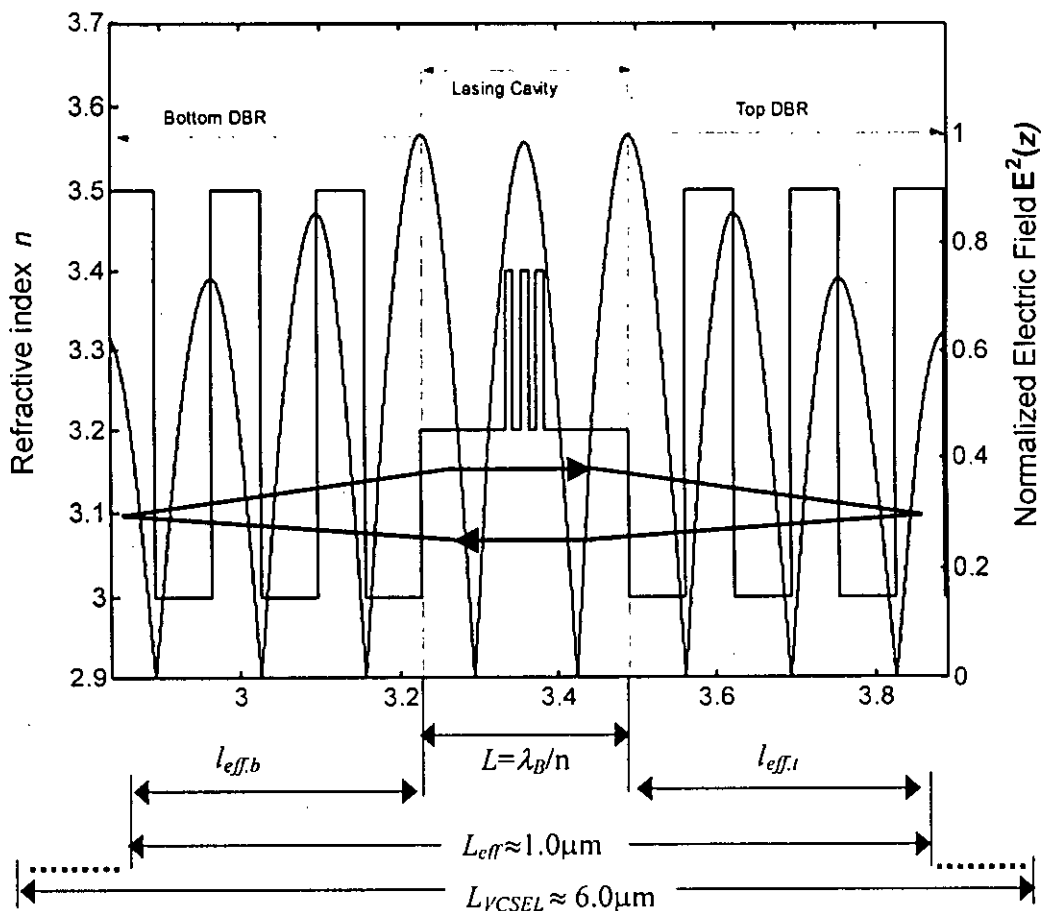


**Figure. 3.18** Spatial distribution of the normalized electric field amplitude of a VCSEL. Illustration shows the field in the cavity region and 3 top and bottom DBRs only. The length of the cavity region is 1 wavelength and the top and bottom DBR has 18 and 24.5 pairs of dielectric layers.

Figure 3.17 shows the result of a numerical calculation of the electric field distribution for a model VCSEL that contains three 10 nm active AlGaAs QWs in the center, an 18 pairs GaAs/AlAs top and a 24.5 pairs GaAs/AlAs bottom Bragg reflector. It is seen that, due to the high reflectivities of the mirrors, a pronounced resonant enhancement of the field amplitude is built up. In the given example, the half width of the envelope is 1.4  $\mu\text{m}$ .

### 3.10 Relative Confinement Factor of a VCSEL

An idealized quantum well VCSEL consists of upper and lower Bragg reflectors that are separated by upper and lower cladding layers and active layers of thickness  $d_a$ , as illustrated in Figure 3.18. Cladding and active layers form the laser cavity of length  $L$ . Bragg mirrors have the maximum reflectivity at the Bragg wavelength  $\lambda_B$ . The laser length is chosen as the material wavelength

$$L = \frac{\lambda_B}{n} \quad (3.39)$$

where  $n$  is the refractive index averaged over active and cladding regions. In the Bragg mirrors the thickness of individual layers is  $\lambda_B/(4n_l)$  and  $\lambda_B/(4n_h)$  for the low index AlAs and high index GaAs layers, respectively. The refractive indices are  $n_l \approx 3.0$  for AlAs and  $n_h \approx 3.56$  for GaAs.

Applying the approach from the previous section, figure. 3.18 indicate the standing wave pattern of the electric field established in the cavity and in 3 mirror pairs of each surrounding Bragg region for clarity. The photons penetrate into the Bragg reflectors such that the effective photon round trip length  $2L_{eff}$  becomes larger than  $2L$ . An analytical expression for the penetration depth has been discussed in the section 3.7. With top and bottom penetration depths  $l_{eff,t}$  and  $l_{eff,b}$ , respectively, the effective resonator length  $L_{eff}$  is found to  $\approx 1.0\mu\text{m}$ .

An important difference between a VCSEL cavity and a conventional EEL cavity arises from the fact that the active gain region does not extend over the full cavity length  $L$  but is enclosed by larger bandgap layers to form a double heterostructure. Therefore, for an arbitrary position and total thickness  $d_a$  of the active layers, one has to take into account the overlap with the standing wave pattern  $E(z)$  in order to obtain the average gain in the cavity [37].

The relative confinement factor or gain enhancement factor  $\Gamma_r$  can be defined as the ratio of the intensity of the light existing in the active layer to the total light intensity in the cavity [27]. Since the light intensity is proportional to the square of the electric field intensity hence  $\Gamma_r$  can be written as

$$\Gamma_r = \frac{L}{d_a} \frac{\int_{-d_a/2}^{d_a/2} |E(z)|^2 dz}{\int_{-L/2}^{L/2} |E(z)|^2 dz} = \frac{L}{d_a} \frac{\int_{-d_a/2}^{d_a/2} |E(z)|^2 dz}{\int_{-L/2}^{L/2} |E(z)|^2 dz} \quad (3.40)$$

with  $z=0$  at center of the active region.

If  $g$  is the gain in the quantum well, the average gain in the cavity is given by  $\Gamma_r g$ . The intensity profile plotted in Figure. 3.18 can be approximated for the inner cavity region as

$$E^2(z) = E_0^2 \cos^2\left(\frac{2\pi mz}{\lambda}\right) \quad (3.41)$$

Putting the value of  $E^2(z)$  from equation (3.41) in to the equation (3.40), relative confinement factor  $\Gamma_r$  can be simplified as

$$\Gamma_r = 1 + \frac{\sin\left(\frac{2\pi n d_a}{\lambda}\right)}{\frac{2\pi n}{\lambda} d_a} \quad (3.42)$$

Figure 3.19 plots the confinement factor  $\Gamma_r$  as a function of the thickness  $d_a$  of GaAs active layer for wavelength  $\lambda = 850\text{nm}$  and average refractive index  $n = 3.3$ . It is seen that  $\Gamma_r$  behaves like *sinc* function with the amplitude shifted by one i.e. it reaches its maximum value of 2 for a thin quantum well and equals one for thicknesses of multiple integers of  $\lambda/2n$ . For a VCSEL with three 8 nm thick quantum wells separated by 10 nm barriers located in the center of the cavity has  $\Gamma_r \approx 1.8$ . By exploiting the standing wave effect, one can therefore almost double the available amount of optical amplification. Obviously it is required that the quantum well be placed in an antinode of the standing wave pattern to provide a good coupling between electrons and photons.

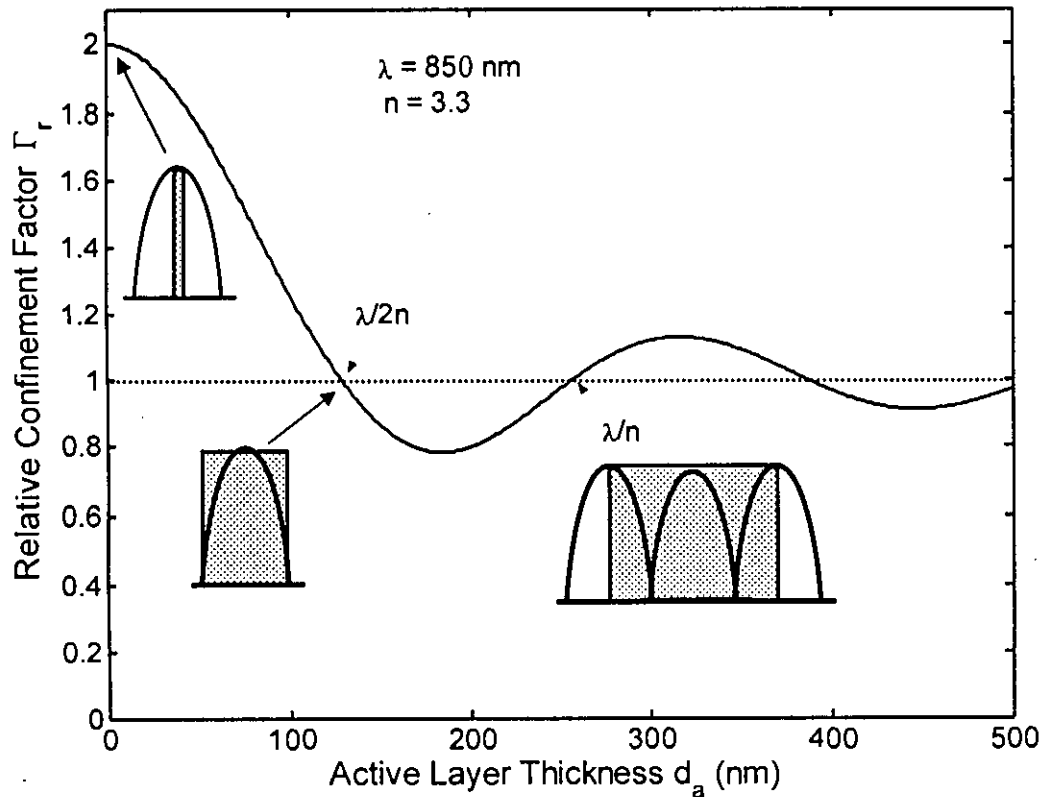


**Figure. 3.19** Dependence of the relative confinement factor  $\Gamma_r$  on the thickness  $d_a$  of the active layer.

### 3.11 Threshold Gain and Photon Lifetime

For lasing, the gain in the cavity has to balance the losses. With intrinsic losses  $\alpha_i$  and  $\alpha_a$  in the passive and active sections, respectively, considerations of gain enhancement and penetration of the waves into the Bragg reflectors lead to the lasing threshold condition

$$g_{th} = \alpha_a + \frac{1}{\Gamma_r d_a} \left[ \alpha_i (L_{eff} - d_a) + \ln \frac{1}{\sqrt{R_t R_b}} \right] \quad (3.43)$$

where  $L_{eff}$  is the effective resonator length given by equation (3.19). In general,  $\alpha_i$  is a spatial average over the locally varying absorption coefficient, where weighting with the standing-wave intensity profile has to be applied. The intensity reflection coefficients  $R_t$  and  $R_b$  are valid for lossless top and bottom mirrors, respectively, and can, in the most simple cases, be determined from equation ( ) by using the transfer matrix method. Alternatively, the threshold condition can be formulated using the maximum reflectivity of a Bragg mirror with homogeneously distributed losses

$$R_a = \text{Re} \exp(-2\alpha_i l_{eff}) \approx R(1 - 2\alpha_i l_{eff}) \quad (3.44)$$

Where in the small losses with  $2\alpha_i l_{eff} \ll 1$  the approximation in the right hand side can be applied. Thereby it is assumed that the wave travels the distance  $l_{eff}$  back and forth and experiences losses  $\alpha_i$ .

Using the equation (3.44), the threshold condition of (3.43) is now can be written as

$$g_{th} = \alpha_a + \frac{1}{\Gamma_r d_a} \left[ \alpha_i (L - d_a) + \ln \frac{1}{\sqrt{R_{ta} R_{ba}}} \right] \quad (3.45)$$

where the effective resonator length  $L_{eff}$  is now replaced by the inner cavity length  $L$ . Assuming equal intrinsic losses  $\alpha_i = \alpha_a$  the photon lifetime  $\tau_p$  in the cavity can be expressed as

$$\frac{1}{\tau_p} = \frac{d_a}{L_{eff}} \langle v_{gr} \rangle \Gamma_r g_{th} \approx \frac{c}{\langle n_{gr} \rangle} \left( \alpha_i + \frac{1}{L_{eff}} \ln \frac{1}{\sqrt{R_t R_b}} \right) \quad (3.46)$$

with the first approximation holding for the usually satisfied conditions  $\alpha_a \ll g_{th}$  and  $d_a \ll L_{eff}$ . The average group velocity  $\langle v_{gr} \rangle$  is related to the vacuum velocity of light  $c$  as  $\langle v_{gr} \rangle = c / \langle n_{gr} \rangle$ . As an example with  $n_{gr} = 3.69$ ,  $L_{eff} = 1.0 \mu\text{m}$ ,  $R_t = R_b = 99.5\%$  and  $\alpha_i = 10 \text{ cm}^{-1}$  one can obtain the photon lifetime  $\tau_p = 2.05 \text{ ps}$  and the threshold gain  $g_{th} = 1390 \text{ cm}^{-1}$  for the active region thickness  $d_a = 24 \text{ nm}$  and confinement factor  $\Gamma_r = 1.8$ .

### 3.12 Radiation Efficiency and Conversion Efficiency

Figure 3.20 schematically shows the current versus light output ( $I$ - $L$ ) characteristics of the semiconductor lasers. As shown in Figure. 3.20, when the injection current  $I$  exceeds the threshold current  $I_{th}$ , laser beams are emitted outward. To evaluate radiation efficiency of the semiconductor lasers, the slope efficiency and the external differential quantum efficiency are used.

The slope efficiency  $S_{dj}$  (in units of mW/mA or W/A) per facet is defined as the ratio of the increase in light intensity  $\Delta P_j$  ( $j = t, b$ ) to the increase in injection current  $\Delta I$ , which is given by [27]

$$S_{dj} = \frac{\Delta P_j}{\Delta I} \quad (3.47)$$

The slope efficiency for the total light output is obtained as

$$S_{d,tot} = \frac{\Delta P_t + \Delta P_b}{\Delta I} = \frac{\Delta P}{\Delta I} \quad (3.48)$$

where  $\Delta P_t$  and  $\Delta P_b$  are the increase in light intensity output from the top and bottom DBR respectively.  $\Delta P$  is an increase in total light intensity.

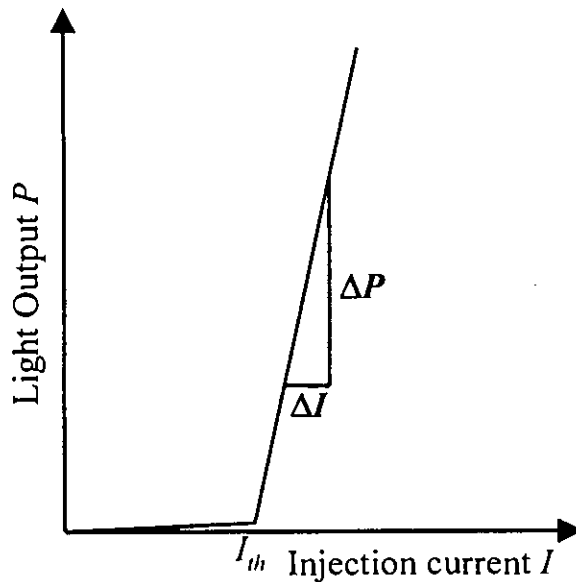


**Figure 3.20** Current versus light output characteristics

The external differential quantum efficiency  $\eta_d$  (in no units) is defined as the number of photons emitted outward per injected carrier. The external differential quantum efficiency  $\eta_d$  for the total light output is given by

$$\eta_d = \frac{\frac{\Delta P}{\Delta I}}{\frac{q}{h\omega}} = \frac{\Delta P}{\Delta I} \frac{q}{h\omega} = S_{d,tot} \frac{q}{h\omega} \quad (3.49)$$

where  $\omega$  is an angular frequency of the light,  $\hbar = h/2\pi$  is Dirac's constant, and  $q$  is the elementary charge.

Total loss of a VCSEL is the sum of the internal loss and the mirror loss. For a reference system placed outside the optical cavity, the mirror loss indicates the light emission rate from the optical cavity. As a result, using the internal quantum efficiency  $\eta_i$ , which is defined as the number of photons emitted inside the optical cavity per injected carrier, the external differential quantum efficiency  $\eta_d$  is expressed as

$$\eta_d = \eta_i \frac{\text{MirrorLoss}}{\text{TotalLoss}} = \eta_i \frac{\frac{1}{L} \ln \frac{1}{\sqrt{R_t R_b}}}{\alpha_i + \frac{1}{L} \ln \frac{1}{\sqrt{R_t R_b}}} = \eta_i \frac{\frac{1}{2L} \ln \frac{1}{R_t R_b}}{\alpha_i + \frac{1}{2L} \ln \frac{1}{R_t R_b}} \quad (3.50)$$

where the optical losses at the top and bottom DBR due to the absorption or the scattering were assumed to be negligible. In a well designed VCSEL with high quality QWs,  $\eta_i > 90\%$  can be achieved. For  $L = 1\mu\text{m}$ ,  $R_t = R_b = 99.5\%$ , and  $\alpha_i = 10\text{ cm}^{-1}$ ,  $\eta_d = 75\%$  can be found.

To determine the external differential quantum efficiency of the top and bottom mirror one can consider the VCSEL cavity region as shown in the figure 3.12. Consider the light outputs  $P_t$  and  $P_b$  from the top and bottom DBR respectively. Assume that the light intensities in the vicinity of the facets inside the optical cavity are  $P_1$ ,  $P_2$ ,  $P_3$ , and  $P_4$ , the power reflectivities of the facets are  $R_t$  and  $R_b$ , and the power transmittivities of the facets are  $T_t$  and  $T_b$ .

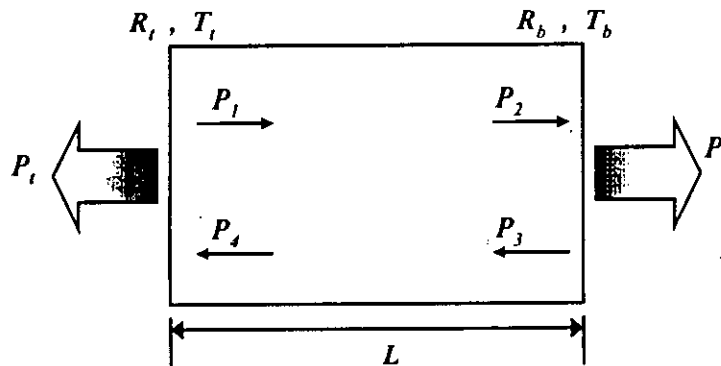


**Figure 3.21** Light intensities inside and outside the Laser cavity

Here, the arrows (as shown in the figure 3.21) indicate the propagation directions of the lights. Among the light intensities in a steady state, the following relationship can be written according to equation (rm)(tm)and (R)

$$P_1 = R_t P_4 \quad (3.51)$$

$$P_2 = e^{gL} P_1 \quad (3.52)$$

$$P_3 = R_b P_2 \quad (3.53)$$

$$P_4 = e^{gL} P_3 \quad (3.54)$$

$$P_t = T_t P_4 \quad (3.54)$$

$$P_b = T_b P_2 \quad (3.55)$$

Here,  $g$  is the optical power gain coefficient and  $L$  is the cavity length. The equations from (3.51) to (3.55) can be rearranged as

$$\frac{P_t}{P_b} = \frac{T_t P_4}{T_b P_2} \quad (3.56)$$

$$\frac{P_4}{P_2} = \frac{P_3}{P_1} \quad (3.57)$$

$$\frac{P_3}{P_1} = \frac{R_b P_2}{R_t P_4} \quad (3.58)$$

Therefore  $\frac{P_4}{P_2} = \frac{\sqrt{R_b}}{\sqrt{R_t}}$  (3.59)

Finally  $\frac{P_t}{P_b} = \frac{T_t \sqrt{R_b}}{T_b \sqrt{R_t}}$  (3.60)

Substituting total power output  $P = P_t + P_b$  into the equation (3.60) one can write

$$P_t = \frac{T_t \sqrt{R_b}}{T_t \sqrt{R_b} + T_b \sqrt{R_t}} P \text{ and } P_b = \frac{T_b \sqrt{R_t}}{T_t \sqrt{R_b} + T_b \sqrt{R_t}} P \quad (3.61)$$

Hence, by comparing the equation (3.61) with the equation (3.49), the external differential quantum efficiencies  $\eta_{dt}$  and  $\eta_{db}$  for each light output are written as

$$\eta_{d,t} = \frac{T_t \sqrt{R_b}}{T_t \sqrt{R_b} + T_b \sqrt{R_t}} \eta_d \text{ and } \eta_{d,b} = \frac{T_b \sqrt{R_t}}{T_t \sqrt{R_b} + T_b \sqrt{R_t}} \eta_d \quad (3.62)$$

where  $\eta_d$  is the external differential quantum efficiency for the total light output. When the optical losses at the facets are negligible, we have  $T_1 = 1 - R_1$  and  $T_2 = 1 - R_2$ .

Hence, above threshold current  $I_{th}$ , top and bottom light output powers  $P_t$  and  $P_b$  linearly increase with driving current  $I$  as

$$P_{t,b} = \eta_t \eta_{d,t} \frac{\hbar \omega}{q} (I - I_{th}) \quad (3.63)$$

Conversion efficiency  $\eta_c$  for emission through the top or bottom mirror is defined as the ratio of coherent light output power and electrical input power

105832

8



$$\eta_{cl,b} = \frac{P_{l,b}}{VI} \quad (3.64)$$

where  $V$  is the voltage applied across the VCSEL. In an ideal device, the current-voltage characteristics can be approximated as

$$V \approx V_k + R_s I \quad (3.65)$$

where  $R_s = dV/dI$  denotes the differential series resistance, and the kink voltage  $V_k$  is related to the separation of the quasi-Fermi energies but can be approximated by  $V_k \approx \hbar\omega/q$ . Non-perfect grading of heterointerfaces induces a larger voltage offset accompanied by a pronounced curvature of the  $I$ - $V$  characteristics. Combining (3.62), (3.64) and (3.65) leads to

$$\eta_{cl,b} = \eta_{di,b} \eta_i \frac{\hbar\omega}{q} \frac{I - I_{th}}{IV_k - I^2 R_s} \quad (3.66)$$

showing that for  $I \gg I_{th}$  the series resistance is responsible for the decrease of  $\eta_{cl,b}$  with increasing current.

### 3.13 Summary

With necessary diagrams, the construction of a VCSEL is presented at the beginning of this chapter. A comparison of the operating parameters of VCSEL and the same of the Edge Emitting lasers has been presented next. The construction and working principle of a Distributed Bragg Reflector (DBR) stacks has been presented. The variety of refractive index with wavelength of different materials such as AlAs, GaAs and AlGaAs has been presented. The computation of reflectivity spectrum of a DBR stacks using Transfer Matrix Method (TMM) has been presented. Same computation for a VCSEL has been presented. Variation of the reflectivity of a DBR mirror with the number of pairs of the DBR layers has also been presented. Next, the electric field distribution inside a VCSEL has been computed using the TMM. Confinement factor of a VCSEL has been presented in details. In the last section, radiation efficiency, conversion efficiency and the output power from the two facet of a VCSEL have been presented in the form of equation.

## Chapter 4

### Rate Equation Based VCSEL model

#### 4.1 Introduction

The rate equations of a semiconductor laser represent the rate of change of carrier density with time and also the rate of change of photon density with material gain and carrier density. Three equations are necessary to obtain the variation of carrier density, photon density and the photon phase against time. In this chapter the equations which will represent the variation of carrier density and photon density inside a semiconductor laser will be written and analyzed for conventional as well as for Vertical Cavity Surface Emitting Laser (VCSEL).

#### 4.2 Rate Equations of a Semiconductor Laser

Let consider that,  $J$  is the injection current density in a semiconductor laser. This means that the electric current flowing through a unit area of the laser. In such a laser  $q$  is the electronic charge,  $d$  is thickness of the active layer of a semiconductor laser,  $G(N)$  is the amplification rate due to the stimulated emission,  $\tau_s$  is the carrier lifetime,  $\tau_{ph}$  is the photon lifetime,  $\beta_{sp}$  is the spontaneous emission coupling factor, and  $\tau_r$  is the radiative recombination lifetime due to the spontaneous emission.

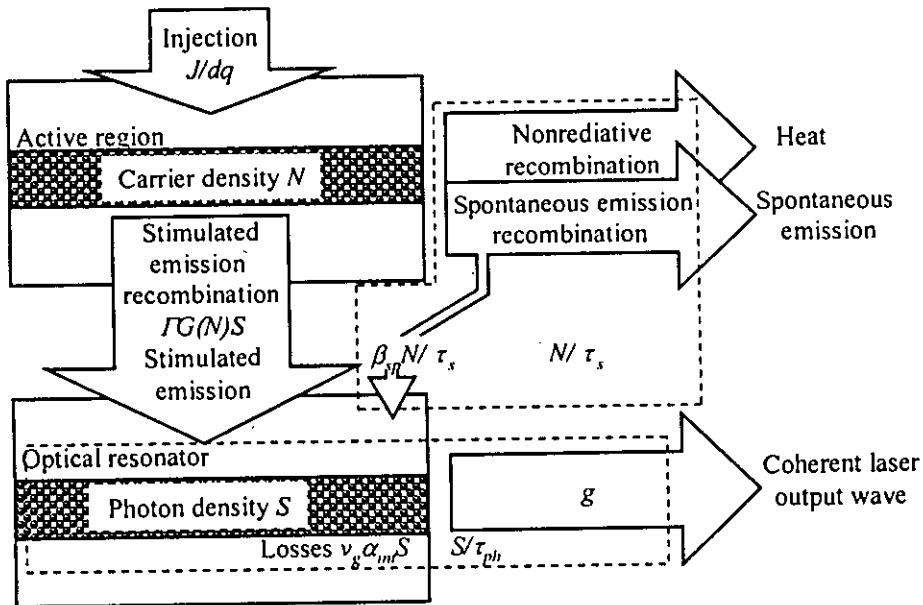


**Figure 4.1** Diagram of the rate equations for a semiconductor laser

The different types of electron-hole recombination, photon absorption and photon emission which are take place in a semiconductor laser are shown in figure 4.1. This figure actually represents the processes introduced during the operation of a semiconductor laser.

### 4.3 Rate Equation for Carrier Density

The equivalent equation of the rate of change of electron density  $N$  within the active region of a semiconductor laser can be written as [28].

$$\frac{dN}{dt} = -\Gamma G(N)S - \frac{N}{\tau_s} + \frac{J}{dq} \quad (4.1)$$

Here, the first term  $(-\Gamma G(N)S)$  of the right hand side of equation (4.1) is the rate of removal of electrons from the active region caused by stimulated recombination associated with the material optical gain. It is directly proportional to the photon density  $S$ . The second term  $(N/\tau_s)$  gives the net spontaneous recombination or decay rate of carrier concentration with carrier life time  $\tau_s$ . The final term  $(J/dq)$  represents the rate of electrons pushed into the conduction band within the active region.

### 4.4 Rate Equation for Photon Density

The equivalent equation of the rate of change of photon density  $S$  within the active region of a semiconductor laser can be written as [28]

$$\frac{dS}{dt} = \Gamma G(N)S - \frac{S}{\tau_{ph}} + \frac{\beta_{sp} N}{\tau_r} \quad (4.2)$$

Here, the first term  $(\Gamma G(N)S)$  of equation (4.2) shows an increased rate of the photon density  $S$  due to the stimulated emission. The second term  $(-S/\tau_{ph})$  is a decreased rate of the photon density inside the optical cavity due to the absorption and light emission toward the outside of the optical cavity. The final term  $(\beta_{sp} N/\tau_r)$  represents a coupling rate of spontaneously emitted photons to the lasing mode, which is a resonance mode of the cavity.

### 4.5 Rate Equation for the Optical Phase

Equation (4.2) is appropriate for describing the temporal variation in the optical intensity, however it is not possible to obtain the phase of the optical field using this equation. In order to carry out the analysis on the laser characteristics related to the optical phase, another equation is required for describing the time variation in the phase. For the analysis of optical feedback from any external reflector it is necessary to know the photon phase. It is well known that the optical field  $E$  in semiconductor laser can be written as  $E(r,t) = E(r) \exp(-i\omega t) E(t)$ . Now considering  $E(t)$  as a complex function, let  $\phi(t)$  be the phase. Then one can write  $E(t) = |E(t)| \exp[-i\phi(t)]$ . The instantaneous frequency of  $E$  is given by

$$\omega(t) = \omega + \delta\omega(t) \quad (4.3)$$

$$\text{where, } \delta\omega(t) = \frac{d\phi(t)}{dt} \quad (4.4)$$

Under the circumstances follows [28], the laser oscillation frequency  $\omega$  can be found from the following equation

$$2L \left( \beta(\omega) + \frac{\Gamma \omega}{c} \Delta n \right) = 2m\pi \quad (4.5)$$

Here,  $L$  is the length of the laser,  $\beta$  is the complex propagation constant,  $c$  is the velocity of light and  $\Delta n$  is the refractive index change. Generally  $\Delta n$  varies with time and accordingly  $\omega$  determined by the above equation also varies with time. Let  $\omega_{th}$  and  $\Delta n_{th}$  be the values of  $\omega$  and  $\Delta n$  respectively at threshold, and put  $\omega(t) = \omega_{th} + \delta\omega_{th}$  and  $\Delta n = \Delta n_{th} + \delta\Delta n_{th}$ , then from the above equations the following equations may be obtained.

$$\beta(\omega_{th}) + \frac{\Gamma \omega_{th}}{c} \Delta n_{th} = \frac{2m\pi}{2L} \quad (4.6)$$

$$\delta\omega = -\frac{\Gamma \omega_{th}}{c} \frac{\delta n}{\partial \beta / \partial \omega} = -\frac{\Gamma \omega_{th}}{n_g} \delta n \quad (4.7)$$

where,  $n_g$  is the group refractive index for the guided mode and use has been made of a relation  $1/(\partial \beta / \partial \omega) = v_g = c/n_g$ . Now, from equation (4.4) and (4.7) one can write the rate of change of phase as

$$\frac{d\phi}{dt} = -\frac{\Gamma \omega}{n_g} \delta n \quad (4.8)$$

The refractive index change  $\delta n$  is correlated with the gain change  $\delta G = G(N) - G_{th}$  through the Kramers–Kronig relation [28], and the index change is proportional to the gain change. Using the antiguiding factor  $\alpha_c$ , defined by [ratio of susceptibility],  $\delta n$  can be written as [28].

$$\delta n = -\frac{\alpha_c c}{2\omega} \frac{\delta G(N)}{v_g} = -\frac{\alpha_c n_g}{2\omega} \delta G(N) = -\frac{\alpha_c n_g}{2\omega} \left( G(N) - \frac{1}{\Gamma \tau_{ph}} \right) \quad (4.9)$$

Therefore, equation (4.8) can be written as

$$\frac{d\phi}{dt} = \frac{a_c}{2} \left( \Gamma G(N) - \frac{1}{\tau_{ph}} \right) \quad (4.10)$$

It is necessary to explain  $G(N)$ , carrier lifetime  $\tau_n$ , photon lifetime  $\tau_{ph}$ , and spontaneous emission coupling factor  $\beta_{sp}$  in more detail. With the transparent carrier concentration  $N_0$ , in which a material is transparent, material power gain per unit time  $G(N)$  can be expressed as

$$G(N) = g_0 (N - N_0) \text{ for a device with bulk active region}$$

$$G(N) = g_0 \ln \left( \frac{N}{N_0} \right) \text{ for a device with quantum well active region.}$$

where,  $g_0$  is the differential optical gain or gain slope.

Carrier lifetime  $\tau_s$  is related with the radiative recombination lifetime  $\tau_r$  and nonradiative recombination lifetime  $\tau_{nr}$  by the relation

$$\frac{1}{\tau_s} = \frac{1}{\tau_r} + \frac{1}{\tau_{nr}} \quad (4.11)$$

The radiative recombination lifetime  $\tau_r$  is determined by the spontaneous emission and is not affected by the stimulated emission. The nonradiative recombination lifetime  $\tau_{nr}$  is related to the recombinations of the injected carriers and the defects or the impurities, which do not emit lights.

The photon lifetime  $\tau_{ph}$  is the time during which the photons stay in the optical cavity; it is expressed as

$$\frac{1}{\tau_{ph}} = \frac{c}{n_{gr}} \left( \alpha_i + \frac{1}{L} \ln \frac{1}{\sqrt{R_1 R_2}} \right) \quad (4.12)$$

Here,  $c$  is the velocity of light in the free space,  $n_{gr}$  is the group refractive index of the material,  $\alpha_i$  is the intrinsic loss of the material,  $R_1$  and  $R_2$  is the reflectivity of the mirrors.

The spontaneous emission coupling factor  $\beta_{sp}$  is defined as the ratio of spontaneous emission coupling rate to the lasing mode to the total spontaneous emission rate. [27]

$$\beta_{sp} = \frac{\Gamma \lambda^4}{4\pi^2 n_{gr}^3 V \Delta \lambda} \quad (4.13)$$

where  $\Gamma$  is the optical confinement factor of the active layer and  $\Delta \lambda$  is the FWHM of the spontaneous emission spectrum in units of wavelength. From equation (4.13), it is found that the spontaneous emission coupling factor  $\beta_{sp}$  increases with a decrease in the volume  $V_a$  of the active region and the spectral linewidth  $\Delta \lambda$ .

## 4.6 Threshold Current Density and Threshold Carrier Density of a Semiconductor Laser

The rate equations of a semiconductor laser can be graphically represented as shown in the figure 4.1 [28]. To determine the threshold current density and threshold carrier density, rate equations for carrier density and photon density can be approximated by considering  $\tau_s \approx \tau_r$  as [27]

$$\frac{dN}{dt} = -\Gamma G(N)S - \frac{N}{\tau_s} + \frac{J}{dq} \quad (4.14)$$

$$\frac{dS}{dt} = \Gamma G(N)S - \frac{S}{\tau_{ph}} + \frac{\beta_{sp} N}{\tau_s} \quad (4.15)$$

Bellow threshold, the stimulated emission is negligible and  $S$  can be considered to negligibly small. At steady state, equation (4.14) can be written as

$$0 = -\frac{N}{\tau_s} + \frac{J}{dq} \text{ or } N = \frac{J}{dq} \tau_s, \text{ and } S \approx 0 \quad (4.16)$$

It is seen from equation (4.16) that the carrier density  $N$  is increased with the increase in current  $J$ . Threshold carrier  $N_{th}$  density is defined as the value of carrier density at which lasing starts. The current density which is required to attain this  $N_{th}$  is called threshold current density  $J_{th}$ . From equation (4.16) the threshold current density can be written as

$$J_{th} = \frac{dq}{\tau_s} N_{th} \quad (4.17)$$

From equation (4.17), it is found that a small  $N_{th}$  and a long  $\tau_n$  lead to a low  $J_{th}$ . Because the optical confinement factor  $\Gamma$  of the active layer depends on the active layer thickness  $d$ , the threshold current density  $J_{th}$  is a function of  $d$  and there exists an optimum  $d$  value to achieve the lowest  $J_{th}$ .

The threshold carrier density  $N_{th}$  can be calculated by using the rate equations above the threshold. In usual semiconductor lasers, the spontaneous emission coupling factor  $\beta_{sp}$  is on the order of  $10^{-5}$ . Therefore, as the first approximation, the term  $\beta_{sp}N/\tau_s$  of equation (4.15) can be neglected. Because (4.15) is valid for any  $S$  value in a steady state, so one can write

$$\Gamma G(N) = \frac{1}{\tau_{ph}} = \Gamma g_0 (N - N_0) \quad (4.18)$$

$$N = N_0 + \frac{1}{\Gamma g_0 \tau_{ph}} \quad (4.19)$$

The threshold carrier density  $N_{th}$  can be written as

$$N_{th} = N_0 + \frac{1}{\Gamma g_0 \tau_{ph}} \quad (4.20)$$

In semiconductor lasers, changes in the cavity length, the facet reflectivities, and the refractive indexes during laser operation are small, and the right hand sides of (4.19) and (4.20) are considered to be constant. Therefore, above the threshold, the carrier density  $N$  is clamped on the threshold carrier density  $N_{th}$ .

Finally from equation (4.17) and (4.20), the threshold current density can be written as

$$J_{th} = \frac{dq}{\tau_s} N_{th} = \frac{dq}{\tau_s} \left( N_0 + \frac{1}{\Gamma g_0 \tau_{ph}} \right) \quad (4.21)$$

The expression for the threshold current density in equation (4.21) shows that attainment of a low threshold requires an active layer of small carrier density  $N_0$  at transparency and a large differential gain coefficient  $g_0$ . From this viewpoint, quantum well structures are advantageous compared with bulk DHs.

## 4.7 Current versus Light Output of a Semiconductor Laser

When the spontaneous emission coupling factor  $\beta_{sp}$  is small, coupling of the spontaneous emission to the lasing mode can be neglected. Below the threshold, with an increase in  $J$ , the carrier density  $N$  increases according to (4.17), but the photon density  $S$  is 0. Above the threshold,  $N$  does not increase any more and remains at the threshold carrier density  $N_{th}$ , while  $S$  drastically increases with  $J$ , because the excess carriers ( $N - N_{th}$ ) are converted to photons.

From (4.14), the steady-state photon density  $S$  above the threshold is obtained as

$$S = \frac{1}{\Gamma G(N)} \left( \frac{J}{dq} - \frac{N_{th}}{\tau_s} \right) \quad (4.22)$$

Substituting (4.17) and (4.18) into (4.22) results in

$$S = \frac{\tau_{ph}}{dq} (J - J_{th}) \quad (4.23)$$

In summary, dependence of the carrier density  $N$  and the photon density  $S$  on the injection current density  $J$  is expressed as

For  $J < J_{th}$

$$N = \frac{J}{dq} \tau_s \text{ and } S=0 \quad (4.24)$$

For  $J > J_{th}$

$$N = \frac{J_{th}}{dq} \tau_s \text{ and } S = \frac{\tau_{ph}}{dq} (J - J_{th}) \quad (4.25)$$

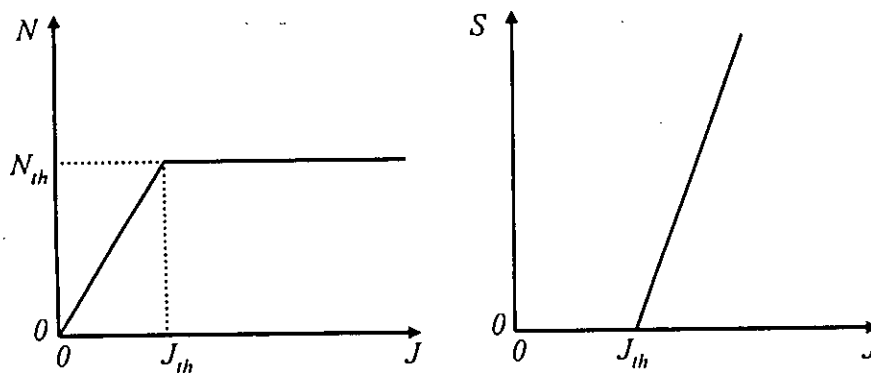


**Figure 4.2** Carrier density  $N$  and photon density  $S$  when coupling of the spontaneous emission to the lasing mode is neglected

In a steady state, when the coupling of the spontaneous emission to the lasing mode is included, (4.14) and (4.15) can be written as

$$\frac{J}{dq} = \Gamma G(N)S + \frac{N}{\tau_s} \quad (4.26)$$

$$\frac{S}{\tau_{ph}} = \Gamma G(N)S + \frac{\beta_{sp} N}{\tau_s} \quad (4.27)$$

Now, putting the value of  $G(N)$  from equation (4.8) into the equation (4.26) and (4.27) the carrier density  $N$  and the photon density  $S$  are given by

$$N = \frac{N_{th}}{2(1-\beta_{sp})} (A - \sqrt{A^2 - B}) \quad (4.28)$$

$$S = \frac{\beta_{sp}}{\Gamma g_0 \tau_s} \frac{A - \sqrt{A^2 - B}}{2(1-\beta_{sp}) - (A - \sqrt{A^2 - B})} \quad (4.29)$$

where,

$$A = 1 + \frac{J}{J_{th}} - \beta_{sp} \frac{N_0}{N_{th}} \quad \text{and} \quad B = 4(1-\beta_{sp}) \frac{J}{J_{th}} \quad (4.30)$$

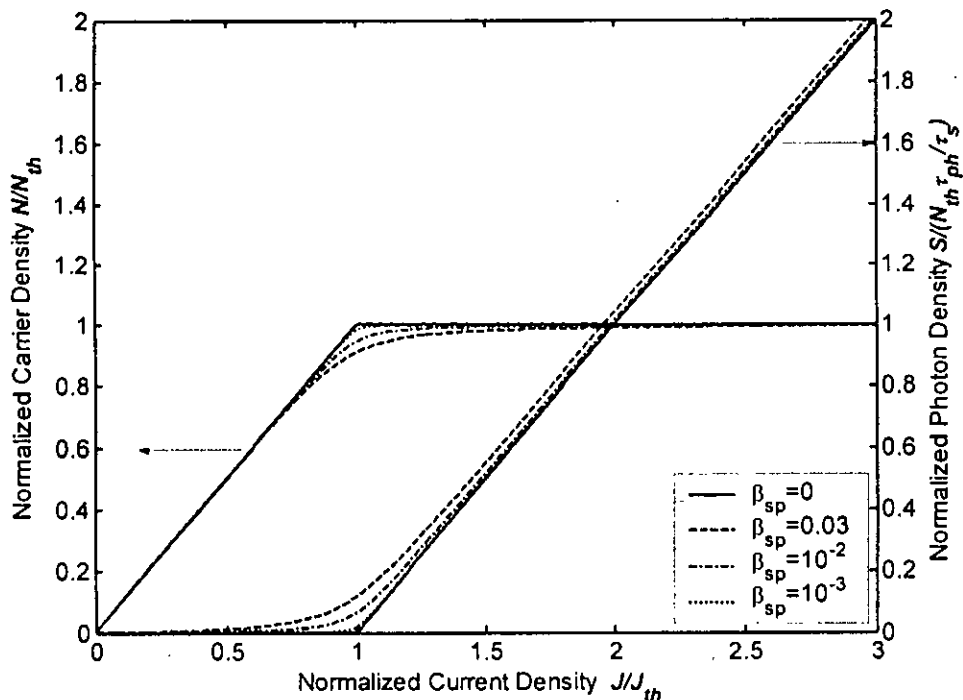


**Figure 4.3** Dependences of the carrier density and photon density on the injection current density.

The dependences of the carrier density and the photon density on the injection current density are plotted in Figure.4.3 using normalized variables where solid and broken lines correspond to  $\beta_{sp} =$



0 and  $\beta_{sp} > 0$ . The result shows that, with a large contribution of the spontaneous emission represented by a large  $\beta_{sp}$ .

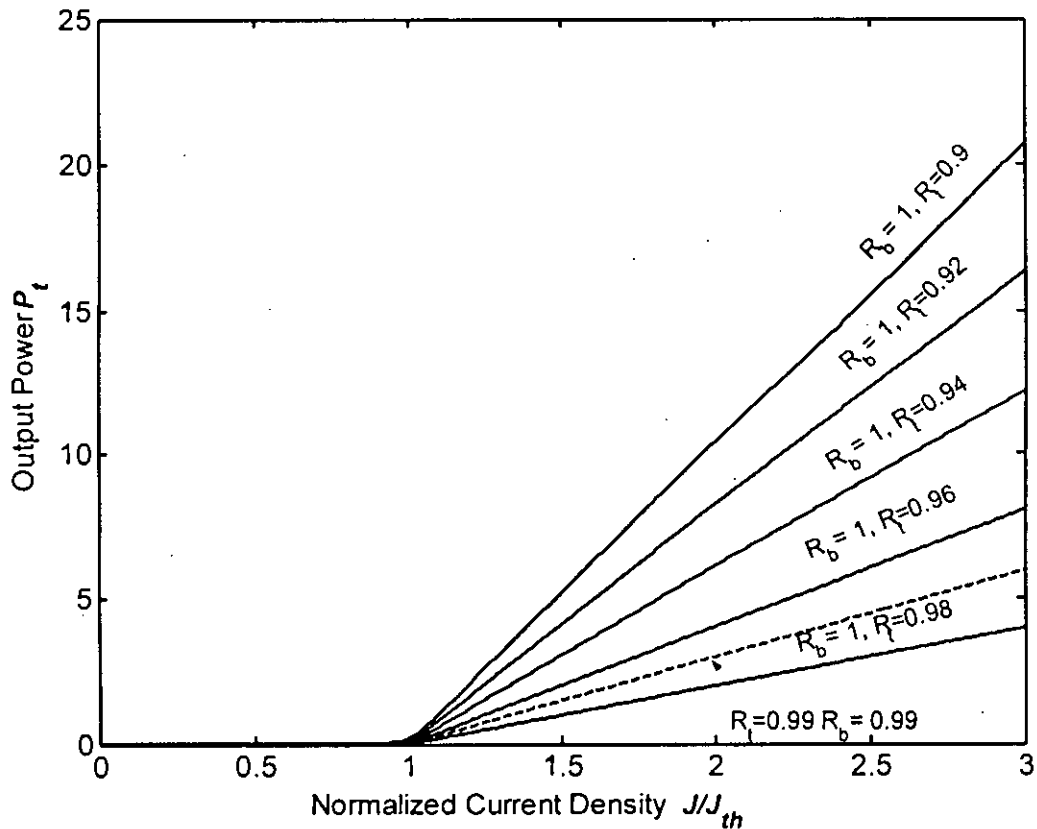


**Figure 4.4** Output optical power versus injection current density depending on the facet mirror reflectivity.

Since the optical field in the resonator can be expressed  $E(\mathbf{r}, t) = E(\mathbf{r}) \exp(-i\omega t) E(t)$ . Using the normalized mode function  $E(\mathbf{r})$ , the stored optical energy in the resonator is given by  $|E(t)|^2 = h\omega V_\omega S / 2\pi$  with the photon density  $S$  [28]. On the other hand, the value of the power output from the top and bottom mirror can be determined by using the equation (3.61). Power output from the top mirror for different values of mirror reflectivity is plotted in the figure 4.4.

The laser output power starts to increase at values of  $N$  smaller than the threshold value  $N_{th}$  given by Equation (4.21), and as a result the bend in the graph for the output power versus the injection current density at the threshold is rounded. A semilogarithmic plot of the injection current density dependence of the output power (photon density) is shown in Figure.4.5. The graph shows that the output power changes by several orders of magnitude depending on  $\beta_{sp}$  in the vicinity of the threshold.

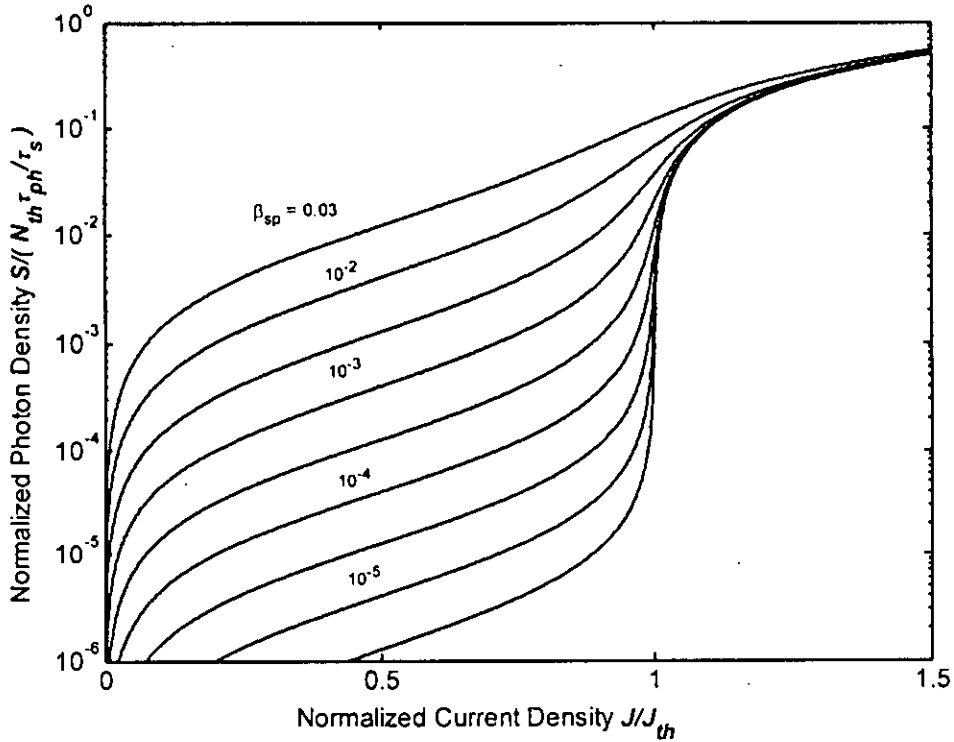


**Figure 4.5** Photon density versus injection current density depending on the spontaneous emission coupling coefficient

## 4.8 Rate Equations of a VCSEL

Construction of the cavity of a VCSEL is different from a Fabry-Perot laser or edge emitting laser. The cavity of a VCSEL contains of several quantum wells separated by barrier layers and two spacer layers are placed at the end of the cavity. The construction of the cavity of a VCSEL is shown in the figure 4.6. Many researchers have been deduced the rate equations of a VCSEL in different ways. Rate equation for Carrier density of a VCSEL is described by a single equation [21], or two different equations [38,39]. In two level model, where the rate equation for carrier density is described by two different equations is more accurate than single rate equation for carrier density. In two level model, one equation describe the carrier density in the barrier region while the other describe the carrier density in the quantum well.

The active region of the VCSEL shown in the figure 4.6 contains of three quantum wells of thickness  $d$ . The length of the carrier confinement region is  $l_c$  and the effective length of the VCSEL is  $L_{eff}$ . An external current source provides the barriers of volume  $V_b = A_{act} (l_c - d)$  with current  $I$ . The rate of change of the electrons density  $N_b$  in these barriers is given by

$$\frac{dN_b}{dt} = \frac{I}{qV_b} + \frac{N_w V_w}{\tau_c V_b} - \frac{N_b}{\tau_s} - \frac{N_b}{\tau_{sp,b}} \quad (4.31)$$

The different terms in the right hand side of this equation represent respectively the external electron density from the current source ( $I / qV_a$ ), the escape of carriers from the wells of volume  $V_w = A_{act} d$  and of electron density  $N_w$  into the barriers with  $\tau_c$ , the carriers diffusion into undoped potential wells with a transport time  $\tau_s$ , and finally the removed carriers from the barriers by

spontaneous emission with time constant  $\tau_{sp,b}$ . Carriers captured in the well can take part in emission and absorption transitions. Spontaneous emission is characterized by introducing the carrier lifetime  $\tau_{sp,w}$ .

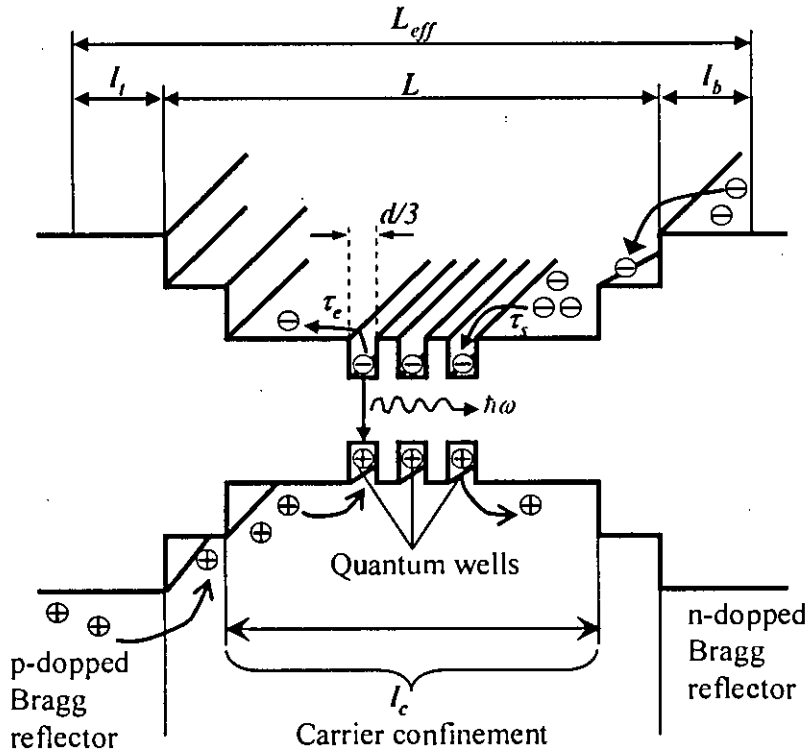


**Figure 4.6** Schematic representation of a VCSEL active region, indicating electron injection into barriers as well as diffusion into and escape from the quantum wells.

Stimulated emission processes depend on the modal material gain coefficient  $G(N_w)$  and the photon density  $S$  in the mode under consideration. Since the position of the quantum wells relative to the standing wave pattern in the cavity is very important as has been mentioned in Sect. 3.10, the relative confinement factor  $\Gamma_r$  has to be considered in the stimulated emission processes.

Hence the rate equation for the electron density in the quantum well is written as

$$\frac{dN_w}{dt} = \frac{N_h V_h}{\tau_s V_w} - \frac{N_w}{\tau_c} - \frac{N_w}{\tau_{sp,w}} - \frac{\Gamma_r v_{gr} G(N_w) S}{1 + \epsilon S} \quad (4.32)$$

Here,  $v_{gr}$  is the group velocity. The material power gain  $G(N_w) = g_0 \ln(N_w/N_{t,w})$  per unit time is discussed in section 4.5.  $N_{t,w}$  is the transparency carrier density of quantum well and at lasing condition  $N_w > N_{t,w}$ . Gain compression due to effects like carrier leakage by heating, or spatial hole burning by photons is accounted by the denominator  $(1 + \epsilon S)$ . The gain compression parameter  $\epsilon$  is estimated as

$$\epsilon = \frac{\lambda^2 c \tau_{int,ru}^2}{2\pi n^3 \tau_{sp,w}} \quad (4.33)$$

where,  $c$  is the velocity of light in the vacuum and  $\tau_{intra} \approx 100$  fs is the intraband relaxation time.

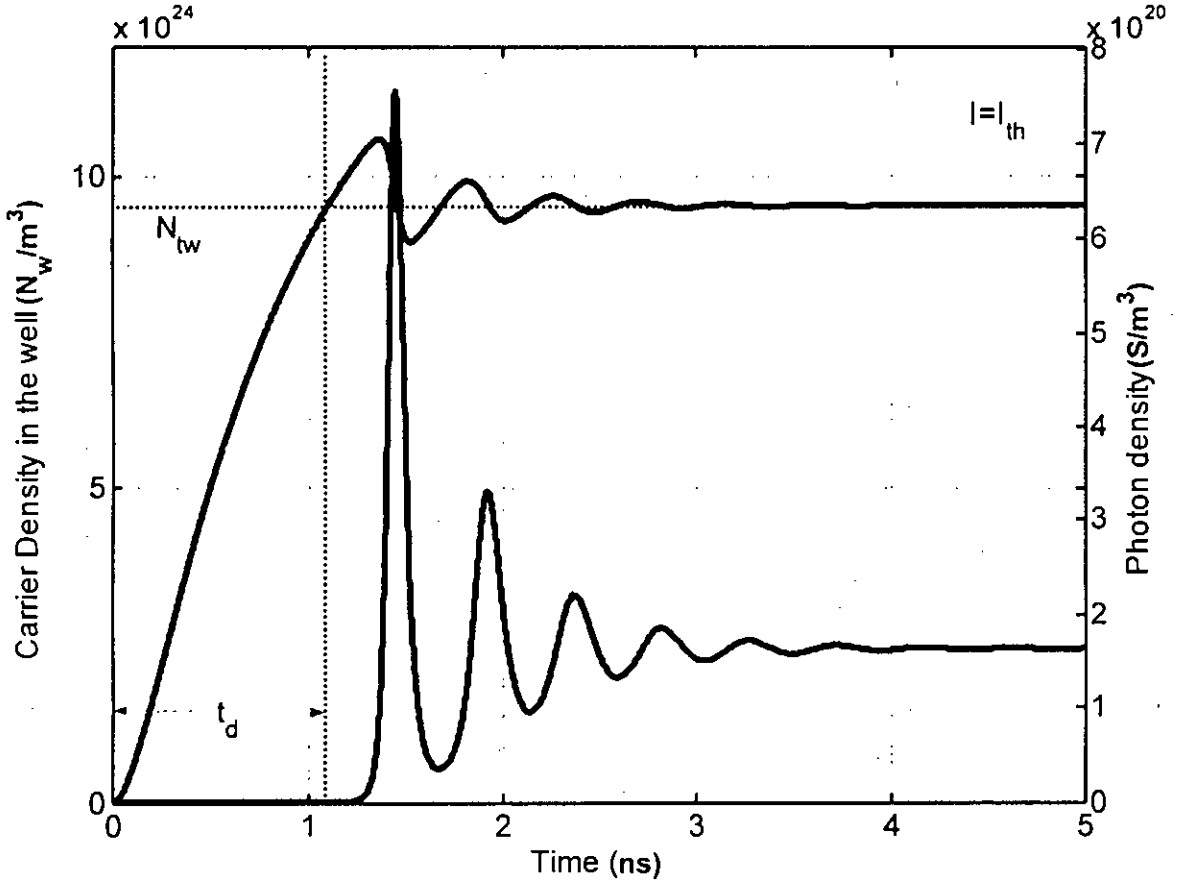


**Figure 4.7** Simulation results of the carrier density ( $N_w$ ) in the quantum well region and the photon density ( $S$ ) in the active region of a 980 nm VCSEL at an injection current  $I = 1.8I_{th}$ .

The rate equation for the photon density can be written as

$$\frac{dS}{dt} = \beta_{sp} \frac{V_w}{V_b} \frac{N_w}{\tau_{sp,w}} - \frac{S}{\tau_p} + \frac{V_w}{V_b} \frac{\Gamma_r v_{gr} G(N_w) S}{1 + \epsilon S} \quad (4.34)$$

cavity losses described by a photon lifetime  $\tau_p$  and stimulated as well as spontaneous emission are important. Furthermore, for density related equations the ratio of well volume  $V_w$  for interacting electrons and cavity volume  $V_p$  for interacting photons comes into play. This ratio is also important for the stimulated emission rate. The electron rate equations (4.31) and (4.32) as well as the photon rate equation (4.34) govern dynamics and noise of quantum well VCSELs.

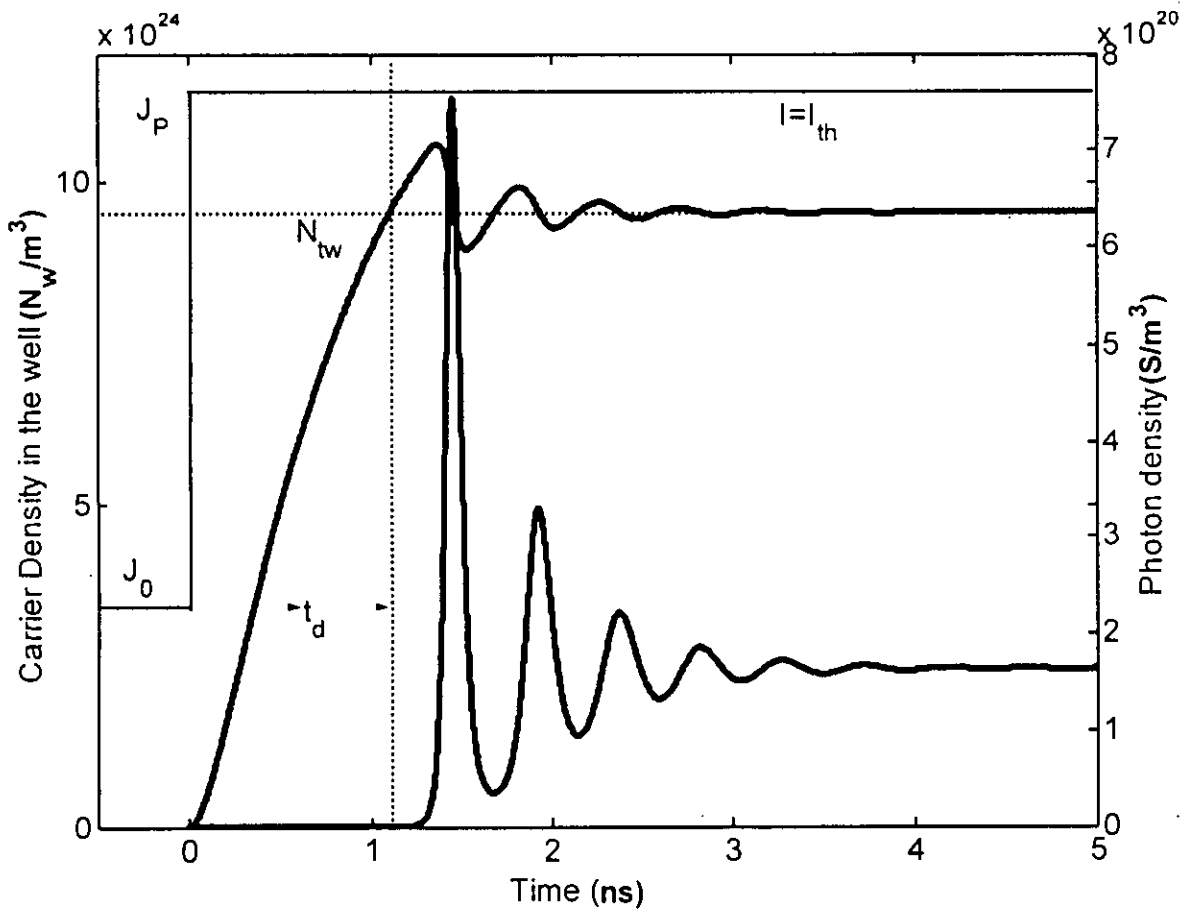


**Figure 4.8** Simulation results of the carrier density ( $N_w$ ) in the quantum well region and the photon density ( $S$ ) in the active region of a 980 nm VCSEL at an injection current  $I = 1.8 I_{th}$ . Step current pulse  $I_p = 1.8 I_{th}$  has been applied at the time  $t > 0$ . Laser oscillation starts after a time delay  $t_d$  called turn on delay. Carrier density in the quantum well region ( $N_w$ ) reaches to the transparent carrier density after the time  $t_d$ .

## 4.9 Calculation of Turn on delay of a VCSEL

Laser oscillation starts with a delay after the start of carrier injection (current application) as shown in the figure 4.7. This turn-on delay is undesirable phenomenon for applications of semiconductor lasers because the higher the turn on delay the lower the modulation speed of a laser. Turn on delay is the time required for carrier accumulation up to the threshold carrier density. The delay, however, can easily be avoided by giving a bias current close to the threshold. Then the extinction ratio of the modulated output may deteriorate. An appropriate bias level must be set in order to avoid substantially the delay and deterioration of the extinction ratio.

Assume that a step pulsed current is injected into a semiconductor laser. As shown in figure 4.8, a bias current density  $J_0$  is below the threshold current density  $J_{th}$ , and a pulsed current density  $J_p$  is injected to the semiconductor laser at time  $t = t_{on} = 0$ . Note that the pulse width is much larger than the carrier lifetime  $\tau_s$ . The carrier concentration  $N$  increases from the initial value  $N_0$  with a time constant  $\tau_s$  and reaches the threshold carrier concentration  $N_{th}$  at  $t = t_d$ , as shown in figure 4.8. This  $t_d$  is called the turn-on delay time, and at  $t = t_d$  laser oscillation starts. After the start of laser oscillation,

the carrier concentration  $N$  and the photon density  $S$  show relaxation oscillations, as shown in figure 4.8. The turn-on delay time  $t_d$  can be calculated by using the rate equation (4.14). For simplicity, coupling of the spontaneous emission to the lasing mode can be neglected. Therefore, when  $N < N_{th}$ , the photon density is  $S = 0$ . As a result, equation (4.14) has been reduced to

$$\frac{dN}{dt} = \frac{J}{dq} - \frac{N}{\tau_s} \quad (4.35)$$

$$J = J_p \cdot u(t) + J_0 \quad (4.36)$$

$$u(t) = \begin{cases} 0 & (t < 0) \\ 1 & (t \geq 0) \end{cases} \quad (4.37)$$

Putting the equation (4.36) into equation (4.35), equation (4.38) can be written as

$$\frac{dN}{dt} = \frac{J_p \cdot u(t) + J_0}{dq} - \frac{N}{\tau_s} \quad (4.38)$$

Laplace transformation of the equation (4.68) is done by considering a Laplace transform of the carrier density  $N(t)$  as  $N(s)$  and also considering the initial carrier density  $N(0) = N_0 = \tau_s J_0 / (qd)$ .

$$sN(s) - N(0) = \frac{J_p + J_0}{qd} \frac{1}{s} - \frac{1}{\tau_s} N(s) \quad (4.39)$$

$$sN(s) - \frac{\tau_s J_0}{qd} = \frac{J_p + J_0}{qd} \frac{1}{s} - \frac{1}{\tau_s} N(s) \quad (4.39)$$

Hence  $N(s)$  can be written as

$$N(s) = \left( \frac{1}{s} - \frac{1}{s + \frac{1}{\tau_s}} \right) \frac{(J_p + J_0)\tau_s}{qd} + \frac{1}{s + \frac{1}{\tau_s}} \frac{\tau_s J_0}{qd} \quad (4.40)$$

Now, taking the inverse Laplace transform of  $N(s)$  of equation (4.40)  $N(t)$  can be written as

$$N(t) = \frac{(J_p + J_0)\tau_s}{qd} u(t) - \frac{(J_p + J_0)\tau_s}{qd} e^{-t/\tau_s} + \frac{\tau_s J_0}{qd} e^{-t/\tau_s} \quad (4.41)$$

$$N(t) = \frac{(J_p + J_0)\tau_s}{qd} u(t) - \frac{J_p \tau_s}{qd} e^{-t/\tau_s} \quad (4.42)$$

The carrier density at  $t \geq 0$  can be found from the equation (4.42) by putting  $u(t)=1$  in to the equation (4.42)

$$N(t) = \frac{\tau_s J}{qd} - \frac{\tau_s J_p}{qd} e^{-t/\tau_s} \quad (4.43)$$

Here,  $J = J_p + J_0$ . The carrier density at  $t = t_d$  can be found from the equation (4.43) by putting  $t = t_d$  in to the equation (4.43)

$$N(t_d) = \frac{\tau_s J}{qd} - \frac{\tau_s J_p}{qd} e^{-t_d/\tau_s} \quad (4.44)$$

Turn on delay  $t_d$  has been defined as the time required to reach the carrier density to its threshold carrier density  $N_{th}$  i.e.  $N_{th} = N(t_d)$ . By using the equation (4.21), the threshold carrier density can be written as

$$N_{th} = \frac{\tau_s J_{th}}{qd} = N(t_d) \quad (4.45)$$

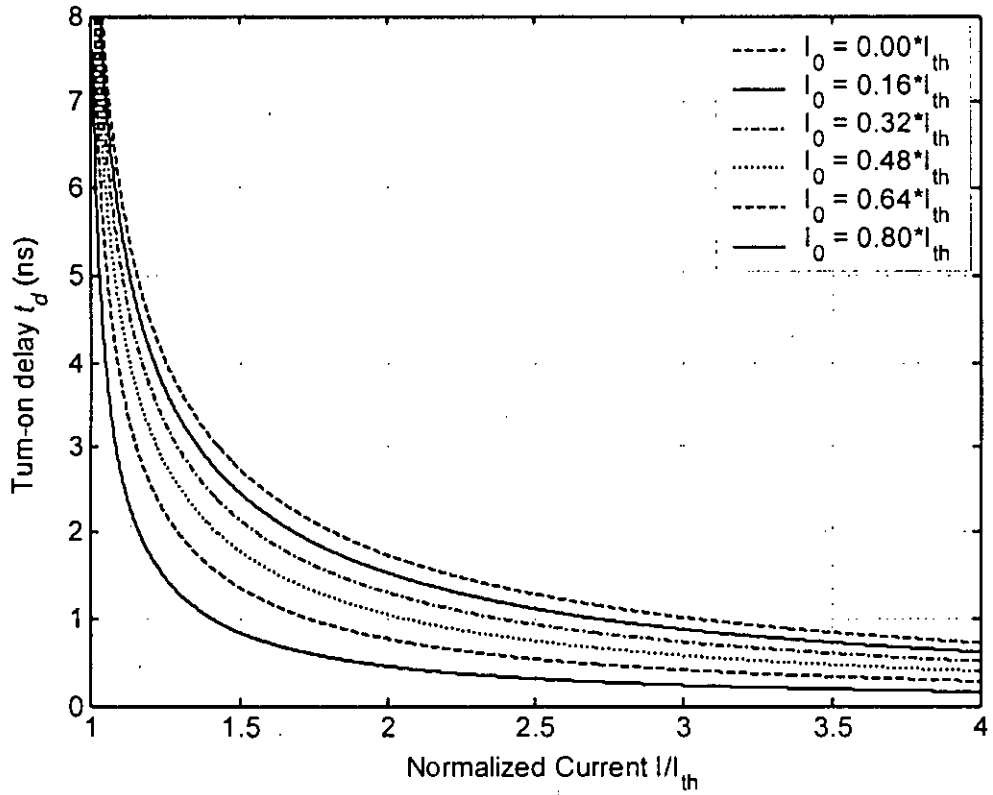
Now putting the value of  $N(t_d)$  in the equation (4.44), the turn-on delay  $t_d$  can be written as

$$t_d = \tau_s \ln \frac{J - J_0}{J - J_{th}} \quad (4.46)$$

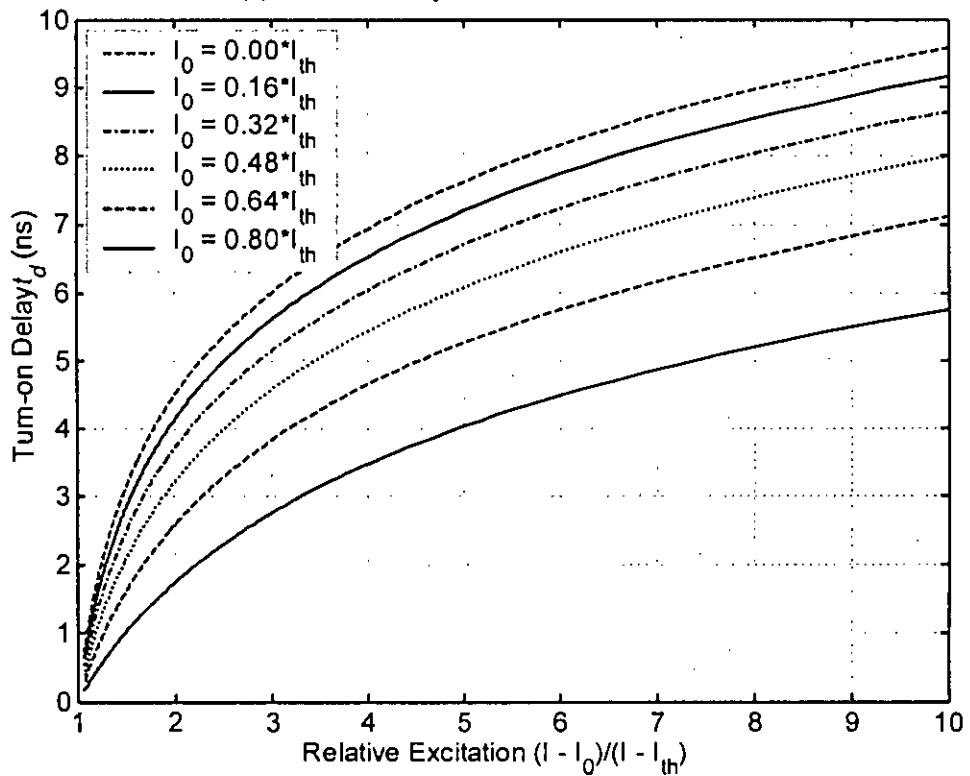
To generate high speed optical signals by modulating the injection current into the semiconductor lasers, the turn-on delay time  $t_d$  should be short. From equation (4.46), it is found that a large bias current density  $J_0$ , a low threshold current density  $J_{th}$ , and a short carrier lifetime  $\tau_s$  are suitable for high-speed modulations. From equation (4.46), turn-on delay  $t_d$  can be written in terms of injection current as

$$t_d = \tau_s \ln \frac{I - I_0}{I - I_{th}} \quad (4.47)$$

Turn on delay of a semiconductor laser has been computed by using the equation (4.47) for the different values of injection current and the results are plotted in the figure 4.9. Turn on delay versus normalized current ( $I/I_{th}$ ) has been plotted in the figure 4.9 (a). It is clear from the figure 4.9 (a) that turn on delay of the semiconductor laser can be reduced from excess over 8 ns to less than 1.8 ns if the injection current is made double from its threshold value. It is also noticeable that turn on delay of the semiconductor laser can be reduced to less than 500 ps by injecting the same current ( $2I_{th}$ ) if the initial injected current or initial bias current  $I_0$  is made nearly equal ( $0.8I_{th}$ ) to the threshold current. Reduction of turn on delay is very small if the injected current is made over 3 times of the threshold current. Figure 4.9 (b) shows the plot of turn on delay versus relative excitation  $(I - I_0) / (I - I_{th})$ . It clear from the figure that the turn on delay of a semiconductor laser can be reduced the nearly equal zero if the relative excitation of the laser can be made tends to unity.



(a) turn-on delay vs normalized current



(b) turn-on delay vs relative excitation

**Figure 4.9** Plot of turn on delay  $t_d$  with respect to different values of the injection current of a semiconductor laser.



The time delay  $t_d$  of a VCSEL can be obtained from the rate equation (4.31) and (4.32) as

$$t_d = \tau_{sp,w} \ln \frac{I - I_0}{I - I_{th}} \quad (4.48)$$

Here,  $\tau_{sp,w}$  is the carrier lifetime in the quantum well region. Equation (4.48) is identical with the equation (4.47) and it is clear that the turn on delay of a VCSEL is a function of the carrier lifetime in the quantum well. To understand the phenomena of the reduction of turn on delay, output power (discussed in the next section) of a VCSEL has been plotted in the figure 4.10 for two different values of injection current. At a value of injection current  $I = I_{th}$ , laser starts to oscillate at  $t = 1.2$  ns and when the injection current is set to  $I = 2I_{th}$  then the laser starts to oscillate at  $t = 0.6$  ns.

Turn on delay of a VCSEL for different values of injection current have been computed by using the equation (4.48) and plotted in to the figure 4.11 (dashed line). Same computations have been performed by solve the rate equations of the VCSEL by using the Finite Difference (FD) method. Results are also plotted in the figure 4.11 (solid line with asterisks). Turn on delay decreases with the increase of the injection current.

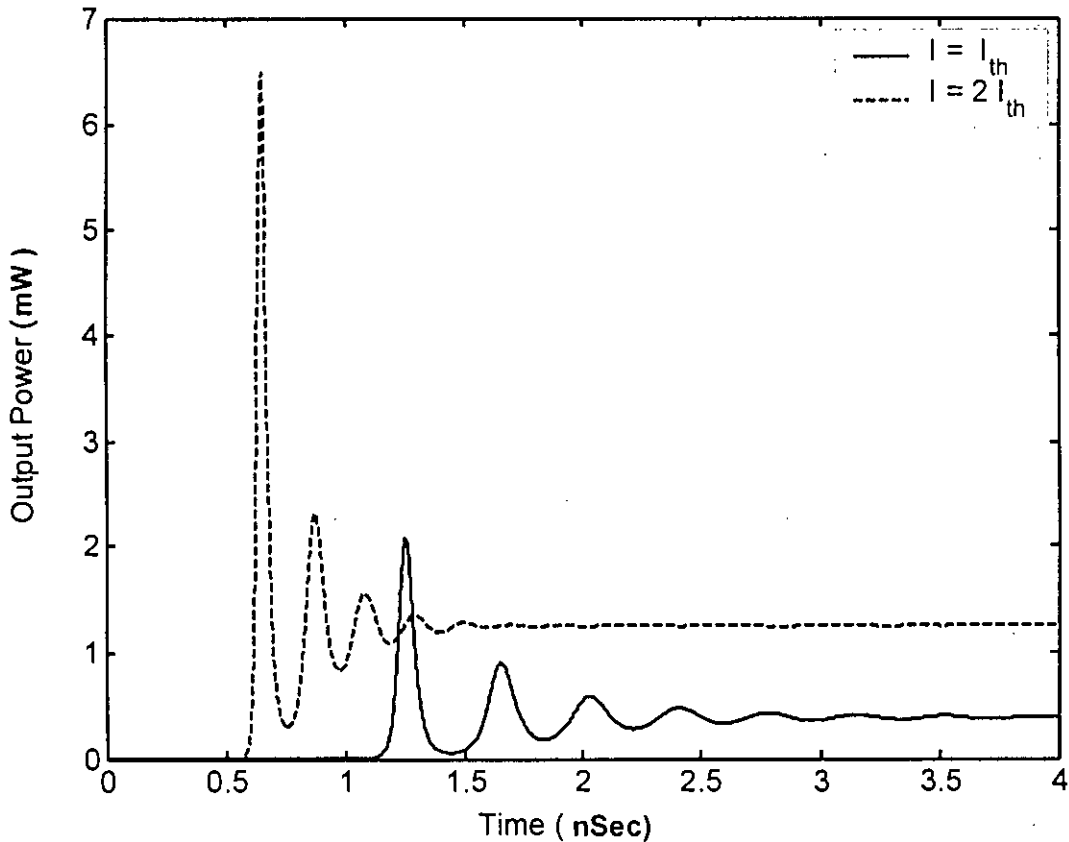


**Figure 4.10** Simulation results of output power from the top DBR of a 980 nm VCSEL at  $I = I_{th}$  (solid line) and at  $I = 2I_{th}$  (dashed line). Result shows that laser oscillation start earlier if the injection current is increased.

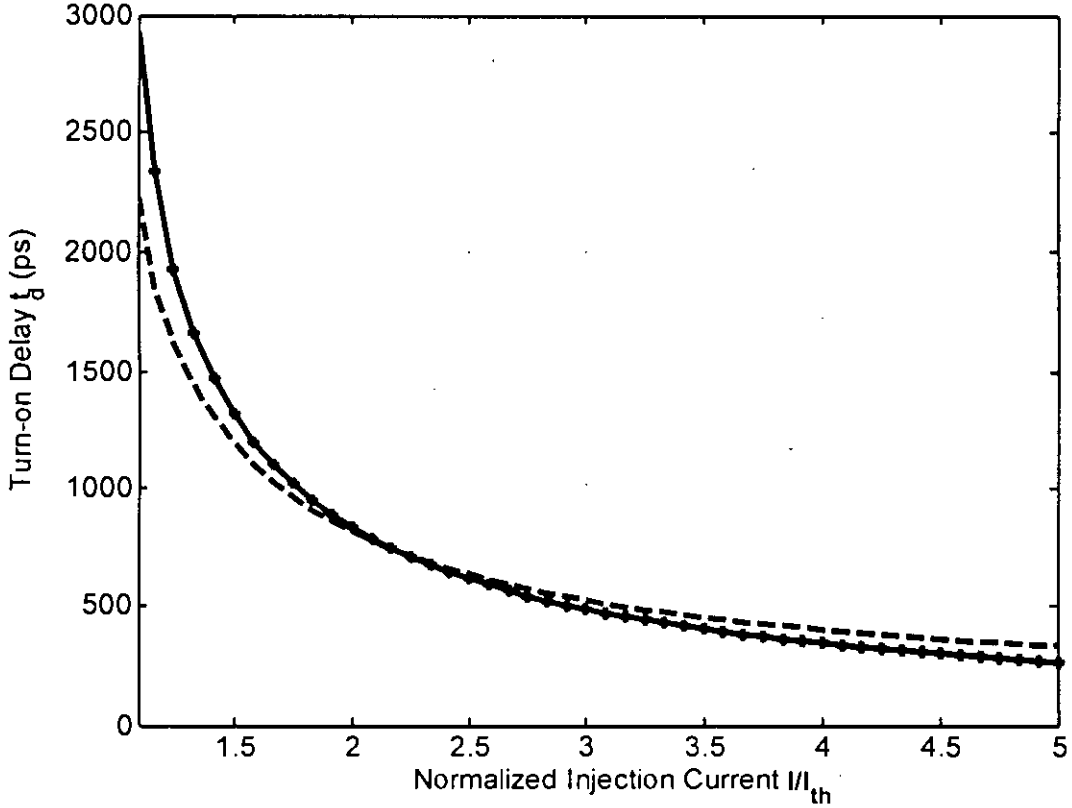


**Figure 4.11** Plot of turn on delay  $t_d$  with respect to different values of the injection current of a VCSEL. Dashed line is plotted by using the equation (4.48) where as the solid line with asterisks is plotted from the simulation result of the carrier densities for different values of injection current. Initial bias current  $I_0$  has been set to 0 mA.

## 4.10 Output Power of a VCSEL

Equation of output power of VCSEL in terms of injected current has been derived in the Section 3.12. In this section, output power of a VCSEL will be computed by solving the rate equations. Solution of the rate equations (4.31), (4.32) and (4.34) will give the carrier density in the barrier region, carrier density in the quantum well and the photon density in the active region. Output optical power from the top and bottom facet of a VCSEL is related with the photon number and can be written as [39]

$$P_{t,b}(t) = \eta_{dt,b} S(t) \frac{V_{act} hc}{\Gamma \tau_p \lambda_0} \quad (4.49)$$

where,  $S(t)$  is the photon density,  $V_{act}$  is the volume of the active layer,  $h$  is the Plank's constant,  $c$  is the velocity of light,  $\Gamma$  is the optical confinement factor,  $\tau_p$  is the photon lifetime,  $\lambda_0$  is the wavelength of the emitted light and  $\eta_{dt,b}$  is the external differential quantum efficiency of the top facet and bottom facet respectively. Total power output  $P_{tot}(t)$  from a VCSEL will be the summation of the power output from the top  $P_t(t)$  and bottom facet  $P_b(t)$ .

$$P_{tot}(t) = P_t(t) + P_b(t) \quad (4.50)$$

Now, the rate equations (4.31), (4.32) and (4.33) have been solved simultaneously by using the Finite Difference method to get the photon density. Output power has been computed by using the equation (4.49) and plotted into the figure 4.10.

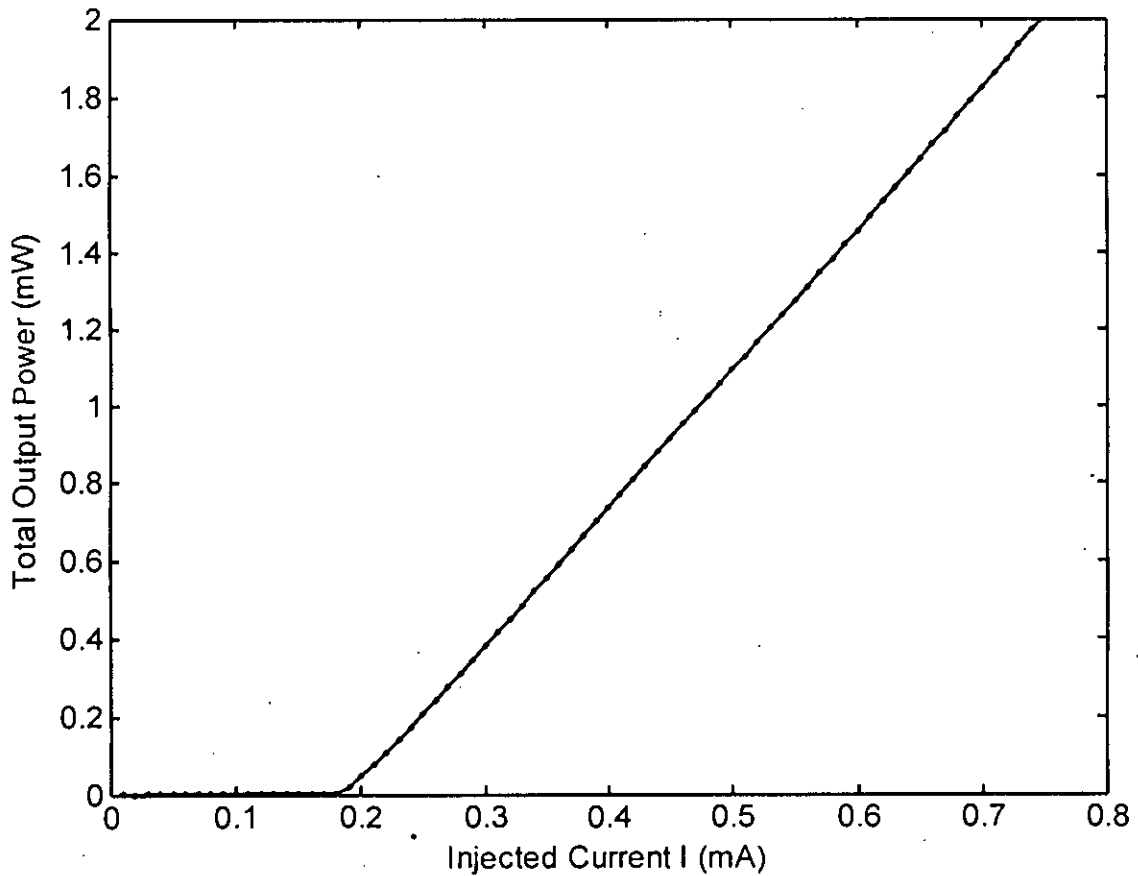
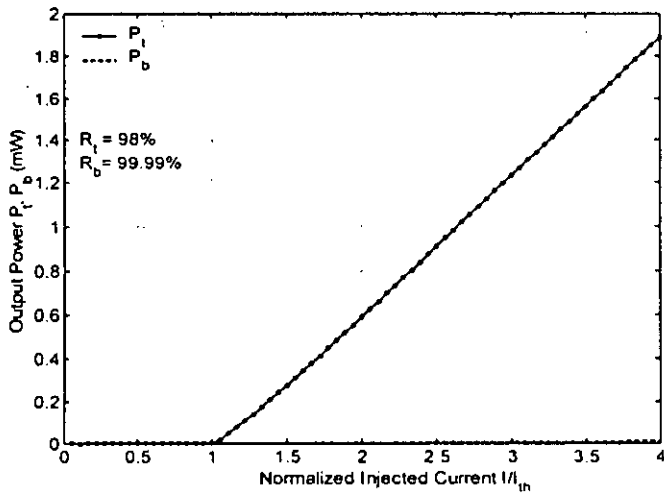


**Figure 4.12** Plot of total output power versus injection current of a VCSEL. Emission wavelength of the VCSEL has been taken as 980 nm.

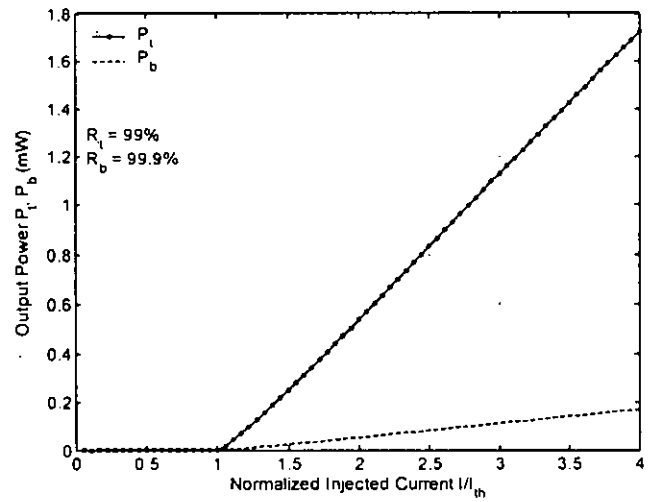
Light current characteristics of a VCSEL can be determined by computing the output power for different values of injected current. Output power of a VCSEL can be written in terms of injected current as

$$P_{tot}(I) = \overline{P_{tot}(t)} \tag{4.51}$$

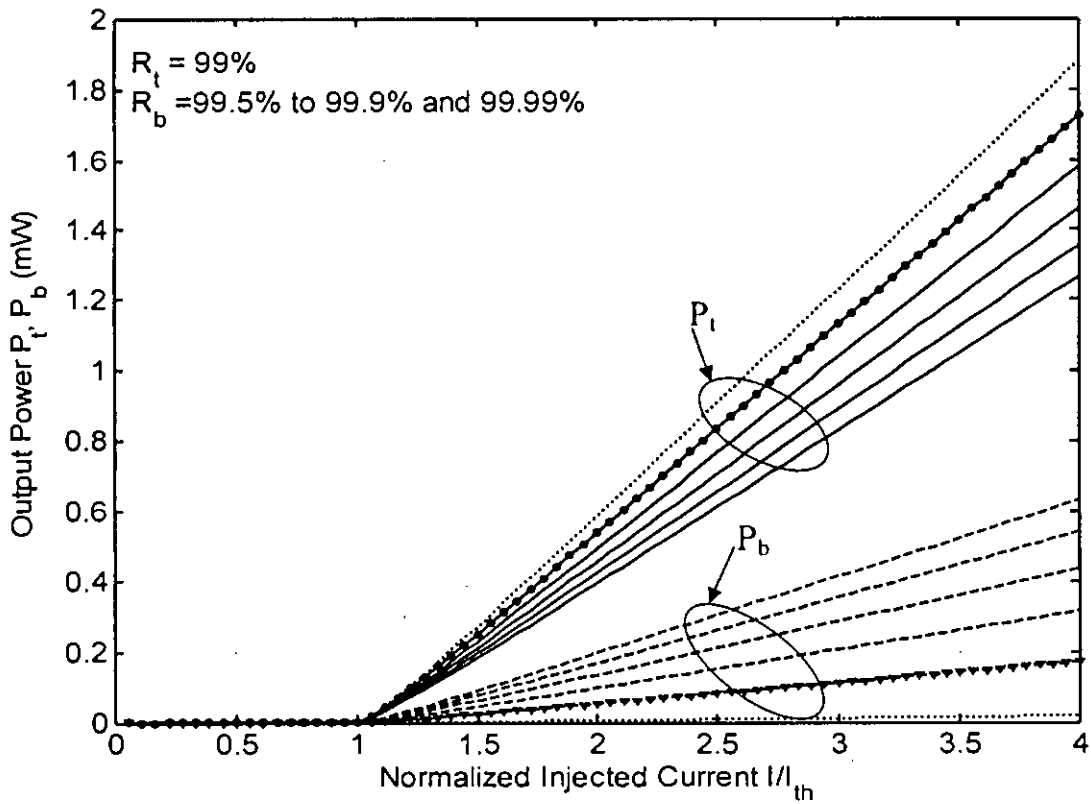
Here,  $\overline{P_{tot}(t)}$  is the average value of the total output power  $P_{tot}(t)$ . To determine the output power versus injected current,  $P_{tot}(t)$  has been computed for different values of injected current then taking the average of  $P_{tot}(t)$  has been plotted with the injected current. Curve has been shown in the figure 4.12. From figure 4.12, the threshold current of the VCSEL has been found to be 0.18mA. Injected current, before to reach the threshold current, the output power is negligible because stimulated emission has not been started yet. When the injected current exceeds the threshold level, output power of the VCSEL starts to increase rapidly.



(a)



(b)



(c)

**Figure 4.13** Light-Current ( $L-I$ ) characteristics of a VCSEL. (a) Shows the power output from the top and bottom facet of the VCSEL having the power reflectivity of the top and bottom mirror are  $R_t = 98\%$  and  $R_b = 99.99\%$  respectively. (b) Shows the power output from the top and bottom facet of the VCSEL having the power reflectivity of the top and bottom mirror are  $R_t = 99\%$  and  $R_b = 99.9\%$  respectively. (c) Shows the power output from the top and bottom facet of the VCSEL having the power reflectivity of the top mirror  $R_t = 99\%$  and the power reflectivity of the bottom mirror has different values. Dotted lines of the figure (c) represent the output power when the value of  $R_b$  has been set to 99.99%.

Output power per facet of a VCSEL is a function of external differential quantum efficiency of that facet. External differential quantum efficiency of the facet is a function of the power reflectivity of the facet as discussed in the Section 3.12. Hence the output power per facet of a VCSEL will vary with the reflectivity of the top or bottom mirror. Output power from the top and bottom facet of a VCSEL has been computed for different values of the facet reflectivity and plotted in the figure 4.13. Figure 4.13 (c) shows that, when the reflectivity of one facet of the VCSEL is increased the output power of that facet will decrease and the power output from the other facet will increase.

## 4.12 Summary

At the beginning of this chapter, rate equations of the semiconductor laser have been introduced. Equations of the threshold current density and the threshold carrier density of a semiconductor laser have been derived. Current versus light output power characteristics of a semiconductor laser has also been presented. Next, the rate equations of a VCSEL have been discussed briefly. Computation of turn on delay of a semiconductor laser has been presented and the technique of the reduction of turn on delay has been discussed. Finally, the total output power of a VCSEL and the power output per facet of a VCSEL has been computed.

## Chapter 5

### Transfer Matrix Method (TMM) Based Analysis a VCSEL

#### 5.1 Introduction

In this chapter the Transfer Matrix Method (TMM) will be discussed clearly. The reflectivity and transmittivity of a step index DBR stack as well as a complete VCSEL will be computed by using TMM. The electric field distribution inside a VCSEL will also be computed by using TMM.

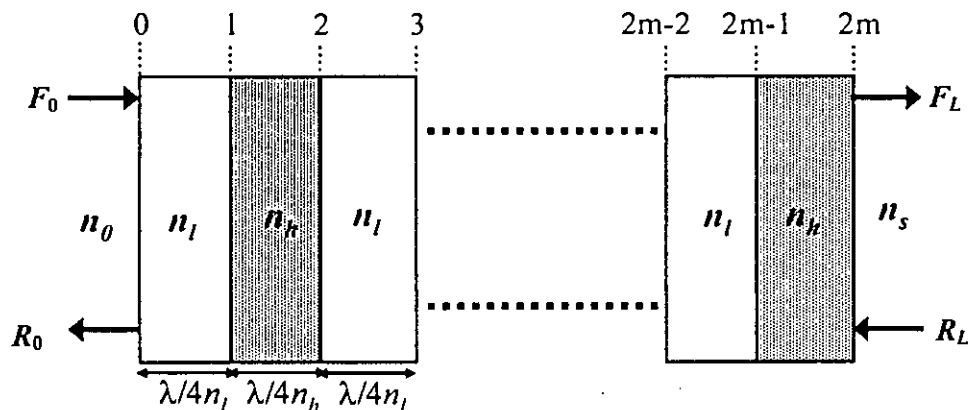


**Figure 5.1** Schematic representation of a GaAs/AlAs Bragg Reflector consisting of  $m$  pairs of low and high indices layers. The indices of the two sides of the Bragg Reflector are  $n_0$  and  $n_s$ .  $F_0$  and  $R_0$  are the incident and reflected wave at the input interface.  $F_L$  and  $R_L$  are the reflected and incident wave at the output interface. The thickness of each layer is quarter wavelength ( $\lambda_B/4n_{l,h}$ ).

#### 5.2 Calculation of Reflectivity and Transmittivity of DBR Stacks by using TMM

As discussed before that the refractive index of the materials varies with the wavelength, the reflectivity of the DBR will also vary with the wavelength. This variation can be determined by using the transfer matrix method as discussed bellow. Consider the DBR shown in the figure 5.1 has  $m$  pairs of alternate low and high refractive index layers. The forward and backward traveling plane wave's amplitude at the input plane and output plane are  $F_0$ ,  $R_0$  and  $F_L$ ,  $R_L$  respectively. Relation between the waves at input and output plane can be written as [17].

$$\begin{bmatrix} F_0 \\ R_0 \end{bmatrix} = M \begin{bmatrix} F_L \\ R_L \end{bmatrix} = \begin{bmatrix} M_{11} & M_{12} \\ M_{21} & M_{22} \end{bmatrix} \begin{bmatrix} F_L \\ R_L \end{bmatrix} \quad (5.1)$$

$$M = M_{01} \prod_{i=1}^{2m} [M_{i\varphi} M_{i\psi}] \quad (5.2)$$

where  $M_{it}$  is the interface matrix of the  $i_{th}$  interface between the layer of index  $n_i$  and  $n_{i+1}$ . The matrix  $M_{i\phi}$  is the phase matrix of the layer of index  $n_i$  and thickness  $d_i$ . The interface matrix and the phase matrix can be determined as

$$M_{it} = \frac{1}{2n_i} \begin{bmatrix} n_i + n_{i+1} & n_i - n_{i+1} \\ n_i - n_{i+1} & n_i + n_{i+1} \end{bmatrix} \quad (5.3)$$

$$M_{i\phi} = \begin{bmatrix} \exp^{j\phi_i} & 0 \\ 0 & \exp^{-j\phi_i} \end{bmatrix} \quad (5.4)$$

Where  $\phi_i = 2\pi n_i d_i / \lambda$  is the phase change of the plane wave into the layer of index  $n_i$ .

The amplitude reflection coefficient of the DBR can be defined as the ratio of the reflected wave to the incident wave at the input plane with no incident wave at the output plane.

$$r = \frac{R_0}{F_0} = \frac{M_{11}}{M_{21}} \quad (5.5)$$

The power reflectivity  $R$  is related with the amplitude reflection coefficient by the following relation

$$r = \sqrt{R} \exp(j\phi_r) \quad (5.6)$$

Where  $\phi_r$  is the phase of the reflection.

Similarly, the amplitude transmission coefficient of the DBR can be defined as the ratio of the reflected wave to the incident wave at the input plane with no incident wave at the output plane.

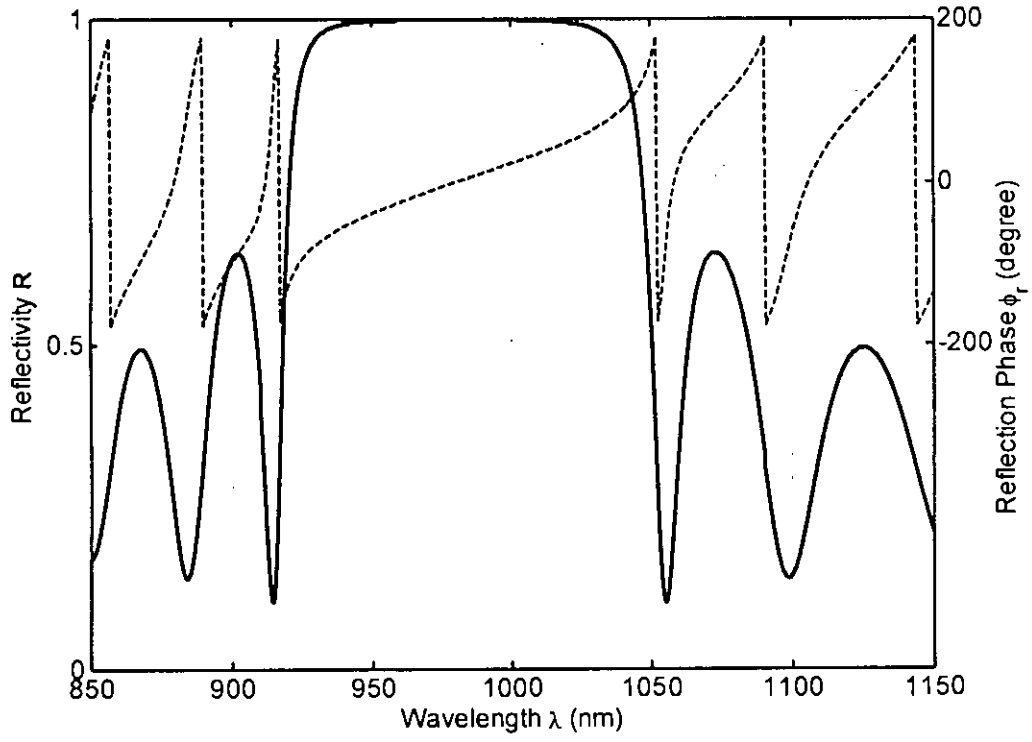
$$t = \frac{F_t}{F_0} = \frac{1}{M_{11}} \quad (5.7)$$

The power transmittivity  $T$  is related with the amplitude transmission coefficient by the following relation

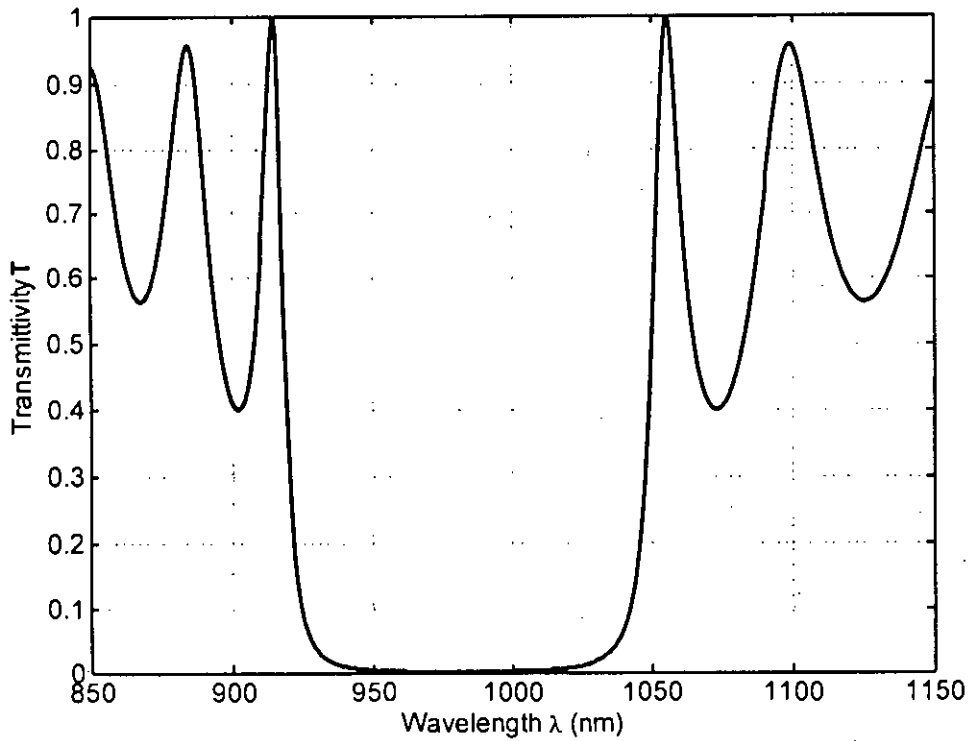
$$t = \sqrt{T} \exp(j\phi_t) \quad (5.8)$$

For loss less media  $R+T=1$ .

Transfer matrix of the DBR can now be computed by using the equations (5.2), (5.3) and (5.4). Once the transfer matrix of the DBR has computed, the reflectivity and the transmittivity of the DBR stacks can be computed by using the equations (5.6) and (5.8). Reflectivity spectrum indicates that there is a stop band for which the reflectivity is greater than 99%.



(a)



(b)

**Figure 5.2** Spectral dependence of the (a) power reflectivity  $R$ , phase  $\phi_r$  of the amplitude reflectivity and (b) the power transmittivity of a Bragg mirror consisting of 20 pairs of AlAs/GaAs layers.



### 5.3 Calculation of Reflectivity and Transmittivity of a Complete VCSEL by using TMM

Technique of calculating the reflectivity and transmittivity of a DBR has been discussed in the previous section. Following the same technique the reflectivity and transmittivity spectra of VCSEL resonator will be determined in the following section.

Figure 5.3 shows the layered arrangement of a VCSEL. One important point to take note is that the order of arrangement of the layers must be symmetrical at both sides. In other words, if a refractive index,  $n_l$  on the left side of the cavity, a refractive index,  $n_l$ , must be placed at the right side of the cavity region. Low index and high index materials must be arranged alternatively.

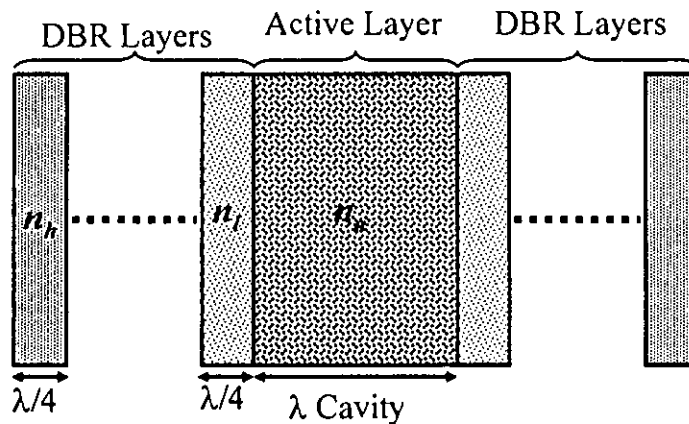


**Figure 5.3** Arrangement of different layers of semiconductor materials of a VCSEL.

The transfer matrix  $M_t$  of the Top DBR and  $M_b$  of the bottom DBR can be calculated by using the technique described in the chapter 2. Then the transfer matrix  $M_{act}$  of the active layer will be calculated. Now, the transfer matrix  $M_{VCSEL}$  of the whole VCSEL will be formed by multiplying all of the transfer matrices for each sections.

$$M_{VCSEL} = M_b \times M_{act} \times M_t \quad (5.7)$$

Figure 5.4 shows the reflectivity and transmittivity spectra of a VCSEL. The top and bottom DBR stacks of the VCSEL have 20 pairs of GaAs/AlGaAs layers and the active layer is constructed by  $Al_{0.8}Ga_{0.2}As$  layer. Thickness of the active layer has been taken as 1 wavelength. Once the transfer matrix of the complete VCSEL is computed the reflectivity and transmittivity spectra of the VCSEL can be computed by using the equations (5.6) and (5.8).

Transmittivity spectrum of figure 5.4 (b) indicates that the light of 980 nm wavelength will come out from the VCSEL because the transmittivity of the complete VCSEL is maximum at this wavelength.

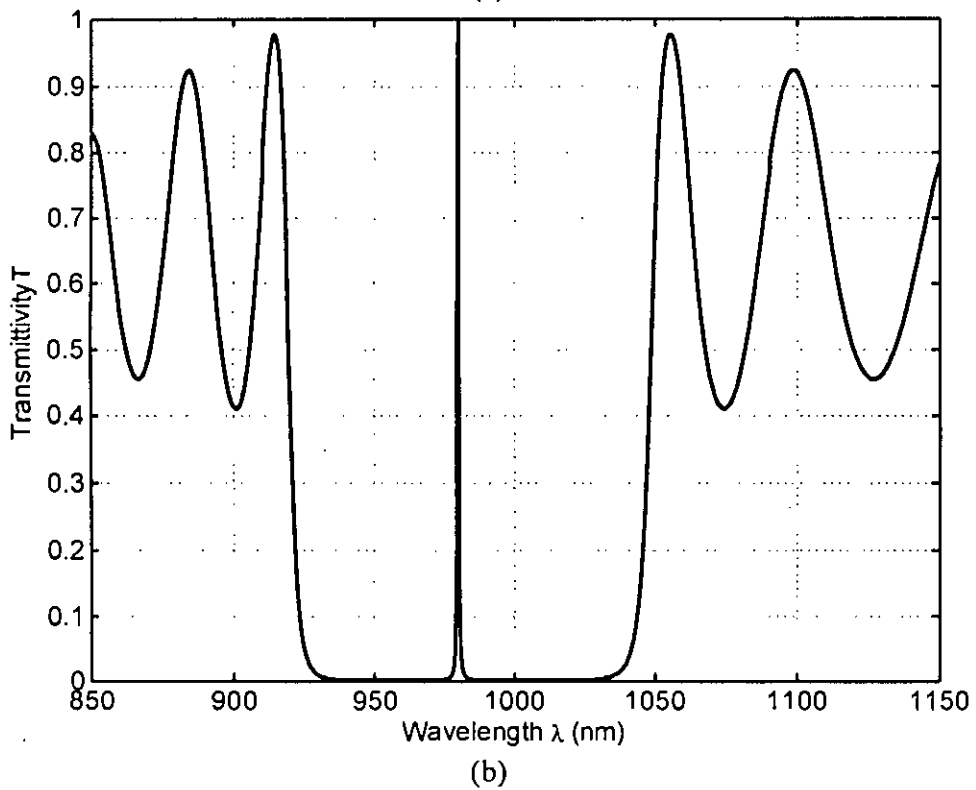
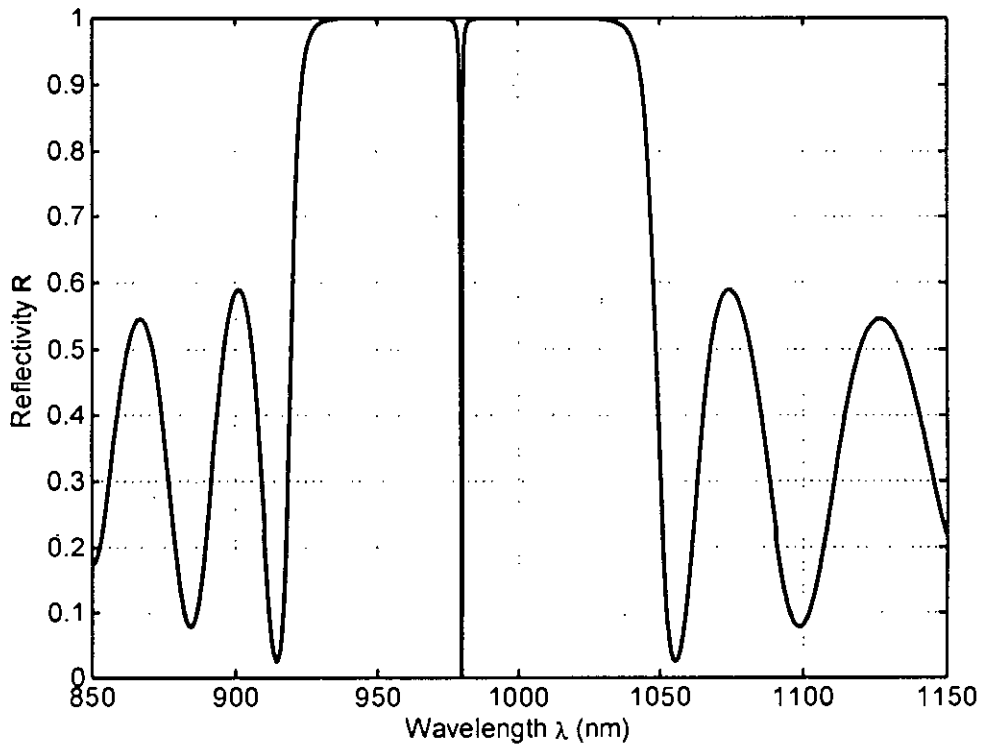


**Figure 5.4** Reflectivity and transmittivity spectra of a  $\lambda$  cavity VCSEL. Top DBR has 18 pairs and bottom DBR has 20 pairs of  $\text{Al}_{0.2}\text{Ga}_{0.8}\text{As}/\text{Al}_{0.9}\text{Ga}_{0.1}\text{As}$  dielectric layers. Bragg wavelength is considered to 980 nm. Material of the active layer has been selected as  $\text{Al}_{0.8}\text{Ga}_{0.2}\text{As}$ .

## 5.4 Summary

In this chapter, transfer Matrix Method (TMM) has been presented. Reflectivity and transmittivity spectra of a step index layered DBR stacks have been computed by using TMM. Reflectivity and transmittivity spectra of a complete VCSEL have also been computed by using TMM.

## Chapter 6

### A Novel Method of Calculating DBR Reflectivity Spectrum and the Electric Field Distribution inside a VCSEL

#### 6.1 Introduction

Transfer Matrix Method (TMM) of calculating the reflectivity and transmittivity of a DBR stack and VCSEL has been presented in chapter 5. It has also been discussed that it is not possible to compute the reflectivity and transmittivity of a multilayer stack having graded refractive index variation by using TMM. A new technique termed as Sampled Transfer Matrix Method (STMM) can be able to compute the reflectivity and transmittivity of a multilayer stack having graded refractive index variation as well as step index variation. STMM is also capable to compute the electric field distribution inside a VCSEL even if the DBR stacks have graded refractive index variation. In this chapter, basic theory of STMM is presented. Next, STMM is applied to compute the reflectivity and transmittivity of a DBR having step index change as well as DBR having different types of graded index layers. Reflectivity and transmittivity of a VCSEL has been computed by using STMM. Finally, the electric field distribution inside a VCSEL has been computed by using the STMM.

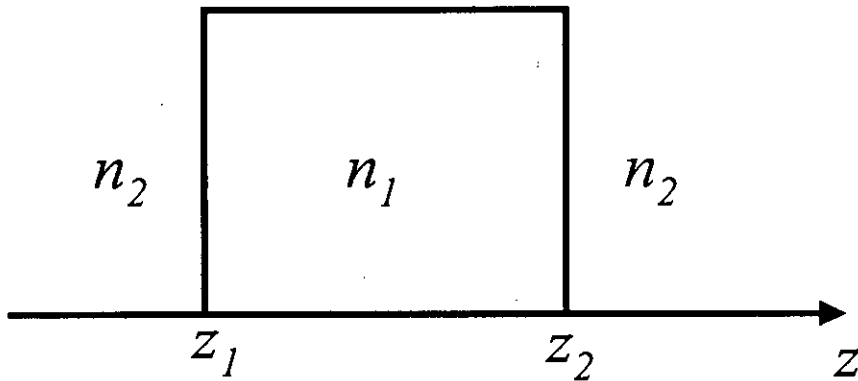


**Figure 6.1** Representation of a constant index layer sandwiched between two different layers.

#### 6.2 Basic Idea of Sampled Transfer Matrix Method (STMM)

The technique of calculating the Transfer Matrix of a multilayer stack with step refractive index variation has been discussed in the section 5.2. If the refractive indexes of the layers are continuously varying with distance, then the method discussed in the section 5.2 will not be able to compute the Transfer Matrix of the layers accurately. The Transfer Matrix of smoothly varying index multilayer stacks can be calculated by using a newly developed method named Sampled Transfer Matrix Method (STMM).

The transfer matrix  $M$  of the layer between  $z_1$  and  $z_2$  as shown in the figure 6.1 can be written by following the equations (5.2), (5.3) and (5.4) as

$$M = M_{I1} M_{\phi} M_{I2} \quad (6.1)$$

Here  $M_{I1}$  and  $M_{I2}$  are the interface matrixes of the interfaces at  $Z_1$  and  $Z_2$  respectively.  $M_\phi$  is the phase matrix for the layer of index  $n_1$ . The interface matrixes  $M_{I1}$  and  $M_{I2}$  can be computed by using the equation (5.3) and the phase matrix  $M_\phi$  can be computed by using the equation (5.4).

STMM is derived from the TMM discussed in the section 5.2. In TMM the interface matrix arose for the change in refractive indexes. The change of refractive index will cause a propagating wave to be scattered. The phase matrix in TMM arose for the layer of constant index  $n$ . This layer causes no scattering of a propagating wave but only change the phase of the wave.

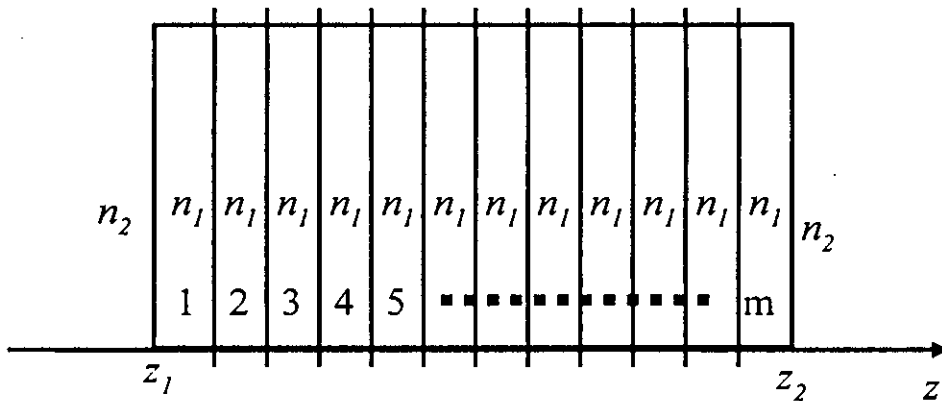


**Figure 6.2** Representation of the previous figure after sampling into  $m$  number of layers of constant thickness  $d$ .

If the constant layer is considered as a number of sampled layers of same refractive index, then the interfaces which will appear due to the sampled layers will be virtual interfaces. Actually there will be no scattering from those interfaces. Because the refractive index before and after those interfaces are equal. Hence the interface matrix will be a diagonal matrix according the equation (5.3).

Since the interface matrixes due to the virtual interfaces are diagonal matrix, product of the entire interface and phase matrix of the sampled layers except the first and last interface matrix will be equal to the phase matrix of the un-sampled layer. In this way one can compute the transfer matrix of any layer structure even the layers having uniformly varying refractive index.

Figure 6.2 represent the sampled version of the layer shown in figure 6.1. If  $m$  is the number of sampled layers then there will be total  $m+1$  interfaces instead of two interfaces of figure 6.1. Now the same transfer matrix  $M$  of equation 6.1 can be computed from the sampled layers of figure 6.2 and using the following equation

$$M = M_{01} \prod_{i=1}^m [M_{i\phi} M_{iI}] \quad (6.2)$$

Here,  $M_{iI}$  is the interface matrix for the first interface.  $M_{iI}$  is the interface matrix between the  $i$  th and  $i+1$  th layers. Similarly  $M_{i\phi}$  is the layer matrix for the  $i$  th layer. From the above discussion it is found that the transfer matrix  $M$  of equation (6.1) and (6.2) must be same.

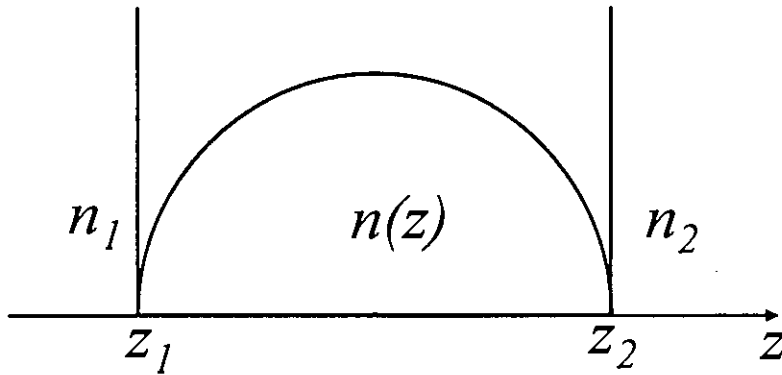


**Figure 6.3** Schematic representation of a Semiconductor/Dielectric layer having smooth variation of refractive index  $n(z)$  with distance  $z$ . Two layers of Semiconductor/Dielectric are on its two sides having refractive indexes  $n_1$  and  $n_2$ .

Now consider the refractive index of the layer between two points  $Z_1$  and  $Z_2$  of figure 6.1 is uniformly varying with space. Figure 6.3 shows that uniformly varying refractive index layer. It is not possible to compute the transfer matrix of this layer accurately by using the equation (6.1). In this case, waves traveling from the point  $Z_1$  to  $Z_2$  will have transmission and reflection at every plane between these two points due to this uniform variation of refractive index. STMM is capable to compute the transfer matrix of this layer accurately.

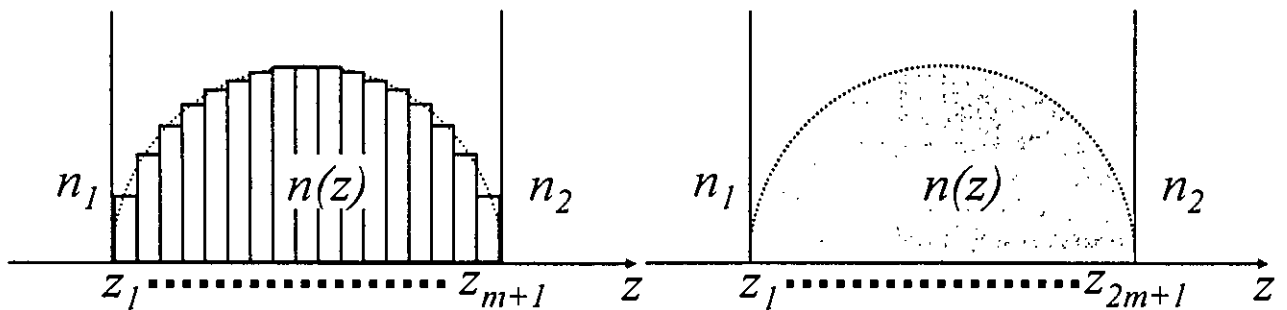


**Figure 6.4** Sampled version of the dielectric layer containing uniformly varying refractive index. (a) with  $m$  number of sampled layer (b) with  $2m$  number of sampled layer.

The transfer matrix  $M$  of the layer shown in the figure 6.3 can be computed accurately by using the equation (6.2). First of all the layer needs to be sampled in to many layers of constant thickness. Figure 6.4 (a) and (b) represents the layer of figure 6.3 after sampling into  $m$  and  $2m$  number of layers respectively. Computation of transfer matrix  $M$  will be more accurate if the value of  $m$  increased. This has been shown in the next section.

Up to this, the technique of computing the transfer matrix of a single layer of semiconductor material or dielectric material has been presented. Incase of multilayer structure (DBR or VCSEL), either step index layer or graded index layer, the transfer matrix of the whole structure can be computed by using STMM. Sampling can be done in two different ways; i) Sample the total length of the multilayer stack, ii) sample the each layer of the multilayer stacks separately and by cascading the transfer matrixes of each of the layers, total transfer matrix can be computed. After computing the

transfer matrix of the multilayer stacks, reflectivity and transmittivity of the stacks can be computed by using the equations (5.5) and (5.7).

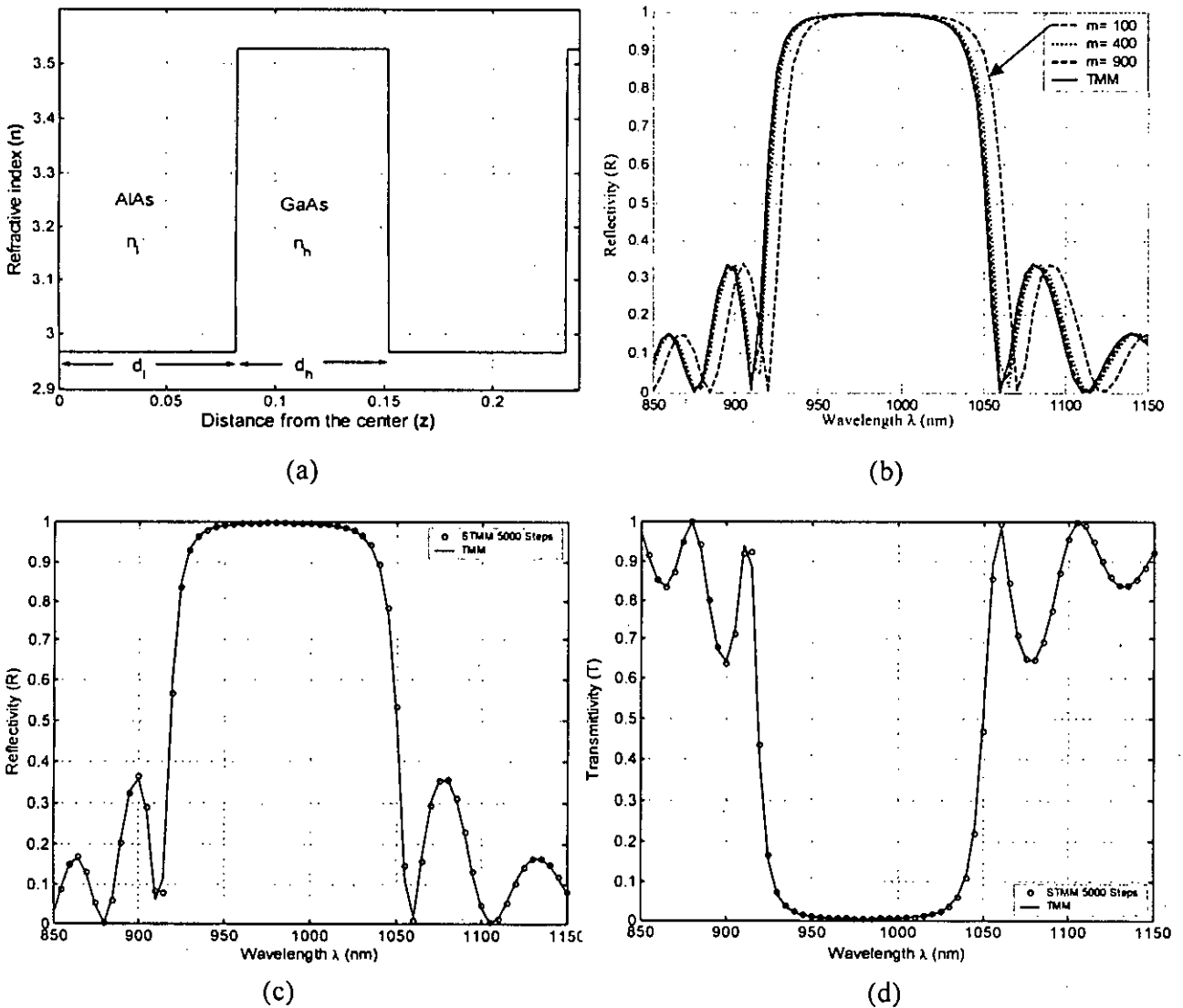
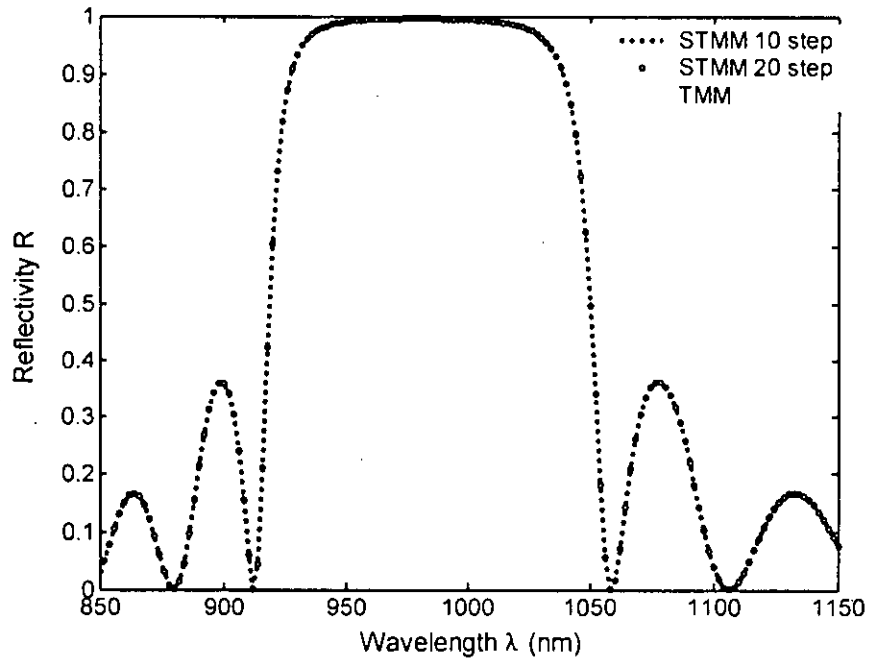


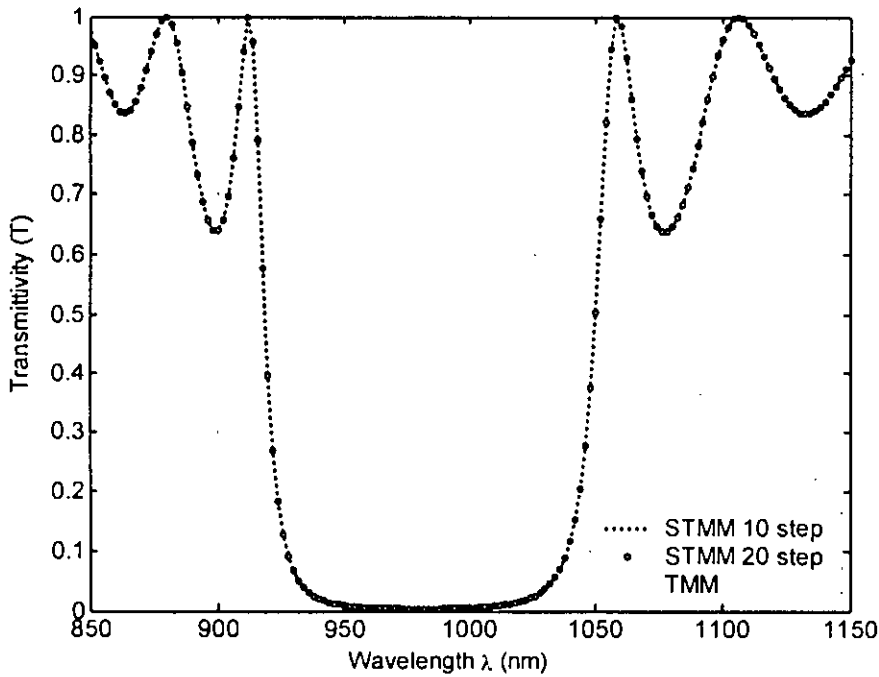
**Figure 6.5** Computation of refractive index, reflectivity and transmittivity of a 20 pair AlAs/GaAs DBR mirror. (a) Plot of refractive index vs. distance showing the layer thickness of  $1\frac{1}{2}$  pair of low and high refractive index materials of the DBR mirror. (b) plot of reflectivity spectra of the DBR mirror due to different number of sampled layer  $m$ . Solid line represent the simulation result using TMM where as the dashed lines are representing the results of STMM. (c) and (d) show the plot of reflectivity and transmittivity spectra of the DBR mirror obtained by using STMM and TMM. Here, whole length of the DBR has been sampled into 5000 layers.

### 6.3 Computation of Reflectivity and Transmittivity of a Generalized DBR Stack using STMM

Distributed Bragg Reflectors (DBRs) are used as mirrors in different types of semiconductor lasers such as Distributed Feedback (DFB) Laser, Distributed Bragg Reflector (DBR) Laser and Vertical Cavity Surface Emitting Laser (VCSEL). Construction of a DBR has been explained in Sections 3.5 and 3.7. The schematic representation of a generalized DBR with step index change between the low refractive index ( $n_l$ ) material (AlAs) and the high refractive index ( $n_h$ ) material-



(a)



(b)

**Figure 6.6** (a) Reflectivity and (b) Transmittivity spectra of a 20 pair AlAs/GaAs DBR mirror obtained by using STMM and TMM. Solid line represents the simulation result obtained by using TMM whereas the dashed lines and small circles are obtained by using STMM for  $m=10$  and  $m=20$  respectively. Figure (a) and (b) show that the reflectivity and transmittivity spectra of the DBR mirror obtained by using STMM and TMM are exactly same.

-(GaAs) has been shown in figure 5.1. Refractive indices of the two sides of the DBR are  $n_0$  and  $n_s$ . STMM can be used to compute the reflectivity and transmittivity spectra of the DBR in two different ways. Firstly, computing the transfer matrix of the DBR mirror by dividing the whole length of the



DBR in to  $m$  sampled layers and secondly, computing the transfer matrix of the DBR mirror by sampling each of the layers independently. Now, from the computed transfer matrix, reflectivity and transmittivity spectra of the DBR mirror can be determined by using the equations (5.5) and (5.7).

Figure 6.5 shows the simulation result of reflectivity  $R$  and transmittivity  $T$  of a 20 pairs of AlAs/GaAs DBR mirror. Bragg wavelength of the mirror is chosen as  $\lambda_B = 980$  nm. Simulation has been done following the first technique of the STMM as mention in the previous paragraph. From figure 6.5 (b) it is clear that the result obtained by STMM come closer to the result obtained by TMM when the number of sampled layer  $m$  increased.

In figure 6.5 (b), the farthest dashed line (by STMM) curve from the solid line (by TMM) curve has been obtained for the value of  $m=100$  and the closest dashed line curve has been obtained for the value of  $m=900$ . If the value of  $m$  becomes very high then the result obtained by STMM will be exactly same as that obtained by TMM. Figure 6.5 (b) and (c) show that result obtained by STMM with  $m=5000$  is almost same of the result obtained by TMM.

Figure 6.6 shows the result obtained by the second technique of STMM, i.e. by cascading the transfer matrixes of each layer obtained after sampling the each of the layer into  $m$  sampled layer independently. Figure 6.6 (a) shows the simulation result of reflectivity spectra of the above mentioned DBR of 20 pairs of AlAs/GaAs materials. Solid line represents the result obtained by TMM where as the dotted line ( $m=10$ ) and the small circles ( $m = 20$ ) represent the result obtained by using STMM. Figure 6.6 (a) shows the simulation result of transmittivity spectra of the same DBR. Solid line represents the result obtained by TMM where as the dotted line ( $m=10$ ) and the small circles ( $m = 20$ ) represent the result obtained by using STMM.

Both of the figures 6.5 and 6.6 show the STMM is capable to compute the reflectivity and transmittivity of a step index layered DBR stack accurately. In the next section STMM will be applied to compute the reflectivity of the different types of uniformly graded index layered DBR.

## 6.4 Computation of Reflectivity of Graded Index Layered DBR Stacks using STMM

DBR mirrors are constructed by multiple numbers of quarter wavelength thick low and high refractive index materials alternatively. It is possible to make that quarter wavelength thick layer to have refractive index variation in different ways such as i) step variation, ii) linear variation, ii) trapezoidal variation, iv) sinusoidal variation, v) parabolic variation, etc. Sinusoidal and modified sinusoidal variation of refractive index in the layers of a DBR has been presented and analyzed in the following paragraphs.

The refractive index  $n_{l,h}(z)$  of the layers can be represented by the following equation as.

$$n_{l,h}(z) = n_{avg} \pm \Delta n (\sin \theta_{l,h})^x \quad (6.3)$$

Here,  $x$  represents the degree of variation of the refractive index in the layers. If  $x = 0$  then the DBR will be step index DBR and if  $x = 1$  then the variation of refractive index of the DBR will be sinusoidal.  $n_{avg}$  is the average refractive index of the DBR,  $\Delta n$  is the deviation of refractive index from the maximum or minimum refractive of each of the layers can be written as,

$$n_{avg} = \frac{n_{l,min} + n_{h,max}}{2} \quad (6.4)$$

$$\Delta n = \frac{n_{h,max} - n_{l,min}}{2} \quad (6.5)$$

and

$$\theta_{l,h} = \frac{\pi}{d_{l,h}} z \quad (6.6)$$

where,  $d_l$  is the thickness of the low refractive index layers and  $d_h$  is the thickness of the high refractive index layers. Values of  $d_l$  and  $d_h$  can be calculated by the following equations.  $z$  is the distance starting from each of the layers and the value of  $z$  is from 0 to  $d_{l,h}$ .

$$d_l = \frac{\lambda_B}{4n_{l,min}} \quad (6.7)$$

$$d_h = \frac{\lambda_B}{4n_{h,max}} \quad (6.8)$$

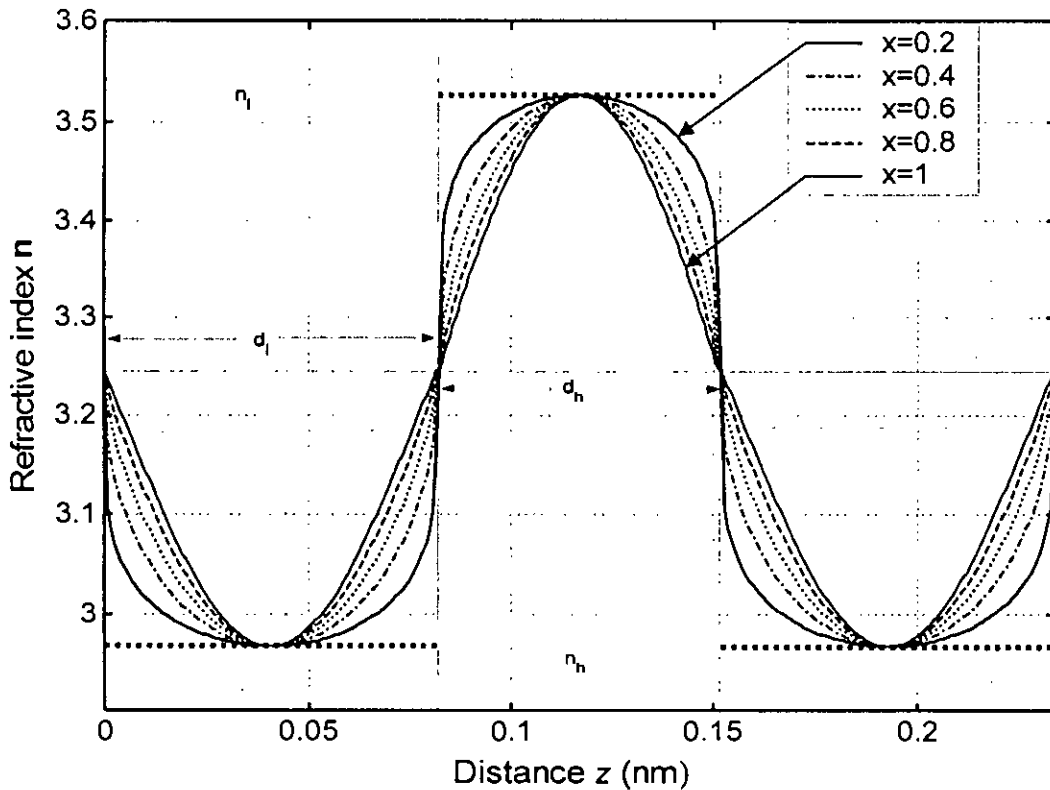


**Figure 6.7** Representation of the first three layers of a 20 pairs DBR mirror. Refractive index of each layer is uniformly varying according to the equation (6.3). Maximum and minimum refractive indexes of the layers are  $n_{h,max} = 3.53$  and  $n_{l,min} = 2.97$  respectively. Bragg wavelength of this DBR is set to  $\lambda_B = 980$  nm.

The structure of the DBR having uniform refractive index variation in the layers is shown in the figure 6.7. Different types of variation in refractive index are plotted in the figure 6.7. When the value of  $x$  in the equation (6.3) is set to 1 then the variation will be pure sinusoidal as shown by the inner solid curve of figure 6.7. Other curves of figure 6.7 are plotted for the decreasing value of  $x$ . Outer solid curve is obtained by setting the value of  $x$  is to 0.2 in the equation (6.3). When the of  $x$  is set to 0 then the variation of refractive index will be step index change as shown by the thick dotted line in the figure 6.7.

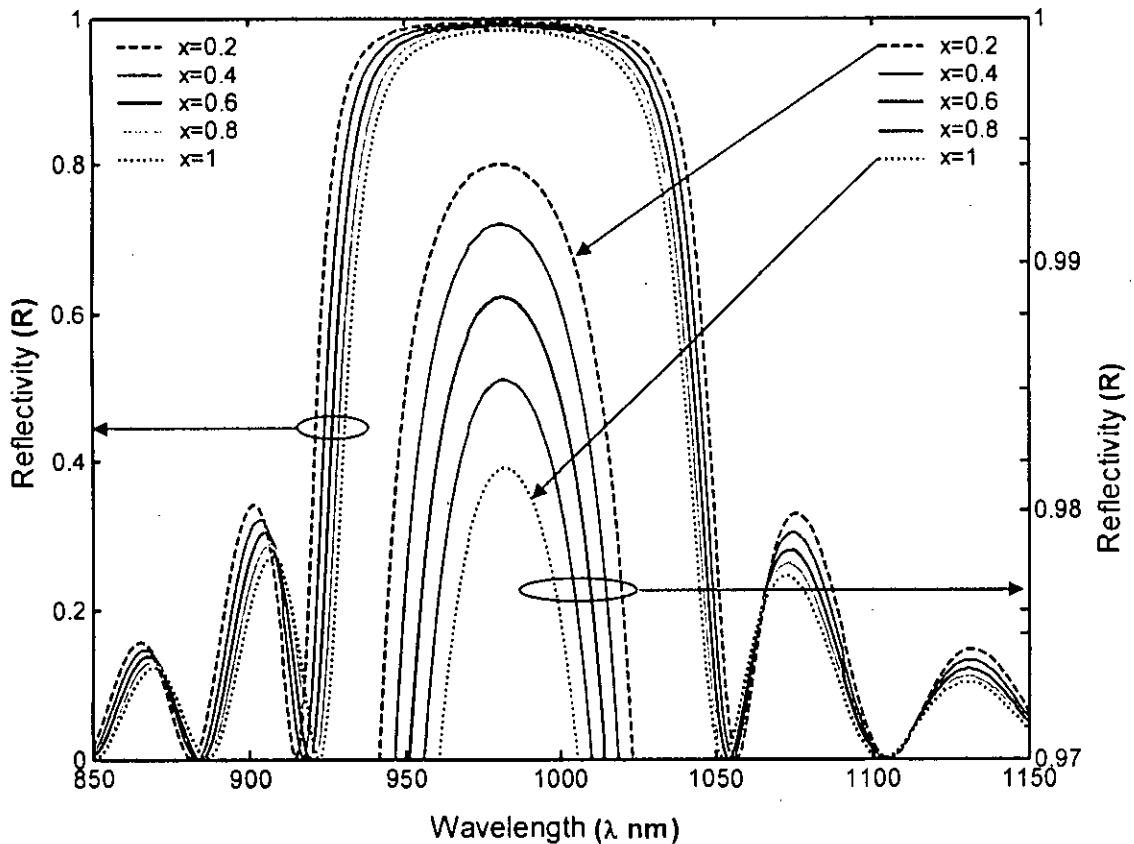


**Figure 6.8** Simulation result of reflectivity spectra of the DBRs shown in the figure 6.7. Each layer of the DBR is divided into 50 sampled layers during simulation. Thin lines are representing the reflectivity spectra of each DBR for the wavelength range from 850 nm to 1150 nm where as the thick lines are representing the reflectivity spectra near the Bragg wavelength region. Results show that the each of the DBRs has the peak reflectivity at the Bragg wavelength. DBR with  $x = 0.2$  has the height peak reflectivity and the DBR with  $x = 1$  has the lowest peak reflectivity.

Reflectivity spectra of the DBRs shown in the figure 6.7 has been computed and plotted in the figure 6.8 by using STMM. Transfer matrix of the whole DBR has been computed by cascading the transfer matrixes of each layer. Transfer matrix of each of the layers has been computed by dividing the layer into 50 sampled layers. Finally the reflectivity of the DBR has been computed according the equation (5.7) and plotted in figure 6.8.

Simulation results of reflectivity spectra of the DBRs shown in the figure 6.7 have been plotted in the figure 6.8. Results show that each of the DBRs has peak reflectivity at the Bragg

wavelength. DBR with  $x = 0.2$  has the highest peak reflectivity and the DBR with  $x = 1$  has the lowest peak reflectivity.

The effect of the sampled layer number on the computation of the reflectivity of a DBR having uniformly varying refractive index will be discussed. Select one of the DBRs shown in figure 6.7 which have the value of  $x=0.1$ . Reflectivity of the DBR can be computed by using STMM. Simulation has been performed for  $m= 5, 15, 30, 50$  and  $75$  samples per layer and the results are plotted in the figure 6.9.

Figure 6.9 shows that the peak reflectivity is about 99.1% when the number of samples per layer is 5, whereas the peak reflectivity

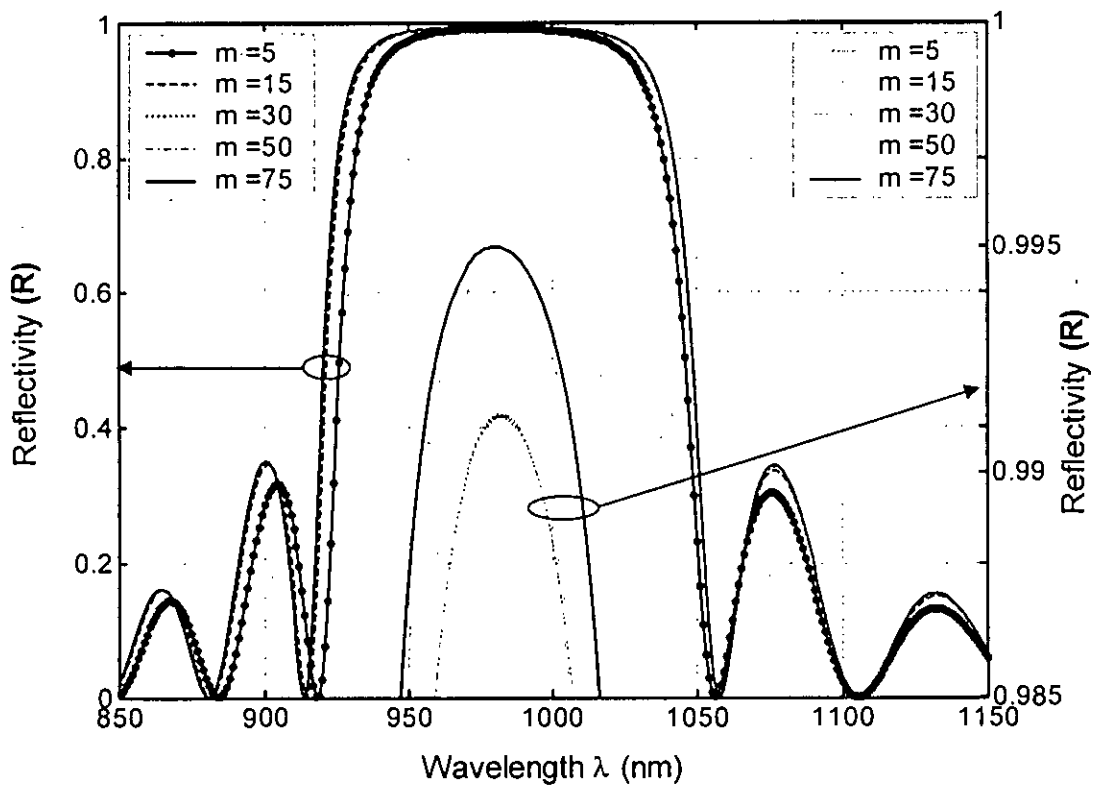


**Figure 6.9** Simulation result of reflectivity spectra of one of the DBRs shown in the figure 6.7. Here the DBR of  $x=0.2$  has been selected. Each layer of the DBR is divided into different number (5 -75) of sampled layers during simulation. Pure solid line and Solid line with small circles show the reflectivity spectra when there were 5 and 75 sampled layers per layer respectively. The reflectivity spectra of the DBR for different number of sampled layers are shown in the left axis where as the reflectivity spectra near the peak reflectivity are shown in the right axis.

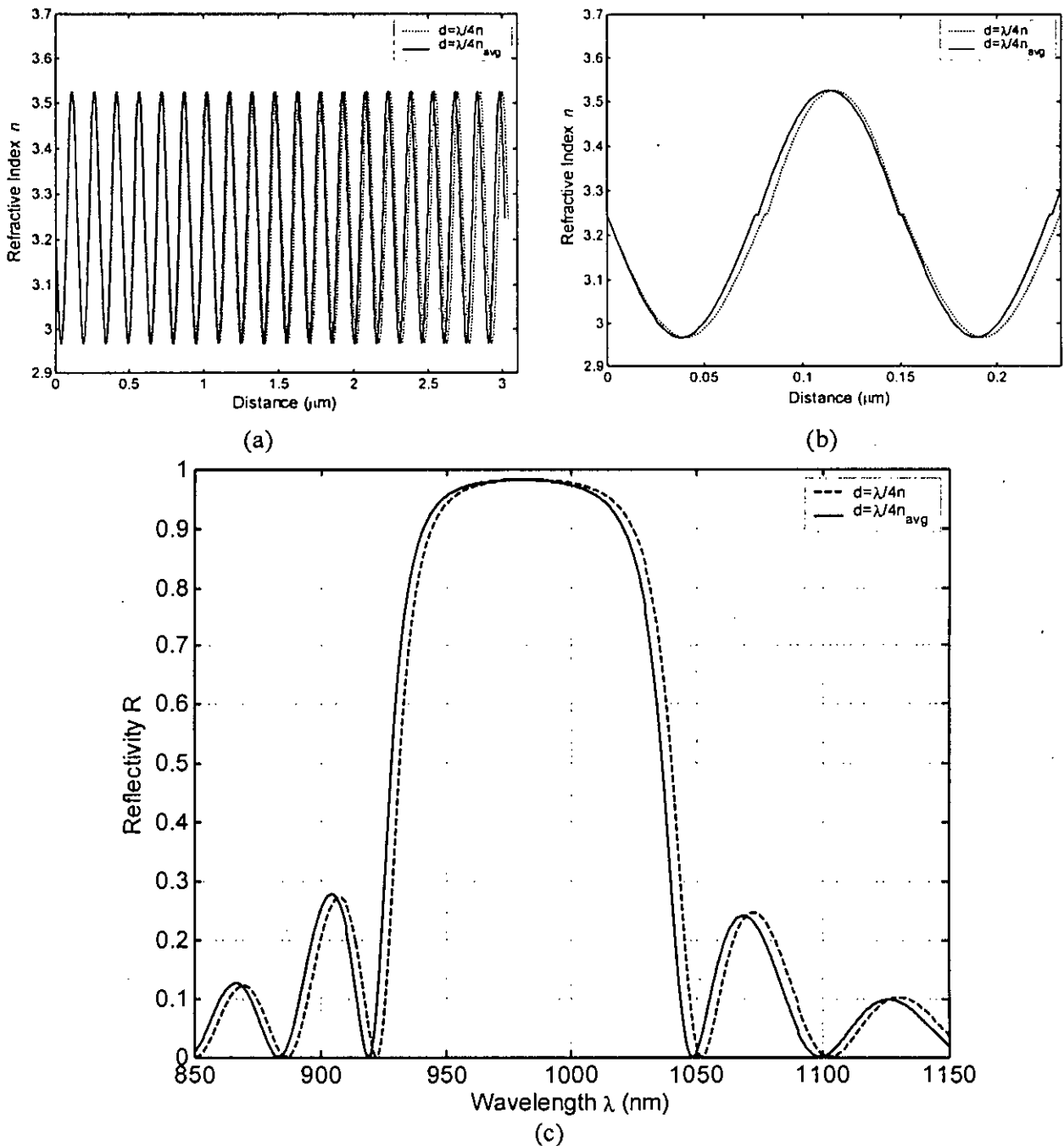


**Figure 6.10** Construction and the reflectivity spectra of DBRs having sinusoidal variation of refractive index. (a) show the total structure of the DBRs, (b) show the first 3 layers of the DBRs and (c) show the reflectivity spectra of the DBRs. Solid lines represent the DBR which have the layer thickness of  $\lambda/4n$  and the dashed line represent the DBR which have the layer thickness of  $\lambda/4n_{avg}$ .

## 6.5 Computation of Reflectivity of DBR Stacks having Sinusoidal Variation in the Refractive Index

Computation of the reflectivity and transmittivity of a DBR having step index layers as well as graded index layers has been presented in the section 6.2 and 6.3. Pure sinusoidal variation of

refractive index in the layers of a DBR can be considered in many ways; two of them are presented and analyzed in this section.

Consider that the thickness of each of the layers of the first DBR are  $d_f = \lambda/4n_{l,min}$  and  $d_h = \lambda/4n_{l,max}$  respectively. The thickness of each of the layers of the second DBR are  $d_f = d_h = \lambda/4n_{avg}$ . The refractive index variations of the DBRs are shown in the figure 6.10 (a) and (b). Figure 6.10 (a) shows the complete 20 pair of the DBR and (b) shows the first 3 layers of the DBR. Dotted line represents the first DBR where as the solid line shows the second DBR.

Simulation results of both of the DBRs are shown in the figure 6.10 (c). STTM has been used to compute the reflectivity spectra of the DBRs. During the simulation, each of the layers has been divided into 150 sampled layers. Figure 6.10 (c) shows that the DBRs presented here have the similar reflectivity spectra as that of the step index layered DBR. These DBRs have smaller peak reflectivity than the step index layered DBR.

Reflectivity spectra near the Bragg wavelength region are shown in the figure 6.11. Result shows that, none of the DBRs have the peak reflectivity at the Bragg wavelength. The deviation of the wavelength at which the peak reflectivity occurred is about 3 nm and 1 nm for the first and second DBR respectively

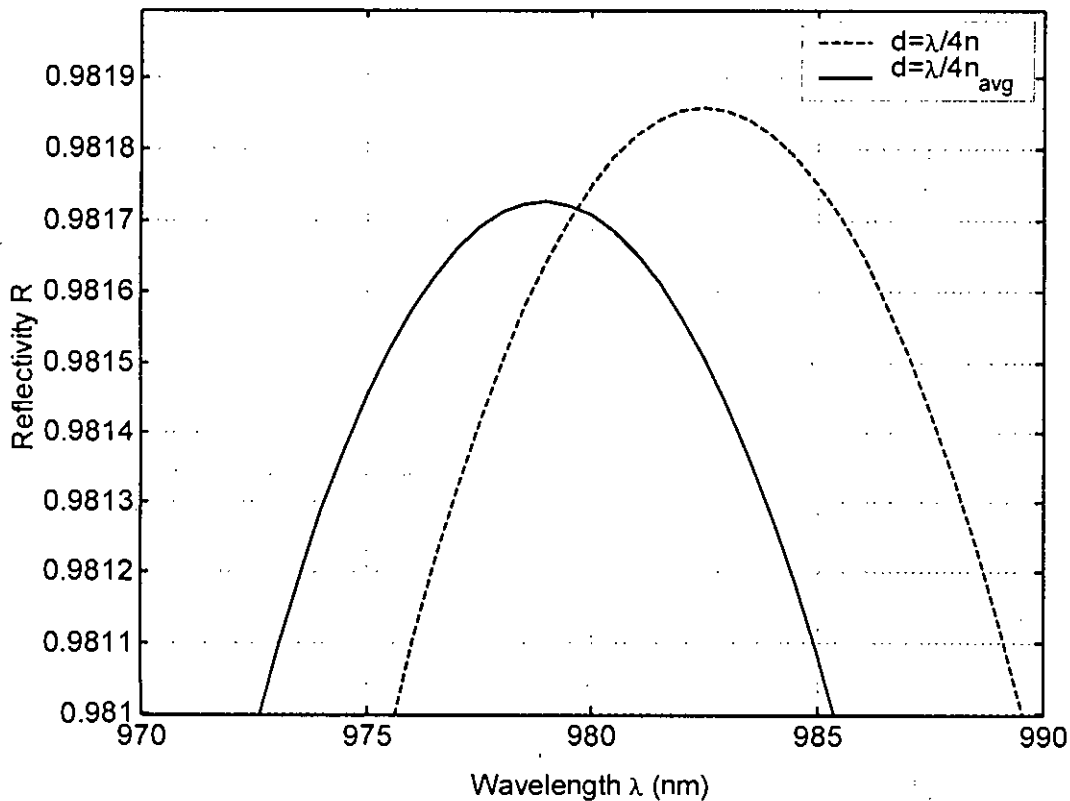


**Figure 6.11** Variation of the reflectivity near the Bragg wavelength region. Dashed line represents the result of the reflectivity of the DBR having the layer thickness of thickness of  $\lambda/4n$  and the solid line represents the DBR which have the layer thickness of  $\lambda/4n_{avg}$ .

## 6.6 Reflectivity and Transmittivity Spectra of a Complete VCSEL

Technique of calculating the reflectivity and transmittivity of a DBR by using the technique based on STMM has been discussed in the section 6.3. Following the same technique the reflectivity and transmittivity spectra of a complete VCSEL will be determined in the following section.

Figure 6.12 shows the layered arrangement of a generalized VCSEL. The active layer of the VCSEL contains  $\text{Al}_{0.2}\text{Ga}_{0.8}\text{As}$  active material whose refractive index is  $n_a$ . Thickness of the active layer has been chosen as  $\lambda/n_a$ . The VCSEL has 20 pairs of top and bottom DBR mirror of alternative  $\text{AlAs}/\text{GaAl}$  layers. One important point to take note is that the order of arrangement of the layers must be symmetrical at both sides. In other words, if there is a refractive index,  $n_l$  on the left side of the cavity, a refractive index,  $n_r$  must be placed at the right side of the cavity region. Low index and high index materials must be arranged alternatively.

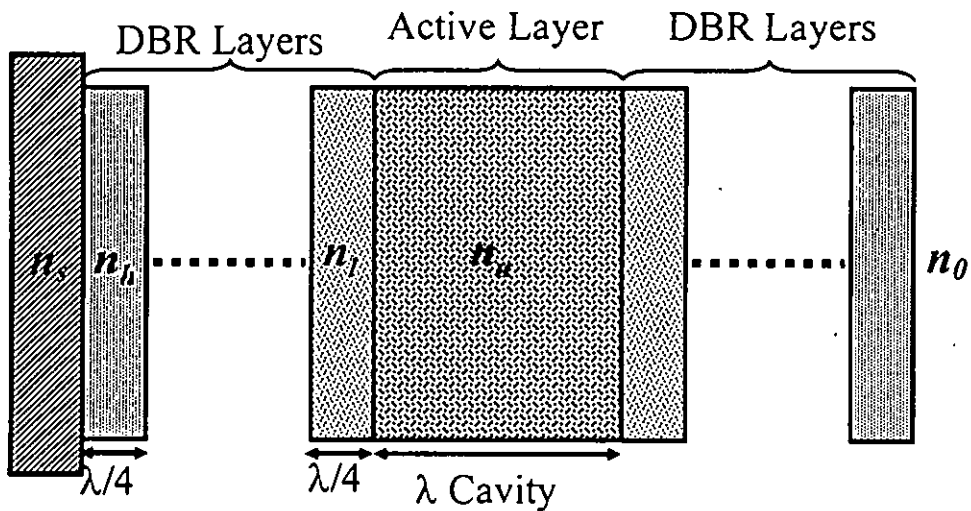


**Figure 6.12** Arrangement of different layers of semiconductor materials of a generalized VCSEL. The layers of a VCSEL consisting of a stack of DBR layers on the left, a stack of DBR layers on the right and there is an active layer sandwiched between the two stacks. There are another two layers having refractive index  $n_s$  and  $n_0$ .

The complete VCSEL, as shown in the figure 6.12 is comparable with the DBR shown in the figure 5.1 in a sense that both of them have multiple layers of different semiconductor materials. Only difference is that all of the layers of DBR are quarter wave length thick, whereas all of the layers of a VCSEL are not quarter wavelength. Hence, the transfer matrix of the VCSEL can be computed by using the same technique applied for the computation of the transfer matrix of a DBR. The transfer matrix  $M_{\text{VCSEL}}$  of the whole VCSEL can be calculated by using the technique described in section 6.2. After computing the transfer matrix, reflectivity and transmittivity of the VCSEL is computed by using the equations (5.6) and (5.8).

Figure 6.13 shows the reflectivity spectrum of a VCSEL. The top and bottom DBR have 20 pairs of  $\text{GaAs}/\text{AlGaAs}$  layers and the active layer is constructed by  $\text{Al}_{0.8}\text{Ga}_{0.2}\text{As}$  layer. Thickness of the active layer is taken as 1 wavelength. Transmittivity spectrum of figure 6.13 (b) and (d) indicates

that the light of 980 nm wavelength will come out from the VCSEL because the transmittivity of the complete VCSEL is maximum at this wavelength.

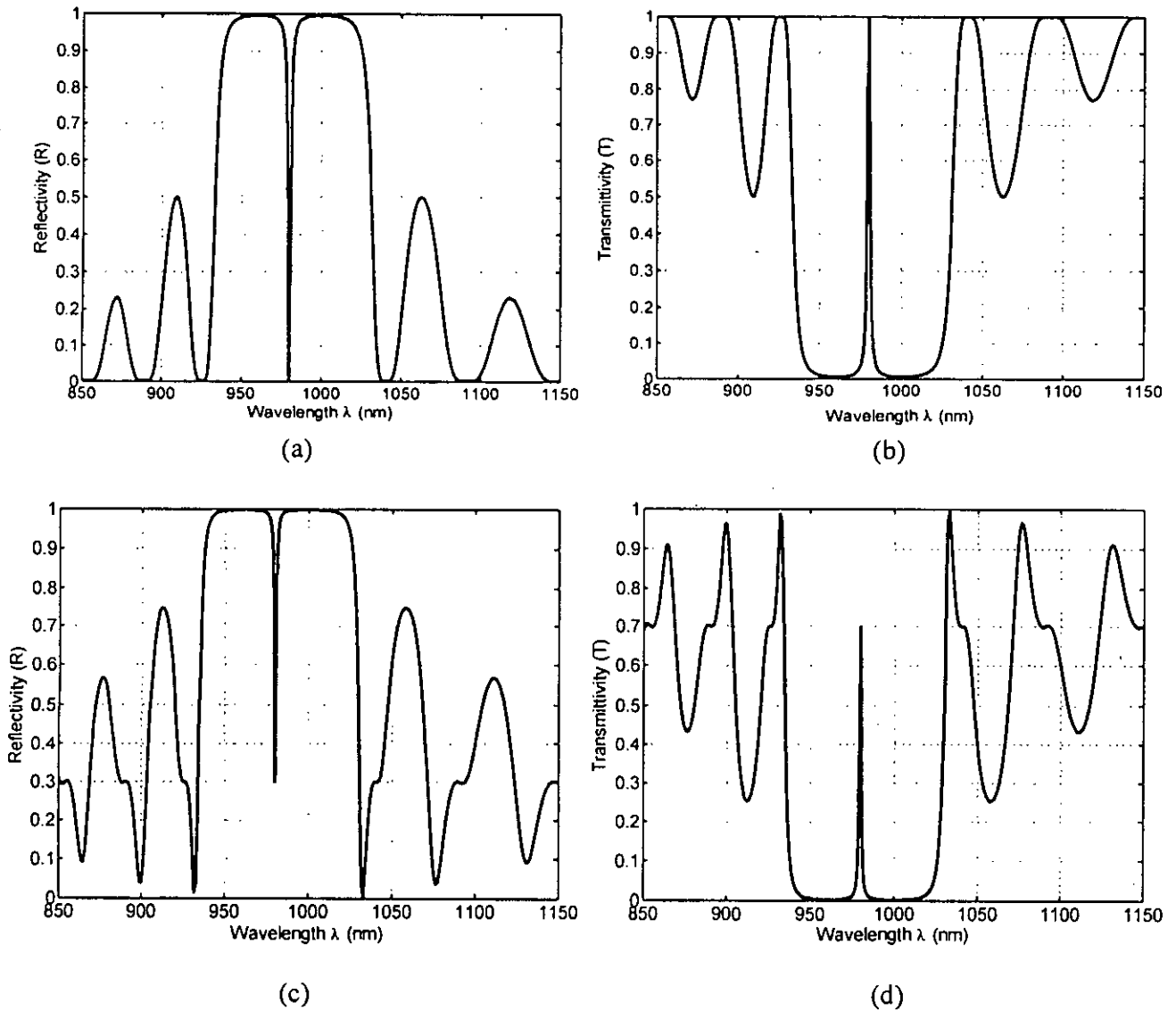


**Figure 6.13** Reflectivity and Transmittivity spectrum of a generalized 980 nm VCSEL. Each of the top and bottom DBR has 20 pairs of dielectric layers. Figure (a) and (b) shows the simulation result considering the values of  $n_s = n_0 = n_h$  where as (c) and (d) shows the reflectivity and transmittivity spectrum of the VCSEL considering the values of  $n_s = n_h$  and  $n_0 = 1$  (air).

It has been discussed in the chapter 3 that to improve the electrical and optical performance several structures of VCSEL have been introduced. To reduce the threshold current, carrier confinement in the active region is necessary. Quantum wells and the spacer layers in the active region are used to confine the carrier hence reduce the threshold current. Schematic representation of such a VCSEL is shown in the figure 6.14. The VCSEL has 25 pairs of dielectric materials in the bottom DBR where as 18 pairs in the top DBR to make the VCSEL top emitting. The layers of the DBR are composed of  $Al_{0.8}Ga_{0.2}As/Al_{0.8}Ga_{0.2}As$  materials. Optical cavity of the VCSEL is formed by quantum wells, barrier layers and spacer layers placed between the top and bottom DBRs. At the center of the active layer there are three 8 nm thick GaAs quantum wells. Quantum wells are separated by four  $Al_{0.5}Ga_{0.5}As$  barrier layers. Two of the barrier layers, which are placed between the



quantum wells has the thickness of 10 nm each and the thickness of another two barrier layers are 40 nm each. Thicknesses of two  $\text{Al}_{0.75}\text{Ga}_{0.25}\text{As}$  spacer layers are select as 80.2 nm each to make the cavity length equal to 1 wavelength.

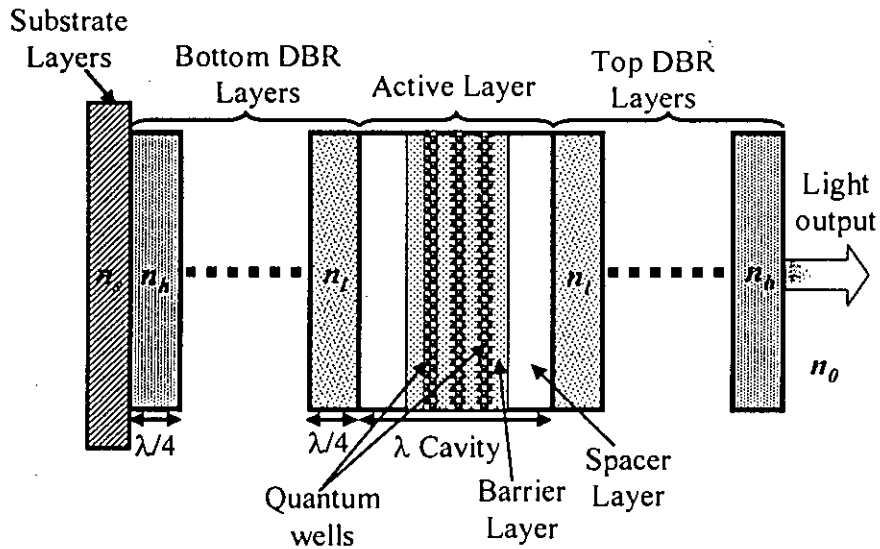


**Figure 6.14** Schematic representation of a VCSEL having  $\lambda$  cavity. In the cavity region there are three 10 nm thick GaAs quantum wells, four  $\text{Al}_{0.5}\text{Ga}_{0.5}\text{As}$  barrier layers and two  $\text{Al}_{0.5}\text{Ga}_{0.5}\text{As}$  spacer layers. Top and bottom DBR have 25 and 18 pairs of  $\text{Al}_{0.8}\text{Ga}_{0.2}\text{As}/\text{Al}_{0.2}\text{Ga}_{0.8}\text{As}$  quarter wavelength thick dielectric layers respectively. There are another two layers having refractive index  $n_s$  of the substrate layer normally use GaAs and  $n_0$  of the media where the light has to be come out.

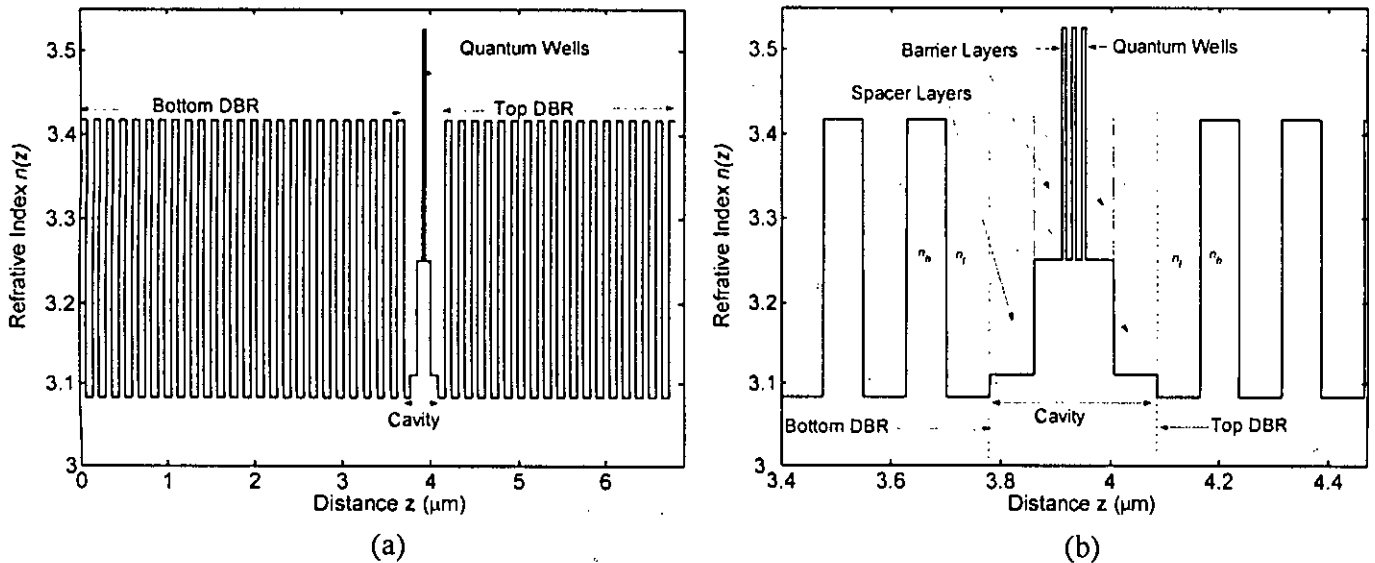


**Figure 6.15** Variation of refractive index of different layers of a VCSEL. Figure (a) shows the refractive index of the complete VCSEL where as figure (b) shows the refractive index of the cavity region (refractive index of the quantum wells, barrier layers and spacer layers) and the DBR layers just near the cavity region.

Refractive index of the different layers of the VCSEL has been computed by using the equation (3.6) for  $\lambda = 980$  nm. Refractive index variation of the complete VCSEL along with the distance  $z$  from the substrate layer is shown in the figure 6.15 (a). Refractive index of the quantum wells, barrier layers, spacer layers and few of the top and bottom DBR layers have been shown in the figure 6.15 (b).

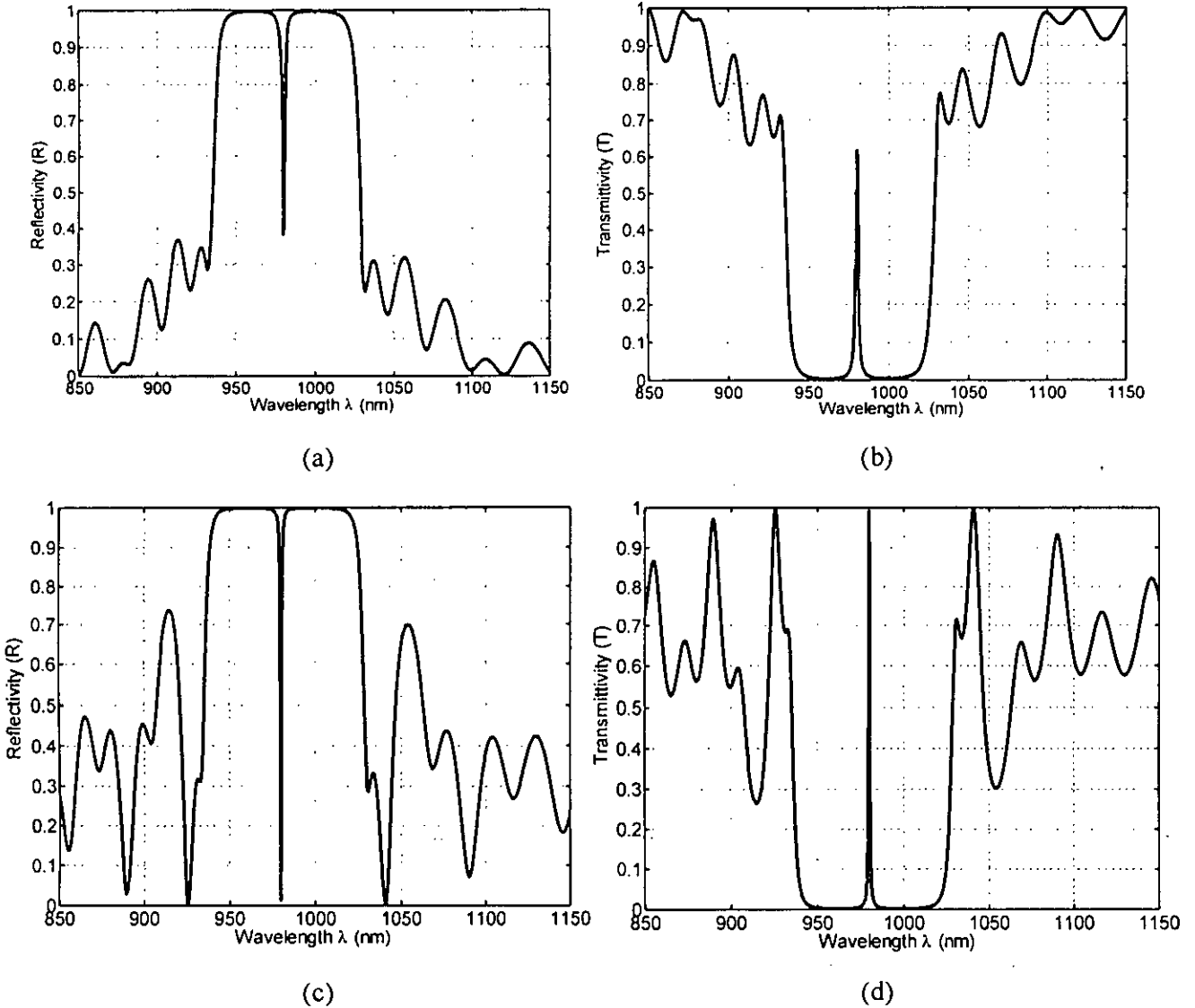


**Figure 6.16** Reflectivity and Transmittivity spectrum of a GaAs based  $\lambda$  cavity VCSEL. Optical cavity of the VCSEL consists of three 10 nm thick GaAs quantum wells, four  $\text{Al}_{0.5}\text{Ga}_{0.5}\text{As}$  barrier layers and two  $\text{Al}_{0.5}\text{Ga}_{0.5}\text{As}$  spacer layers. Top and bottom DBR have 18 and 25 pairs of  $\text{Al}_{0.8}\text{Ga}_{0.2}\text{As}/\text{Al}_{0.2}\text{Ga}_{0.8}\text{As}$  quarter wavelength thick dielectric layers respectively. There are another two layers having refractive index  $n_s$  of the substrate layer normally use GaAs and  $n_0$  of the media where the light has to be come out. Figure (a) and (b) shows the reflectivity and transmittivity spectrum of the VCSEL considering the values of  $n_s = n_0 = n_h$  where as (c) and (d) shows the reflectivity and transmittivity spectrum of the VCSEL considering the values of  $n_s = n_h$  and  $n_0 = 1$  (air).

## 6.7 Electric Field Distribution inside the VCSEL

For designing high performance VCSELs it is important to know the electric field distribution in the resonator. Different techniques like coupled mode theory and transfer matrix method has been used previously [18, 40] to calculate the electric field distribution inside the VCSEL. A new technique to calculate the electric field distribution inside a VCSEL will be discussed in the following section.

A technique of calculating the electric field distribution of Fiber Bragg Gratings (FBG) by using transfer matrix method was presented by Muriel and Carballar [9]. Following this technique a new method for calculating the transfer matrices of the active layers and DBR layers of a VCSEL will be discussed in the following paragraph.

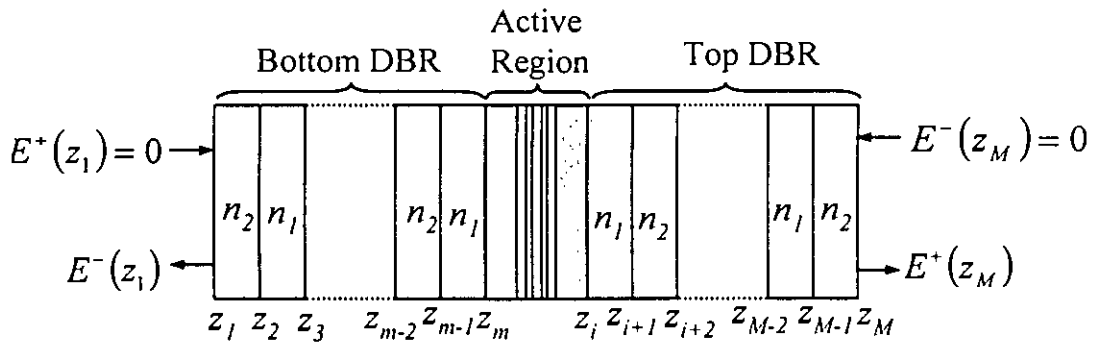


**Figure 6.17** Representation of the different layers of a VCSEL. The bottom DBR, Active region and top DBR layers are indicated. All of the layers have step refractive index variation. Active region of the VCSEL contains 3 quantum wells.

A VCSEL comprising a number of DBR layers on the two sides of the active layers as shown in Figure-6.17. DBR is formed by arranging several numbers of low and high refractive index materials having a thickness of  $\lambda/4n$  in each layer. In order to develop the transfer matrix of the VCSEL let us consider a basic layer of dielectric material with interface layer at both sides as shown in figure 6.18. Refractive index  $n(z)$  of the layer is a function of  $z$ .

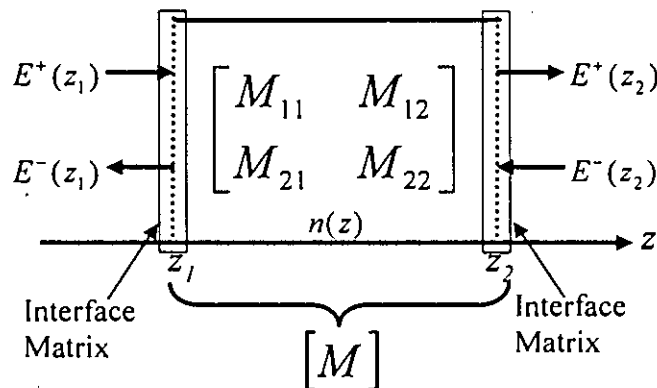


**Figure 6.18** Transfer matrix notation of a single layer of VCSEL. Transfer matrix  $M$  of the layer is the product of two interface matrices and the phase matrix of the layer as shown in the figure 6.18.

Electric field distribution inside a VCSEL can be computed by using the technique based on STMM. Let,  $E^+(z)$  and  $E^-(z)$  be the forward and backward traveling plane waves at an arbitrary

plane  $z$ . Then from Figure-6.18, the relationship between the waves at the plane  $z_1$  and the waves at the plane  $z_2$  can be written as

$$E^+(z_1) = M_{11}E^+(z_2) + M_{12}E^-(z_2) \quad (6.3)$$

$$E^-(z_1) = M_{21}E^+(z_2) + M_{22}E^-(z_2) \quad (6.4)$$

Equation (6.3) and (6.4) can be written in matrix form as

$$\begin{bmatrix} E^+(z_1) \\ E^-(z_1) \end{bmatrix} = \begin{bmatrix} M_{11} & M_{12} \\ M_{21} & M_{22} \end{bmatrix} \begin{bmatrix} E^+(z_2) \\ E^-(z_2) \end{bmatrix} \quad (6.5)$$

$$[E(z_1)] = [M][E(z_2)] \quad (6.6)$$

where,  $M_{11}$ ,  $M_{12}$ ,  $M_{21}$ ,  $M_{22}$  are coefficients of transfer matrix  $M$ .

The transfer matrix  $M$  is the product of interface matrices ( $M_{I1}$ ,  $M_{I2}$ ) and layer matrix ( $M_\phi$ ) shown in figure 6.18.

$$M = M_{I1}M_\phi M_{I2} \quad (6.7)$$



**Figure 6.19** Two basic elements used in forming the transfer matrices: (a) Interface between two media with different refractive indices  $n_i$  and  $n_j$  and (b) layer with refractive index  $n_i$  and thickness  $d_i$ .

The interface matrix appears because of the interface of different materials having different refractive index  $n_i$  and  $n_j$  as shown in figure 6.19 (a). The plane wave incident at this interface will be scattered. The layer matrix appears due to the layer of uniform material having the refractive index ( $n_i$ ) and thickness ( $d_i$ ) as shown in figure 6.19 (b).

The interface matrix can be formed by the relation [7].

$$[M_I] = \frac{1}{2n_i} \begin{bmatrix} n_i + n_j & n_i - n_j \\ n_i - n_j & n_i + n_j \end{bmatrix} \quad (6.8)$$

The layer matrix can be formed by the relation [7].

$$[M_\varphi] = \begin{bmatrix} e^{j\varphi} & 0 \\ 0 & e^{-j\varphi} \end{bmatrix} \quad (6.9)$$

Here,  $\varphi = \beta d_i = \frac{2\pi}{\lambda} n_i d_i$  is the phase quantity.

If there is no input from the right side of figure 6.18 i.e,  $E^-(z_2) = 0$  the electric field amplitude reflection coefficient  $r$  for that single layer can be defined as the ratio of reflected wave to the incident wave. Putting  $E^-(z_2) = 0$  in the equation 6.3 and equation 6.4 then by dividing 6.4 by 6.3 the following relation can be found.

$$r = \left. \frac{E^-(z_1)}{E^+(z_1)} \right|_{E^-(z_2)=0} = \frac{M_{21}}{M_{11}} \quad (6.10)$$

$$E^-(z_1) = rE^+(z_1) \quad (6.11)$$

The transmission coefficient  $t$  for that single layer can be defined as the ration of transmitted wave to the incident wave. Putting  $E^-(z_2) = 0$  in the equation 6.3 the following relation can be found.

$$t = \left. \frac{E^+(z_2)}{E^-(z_1)} \right|_{E^-(z_2)=0} = \frac{1}{M_{11}} \quad (6.12)$$

$$E^+(z_2) = tE^-(z_1) \quad (6.13)$$

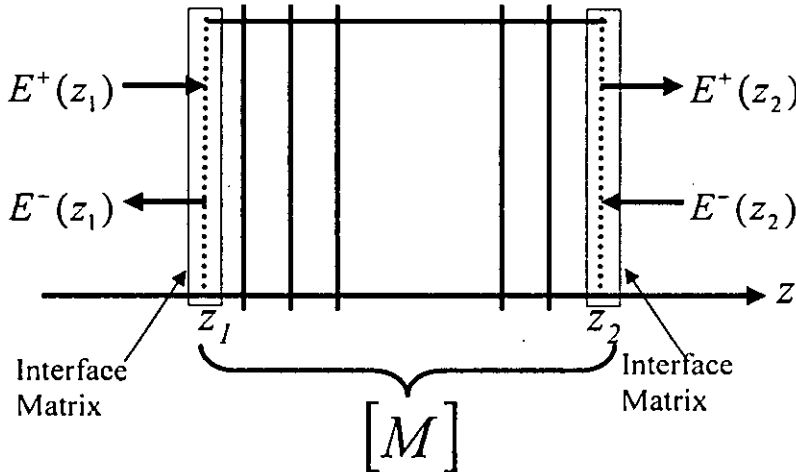


**Figure 6.20** Representation of sampled single layer of a DBR

Now using the equations 6.4, 6.11 and 6.13

$$\begin{bmatrix} E^+(z_1) \\ rE^+(z_1) \end{bmatrix} = \begin{bmatrix} M_{11} & M_{12} \\ M_{21} & M_{22} \end{bmatrix} \begin{bmatrix} tE^-(z_1) \\ 0 \end{bmatrix} \quad (6.14)$$

$$\begin{bmatrix} 1 \\ r \end{bmatrix} = \begin{bmatrix} M_{11} & M_{12} \\ M_{21} & M_{22} \end{bmatrix} \begin{bmatrix} t \\ 0 \end{bmatrix} \quad (6.15)$$

The single layer of figure 6.18 now be considered to made up of several sampled layer as shown in figure 6.20. The transfer matrix  $M$  of the sampled layers can then be calculated by multiplying all of the interface matrices and layer matrices starting from left to right. The amplitude transmission coefficient  $t$  is then calculated using the equation 6.12. The above mentioned procedure of calculating the matrix  $M$  is termed as Sampled Transfer Matrix Method (STMM).

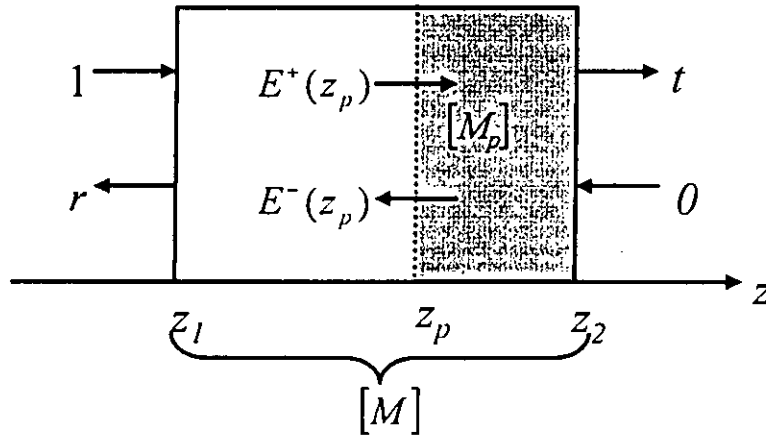


**Figure 6.21** Calculation of electric field distribution at any point inside the layer by using Sampled Transfer Matrix Method (STMM).  $E^+(z_p)$  and  $E^-(z_p)$  are the forward and backward traveling plane waves at an imagined plane at  $z_p$  between two planes at  $z_1$  and  $z_2$ .

The electric field intensity at any point inside the layer can be calculated by considering an imagined plane ( $z_p$ ) at that point as shown in figure 6.21. Then calculate the transfer matrix  $M_p$  for the layer starting from the plane  $z_p$  to plane  $z_2$ . Then the forward and backward propagating wave at the plane  $z_p$  may be calculated by using equation 6.16 as

$$\begin{bmatrix} E^+(z_p) \\ E^-(z_p) \end{bmatrix} = \begin{bmatrix} M_{p11} & M_{p12} \\ M_{p21} & M_{p22} \end{bmatrix} \begin{bmatrix} t \\ 0 \end{bmatrix} \quad (6.16)$$

where,  $M_{p11}$ ,  $M_{p12}$ ,  $M_{p21}$ ,  $M_{p22}$  are coefficients of transfer matrix  $M_p$ . Finally, by summing the backward and forward wave component at the plane  $z_p$ , the electric field intensity at the plane  $z_p$  can be found as

$$E(z_p) = E^+(z_p) + E^-(z_p) = \frac{(M_{p11} + M_{p21})}{M_{11}} \quad (6.17)$$

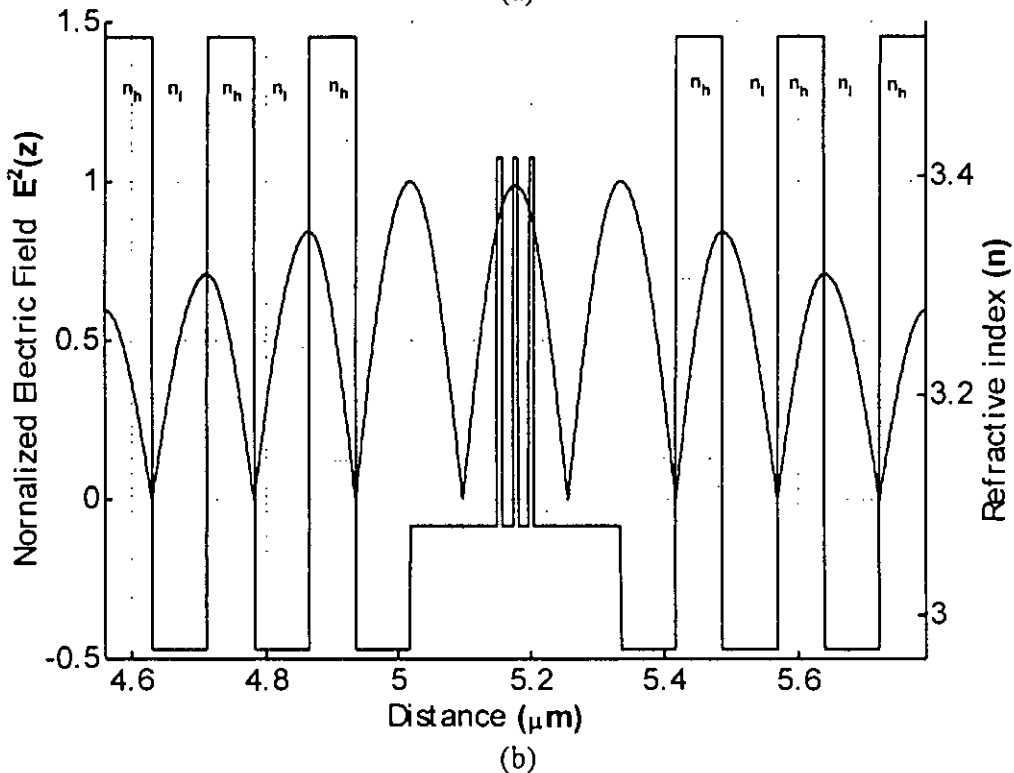
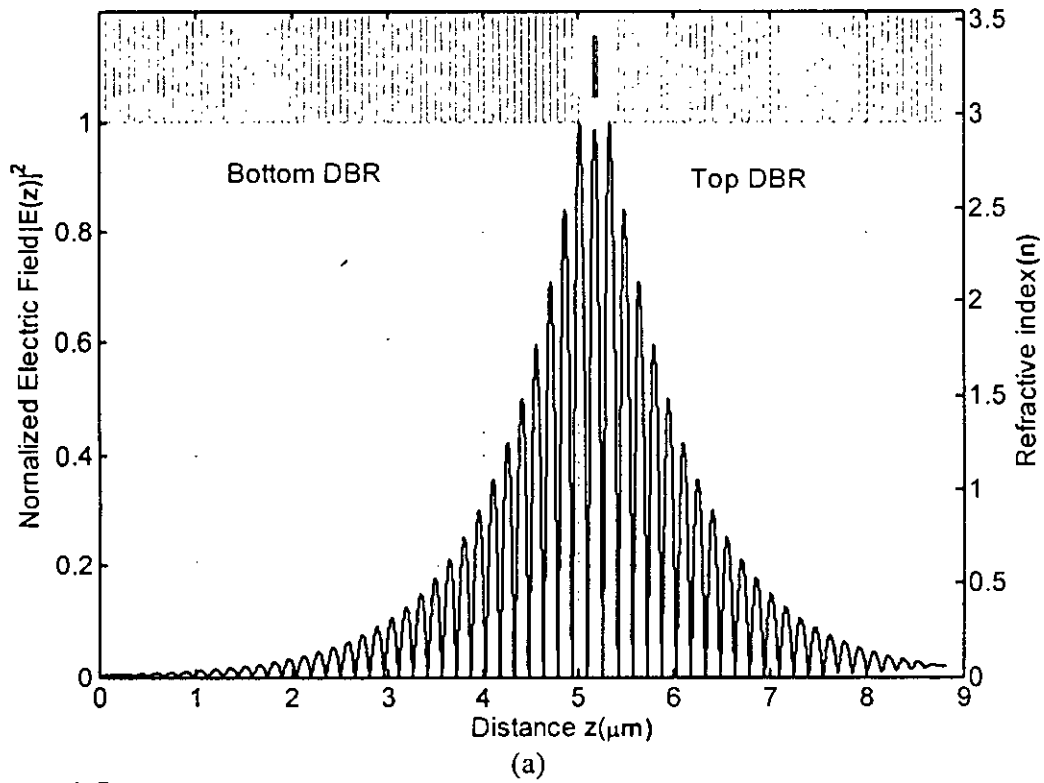


**Figure 6.22** Electric field distribution inside a VCSEL having  $\lambda$  cavity. In the cavity region there are three 10 nm thick  $\text{Al}_{0.2}\text{Ga}_{0.8}\text{As}$  quantum wells, two 11 nm thick barrier layers and two 130 nm thick spacer layers of  $\text{Al}_{0.8}\text{Ga}_{0.2}\text{As}$  materials. Top and bottom DBR have 33 and 23 pairs of GaAs/ AlGaAs quarter wavelength thick dielectric layers respectively. Figure (a) shows the refractive index variation and electric field distribution for a complete VCSEL where as figure (b) shows the refractive index variation and electric field distribution in the cavity region (quantum wells, barrier layers and spacer layers) and few of the DBR layers just near the cavity region.

The VCSEL is a stack of layers of different materials shown in figure-6.14. The structure of VCSEL can be considered as a single layer with varying refractive index  $n(z)$  along the axis  $z$ . In a VCSEL there is no field input from the outside of top and bottom DBR. The optical fields are generated inside the active region and propagate through the top and bottom DBR. Hence the field distributions inside the VCSEL can be calculated by following the procedure discussed above.

The optical power is the absolute square of the electric field amplitude [6]. The optical field intensity inside the VCSEL can be calculated by calculating the field amplitude transmission coefficient using the technique discussed above. Hence the light output from a VCSEL can also be computed by determining the electric field amplitude at the end of the top DBR.

## 6.8 Field Intensity in Different Types of VCSEL Resonator

Now, the electric field intensity inside a new type of VCSEL has been computed by using STMM based model presented in this work. Here two types of VCSEL have been taken for the computation. Both of the VCSEL have the same active layers. Only differences are in the DBR layers. DBR layers of the first VCSEL has pure sinusoidal variation in the refractive index where as the DBR layers of the second VCSEL has the variation in refractive index quite similar to the step index. These types of DBR have been discussed in the Section 6.4. DBR stacks of the first types of the VCSEL can be constructed by setting the value of  $x = 1$  in the equation (6.3). DBR stacks of the second types of the VCSEL can be constructed by setting the value of  $x = 0.2$  in the equation (6.3). Active layer of both of the VCSEL have three GaAs quantum wells each having a thickness of 10 nm. Two barrier layers of  $\text{Al}_{0.5}\text{Ga}_{0.5}\text{As}$  materials each having a thickness of 10 nm are placed between the quantum wells. Two 30 nm thick  $\text{Al}_{0.5}\text{Ga}_{0.5}\text{As}$  spacer layers are placed at the two sides of the quantum wells. Finally, another two 70 nm thick  $\text{Al}_{0.75}\text{Ga}_{0.25}\text{As}$  spacer layers are added at the two end of the cavity to make the thickness of the cavity equal to 1 wavelength.

STMM based model has been used to compute the electric field distribution inside the mentioned in the above paragraph. Electric field distribution inside the first VCSEL has been shown in the figure 6.23. Figure 6.23 (a) shows that the field pattern has the quite similar pattern obtained for the VCSEL having step index layered DBR stacks. Figure 6.23 (b) clearly shows that the maximum value of the electric field occurs at the point from where the DBR layers are started i.e., at the both end of the active layers. Field intensity decreases gradually when travels through the DBR layers. This shows a good agreement with the result obtained by using TMM for the VCSEL having step index layered DBR stacks.

The electric field distribution inside the second type of VCSEL has been shown in the figure 6.24. Figure 6.24 (a) shows that the field pattern has the quite similar pattern obtained for the VCSEL having step index layered DBR stacks. Figure 6.24 (b) clearly shows that the maximum value of the electric field occurs at the point from where the DBR layers are started i.e., at the both end of the active layers. Field intensity decreases gradually when travels through the DBR layers. This also shows a good agreement with the result obtained by using TMM for the VCSEL having step index layered DBR stacks.



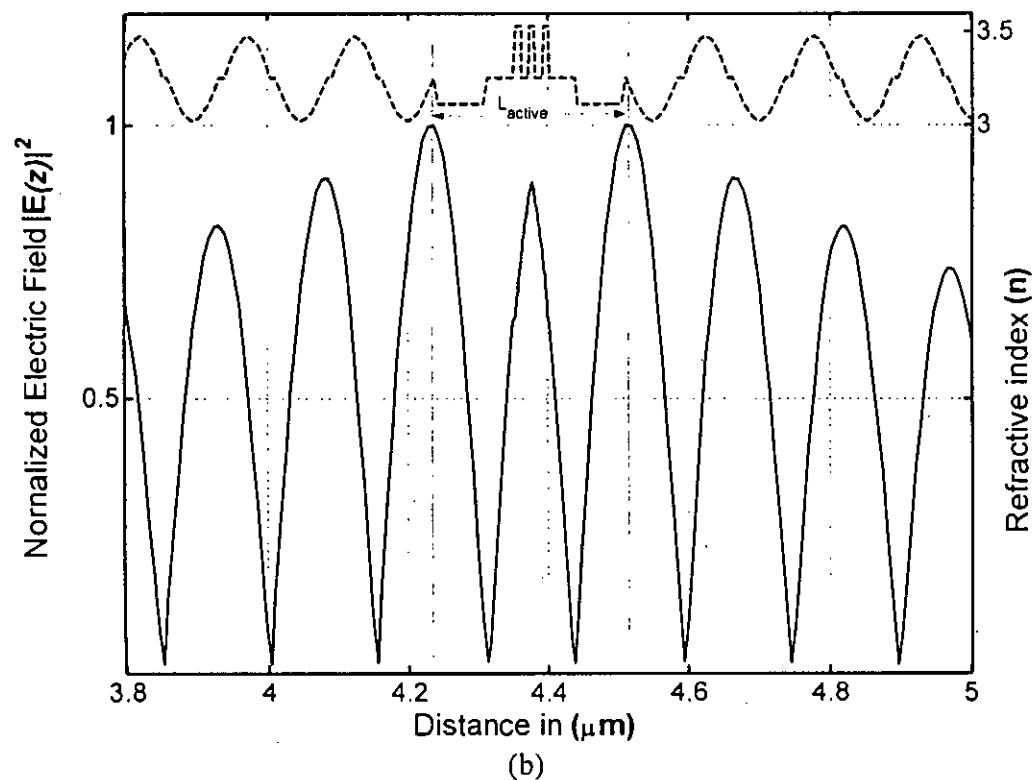
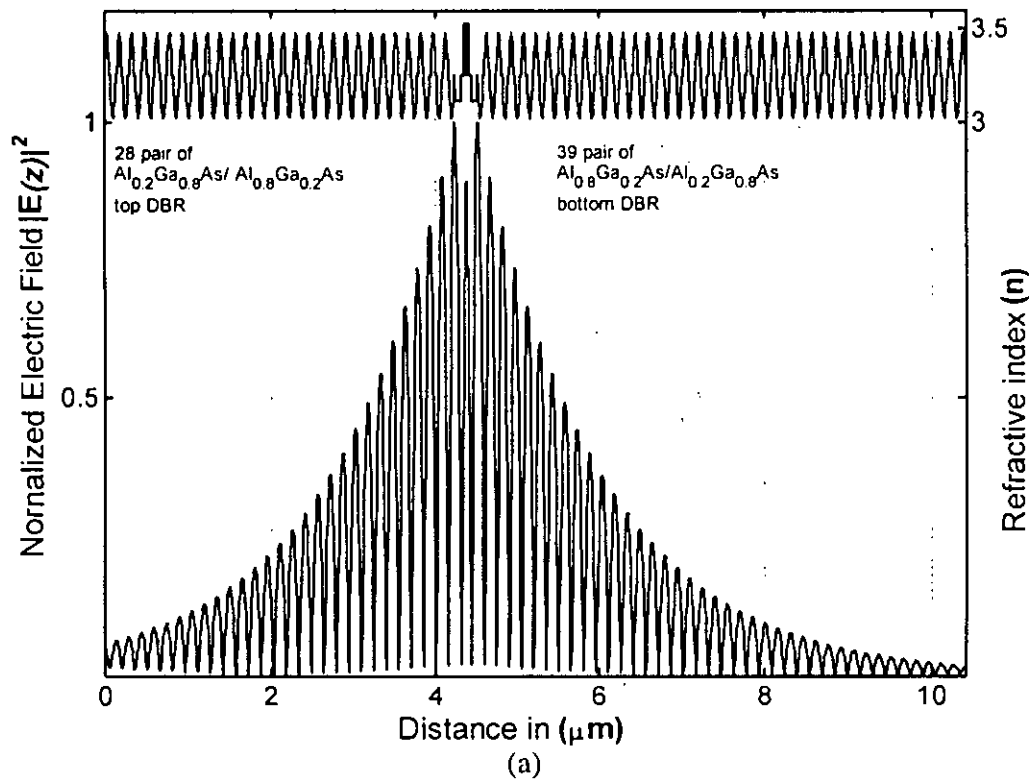
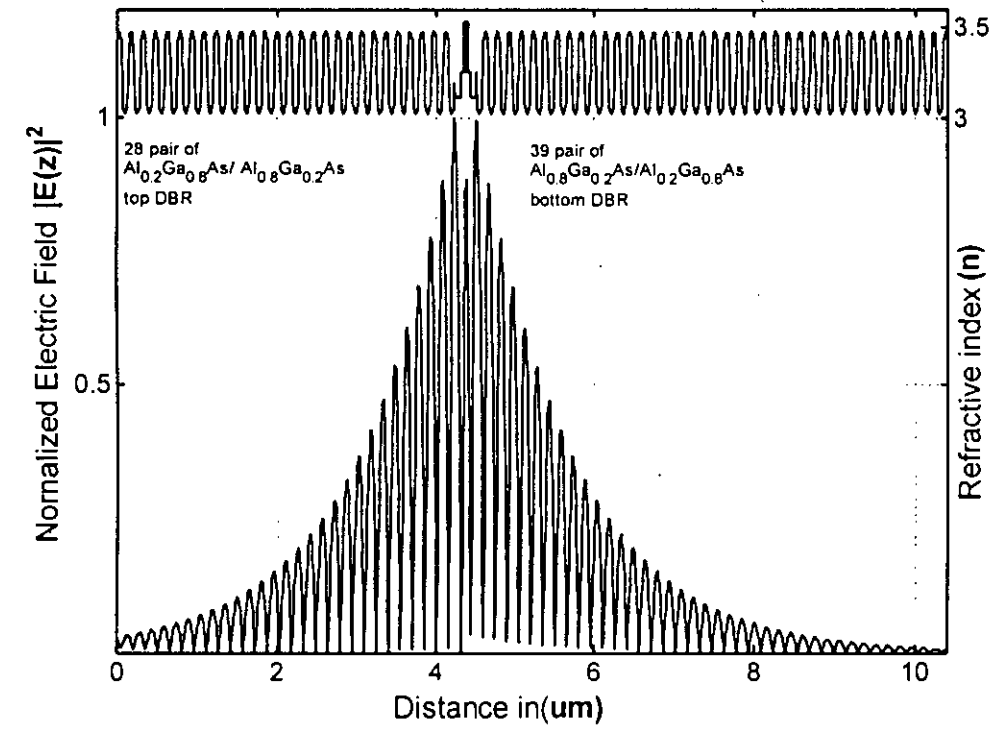
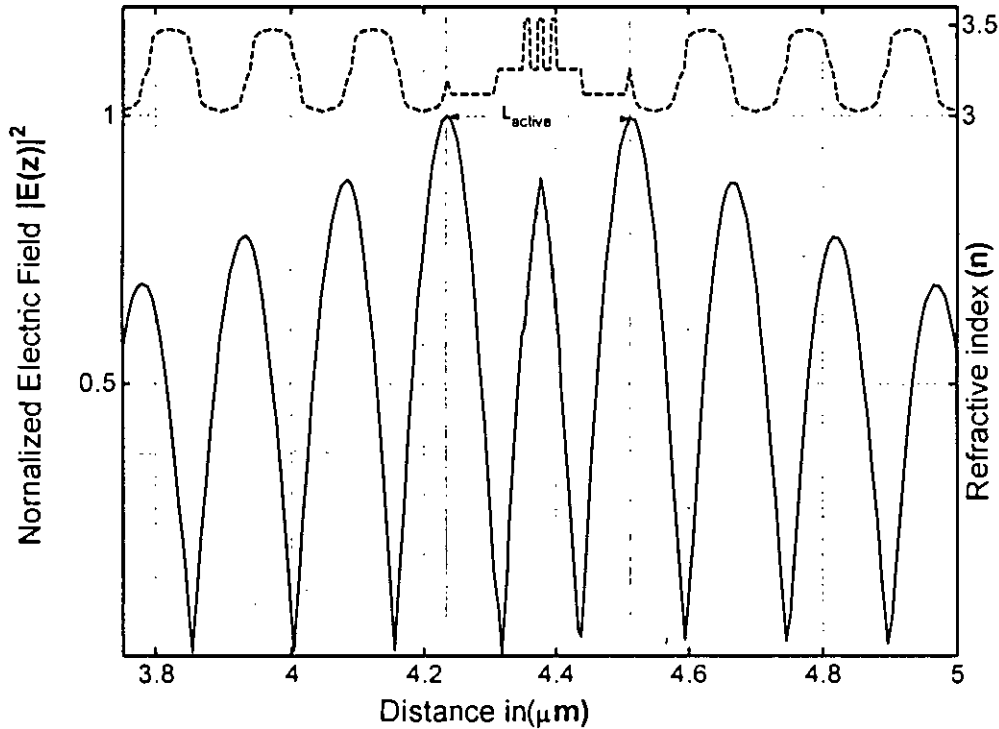


**Figure 6.23** Electric field distribution inside a VCSEL having  $\lambda$  cavity. Top and bottom DBR have 28 and 39 pairs of  $\text{Al}_{0.2}\text{Ga}_{0.8}\text{As}/\text{Al}_{0.8}\text{Ga}_{0.2}\text{As}$  quarter wavelength thick dielectric layers respectively. Variation of refractive index in the layers of the DBR is pure sinusoidal. Figure (a) shows the refractive index variation and electric field distribution for a complete VCSEL where as figure (b) shows the refractive index variation and electric field distribution in the cavity region (quantum wells, barrier layers and spacer layers) and few of the DBR layers just near the cavity region.



(a)



(b)

**Figure 6.24** Electric field distribution inside a VCSEL having  $\lambda$  cavity. Top and bottom DBR have 28 and 39 pairs of  $\text{Al}_{0.2}\text{Ga}_{0.8}\text{As}/\text{Al}_{0.8}\text{Ga}_{0.2}\text{As}$  quarter wavelength thick dielectric layers respectively. Variation of refractive index in the layers of the DBR is quite similar to step index. Figure (a) shows the refractive index variation and electric field distribution for a complete VCSEL where as figure (b) shows the refractive index variation and electric field distribution in the cavity region (quantum wells, barrier layers and spacer layers) and few of the DBR layers just near the cavity region.

## 6.9 Summary

Basic idea of Sampled Transfer Matrix Method (STMM) has been presented at the beginning of this chapter. Reflectivity and transmittivity of a DBR stack having step index variation in the layers have been computed by using TMM and STMM. Comparing the results obtained by these two methods, accuracy of the STMM has been discussed. Reflectivity of a DBR stack having smooth variation of refractive index in the layers has been computed using STMM. Next, reflectivity and transmittivity of a complete VCSEL has also been computed by using STMM. An STMM based model for computing the electric field distribution inside a VCSEL has been discussed. Electric field distribution inside a VCSEL having step index layered DBR stacks have been computed by using the model presented in this work. Same computation has been done for the VCSELs having smoothly varying refractive index layered DBR stacks.

## Chapter 7

### Operation of a VCSEL in the Presence of External Optical Feedback

#### 7.1 Introduction

Amplitude of the electric field inside a VCSEL has its maximum value at the active region since it is amplified in this region. On the other hand, the field intensity decreases with the distance from the active region towards the top or bottom facet due to reflection at different interfaces and the intrinsic losses of the DBR materials. It is important to know the exact distribution of electric field inside the VCSEL to design a device properly as well as to analyse the optical feedback from an external reflector to the VCSEL. An STMM based new technique of computing the electric field distribution inside the multilayer semiconductor or dielectric material stacks has been discussed in details in the chapter 6. By using the same technique, electric field distribution inside a VCSEL is computed in this chapter considering optical feedback from an external reflector. Next, the intensity of standing wave due to different position of the external reflector is computed. Finally, the variation of the performance parameters of a VCSEL such as output power, threshold current, external differential quantum efficiency are computed at different position of the external reflector.

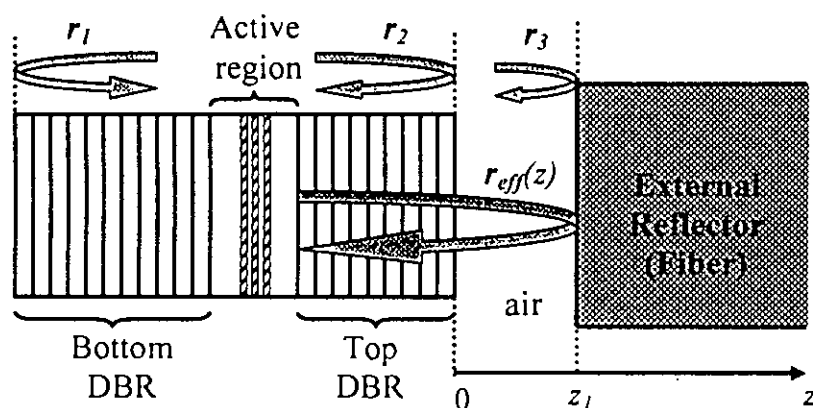


**Figure 7.1** Arrangement of a VCSEL with optical feedback from an external reflector (optical fiber cable).  $r_1$ ,  $r_2$  and  $r_3$  are the field reflectivities of bottom DBR, top DBR and external fiber optic reflector respectively. The effective reflectivity  $r_{eff}(z)$  is defined to consider both  $r_2$  and  $r_3$ .  $r_{eff}(z)$  is a periodic function of external reflector position  $z$ .

#### 7.2 Analytical Model of a VCSEL with Optical Feedback

Here a GaAs/AlGaAs based VCSEL have been selected. The VCSEL have three  $\text{Al}_{0.2}\text{Ga}_{0.8}\text{As}$  quantum wells of 8 nm each located at the center of the cavity.  $\text{Al}_{0.8}\text{Ga}_{0.2}\text{As}$  barrier layers are placed between consecutive quantum well layers and also on the two sides of the quantum well layer. Top and bottom DBR (GaAs/AlAs) stacks have 23 and 33.5 pairs respectively to make the VCSEL top emitting.

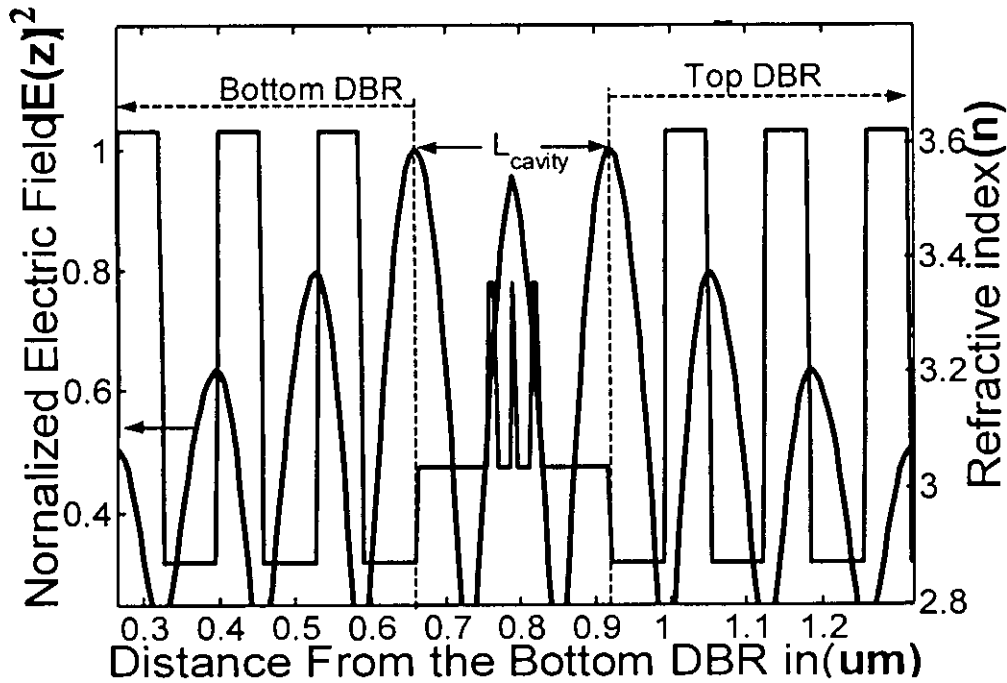


**Figure 7.2** Standing-wave pattern of the electric field in a VCSEL. Standing-wave in the  $\lambda$  cavity region and up to 3 pairs of top and bottom DBR layers has been plotted.

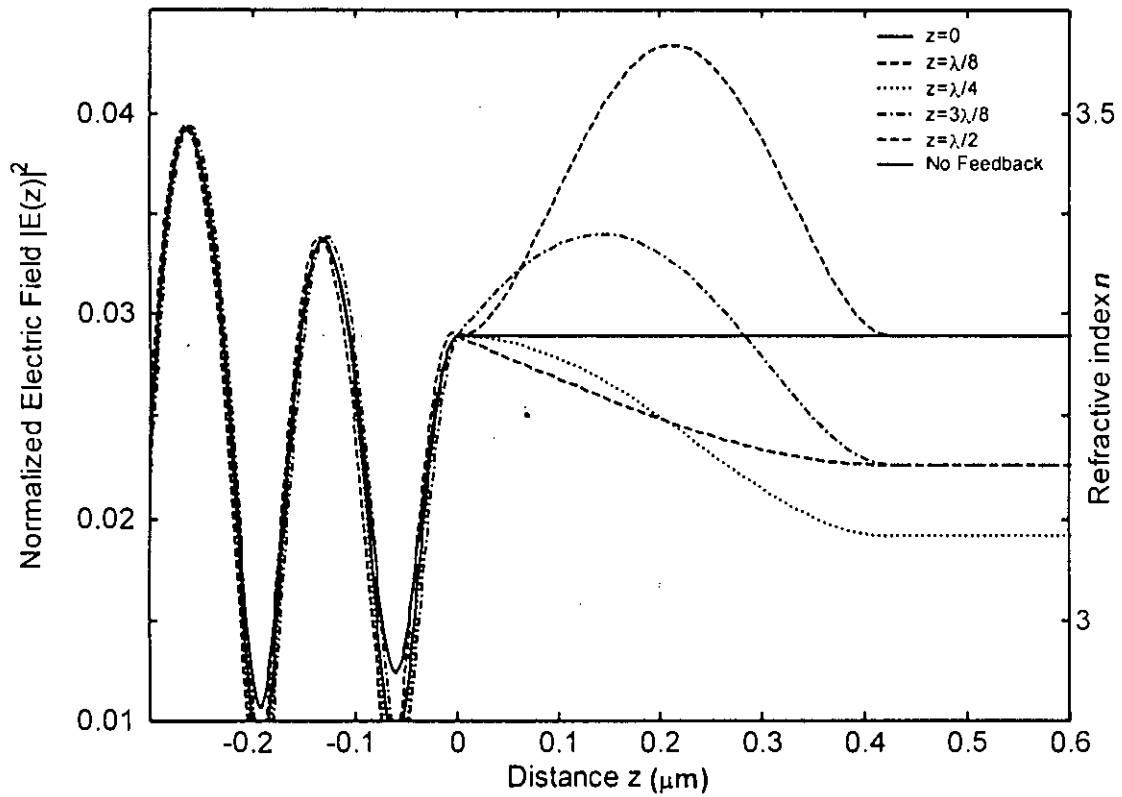
Figure 7.2 shows the electric field distribution for the VCSEL obtained after simulation using the above mentioned parameters and using the STMM model presented in section II. This plot has close resemblance with the similar figure of [40] which was obtained by using a different model.

Schematic diagram of a VCSEL with external optical feedback is shown in the figure 7.1. External reflector (fiber optic cable) is placed at a little distance apart from the top DBR. The medium between the VCSEL and the fiber optic cable is air. Now, Electric field distribution can be computed by using the STMM as discussed in the chapter 6. The only modification needed is to consider the medium between VCSEL and external reflector which is air and the external reflector as two extra layers attached at the end of the top DBR.

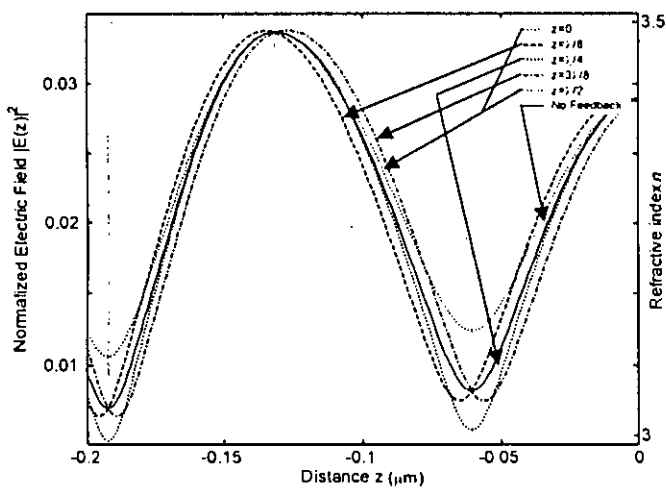
Figure 7.3 (a) shows the simulation results of electric field distribution inside the top DBR region (only few layers) and also inside the external reflector. Figure 7.3 (b) and (c) shows the electric field distribution inside the layers of top DBR near the active region and near the output facet respectively. Simulation has been performed considering i) the optical feedback, ii) without optical feedback and ii) different positions of the external reflector.

Normalized field intensity near the cavity region does not vary noticeably with or without optical feedback as shown in figure 7.3 (c). Near the output facet, the distribution of field intensity is different when optical feedback is considered than that of without optical feedback as shown in the figure 7.3 (b). At the first interface, from the output facet, nodes of standing wave occur in 4 cases: i) when there is no external reflector, ii) when the external reflector is at  $z=0$  distance, iii) when the external reflector is at  $z=\lambda/4$  distance and iv) when the external reflector is at  $z=\lambda/2$  distance from the output face. Similarly, antinodes of the standing wave occur at the second interface from the output facet for the previous 4 cases. But the nodes and antinodes of the standing wave are occurred before

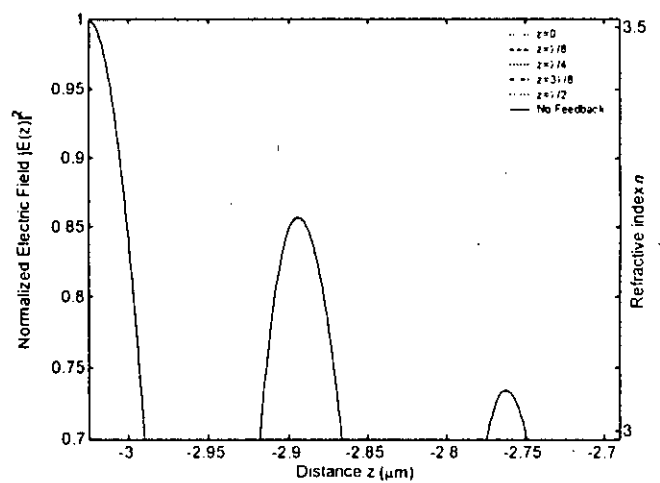
and after the interfaces when the external reflector is placed at  $z=\lambda/8$  and  $z=3\lambda/8$  distances from the output face respectively.



(a)



(b)



(c)

**Figure 7.3** Normalized electric field distribution inside a VCSEL and external reflector with and without optical feedback. Distance ( $z$ ) of external reflector is measured from the output facet. (a) shows the plot of normalized electric field distribution inside few of the top DBR layers and external reflector. (b) shows the plot of normalized electric field distribution inside top DBR near the output facet. (c) shows the plot of normalized electric field distribution inside the top DBR near the active region.

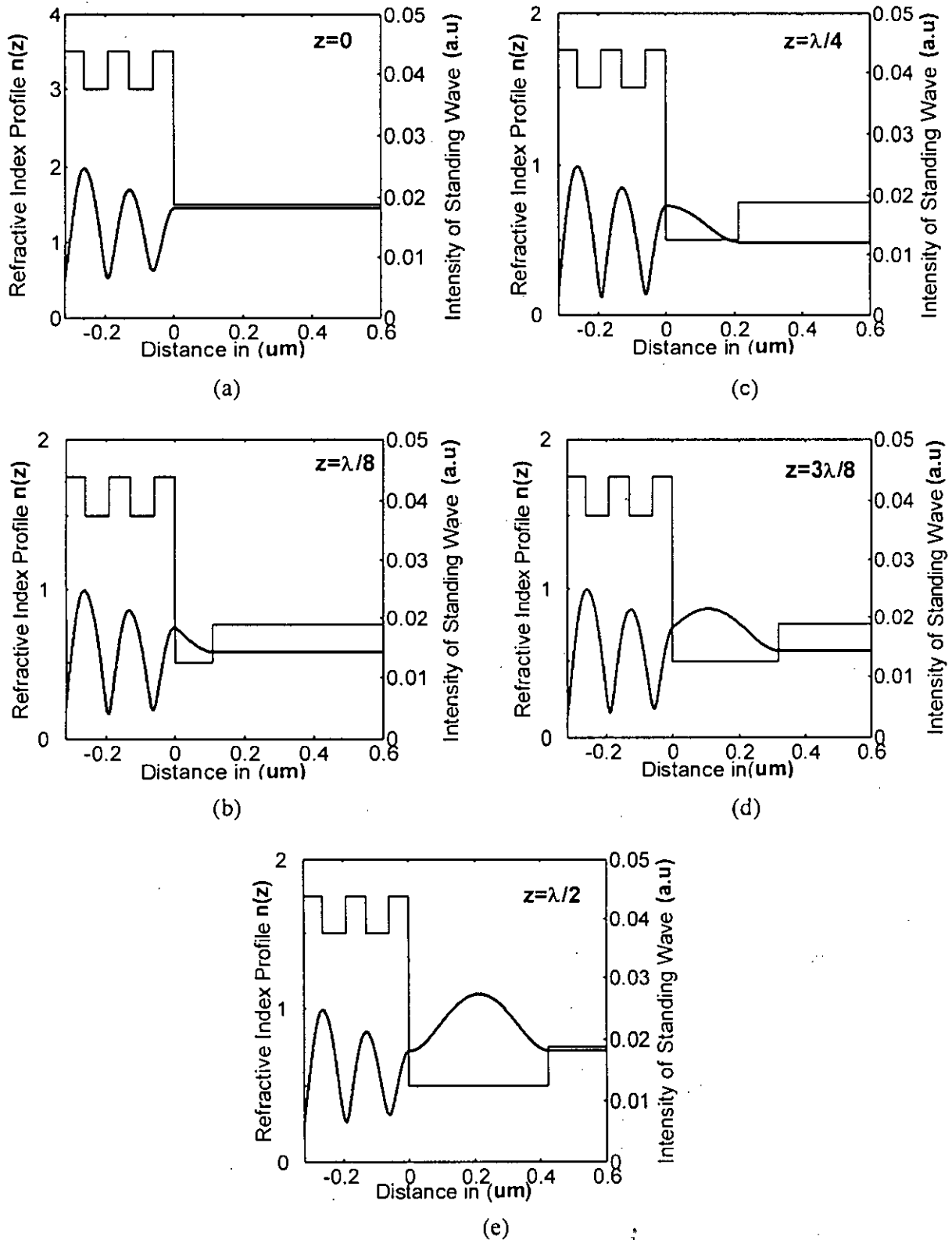


**Figure 7.4** Refractive index of few of the DBR (step change of refractive index) layers of a VCSEL and external reflector (optical fiber) and intensity of standing wave pattern due to different fiber position. Thin line is for refractive index and thick line is for intensity of standing wave. Distance ( $z$ ) of external reflector is measured from the output facet. (a)  $z=0$  (b)  $z=\lambda/8$  (c)  $z=\lambda/4$  (d)  $z=3\lambda/8$  (e)  $z=\lambda/2$

### 7.3 Electric Field Distribution inside a VCSEL due to Different Positions of the External Reflector

Electric field distribution inside a VCSEL due to different positions of the external reflector is computed by using STMM. Parameters of the VCSEL mentioned in the section 7.2 have been used to compute the normalized electric field. Figure 7.4 shows the simulation results of electric field intensities in some of the top DBR layers and external reflectors due to the variation of the external reflector positions. The refractive index of different layers of the DBR varies between 3~3.5. The refractive index  $n_{air}$  of the air gap between the top facet and the external reflector is 1.0. The refractive index  $n_f$  of the external reflector (glass fiber) is 1.5. Figure 7.4 (a) shows that the optical field intensity (square of the electric field intensity) in the fiber is maximum for the fiber position at  $z=0$ . Figure 7.4 (b) shows that the external reflector at  $z=\lambda/8$ , field intensity decreases since it is not in the resonance mode for the external cavity in the region between top DBR and fiber facet. Figure 7.4 (c) indicates that at  $z = \lambda/4$  the field intensity comes down to its minimum value. The field intensity in the fiber increases again for the fiber position at  $z=3\lambda/8$  as shown in Figure 7.4 (d). At  $z=\lambda/2$  the field intensity reaches to its maximum value again since the external cavity between the VCSEL and external reflector is in resonance condition as shown in Figure 7.4 (e).

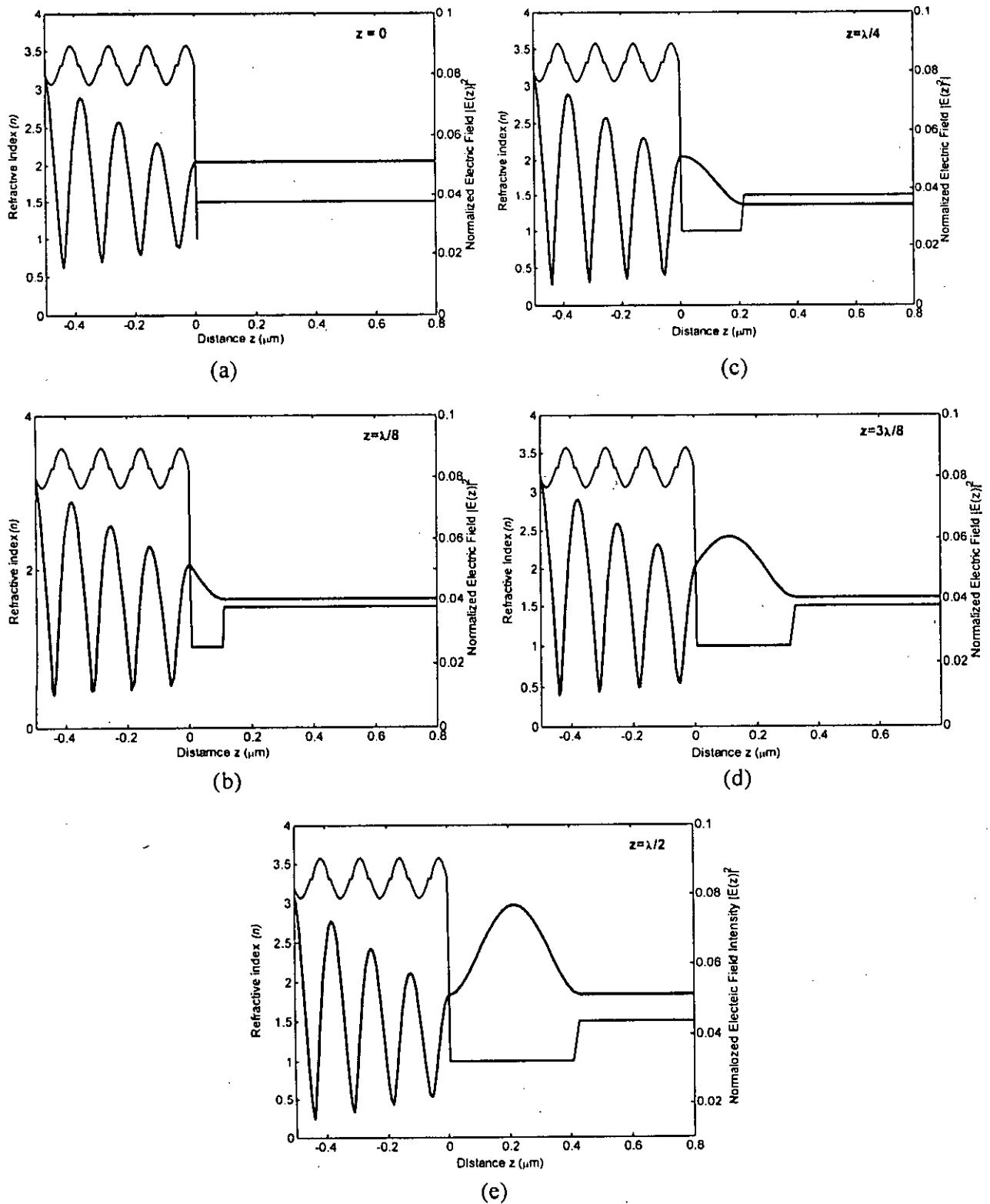
### 7.4 Electric Field Distribution inside a VCSEL having Different DBR Structures due to External Optical Feedback

The construction of the active layer of the VCSEL used for simulation is same as mentioned in the section 7.2. But the top and bottom DBR are different from the section 7.2 by materials and structures. Three types of DBR (step index to sinusoidal variation in refractive index DBR) have been used for simulation. Constructions of such DBR are clearly explained in the chapter 6.

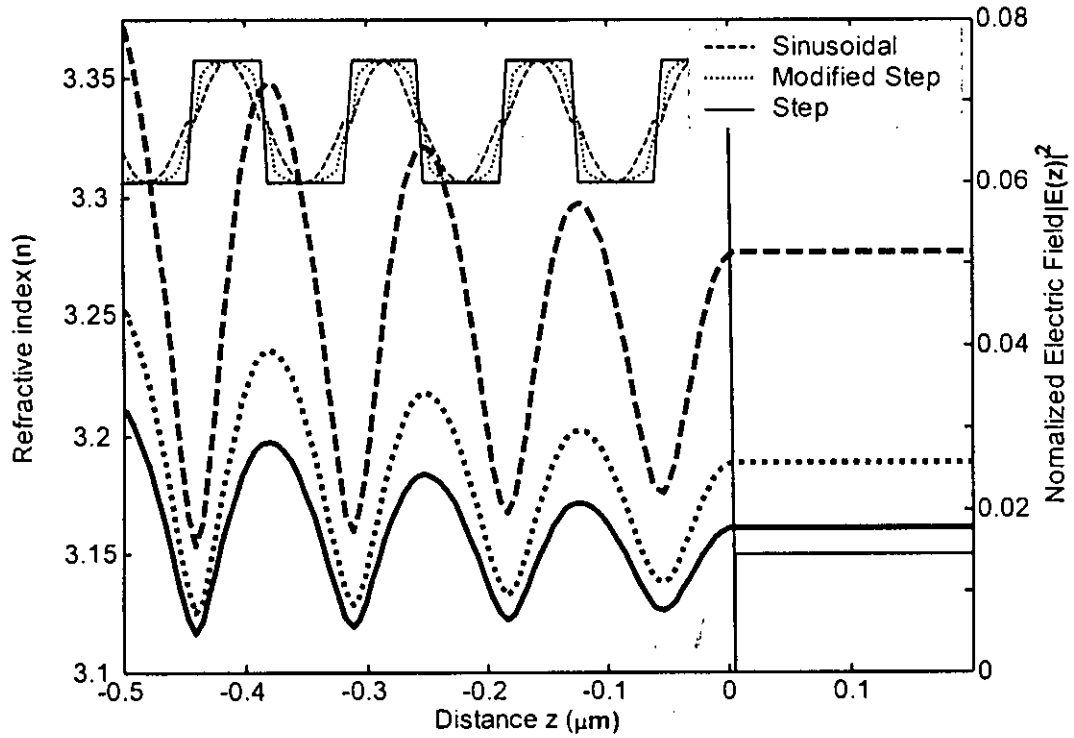
The top DBR and bottom DBR are made of  $Al_xGa_{1-x}As/Al_xGa_{1-x}As$  materials with different values of  $x$  ( $0.1 \leq x \leq 0.9$ ). Material for  $n_{h,max}$  is  $Al_{0.1}Ga_{0.9}As$  and  $Al_{0.9}Ga_{0.1}As$  is used for  $n_{l,min}$ . Top DBR has 26 pairs. Normalized electric field distribution is computed by using STMM and plotted in the figure 7.6. Value of  $x$  in the equation 6.3 is set to 0 to get step index DBR, 0.2 to get modified index DBR and 1 to get sinusoidal DBR. External reflector is placed at  $z=0$  position.

Figure 7.6 shows the simulation result of electric field distribution inside a VCSEL having different types of DBR. For all of the three cases, nodes and antinodes are occurred at the interfaces of the layers. Among them, VCSEL with sinusoidal variation of refractive index in DBR layer have the highest output optical power where as a VCSEL with step index DBR layer have the lowest output optical power. It is obvious because the step index DBR has the highest reflectivity.

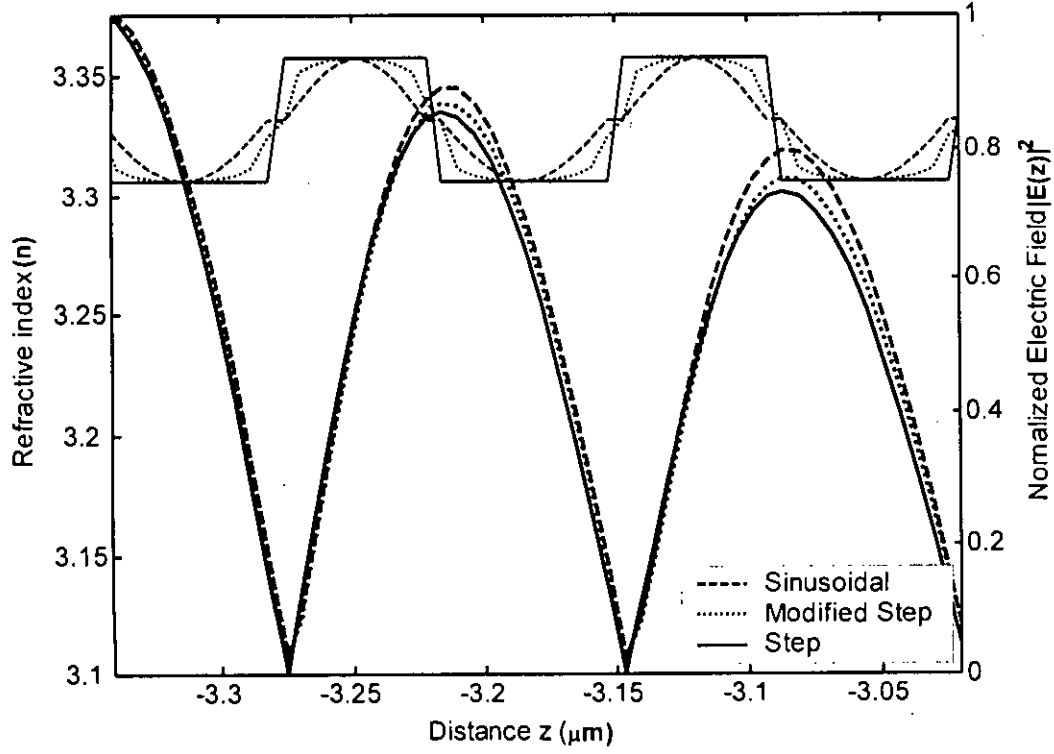




**Figure 7.5** Refractive index of few of the DBR (sinusoidal variation of refractive index) layers of a VCSEL and external reflector (optical fiber) and intensity of standing wave pattern due to different fiber position. Thin line is for refractive index and thick line is for intensity of standing wave. Distance ( $z$ ) of external reflector is measured from the output facet. (a)  $z=0$  (b)  $z=\lambda/8$  (c)  $z=\lambda/4$  (d)  $z=3\lambda/8$  (e)  $z=\lambda/2$



(a)



(b)

**Figure 7.6** Simulation result of electric field distribution of a VCSEL with optical feedback. DBR of the VCSEL have 3 different structures. The external reflector is placed at a distance  $z = 0$  from the top DBR. Thin lines are for refractive index and thick lines are for normalized electric field.

## 7.5 Effects of Optical Feedback on the Operation of a VCSEL

Schematic arrangement of a VCSEL with external optical feedback is shown in the figure 7.1. As discussed in the previous sections that due to optical feedback from an external reflector the electric field distribution inside a VCSEL varies significantly. This external feedback may change the operating parameters of a VCSEL such as threshold current, threshold gain, external differential quantum efficiency and output power. All of these parameters are related to each other. Threshold current depends on threshold gain. Threshold gain and external differential quantum efficiency are depending on the facet reflectivity of the VCSEL. Output power depends on the threshold current and external differential quantum efficiency.

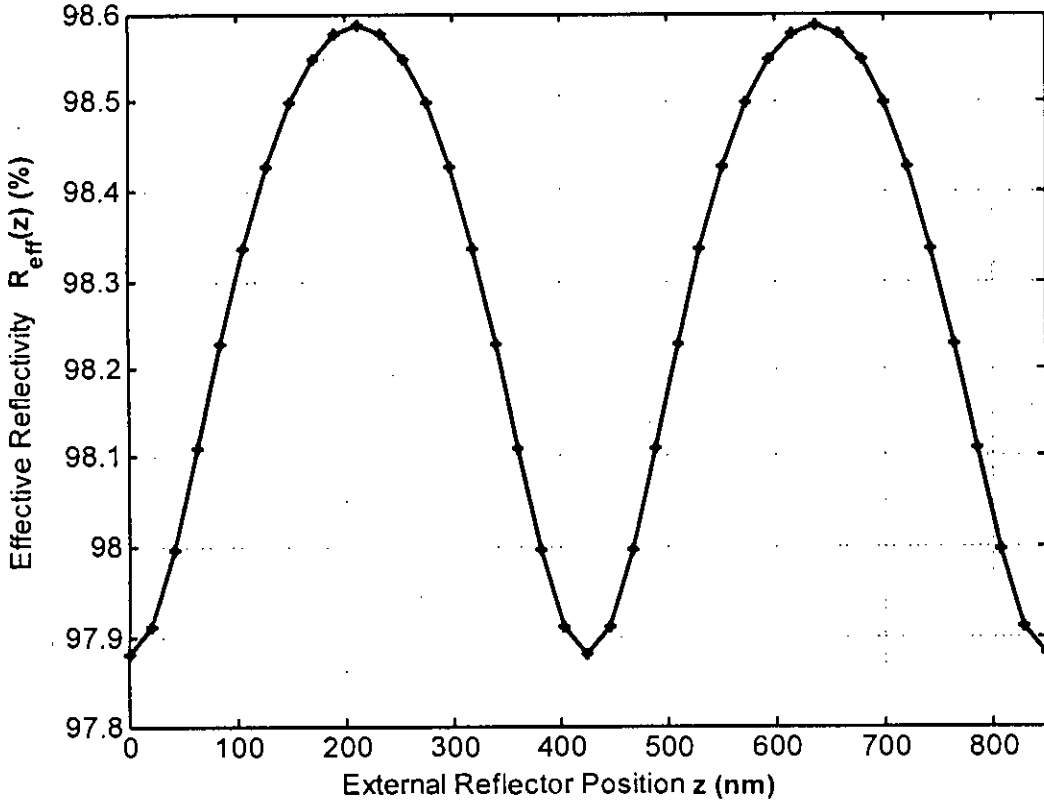


**Figure 7.7** Simulation result of effective reflectivity  $R_{eff}(z)$  for different position of the external reflector.  $R_{eff}(z)$  become maximum for the position of external reflector electric at  $z=\lambda/8$  and  $3\lambda/8$ .  $R_{eff}(z)$  become minimum for the position of external reflector electric at  $z=0$ ,  $z= \lambda/4$  and  $z= \lambda/2$ .

As shown in the figure 7.1, due to external reflector the effective field reflectivity of the top DBR side will be  $r_{eff}(z)$  instead of  $r_2$ . Hence  $r_{eff}(z)$  as well as power reflectivity  $R_{eff}(z)$  will vary with  $z$ . Figure 7.7 shows the simulation result of  $R_{eff}(z)$  as a function of external reflector position  $z$ .  $R_{eff}(z)$  is computed by using STMM. Result shows that when the external reflector is placed at the position  $z=0$ ,  $z=\lambda/4$  and  $z= \lambda/2$  from the output facet then  $R_{eff}(z)$  become its maximum value (98.58%). When the external reflector is placed at the position  $z=\lambda/8$  and  $z= 3\lambda/8$  from the output facet then  $R_{eff}(z)$  become its minimum value (97.88%). These variations of  $R_{eff}(z)$  will affect the other operating parameters discussed in the following sections.

## 7.6 Variation of Threshold Current due to External Optical Feedback

Threshold current density of a semiconductor laser is derived in terms of threshold carrier density and threshold gain in chapter 4. The threshold current density and threshold current for a quantum well VCSEL can be written as [4]

$$J_{th} = J_{th,0} \exp\left(\frac{\Delta g_{th}}{g_0}\right) \quad (7.1)$$

$$I_{th} = I_{th,0} \exp\left(\frac{\Delta g_{th}}{g_0}\right) \quad (7.2)$$

where,  $g_0$  is the peak gain constant,  $J_{th,0}$  is the steady state component of threshold current density,  $I_{th,0}$  is the steady state component of threshold current and  $\Delta g_{th} = g_{th}(z) - g_{th,0}$  is the variation of gain due to the variation of optical feedback level.

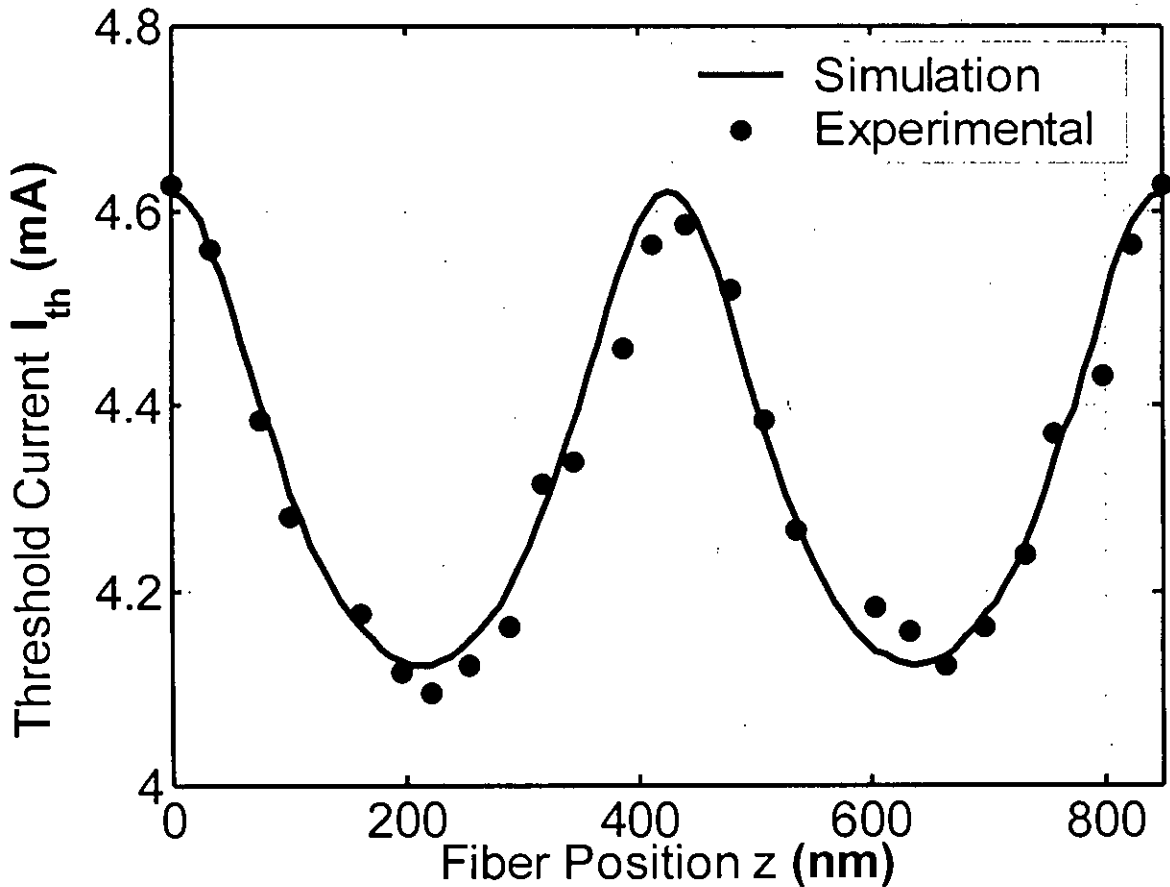


**Figure 7.8** Theoretical threshold current  $I_{th}$  as a function of fiber position. The plot in solid line has been obtained using the analytical expression developed in this work. Superimposed experimental result has been obtained from [4].

Threshold gain for the VCSEL without optical feedback can be calculated by using the following equation [8].

$$g_{th} = \Gamma g = \alpha_i + \alpha_m = \alpha_i + \frac{1}{2L} \ln \frac{1}{R_1 R_2} \quad (7.3)$$

where,  $\Gamma$  is the optical confinement factor,  $g$  is the optical power gain coefficient,  $\alpha_i$  is the internal loss  $= 10 \text{ cm}^{-1}$ ,  $\alpha_m$  is mirror loss and  $R_1$  and  $R_2$  is power reflectivities of bottom and top DBR respectively.

When an external reflector is placed near the light emitting side (top DBR) of the VCSEL then the mirror loss and threshold gain will depend on the effective reflectivity of the top side  $R_{eff}(z)$  rather than only  $R_2$ . Now, the mirror loss and threshold gain can be expressed as a function of the external reflector position by replacing  $R_2$  of equation (12) by  $R_{eff}(z)$ .

$$\alpha_m(z) = \frac{1}{2L} \ln \frac{1}{R_1 R_{eff}(z)} \quad (7.4)$$

$$g_{th}(z) = \alpha_i + \frac{1}{2L} \ln \frac{1}{R_1 R_{eff}(z)} \quad (7.5)$$

The effective power reflectivity due to the different position of external reflector  $R_{eff}(z)$  can be calculated by using the model presented in section II.  $g_{th,0} = g_{th}(z=0)$ , value of  $g_{th,0}$  is chosen from the model ( $g_{th,0} \sim 1650 \text{ cm}^{-1}$ ).  $I_{th,0}$  was set to the corresponding measured value of  $I_{th} = 4.62 \text{ mA}$  [4] and  $g_0 = 2g_{th,0}$ . The variation of  $I_{th}$  over fiber position is shown in figure 7.8.  $I_{th}$  reaches its maximum value at  $z=0$ ,  $\lambda/2$  and  $\lambda$ . This is good agreement with the experimental results in of other researchers [4]. The Experimental values of threshold current have been extracted from the plot presented in [4].

## 7.7 Variation of External Differential Quantum Efficiency

The external differential quantum efficiency  $\eta_d$  without optical feedback has been discussed in the section 3.12. From equation 3.50  $\eta_d$  can be written as.

$$\eta_d = \eta_i \frac{\text{Mirror loss}}{\text{Total loss}} = \eta_i \frac{\alpha_m}{g_{th}} \quad (7.6)$$

where,  $\eta_i$  is the internal quantum efficiency. If an external reflector is present then equation (7.6) can be written as

$$\eta_d(z) = F(z) \eta_i \frac{\alpha_m(z)}{\Gamma g_{th}(z)} \quad (7.7)$$

with,

$$F(z) = \frac{T_{eff}(z)}{(1 - R_{eff}(z)) + \sqrt{\frac{R_{eff}(z)}{R_1}(1 - R_1)}} \quad (7.8)$$

Here,  $F(z)$  is the total power output from the top facet. Determining  $T_{eff}(z)$ ,  $\alpha_m(z)$ ,  $g_{hi}(z)$  and  $\Gamma$  from the model and setting  $\eta_i=0.9$  and  $R_{eff}(z)=1-T_{eff}(z)$ , the variation of differential quantum efficiency can be found that it varies with the fiber position as shown in figure 7.9.

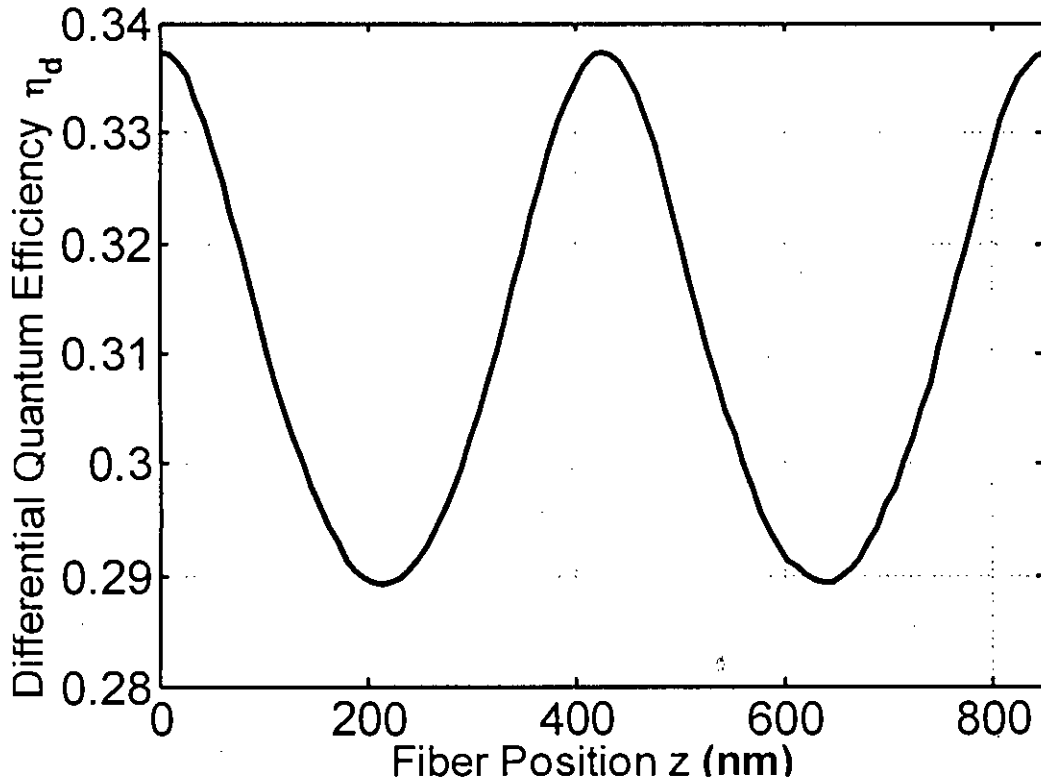


**Figure 7.9** Variation of external differential quantum efficiency  $\eta_d$  as a function of fiber position

## 7.8 Analysis of Output Power Variation of a VCSEL

According to the equation 3.63, Output power from the VCSEL due to variation of external reflector position can be written as

$$P_{out}(z) = \eta_d(z) \frac{\hbar\omega}{q} (I - I_{th}(z)) \quad (7.9)$$

The values of  $\eta_d(z)$  and  $I_{th}(z)$  has been determined in the section 7.7 and 7.6 for varying fiber position and for  $I = 5.0$  mA [4]. Since  $\eta_d(z)$  and  $I_{th}(z)$  are dependent on external reflector positions,  $P_{out}(z)$  obviously vary with  $z$ . Simulation result of output power, varying with the fiber position, is presented in figure 7.10 with superimposed experimental results. The Experimental values of output

power have been extracted from the plot presented in [4]. The simulation results obtained by the developed model show good agreement with the experimental results.

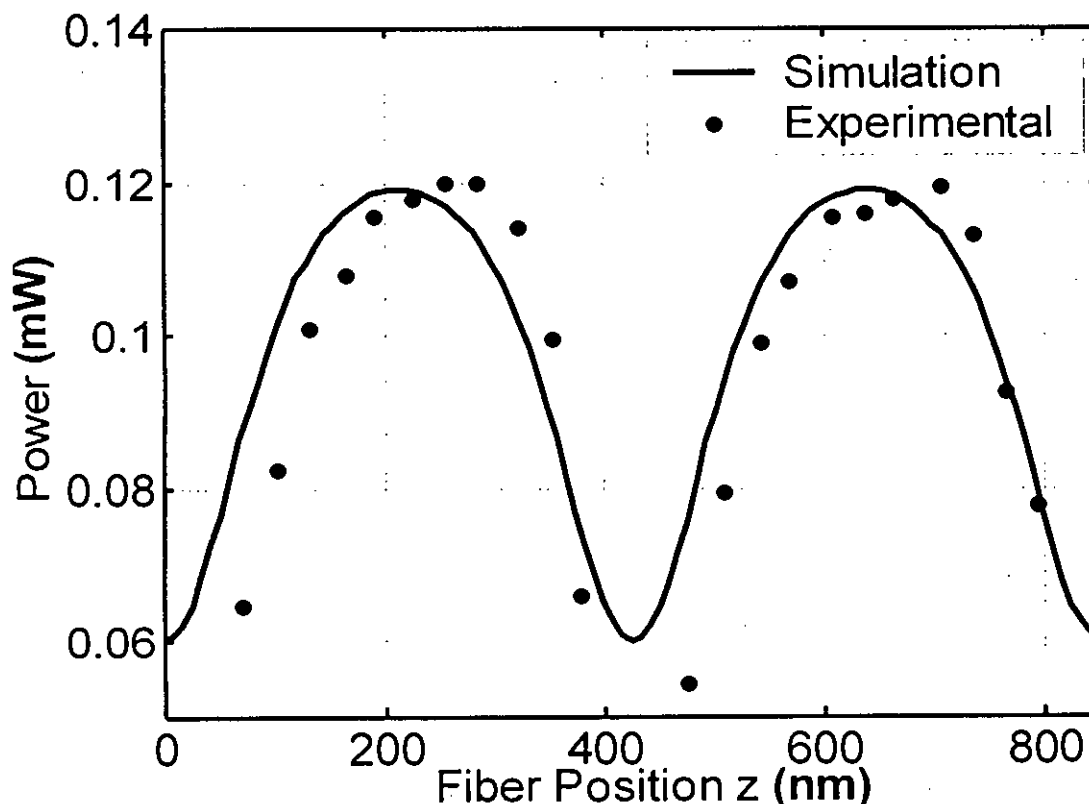


**Figure 7.10** Output power  $P_{out}(z)$  variation as a function of fiber position. The plot in solid line has been obtained using the analytical expression developed in this work. Superimposed experimental result has been obtained from [4].

## 7.9 Summary

An analytical model of a VCSEL considering external optical feedback has been presented at the beginning of this chapter. Electric field distribution inside a VCSEL due to external optical feedback has been computed using the developed STMM based model. Field distribution has also been computed for different position of the external reflector using the developed model. Next, the electric field distribution inside VCSELs having different types DBR stacks have been computed and presented. Computation of the performance parameters of a VCSEL such as threshold current, external differential quantum efficiency and output power due to the optical feedback from the external reflector placed at different positions have also been computed.

## Chapter 8

# Dynamic Behaviour of a VCSEL with and without External Optical Feedback

## 8.1 Introduction

Operation of a Laser is based on the optical transition of electrons between conduction and valence bands. Due to this reason inevitable quantum noise problem comes up in this case. A semiconductor laser usually possesses a high gain, has a wide gain-bandwidth and has a wide longitudinal mode separation. Ordinary FP semiconductor lasers use a resonator consisting of the facet mirrors with low reflectivities. The fluctuation in the carrier density affects the phase of the optical wave since the active region is injected with a high density of carriers. Therefore, semiconductor lasers exhibit unique noise characteristics unlike the noise characteristics of other types of lasers. It is necessary to understand the noise characteristics of all applications of VCSEL, especially for achieving the ultimate performances in long-distance high-speed optical data transmissions and precision optical measurements. Having understood the noise characteristics the next job is to improve the noise characteristics. Noises of the output light from a practical laser are classified into i) intrinsic noises and ii) extrinsic noises. In the following sections the basic concepts of theoretical noise analysis are presented in short. Next, the quantum noises under the single-mode steady-state oscillation are discussed in terms of the intensity and frequency noises. Finally, noises in a VCSEL caused by external feedback are computed and the results are plotted of analysis.

## 8.2 Different Types of Noise in Semiconductor Laser

Noises related to semiconductor lasers may be classified as i) Quantum Noises, ii) Noises in Longitudinal Modes and iii) External Noises. Quantum noises may be divided into i) Amplitude Modulating (AM) noise caused due to the fluctuation in the light amplitude and ii) Frequency Modulating (FM) noise caused due to the fluctuation in the frequency of the emitted light. Noises in Longitudinal Modes may be divided into i) Mode Partition Noise (MPN) and ii) Mode Hopping Noise. External noises may also be divided into i) Optical Feedback Noise and ii) Noise due to fluctuations in temperature, driving current and voltage. The above mentioned noises will be briefly discussed in brief in the following paragraphs.

As mentioned above, quantum noises are divided into Amplitude modulating (AM) noise and frequency modulating (FM) noise. Both of these quantum noises are caused by the spontaneous emission in a free space with random amplitudes, frequencies, and phases of the lights. In addition to spontaneous emission, FM noise is also affected by AM noise as explained below.

Due to AM noise, the amplitude of the light field fluctuates, which modulates the carrier concentration in the active layer and leads to carrier noise. As a result, through the free carrier plasma effect, the refractive indexes of the material of the semiconductor laser fluctuate, which results in FM noise. Also, the carrier noise induced by AM noise generates electric current noise, which changes Joule heating in the active layer. Therefore, the refractive indexes of semiconductors fluctuate, which also results in FM noise. AM noise is also altered by the carrier noise induced by AM noise itself.



Noise in Longitudinal Modes is another type of noise that may affect the operating mode of a semiconductor laser. Mode Partition Noise (MPN) and Mode Hopping Noise are the two types of noise in Longitudinal Modes.

The mode partition noise is observed when a longitudinal mode is selected during multimode operation. This noise is large in low frequencies. In multimode LDs, such as Fabry-Perot LDs under pulsed operations or the gain guiding LDs, a noise for a total light intensity is comparable to the noise in single-mode LDs. However, a noise for each longitudinal mode in the multimode LDs is much larger than the noise in the single-mode LDs. As a result, the mode partition noise causes a serious problem in mode selective systems such as the optical fiber communication systems.

The cause of the mode partition noise is that the optical gain is randomly delivered to each mode during multimode operation. Therefore, to prevent the mode partition noise, single-mode LDs are needed.

The mode hopping noise is generated when a longitudinal mode in the single mode LDs jumps to other modes. This mode hopping is closely related to driving conditions such as temperature and the injection current. At the time of the mode hopping, random oscillations between multiple modes are repeated and the noise increases due to a difference in light intensities between the relevant modes.

When there are two competing modes, the noise is large in a low frequency range below 50 MHz; when there are three or more competing modes, the noise is large up to higher frequencies. Note that the mode partition noise is also large during mode hopping. For analog systems, such as video discs, the RIN has to be lower than  $-140$  dB/Hz, and for digital systems, such as compact discs (CD-ROMs), the RIN should be lower than  $-120$  dB/Hz. The causes of the mode hopping noise are fluctuations of the spontaneous emission and a tendency for the optical gain to concentrate on the oscillation mode. To avoid the mode hopping noise, two opposite ways, such as single mode operations and multimode operations are used.

To achieve highly stable single-mode operations, bi-stable LDs or dynamic single-mode LDs are adopted. Bi-stable LDs containing saturable absorbers have hysteresis in I-L curves, which suppresses the mode competition. However, it is difficult for them to keep stable single-mode operations with large extinction ratio during modulation. Hence, the bi-stable LDs are not categorized in the dynamic single-mode LDs. For systems without mode selectivity, such as video and compact discs, multimode operations are also used to reduce mode hopping noise. Multimode operations have a higher noise level than single-mode operations, but the noise level is stable with changes in temperature or the injection current. Therefore, the maximum noise level is lower than the mode hopping noise.

Due to the self-pulsations, multimode operations with low coherence take place, which results in stable operations against the optical feedback noise. As a result, they are widely used as light sources for video discs and compact discs.

External noises are caused by the External Optical Feedback and due to the change of the operating conditions like, temperature, applied voltage etc. Optical feedback noise is generated when the light emitted from a semiconductor laser is fed back to the semiconductor laser itself. A facet of semiconductor lasers forms external cavities with reflective external objects, such as optical components, optical fibers, and optical discs. These external cavities and the internal cavity of the semiconductor laser compose coupled cavities, which induce optical feedback noise. The optical

feedback noise is noticeable even when the relative feedback light intensity is on the order of  $10^{-6}$ . Due to optical feedback noise, the light output characteristics of the semiconductor laser change intricately, according to the distance between reflective external objects and the semiconductor laser, the feedback light intensity, and driving conditions. In static or time averaged characteristics, the light intensity, the number of lasing modes, and the light output spectra are also modified. In dynamic characteristics, a noise level and the shape of the light pulse are altered.

The most serious problem caused by feedback light is enhancement of noises. Due to the feedback light, the quantum noises increased in a certain frequency region. Moreover, laser oscillations become unstable, and the noise increases in a low frequency range, which is less than several hundred megahertz. The increase in this low frequency noise is caused by the random mode hopping between the longitudinal modes in the internal cavity and those in the external cavity.

To stabilize a longitudinal mode in the internal cavity, single-mode LDs such as the DFB-LDs and the bi-stable LDs are needed. To suppress the interference between the feedback light and the internal light, coherence of the laser light should be reduced by high frequency modulation or self-pulsation. To decrease the feedback light intensity, the requirement is a low coupling rate  $\kappa$ , which is achieved by large facet reflectivity and a long cavity. However, a large reflectivity leads to a low light output, and a long cavity results in a large threshold current. Therefore, the optical isolators are used to decrease the feedback light intensity in the optical fiber communication systems, but the cost and size of the optical systems increase.

### 8.3 Rate Equations of a VCSEL with Various Noise Sources

The noises created in the semiconductor laser due to spontaneous emission are termed as quantum noise. Langevin noise sources are used to analyze the quantum noise in semiconductor laser.

$$\frac{dN_h}{dt} = \frac{I}{qV_h} + \frac{N_w V_w}{\tau_e V_h} - \frac{N_h}{\tau_s} - \frac{N_h}{\tau_{sp,h}} \quad (8.1)$$

$$\frac{dN_w}{dt} = \frac{N_h V_h}{\tau_s V_w} - \frac{N_w}{\tau_e} - \frac{N_w}{\tau_{sp,w}} - \frac{\Gamma_r v_{gr} G(N_w) S}{1 + \epsilon S} + F_N(t) \quad (8.2)$$

$$\frac{dS}{dt} = \beta_{sp} \frac{V_w}{V_h} \frac{N_w}{\tau_{sp,w}} - \frac{S}{\tau_p} + \frac{V_w}{V_h} \frac{\Gamma_r v_{gr} G(N_w) S}{1 + \epsilon S} + F_S(t) \quad (8.3)$$

$$\frac{d\phi}{dt} = \frac{a_c}{2} \left( \Gamma G(N_w) - \frac{1}{\tau_{ph}} \right) + F_\phi(t) \quad (8.4)$$

with  $G(N_w) = g_0 \ln \left( \frac{N_w}{N_w} \right)$  where  $g_0$  is the gain slope and its typical value is  $3 \sim 10 \times 10^5 \text{ m}^{-1}$ .

The terms  $F_N(t)$ ,  $F_S(t)$ , and  $F_\phi(t)$  appended to these equations represent phenomenologically the origins of the quantum noise and are referred to as Langevin noise sources [10]. Since they are random sources, the time averages are zero, i.e.,

$$\langle F_N(t) \rangle = \langle F_S(t) \rangle = \langle F_\phi(t) \rangle = 0 \quad (8.5)$$

$$F_S(t) = \sqrt{\frac{2S(t)\beta_{sp}}{\Delta t}} x_S \quad (8.6)$$

$$F_N(t) = \sqrt{\frac{2N_w(t)}{\tau_s \Delta t V_{active}}} x_N - F_S(t) \quad (8.7)$$

$$F_\phi(t) = \frac{1}{S(t)} \sqrt{\frac{2S(t)\beta_{sp}}{2\Delta t}} x_\phi \quad (8.8)$$

Here,  $x_S$ ,  $x_N$  and  $x_\phi$  are the Gaussian random variable with zero mean and unity variance.

## 8.4 Rate Equations of a VCSEL with External Optical Feedback

In many applications, however, some of the laser output light is reflected by optical elements and returns to the laser. In optical communications systems, reflection at the fiber input and output ports gives rise to optical feedback and, in optical disk systems, reflection at the disk also causes optical feedback. Semiconductor lasers under such operation conditions exhibit complicated behaviors, and the feedback significantly affects the noise characteristics. This section deals with feedback-induced noise. The external feedback and therefore feedback induced noise can be eliminated by inserting a nonreciprocal isolator in the output beam path, since the isolator transmits the forward wave but blocks the reflected backward wave.

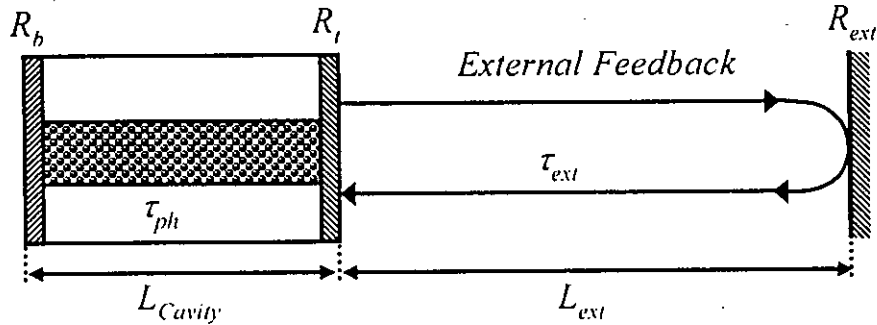


**Figure 8.1** A model for the analysis of optical feedback phenomena. External reflector has been placed at a distance  $L_{ext}$  from the output facet of the VCSEL.  $R_{ext}$  is the power reflectivity of the external reflector.

As a simple model for the analysis of optical feedback from an external reflector, consider a system where an external reflector is positioned at a distance  $D$  from a VCSEL, as shown in Figure 8.1. The laser resonator and the external reflector constitute a composite resonator, and, in the steady state, the laser oscillates in the resonant mode of the composite resonator. Although mathematical formulation of the composite resonator modes is possible, the formulation cannot enable analysis of laser dynamics to be made more rapidly than the round trip time  $\tau_{ext} = 2D/c$  for the distance  $D$ , which

can generally be much longer than the laser resonator length  $L_{cavity}$ . Let  $R_i$  be the power reflectivity of the output facet mirror, and  $R_{ext}$  be the effective power reflectivity of the external mirror, including the optical losses during the round trip between the output facet and the external mirror and the loss in coupling back into the laser waveguide.

Let  $S(t)$  and  $\phi(t)$  be the photon density and the optical phase, respectively, according to the definition in Section 4.4 and 4.5.

The amplitude of the guided wave propagating in the laser towards the output facet is proportional to

$$\sqrt{S(t)} \exp\{-[\omega_{th}t + \phi(t)]\}$$

where,  $\omega_{th}$  is the frequency of oscillation without optical feedback. The wave is reflected at the facet with the amplitude reflection coefficient  $r_i = \sqrt{R_i}$ . The amplitude of the wave component that is fed back into the VCSEL after a round trip to the external mirror, noting the double transmission and the retardation time  $\tau_{ext}$ , can be written as

$$(1 - R_i) \sqrt{R_{ext} S(t - \tau_{ext})} \exp\{-i[\omega_{th}(t - \tau_{ext}) + \phi(t - \tau_{ext})]\}$$

Therefore, omitting the multiple reflection under the assumption  $R_{ext} \ll 1$ , the effective amplitude reflection coefficient for the combination of the output facet mirror and the external reflector can be written as

$$r_{ieff} = r_i + \delta r_i \quad (8.9)$$

$$\text{where, } \delta r_i = (1 - R_i) \sqrt{R_{ext} \frac{S(t - \tau)}{S(t)}} \exp\{i[\omega_{th}\tau_{ext} + \phi(t) - \phi(t - \tau_{ext})]\} \quad (8.10)$$

The variations in the power reflectivity and the reflection phase due to the external feedback are given by [28]

$$\delta R_i = 2r_i \text{Re}\{\delta r_i\} \quad (8.11)$$

$$\delta \phi_i = -\frac{\text{Im}\{\delta r_i\}}{r_i} \quad (8.12)$$

The external optical feedback does not directly affect the carrier density of the VCSEL. The equations for the carrier density given by equations (8.1) and (8.2) should not be modified. Since the photon lifetime  $\tau_{ph}$  included in the equation for the photon density  $S(t)$  given by equation (8.3) is a function of the reflectivity as shown by equation (4.12), the effective value under the perturbation is given by [28]

$$\frac{1}{\tau_{pheff}} = \frac{1}{\tau_{ph}} + \frac{v_{gr}}{2L_{cavity}R_i} \delta R_i \quad (8.13)$$

Thus the effective photon lifetime is not a constant any longer, and varies with time depending on the oscillation state. The longitudinal mode resonance condition (equation (4.5)) used in the derivation of the equation for the optical phase (equation (4.10)) should be rewritten, under the perturbation in the reflection phase, as

$$2L_{cavity} \left( \beta(\omega) + \frac{\Gamma\omega}{c} \Delta n \right) - \delta\phi_l = 2m\pi \quad (8.14)$$

Using the equations (8.1)-(8.4) and (8.9)-(8.14) the modified rate equations of a VCSEL due to external optical feedback can be written as

$$\frac{dN_h(t)}{dt} = \frac{I}{qV_h} + \frac{N_w(t)V_w}{\tau_c V_h} - \frac{N_h(t)}{\tau_s} - \frac{N_h(t)}{\tau_{sp,h}} \quad (8.15)$$

$$\frac{dN_w(t)}{dt} = \frac{N_h(t)V_h}{\tau_s V_w} - \frac{N_w(t)}{\tau_c} - \frac{N_w(t)}{\tau_{sp,w}} - \frac{\Gamma_r v_{gr} G(N_w(t))S(t)}{1 + \epsilon S(t)} + F_N(t) \quad (8.16)$$

$$\begin{aligned} \frac{dS(t)}{dt} = & \beta_{sp} \frac{V_w}{V_h} \frac{N_w(t)}{\tau_{sp,w}} - \frac{S(t)}{\tau_p} + \frac{V_w}{V_h} \frac{\Gamma_r v_{gr} G(N_w(t))S(t)}{1 + \epsilon S(t)} + F_S(t) \\ & + 2k \sqrt{S(t)S(t - \tau_{ext})} \times \cos[\omega_{th} \tau_{ext} + \phi(t) - \phi(t - \tau_{ext})] \end{aligned} \quad (8.17)$$

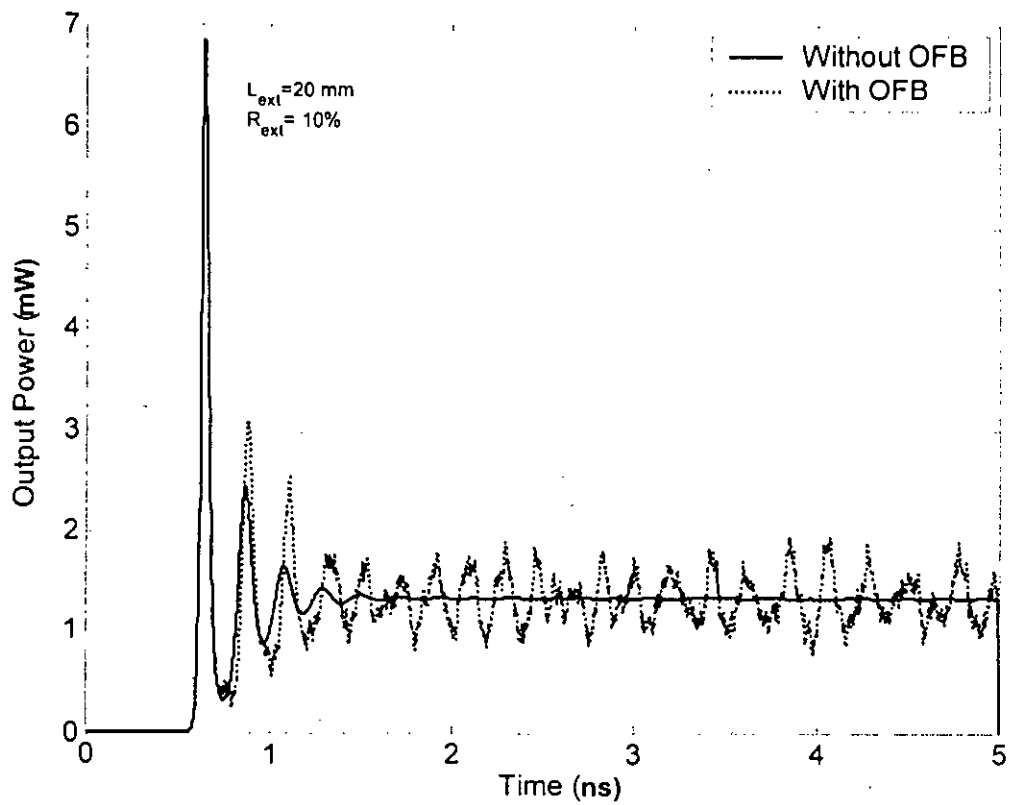
$$\frac{d\phi(t)}{dt} = \frac{a_c}{2} \left( \Gamma G(N_w(t)) - \frac{1}{\tau_{ph}} \right) + F_\phi(t) - k \sqrt{\frac{S(t - \tau_{ext})}{S(t)}} \times \sin[\omega_{th} \tau_{ext} + \phi(t) - \phi(t - \tau_{ext})] \quad (8.18)$$

Here,  $k$  is the magnitude of the external feedback and  $\omega_{th}$  is the threshold oscillation frequency without optical feedback. Assuming attenuation, absorption and diffraction losses in the external cavity negligible, the feedback coefficient  $k$  can be defined as [10]

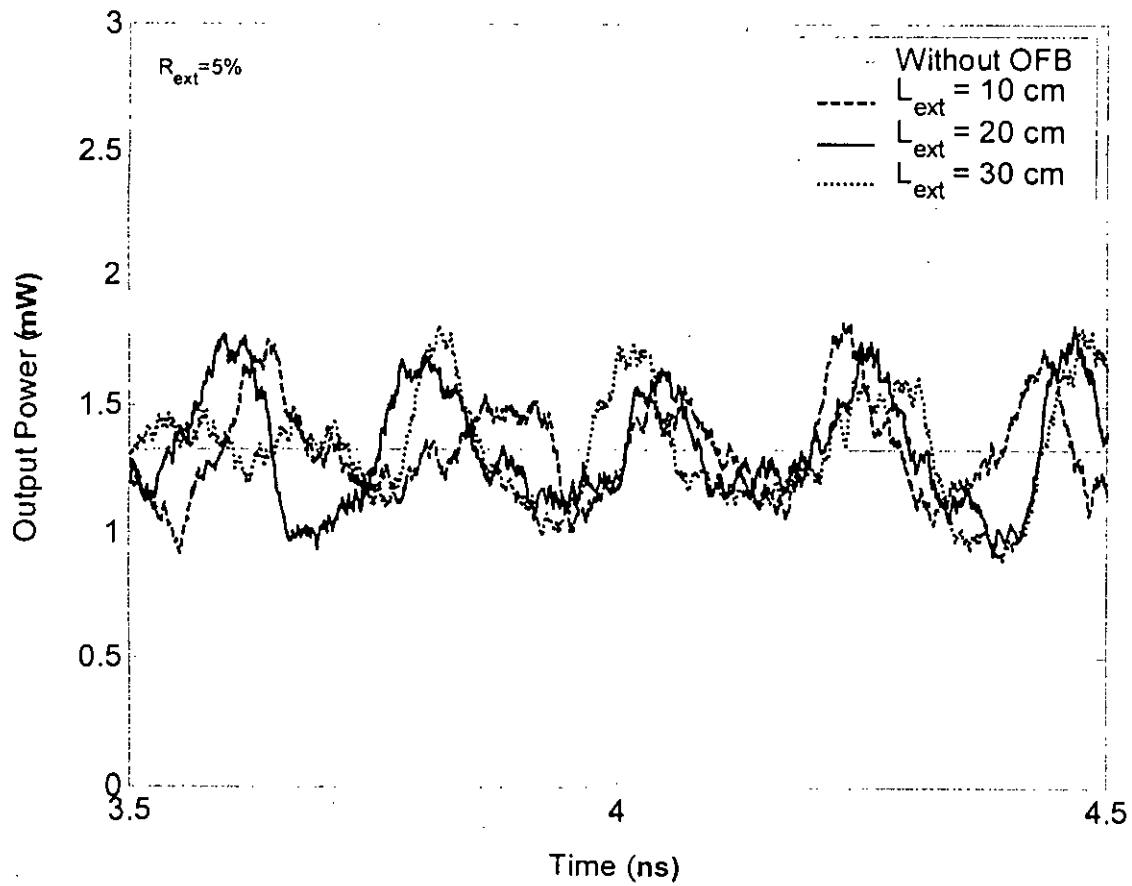
$$k = \eta_{ext} \frac{1 - R_l}{\tau_l} \sqrt{\frac{R_{ext}}{R_l}} \quad (8.19)$$

Where,  $\eta_{ext}$  is the power coupling efficiency between VCSEL and the external cavity,  $\tau_l$  is the laser cavity round trip time and can be written as

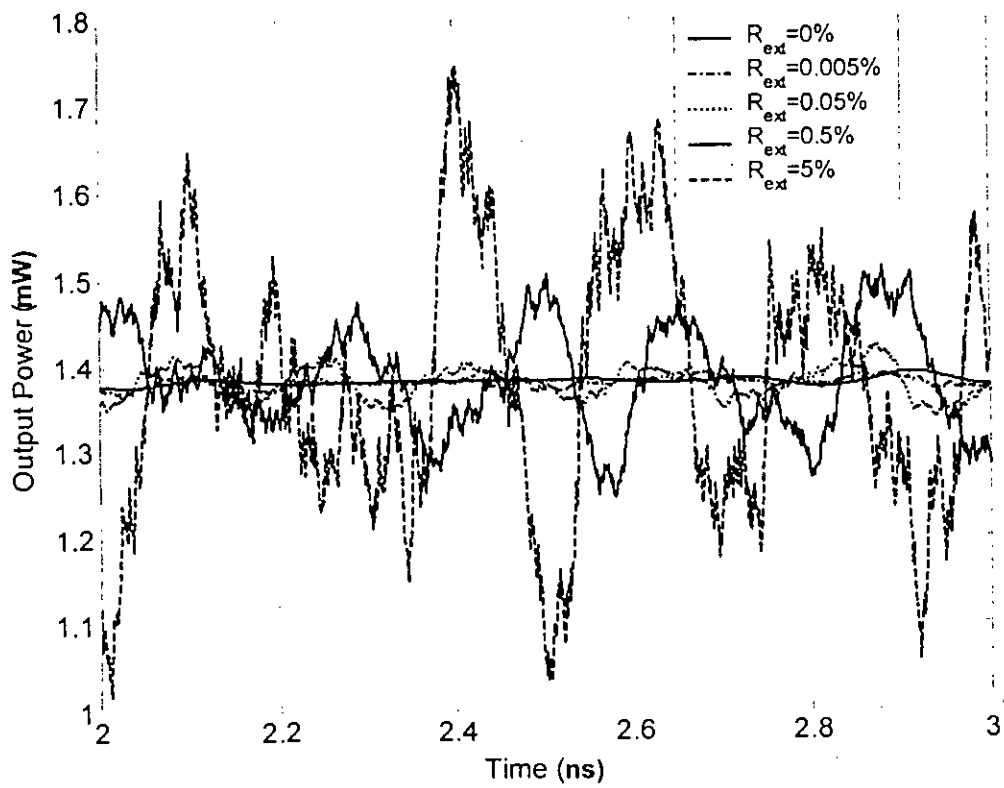
$$\tau_l = \frac{2L_{cavity}}{v_{gr}} \quad (8.20)$$



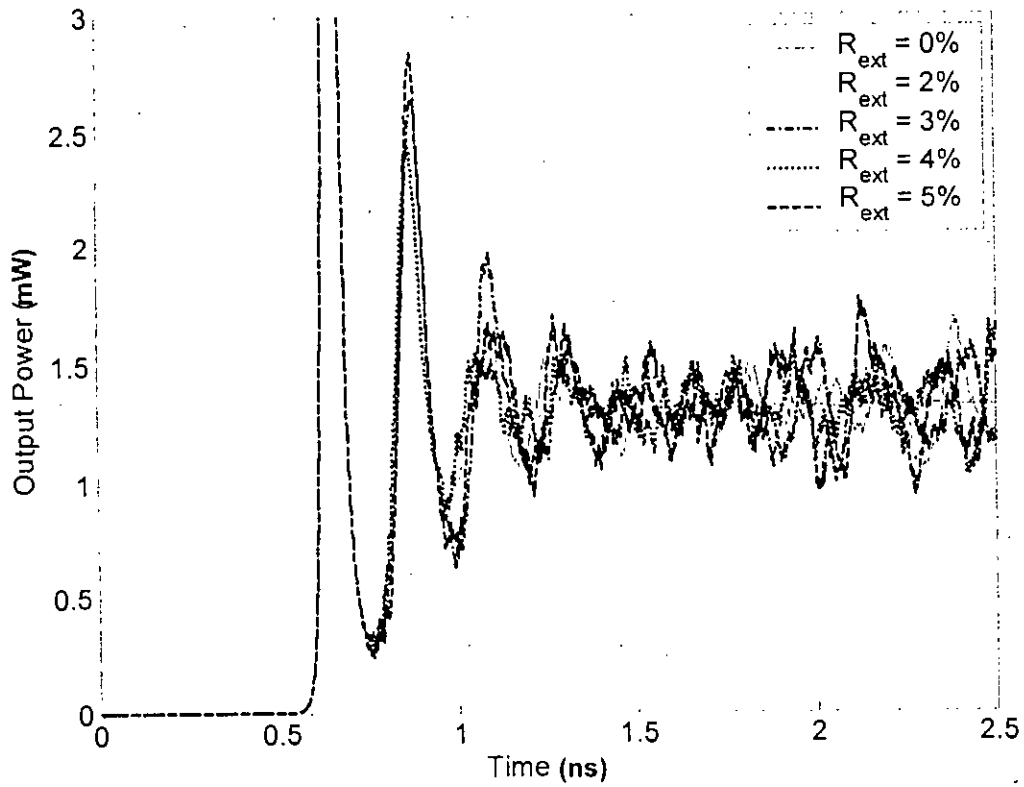
(a)



(b)



(c)



(d)

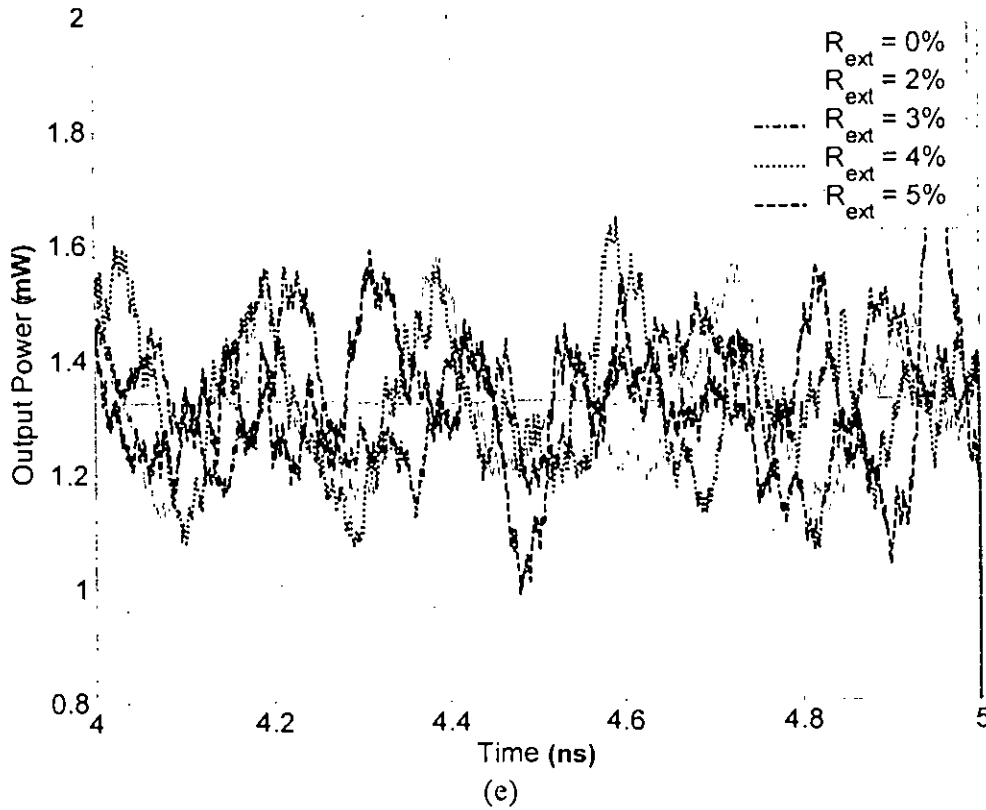


**Figure 8.2** Laser response with and without external optical feedback and also for different level of feedback. (a) for an external reflector 20 mm apart from the top facet of the VCSEL. (b) shows the response for the reflector at different distances. (c-e) shows the response for different values of  $R_{ext}$ .

Rate equations (8.15) to (8.18) of a VCSEL considering external optical feedback have been solved by using finite difference method. Time step for the computation has been set to 1 ps. From the obtained photon density, output power has been computed by using the equation (4.49). Figure 8.2 shows the output power variation of a VCSEL with and without external optical feedback. It is clear from the figure 8.2 that the output power fluctuation increased due to the optical feedback. Magnitude of the fluctuation of the output power depends on the amount of feedback of the external reflectors as shown in the figure 8.2 (c).

## 8.5 Small-Signal Modulation Response

From the rate equations we can infer the dynamic response of the VCSEL to a harmonic variation  $\Delta I(t)$  of the current about an operating point  $I_0 \gg |\Delta I(t)|$ . Equations are first of all linearized with respect to the resulting variations  $\Delta N_w(t)$ ,  $\Delta N_b(t)$ , and  $\Delta S(t)$  which are all small compared to  $N_{w0}$ ,  $N_{b0}$ , and  $S_0$  respectively. Here,  $N_{w0}$ ,  $N_{b0}$ , and  $S_0$  are the steady state value of the carrier density at the well, barrier and photon density respectively. Now perform Fourier transform into quantities  $\Delta I(\nu)$  to obtain the spectral fluctuations as a function of frequency  $\nu$ . The carrier dependent part of the gain coefficient is also linearized to the form



$$G(N_{w0}) = g_0 \ln\left(\frac{N_{w0}}{N_{wt}}\right) \approx \bar{a}(N_{w0} - N_t) \quad (8.21)$$

with differential gain coefficient  $\bar{a}$  with typical value  $2\sim 3 \times 10^{-20}$  and transparency carrier density  $N_t$  expressed as

$$\bar{a} = \frac{g_0}{N_{w0}} \text{ and } N_t = N_{w0} \left( 1 - \ln\left(\frac{N_{w0}}{N_{wt}}\right) \right) \quad (8.22)$$

Noise is not required to take in consideration during the analysis of small signal modulation response. Langevin noise sources  $F_{N(t)}$  and  $F_{S(t)}$  are both set to zero. Neglecting the spontaneous emission contributions in equations (8.1) and (8.2) due to the small magnitude of  $\beta_{sp}$ , the resulting modulation transfer function that relates the photon density fluctuations to the fluctuations of the modulating current is finally obtained as [40]

$$M(\nu) = \frac{\Delta \bar{S}(\nu)}{\Delta I(\nu)/q} = \frac{1}{1 + i2\pi\nu\tau_s} \frac{A}{4\pi^2(\nu_r^2 - \nu^2) + i2\pi\gamma\nu} \quad (8.23)$$

Here,  $A$  is the amplitude factor,  $\gamma$  is the damping coefficient and  $\nu_r$  is the resonance frequency can be written as

$$A = \frac{\eta_I \nu_{gr} \Gamma_r \bar{a} S_0}{V_p \chi (1 + \epsilon S_0)} \quad (8.24)$$

$$\gamma = \frac{1}{\chi \tau_{sp,w}} + A V_p + \frac{\epsilon S_0}{\tau_{ph} (1 + \epsilon S_0)} \quad (8.25)$$

$$\nu_r = \frac{1}{2\pi} \sqrt{A \frac{V_p}{\tau_{ph}} \left( 1 + \frac{\epsilon}{\tau_{sp,w} \nu_{gr} \Gamma_r \bar{a}} \right)} \approx \frac{1}{2\pi} \sqrt{A \frac{V_p}{\tau_{ph}}} \quad (8.26)$$

Where,  $\chi$  is the transport factor related to carrier transport time  $\tau_s$  and carrier escape time  $\tau_e$  can be written as

$$\chi = 1 + \frac{\tau_s}{\tau_e} \quad (8.27)$$

The damping coefficient  $\gamma$  can be rewritten considering the  $K$  factor as

$$\gamma = K \nu_r^2 + \frac{1}{\chi \tau_{sp,w}} \quad (8.28)$$

with

$$K = 4\pi^2 \left( \tau_{ph} + \frac{\epsilon}{v_{gr} \Gamma_r \bar{a} / \chi} \right) \quad (8.29)$$

The maximum 3-dB modulation corner frequency of  $|M(\nu)|^2$  is related to  $K$ . Maximum possible corner frequency is limited by  $K$  as [41]

$$\nu_{max} = \sqrt{2} \frac{2\pi}{K} \quad (8.30)$$

To increase the corner frequency or modulation bandwidth the K-factor has to be minimized.

Small signal modulation response of a VCSEL has been computed by using the equation (8.23) for different values of the injection current and plotted into the figure 8.3.

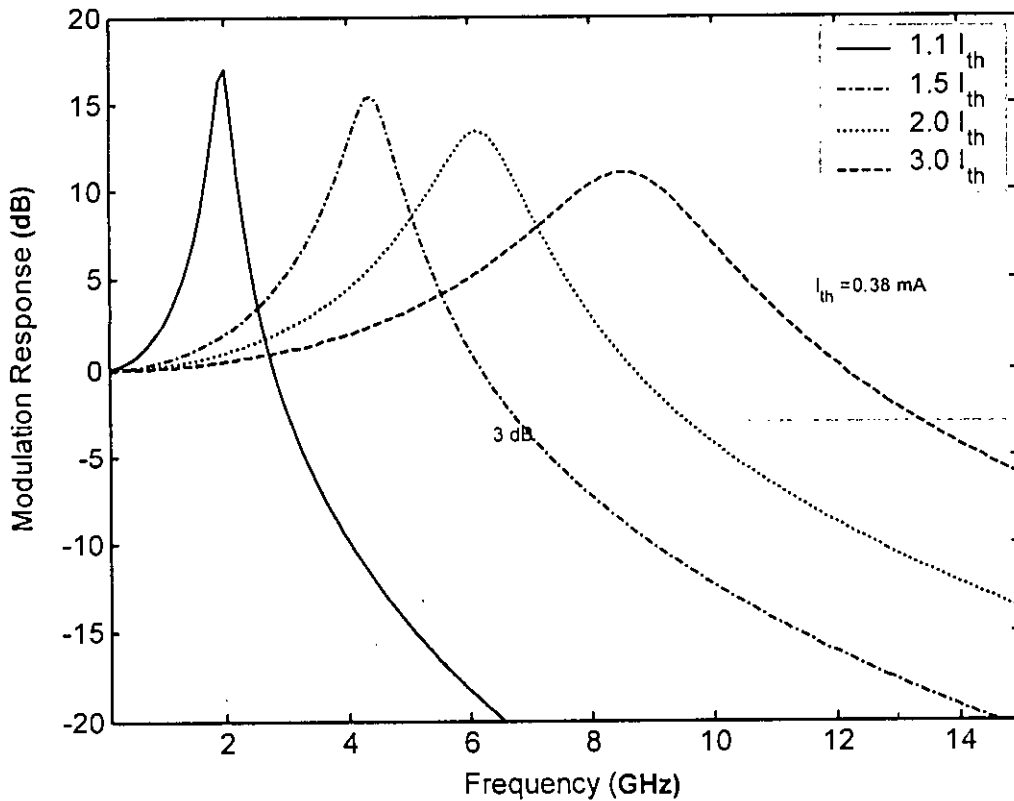


**Figure 8.3** Simulation result of modulation transfer function  $|M(\nu)|^2$  of a single mode oxidized VCSEL for different bias currents above threshold current  $I_{th} = 0.38$  mA.

## 8.6 Determination of Relative Intensity Noise (RIN)

The coupling of the spontaneous emission to the stimulated emission in a semiconductor laser leads to phase and intensity noise in the laser output. The phase noise manifests itself as a finite spectral width of the laser even for cw operation. Low phase noise is needed for lasers used in coherent transmission. The intensity noise arises from the coupling of the electrons in the semiconductor and the photons in the electric field. The intensity noise is generally characterized by

the relative intensity noise (RIN). The RIN value must be sufficiently small if the laser is used in analogue or subcarrier based transmission systems.

Noise in diode lasers originates from both carrier density fluctuations and photon density fluctuations. The relative intensity noise (RIN) spectrum is commonly used to analyse the noise properties of high-speed diode lasers and to determine the modulation bandwidth. The RIN is defined as the ratio of the intensity fluctuations to the averaged intensity as

$$RIN(\omega) = \frac{S_p(\omega)}{P^2} \quad (8.31)$$

$$S_p(\omega) = \int_{-\infty}^{\infty} \langle \delta P(t + \tau) \delta P(\tau) \rangle e^{-i\omega\tau} d\tau = \langle |\delta P(\omega)|^2 \rangle \quad (8.32)$$

Where,  $S_p(\omega)$  is the spectral density of intensity fluctuation,  $P$  is the average power and  $\delta P$  is the from its average value over a period after the transient part.

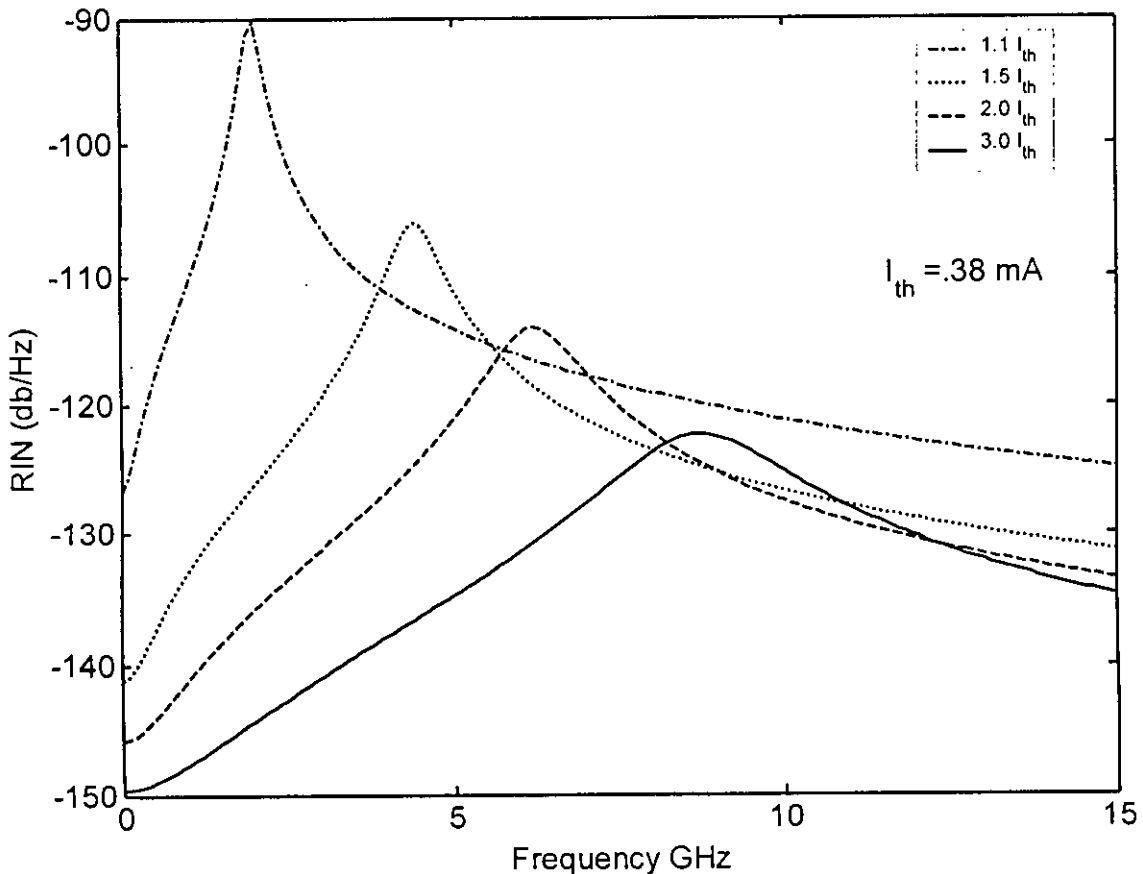


**Figure 8.4** Relative Intensity Noise (RIN) spectra of a VCSEL for different values of the injection current. Curves are plotted by using the analytical expression of RIN given by the equation 8.34.

RIN can be computed in 2 different ways i) by an analytical small signal model ii) by solving the rate equations numerically.

To derive an analytical expression of RIN, first of all the rate equations need to be linearized. The spectral relative intensity noise (RIN) relates the photon density fluctuations to the mean photon density squared as [41]

$$RIN(\nu) = 2 \frac{\langle |\Delta \bar{S}(\nu)|^2 \rangle}{\langle S \rangle^2} = 2 \frac{\langle |\Delta \bar{P}(\nu)|^2 \rangle}{\langle P \rangle^2} = 2 \frac{\langle |\Delta \bar{I}_{PD}(\nu)|^2 \rangle}{\langle I_{PD} \rangle^2} \quad (8.33)$$

where, the angular brackets denote an average over the observation time and  $RIN(\nu)$  is measured in dB/Hz. In equation 8.33 the proportionality between spectral components of photon density fluctuation  $\Delta S(\nu)$ , output power fluctuation  $\Delta P(\nu)$ , and detector photocurrent fluctuation  $\Delta I_{PD}(\nu)$  and correspondingly for the mean values  $\langle S \rangle$ ,  $\langle P \rangle$ , and  $\langle I_{PD} \rangle$  have been made. In contrast to the previous section, a consideration has been made that, the photon density is modulated here by spontaneous emission processes, whereas current density fluctuations can be neglected. Thus, putting  $\Delta I(\nu) = 0$  after linearization and Fourier transformation of (8.1) - (8.3) and inserting proper expressions for the Langevin forces  $F_S, F_N$  leads to the result as [40]

$$RIN(\nu) = \frac{4\beta_{sp}\Gamma N_{w0}}{\tau_{sp,w}\langle S \rangle} \frac{4\pi^2\nu^2 + \gamma^{*2}}{16\pi^4(\nu_r^2 - \nu^2)^2 + 4\pi^2\gamma^2\nu^2} \quad (8.34)$$

with the modified damping coefficient

$$\gamma^* = \gamma - \frac{\varepsilon\langle S \rangle}{\tau_{ph}(1 + \varepsilon\langle S \rangle)} \approx \frac{1}{\chi\tau_{sp,w}} + 4\pi^2\gamma^2\tau_{ph} \quad (8.35)$$

Relative Intensity Noise (RIN) can be computed from the numerical simulation of the output power (or photon density) fluctuation and can be written as [7]

$$RIN = \frac{1}{\bar{P}^2} \left\{ \frac{1}{T} \left| \int_0^T \delta P(\tau) e^{-j\omega\tau} d\tau \right|^2 \right\} \quad (8.36)$$

$$RIN \equiv \frac{1}{\bar{P}^2} \frac{\Delta t^2}{T} |FFT[\delta P(t)]|^2 \quad (8.37)$$

Here,  $\delta P(t) = P(t) - \bar{P}$  is the fluctuation of the output power from its average value,  $T$  is the period of time selected to perform integration and  $\Delta t$  time resolution used for numerical computation. RIN spectra, computed by using the equation (8.37) without external optical feedback or considering the external optical feedback has been computed and presented in the figure 8.5. In this computation, time step  $\Delta t$  has been selected a 1ps. From figure 8.5 it has been observed the RIN level increased due to the external optical feedback.

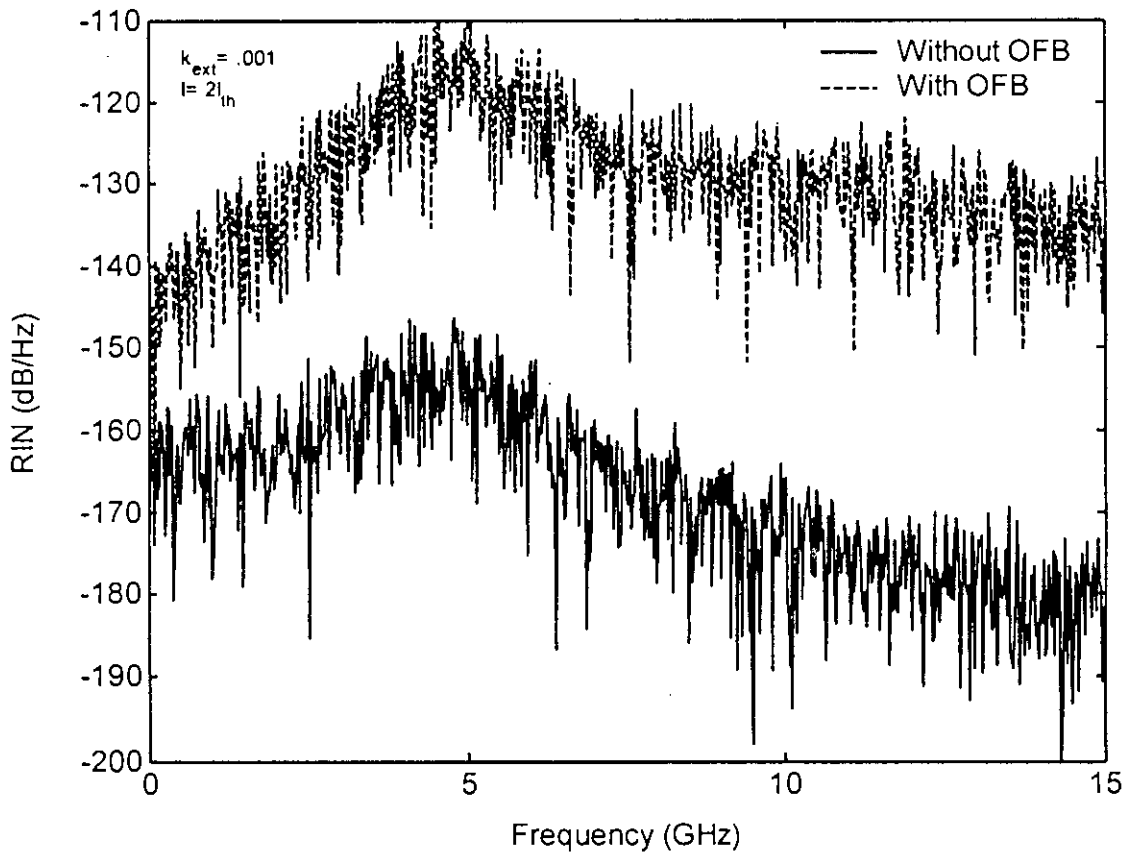


**Figure 8.5** Relative Intensity Noise (RIN) computed from the simulation result of the output power fluctuation of a VCSEL. Solid line represents the RIN spectra of a VCSEL without optical feedback. Dashed line represents the RIN spectra of a VCSEL considering external optical feedback. Feedback coefficient  $k_{ext}$  has been selected as 0.001.

## 8.7 Summary

At the beginning of this chapter, different types of noises in the semiconductor laser have been discussed briefly. Rate equations of the VCSEL have been modified by introducing the noise sources. To analyse the optical feedback from an external reflector, rate equations have been modified again. Next, the rate equations have been solved numerically by using the Finite Difference (FD) method to compute the carrier density, photon density and output power of a VCSEL. Small signal modulation response of a VCSEL has also been presented in this chapter. Finally, Relative Intensity Noise of a VCSEL has been computed with and without optical feedback.

## Chapter 9

### Discussions and Conclusions

#### 9.1 Discussions

In order to obtain the reflectivity of a multilayer semiconductor DBR stack, a number of techniques such as, i) the Transfer Matrix Method (TMM), ii) the technique based on Coupled Mode Theory (CMT), iii) the technique based on Floquet-Bloch Theory (FBT) and iv) the *Tanh* Substitution Technique are developed by various researchers [15] [18] [19] [20]. Among the above mentioned techniques, *Tanh* Substitution Technique, CMT technique and FBT technique are suitable for graded index layered DBR as well as step index layered DBR. In contrast to these techniques, TMM is suitable for calculating the reflectivity of a step index layered DBR but not suitable for graded index layered DBR stacks. It is worthwhile mentioning here that FBT technique and *Tanh* substitution technique can not be used to calculate Electric Field Distribution inside a VCSEL. However, it appears that using the CTM technique it might be possible to calculate Electric Field Distribution inside a VCSEL although no such work has so far been found. Possibilities of such a work needs to be investigated. On the other hand, TMM can be used without any difficulty to calculate the electric field distribution inside a VCSEL having 'step index' layered DBR stacks only. From the above discussion it is evident that none of the above mentioned techniques are suitable for calculating the electric field distribution inside a VCSEL having 'graded index' layered DBR stacks. For 'graded index' layered DBR stacks it was thus necessary to look for a new method of calculating the reflectivity as well as the electric field distribution inside a VCSEL.

Considering the necessity, in this work, a new method of calculating the reflectivity of a graded index layered DBR stacks has been developed. The name of this method has been given as Sampled Transfer Matrix Method (STMM) because the transfer matrix of the complete DBR stack has been developed by cascading a large number of samples of transfer matrices corresponding to small incremental samples of the DBR layers.

The first objective of this work is thus to develop the Sampled Transfer Matrix Method (STMM) to compute the reflectivity of a 'graded index' layered DBR stack as well as 'step index' layered DBR stacks. This objective has been fully achieved. The development of this STMM technique has been presented in Chapter 6. Next, it has been shown that STMM is capable of computing the reflectivity of a graded index layered DBR stacks as well as step index layered DBR stacks. The results obtained by STMM have been compared with the result of previous work of other researchers.

STMM has been applied to compute the reflectivity of the step index layered DBR and got the same result obtained by other researchers. Reflectivity of a DBR having smooth variation of refractive index in the layers has also been successfully computed by using STMM. An idea of a new type of DBR having sinusoidal variation of refractive index in the layers has been presented and the reflectivity spectra of that DBR exhibits the similar reflectivity spectra of the conventional DBR which has step index variation in the layers. Reflectivity and Transmittivity spectra of a complete VCSEL have been also computed by using the newly developed technique based on STMM. Thus the second objective has also been fully achieved.

As mentioned in the first paragraph of this section that TMM can only be used to compute the electric field distribution inside a VCSEL having step index DBR. The second objective of this work is thus to develop a model to compute the electric field distribution inside a VCSEL having smooth variation of refractive index in the layers of the DRB. STMM based model of a VCSEL for computing the electric field distribution inside the VCSEL has been presented in the section 6.7. The developed model can also be used to compute the electric field distribution inside a VCSEL having 'step index' layered DBR. It is also mentioning here that, electric field distribution inside the VCSEL without external optical feedback or with optical feedback from an external reflector can be accurately computed by the STMM based model developed in this work. The model of a VCSEL to take account the effect of optical feedback from an external reflector has been presented in the chapter 7.

Electric field distribution inside a VCSEL having step index layered DBR has been computed by using the model developed in this work. Result obtained by STMM based model has been shown in the chapter 6 and compare with the result obtained by other researchers model. This ensures the accuracy of the new technique presented here. Next, the electric field distribution inside a VCSEL having smooth variation of refractive index in the layers of its DBR is computed and presented in the chapter 6. It is thus clear that the third objective has been fully achieved in this work.

Electric field distribution inside a VCSEL without optical feedback and with optical feedback is computed by using the model discussed in the chapter 7. Standing wave pattern of the light intensity due to the different position of the external reflector is also computed for a VCSEL having step index layered DBR and the result has been compared with the results of the other researchers. Same computation has been done by using the STMM based model for a VCSEL having graded index layered DBR and similar result has been found. Field intensity near the output facet and near the cavity region due to optical feedback has also been computed.

Variation of the performance parameters such as; (i) threshold current, (ii) external differential quantum efficiency and (iii) output power of a VCSEL having step index layered DBR, have been computed due to different positions of the external reflector. Results have been compared with the experimental results of other researchers. Thus the fourth objective has also been fully achieved.

Next, the rate equations of the VCSEL have been deduced from the fundamental rate equations of semiconductor laser. Then the rate equations have been solved numerically by using the 'Finite Difference' method to determine the carrier density, photon density, light output, turn-on delay and Relative Intensity Noise (RIN) of the VCSEL.

Rate equations of VCSEL have also been modified to account the optical feedback phenomena. Output power fluctuation and RIN due to optical feedback is computed numerically. Turn-on delay of a VCSEL has been calculated from the numerical result of the photon density. The result has been compared with the result obtained by using the analytical expression of turn on delay. It has been observed that turn-on delay decreases with the increase of injection current. It has also been observed that RIN is increased with the increase amount of optical feedback. Thus the fifth objective of this work has also been fully achieved.

Finally, the results obtained by using the model presented in this work has been compared with the result of previous other researchers. Good agreement with the previous result has been found. Thus the final objective of his work has been fully achieved.

## 9.2 Suggestions for future work

Distributed Bragg Reflectors (DBRs) are used as the mirror of a VCSEL. Conventional step index layered DBR have quarter wavelength thick layers of alternative low and high refractive index materials as mentioned in the chapter 3. Such type of DBR has the peak reflectivity at the Bragg wavelength. The new types of DBRs introduced in this work have uniform variation of refractive indices in the layers. Thickness of this layers has been determined in two different ways, such as i)  $d=\lambda/4n$  or ii)  $d=\lambda/4n_{avg}$ . In the first case, peak reflectivity of the DBR has been occurred at the wavelength slightly shorter than the Bragg wavelength where as in the second case; peak reflectivity of the DBR has been occurred at the wavelength slightly greater than the Bragg wavelength. One can select the thickness of the layers of the newly introduced DBR in such a way so that the peak reflectivity of the DBR will occur at the Bragg wavelength.

In this work, theoretical analyses of the new types of DBR stacks have been presented. It would have been better if these theoretical computations could be supported by the similar result obtained from fabricated laser and experimental measurements. Such fabrication and experimental measurement to verify the obtained result is defining a good work which can be done in the near future. Reflectivity and transmittivity spectra of a VCSEL having the newly introduced DBRs have been presented in Chapter 6. These results showed a good agreement with the similar results of other conventional VCSELs presented in the other publications [19] [40]. In this work the step index and graded index layers of the DBR stacks of a VCSEL have considered for computing the effects of such layers on different performance parameters of a VCSEL. However, no variation of refractive index in the active layers has been considered. As a future work one may consider the variation of refractive index in the active layers of a VCSEL. With an appropriate development of a model one may compute the performance parameters of a VCSEL and work for betterment.

In the STMM based method, reflectivity and transmittivity of the DBR stacks as well as the VCSEL has been computed by considering the refractive index variation only in the direction of the layers of the VCSEL. It is worthwhile searching for some better performance of a VCSEL by having variation of refractive index of the DBR layers of a VCSEL in either  $x$  or  $y$  directions. Alternating variation in both  $x$  and  $y$  direction may be considered.

## 9.3 Conclusions

A novel method of computing the reflectivity and transmittivity of a graded index layered DBR has been developed. The new technique has been termed as STMM. A model for computing the electric field distribution inside a VCSEL without external optical feedback has also been developed. By extending the method a model for computing the electric field distribution inside a VCSEL in presence of optical feedback has also been developed. The basic idea of the developed STMM was derived from Transfer Matrix Method (TMM). However, the STMM method of calculating the electric field distribution inside a VCSEL has derived by blending TMM and the method used by Muriel and Carballar for Fiber Bragg Grating (FBG). It is expected that, development of this new technique of STMM will open a new horizon in this field and new types of devices can be designed and analyzed by using this technique.

Using the STMM based method one can compute the reflectivity and transmittivity of a multilayer stacks having graded refractive index variation. The technique can equally be applied for DBR layers having step index variation. In this work, at first, reflectivity and transmittivity of a step index DBR has been computed using TMM. Next, the same computation has been performed using STMM. A comparison of these two computations shows that STMM is capable of producing exactly



the same result as the TMM. For a DBR stack having graded index layers one can not perform the above mentioned computations using TMM. However, one can happily perform these computations using the newly developed method of STMM.

One can compute the reflectivity and transmittivity of a VCSEL having DBR stacks made of graded index layers by using STMM. Electric field distribution inside a VCSEL having step index layered DBR has been computed by using the method of STMM and the results show close resemblance with the results of the same quantity obtained by using TMM. Electric field distribution inside a VCSEL having graded index layered DBR has also been computed by using the method of STMM. These computations can not be performed using TMM.

Next, a VCSEL in presence of optical feedback from an external reflector has been taken for computation. For this VCSEL with external reflector the electric field distribution inside the VCSEL has been computed using the STMM method. The above mention computations have been performed for VCSELs having step index layered DBR and also for the VCSELs having graded index layered DBR separately. The results have been presented. The above mentioned computations have also been performed for different positions of the external reflector and the results have been presented. Due to the variation of the positions of the external reflector, various performance parameters of a VCSEL such as output power, threshold current and external differential quantum efficiency has been computed. For these computations it is possible to find the position of the external reflector for which the output power is maximum. In this case, the values of the distance has been found to be  $\lambda/4$ .

In most of the previous works the rate equations for VCSEL have been solved using Runge-Kutta method. It has been reported in [10] that Runge-Kutta method is not expected to give good results in such computation because rate equations of a VCSEL is supposed to be based on stochastic system. Considering this, in this work, the rate equations have been solved with the help of finite difference (FD) method. This is expected to produce more accurate results.

It is necessary to know the turn on delay of a VCSEL because the modulation speed of a VCSEL is dependant on this parameter. In this work, turn on delay has been computed using the expression of turn on delay developed from the rate equation of the carrier density. Next, the turn on delay has been computed from the simulation result of the carrier density. This gives an opportunity of comparing the results of the turn on delay using the two methods. Computation of relative Intensity Noise (RIN) is an important part of a VCSEL. As a result, computation of RIN has been carried out with and without external optical feedback.

Last of all, it is clearly observed that the method of STMM has given a simple way out to perform the computation used to analyse and understand the performance of a VCSEL in the presence of external optical feedback.

## References

- [1] Jungo, M. X., Erni, D. and Baechtold, W., "Quasi-analytic steady-state solution of VCSEL rate equations including spatial hole burning and carrier diffusion losses", *International Journal of Numerical Modelling, Electronic Networks, Devices and Fields*, 2003, 16, pp. 143-159.
- [2] Li, X. F., Pan, W., Luo, B., Ma, D. and Deng, G., "Static and dynamic characteristics of VCSELs with polarisation-selective optical feedback", *IEE Proceedings-Optoelectronics*, Vol. 153, No. 2, April 2006, pp. 67-74.
- [3] Chung, Y. C., and Lee, Y. H., "Spectral characteristics of vertical-cavity surface-emitting lasers with external optical feedback", *IEEE Photonics Technology Letters*, Vol. 3, No. 7, July 1991, pp. 597-599.
- [4] Hsu, A., Seurin, J. F. P., Chuang, S. L. and Choquette, K. D., "Optical Feedback in Vertical-Cavity Surface-Emitting Lasers," *IEEE Journal of Quantum Electronics*, Vol. 37, No. 12, December 2001, pp. 1643-1649.
- [5] Law, J. Y. and Agrawal, G. P., "Effects of optical feedback on static and dynamic characteristics of vertical-cavity surface-emitting lasers", *IEEE Journal of Selected Topics in Quantum Electronics*, Vol. 3, No. 2, April 1997, pp. 353-358.
- [6] Schunk, N. and Petermann, K., "Numerical analysis of the feedback regimes for a single-mode semiconductor laser with external feedback," *IEEE Journal of Quantum Electronics*, Vol. 24, No. 7, July 1988, pp. 1242-1247.
- [7] Ahmed, M. and Yamada, M., "Field fluctuations and spectral line shape in semiconductor lasers subjected to optical feedback" *Journal of Applied Physics* Volume 95, Number 12 15 June 2004, pp. 7573-7583.
- [8] Abdulrhmann, S. G., Ahmed, M., Okamoto, T., Ishimori, W. and Yamada, M., "An Improved Analysis of Semiconductor Laser Dynamics Under Strong Optical Feedback", *IEEE Journal of Selected Topics in Quantum Electronics*, Vol. 9, No. 5, September/October 2003, pp. 1265-1274.
- [9] Muriel, M. A. and Carballar, A., "Internal Field Distributions in Fiber Bragg Gratings," *IEEE Photonics Technology Letters*, Vol. 9, No. 7, July 1997, pp. 955-957.
- [10] Jungo, M. X., Erni, D. and Baechtold, W., "VISTAS: A Comprehensive System-Oriented Spatiotemporal VCSEL Model" *IEEE Journal of Selected Topics in Quantum Electronics*, Vol. 9, No. 3, May/June 2003, pp. 939-948.
- [11] Soda, H., Iga, K., Kitahara, C., and Suematsu, Y., "GaInAsP/InP surface emitting injection lasers", *Jpn. J. Appl. Phys.* Vol. 18, No. 12, December 1979, pp. 2329-2330.
- [12] Jewell, J.L., Scherer, A., McCall, S.L., Lee, Y.H., Walker, S., Harbison, J.P., and Florez, L.T., "Low-threshold electrically pumped vertical-cavity surface-emitting micro-lasers", *IEE Electronics Letters*, Vol. 25, No. 17, August 1989, pp. 1123-1124.
- [13] Adachi, S., "Properties of Group-IV, III-V and II-VI Semiconductors", John Wiley & Sons, 2005. pp. 165-182
- [14] Piprek, J., "Optoelectronic Devices", Springer-Verlag New York, Inc., 2005. pp. 217-246

- [15] Carroll, J., Whiteaway, J. and Plumb, D., "Distributed feedback semiconductor lasers", IEE SPIE Optical Engineering Press, 1998, pp. 128-145.
- [16] Kim, B. G., Garmire, E., "Comparison between the matrix method and the coupled-wave method in the analysis of Bragg reflector structures", Journal of Optical Society America A, Vol. 9, No. 1, January 1992, pp. 132-
- [17] Michalzik, R. and Ebeling, K. J., "Modeling and Design of Proton-Implanted Ultralow-Threshold Vertical-Cavity Laser Diodes", IEEE Journal of Quantum Electronics, Vol. 29, No. 6, June 1993, pp. 1963-1974
- [18] Bhattacharya, P., "Semiconductor Optoelectronic Devices", Marcel Dekker, Inc., 1992, pp. 98-120.
- [19] Leonardis, F. De., Passaro, V. M. N., Magno, F., "Improved simulation of VCSEL distributed Bragg reflectors", Journal of Computational Electronics, Vol. 6, No. 1-3, September 2007, pp. 289-292.
- [20] Corzine, S. W., Yan, R. H., and Coldren, L. A., "A Tanh Substitution Technique for the Analysis of Abrupt and Graded Interface Multilayer Dielectric Stacks", IEEE Journal of Quantum Electronics, Vol. 21, No. 9, September 1991, pp. 2086-2090.
- [21] Langely, L. N. and Shore, K. A., "Effect of Optical Feedback on the Noise Properties of Vertical Cavity Surface Emitting Lasers", IEE Proceedings-Optoelectronics, Vol. 144, No. 1, February 1997, pp. 34-38.
- [22] Yamada, M., "Variation of Intensity Noise and Frequency Noise with the Spontaneous Emission Factor in Semiconductor Lasers", IEEE Journal of Quantum Electronics, Vol. 30, No. 7, July 1994, pp. 1511-1519.
- [23] Masoller, C., Sorrentino, T., Chevrollier, M. and Oria, M., "Bistability in Semiconductor Lasers with Polarization-Rotated Frequency-Dependent Optical Feedback", IEEE Journal of Quantum Electronics, Vol. 43, No. 3, March 2007, pp. 261-268.
- [24] Hong, Y., Paul, J., Spencer, P. S., and Shore, K. A., "The Effects of Polarization-Resolved Optical Feedback on the Relative Intensity Noise and Polarization Stability of Vertical-Cavity Surface-Emitting Lasers", Journal of Lightwave Technology, Vol. 24, No. 8, August 2006, pp. 3210-3216.
- [25] Arteaga, M. A., Unold, H. J., Ostermann, J. M., Michalzik, R., Thienpont, H., and Panajotov, K., "Investigation of Polarization Properties of VCSELs Subject to Optical Feedback From an Extremely Short External Cavity-Part I: Theoretical Analysis," IEEE Journal of Quantum Electronics, Vol. 42, No. 2, February 2006, pp. 89-101
- [26] Iga, K., "Surface-Emitting Laser—Its Birth and Generation of New Optoelectronics Field", IEEE Journal on Selected Topics in Quantum Electronics, Vol. 6, No. 6, November/December 2000, pp. 1201-1215.
- [27] Numai, T., "Fundamentals of Semiconductor Lasers", Springer-Verlag New York, Inc., 2004.
- [28] Suhara, T., "Semiconductor Laser Fundamentals", Marcel Dekker, Inc., 2004.

- [29] Morgan, R.A., Lehman, J.A., and M.K. Hibbs-Brenner, "Vertical-cavity surface-emitting lasers come of age", *Fabrication, Testing, and Reliability of Semiconductor Lasers*, Fallahi, M. and Wang, S.C., (Eds.), *Proceedings of SPIE*, Vol. 2683, April 1996, pp. 18-29.
- [30] Choquette, K.D. and Hou, H.Q., "Vertical-cavity surface emitting lasers: Moving from research to manufacturing", *Proc. IEEE*, Vol. 85, No. 11, November 1997, pp. 1730-1739.
- [31] Huffaker, D.L., Deppe, D.G., Kumar, K. and Rogers, T.J., "Native-oxide defined ring contact for low threshold vertical-cavity lasers", *Applied Physics Letter*, Vol. 65, No. 1, July 1994, pp. 97-99.
- [32] Thibeault, B.J., Scott, J.W., Peters, M.G., Peters, F.H., Young, D.B. and Coldren, L.A., "Integrable InGaAs/GaAs vertical-cavity surface-emitting lasers", *IEE Electronics Letters*, Vol. 29, No. 25, December 1993, pp. 2197-2199.
- [33] Verschaffelt, G., Albert, J., Panajotov, K., Nagler, B., Peeters, M., Thienpont, H., Veretennicoff, I., Danckaert, J., Barbay, S., Giacomelli, G. and Marin, F., "Frequency response of current modulation induced polarization switching in VCSELs", *Proceedings of SPIE*, Vol. 4649, January 2002, pp. 245-256.
- [34] Sale, T. E., "Vertical Cavity Surface Emitting Lasers" John Wiley & Sons Inc., 1995, pp. 33-35.
- [35] [http://www.batop.de/informations/n\\_GaAs.html](http://www.batop.de/informations/n_GaAs.html), "Sellmeyer Equation"
- [36] Adachi, S., "GaAs, AlAs, and  $\text{Al}_x\text{Ga}_{1-x}\text{As}$  Material parameters for use in research and device applications", Vol. 58, No.3, August 1985, pp. R1-R29.
- [37] Corzine, S.W., Geels, R.S., Scott, J.W., Yan, R.-H. and Coldren, L.A., "Design of Fabry-Perot surface-emitting lasers with a periodic gain structure", *IEEE Journal of Quantum Electronics*, Vol. 25, No. 6, June 1989, pp. 1513-1524.
- [38] Yu, S. F., Wong, W. N., Shum, P. and Li, E. H., "Theoretical Analysis of Modulation Response and Second-Order Harmonic Distortion in Vertical-Cavity Surface-Emitting Lasers", *IEEE Journal of Quantum Electronics*, Vol. 32, No. 12, December 1996, pp. 2139-2147.
- [39] Mena, P. V., Kang, Sung-Mo, and De Temple, T. A., "Rate-Equation-Based Laser Models with a Single Solution Regime", *IEEE Journal of Lightwave Technology*, Vol. 15, No. 4, April 1997 pp. 717-730.
- [40] Michalzik, R., Ebeling, K.J., "Operating Principles of VCSELs", Chap. 3 in *Vertical-Cavity Surface-Emitting Laser Devices*, H. Li and K. Iga (Eds.), Berlin: Springer-Verlag, 2003, pp. 53-98.
- [41] Olshansky, R., Hill, P., Lanzisera, V. and Powazinik, W., "Frequency response of  $1.3\mu\text{m}$  InGaAsP high speed semiconductor laser", *IEEE Journal of Quantum Electronics*, Vol. 23, No. 9, September 1987, pp. 1410-1418.